UNITED STATES AIR FORCE

SUMMER RESEARCH PROGRAM -- 1996

GRADUATE STUDENT RESEARCH PROGRAM FINAL REPORTS

VOLUME 8

PHILLIPS LABORATORY

RESEARCH & DEVELOPMENT LABORATORIES

5800 Uplander Way

Culver City, CA 90230-6608

Program Director, RDL
Gary Moore

Program Manager, AFOSR
Major Linda Steel-Goodwin

Program Manager, RDL
Scott Licoscos

Program Administrator, RDL
Johnetta Thompson

Program Administrator
Rebecca Kelly

Submitted to:

AIR FORCE OFFICE OF SCIENTIFIC RESEARCH

Bolling Air Force Base

Washington, D.C.

December 1996   AQ M01- 06 - 1290

20010321 058

REPORT DOCUMENTATION PAGE

Public reporting burden for this collection of information is estimated to average 1 hour per response, including the time for reviewing instructions, sear~~~ the collection of information. Send comments regarding this burden estimate or any other aspect of this collection of information, including sugge~~~ Operations and Reports, 1215 Jefferson Davis Highway, Suite 1204, Arlington, VA 22202-4302, and to the Office of Management and Budget, Paper~~~

AFRL-SR-BL-TR-00-

0738

viewing
~~mation

1. AGENCY USE ONLY *(Leave blank)*	2. REPORT DATE	3. REPOF
	December, 1996	

4. TITLE AND SUBTITLE	5. FUNDING NUMBERS
1996 Summer Research Program (SRP), Graduate Student Research Program (GSRP), Final Reports, Volume 8, Phillips Laboratory	F49620-93-C-0063

6. AUTHOR(S)

Gary Moore

7. PERFORMING ORGANIZATION NAME(S) AND ADDRESS(ES)	8. PERFORMING ORGANIZATION REPORT NUMBER
Research & Development Laboratories (RDL) 5800 Uplander Way Culver City, CA 90230-6608	

9. SPONSORING/MONITORING AGENCY NAME(S) AND ADDRESS(ES)	10. SPONSORING/MONITORING AGENCY REPORT NUMBER
Air Force Office of Scientific Research (AFOSR) 801 N. Randolph St. Arlington, VA 22203-1977	

11. SUPPLEMENTARY NOTES

12a. DISTRIBUTION AVAILABILITY STATEMENT	12b. DISTRIBUTION CODE
Approved for Public Release	

13. ABSTRACT *(Maximum 200 words)*

The United States Air Force Summer Research Program (USAF-SRP) is designed to introduce university, college, and technical institute faculty members, graduate students, and high school students to Air Force research. This is accomplished by the faculty members (Summer Faculty Research Program, (SFRP)), graduate students (Graduate Student Research Program (GSRP)), and high school students (High School Apprenticeship Program (HSAP)) being selected on a nationally advertised competitive basis during the summer intersession period to perform research at Air Force Research Laboratory (AFRL) Technical Directorates, Air Force Air Logistics Centers (ALC), and other AF Laboratories. This volume consists of a program overview, program management statistics, and the final technical reports from the GSRP participants at the Phillips Laboratory.

14. SUBJECT TERMS		15. NUMBER OF PAGES
Air Force Research, Air Force, Engineering, Laboratories, Reports, Summer, Universities, Faculty, Graduate Student, High School Student		16. PRICE CODE

17. SECURITY CLASSIFICATION OF REPORT	18. SECURITY CLASSIFICATION OF THIS PAGE	19. SECURITY CLASSIFICATION OF ABSTRACT	20. LIMITATION OF ABSTRACT
Unclassified	Unclassified	Unclassified	UL

GENERAL INSTRUCTIONS FOR COMPLETING SF 298

The Report Documentation Page (RDP) is used in announcing and cataloging reports. It is important that this information be consistent with the rest of the report, particularly the cover and title page. Instructions for filling in each block of the form follow. It is important to *stay within the lines* to meet *optical scanning requirements.*

Block 1. Agency Use Only *(Leave blank)*.

Block 2. Report Date. Full publication date including day, month, and year, if available
(e.g. 1 Jan 88). Must cite at least the year.

Block 3. Type of Report and Dates Covered. State whether report is interim, final, etc. If applicable, enter inclusive report dates (e.g. 10 Jun 87 - 30 Jun 88).

Block 4. Title and Subtitle. A title is taken from the part of the report that provides the most meaningful and complete information. When a report is prepared in more than one volume, repeat the primary title, add volume number, and include subtitle for the specific volume. On classified documents enter the title classification in parentheses.

Block 5. Funding Numbers. To include contract and grant numbers; may include program element number(s), project number(s), task number(s), and work unit number(s). Use the following labels:

C - Contract	**PR** - Project
G - Grant	**TA** - Task
PE - Program	**WU** - Work Unit
Element	Accession No.

Block 6. Author(s). Name(s) of person(s) responsible for writing the report, performing the research, or credited with the content of the report. If editor or compiler, this should follow the name(s).

Block 7. Performing Organization Name(s) and Address(es).
Self-explanatory.

Block 8. Performing Organization Report Number. Enter the unique alphanumeric report number(s) assigned by the organization performing the report.

Block 9. Sponsoring/Monitoring Agency Name(s) and Address(es).
Self-explanatory.

Block 10. Sponsoring/Monitoring Agency Report Number. *(If known)*

Block 11. Supplementary Notes. Enter information not included elsewhere such as: Prepared in cooperation with....; Trans. of....; To be published in.... When a report is revised, include a statement whether the new report supersedes or supplements the older report.

Block 12a. Distribution/Availability Statement. Denotes public availability or limitations. Cite any availability to the public. Enter additional limitations or special markings in all capitals (e.g. NOFORN, REL, ITAR).

DOD -	See DoDD 5230.24, "Distribution Statements on Technical Documents."
DOE -	See authorities.
NASA -	See Handbook NHB 2200.2.
NTIS -	Leave blank.

Block 12b. Distribution Code.

DOD -	Leave blank.
DOE -	Enter DOE distribution categories from the Standard Distribution for Unclassified Scientific and Technical Reports. Leave blank.
NASA -	Leave blank.
NTIS -	

Block 13. Abstract. Include a brief *(Maximum 200 words)* factual summary of the most significant information contained in the report.

Block 14. Subject Terms. Keywords or phrases identifying major subjects in the report.

Block 15. Number of Pages. Enter the total number of pages.

Block 16. Price Code. Enter appropriate price code *(NTIS only)*.

Blocks 17. - 19. Security Classifications. Self- explanatory. Enter U.S. Security Classification in accordance with U.S. Security Regulations (i.e., UNCLASSIFIED). If form contains classified information, stamp classification on the top and bottom of the page.

Block 20. Limitation of Abstract. This block must be completed to assign a limitation to the abstract. Enter either UL (unlimited) or SAR (same as report). An entry in this block is necessary if the abstract is to be limited. If blank, the abstract is assumed to be unlimited.

PREFACE

Reports in this volume are numbered consecutively beginning with number 1. Each report is paginated with the report number followed by consecutive page numbers, e.g., 1-1, 1-2, 1-3; 2-1, 2-2, 2-3.

This document is one of a set of 16 volumes describing the 1996 AFOSR Summer Research Program. The following volumes comprise the set:

VOLUME	TITLE
1	Program Management Report
	Summer Faculty Research Program (SFRP) Reports
2A & 2B	Armstrong Laboratory
3A & 3B	Phillips Laboratory
4	Rome Laboratory
5A, 5B & 5C	Wright Laboratory
6	Arnold Engineering Development Center, Wilford Hall Medical Center and Air Logistics Centers
	Graduate Student Research Program (GSRP) Reports
7A & 7B	Armstrong Laboratory
8	Phillips Laboratory
9	Rome Laboratory
10A & 10B	Wright Laboratory
11	Arnold Engineering Development Center, United States Air Force Academy, Wilford Hall Medical Center, and Wright Patterson Medical Center
	High School Apprenticeship Program (HSAP) Reports
12A & 12B	Armstrong Laboratory
13	Phillips Laboratory
14	Rome Laboratory
15A&15B	Wright Laboratory
16	Arnold Engineering Development Center

GSRP FINAL REPORT TABLE OF CONTENTS i-x

GSRP FINAL REPORTS

SRP Final Report Table of Contents

SRP Final Report Table of Contents

SRP Final Report Table of Contents

SRP Final Report Table of Contents

SRP Final Report Table of Contents

SRP Final Report Table of Contents

SRP Final Report Table of Contents

SRP Final Report Table of Contents

SRP Final Report Table of Contents

SRP Final Report Table of Contents

INTRODUCTION

The Summer Research Program (SRP), sponsored by the Air Force Office of Scientific Research (AFOSR), offers paid opportunities for university faculty, graduate students, and high school students to conduct research in U.S. Air Force research laboratories nationwide during the summer.

Introduced by AFOSR in 1978, this innovative program is based on the concept of teaming academic researchers with Air Force scientists in the same disciplines using laboratory facilities and equipment not often available at associates' institutions.

The Summer Faculty Research Program (SFRP) is open annually to approximately 150 faculty members with at least two years of teaching and/or research experience in accredited U.S. colleges, universities, or technical institutions. SFRP associates must be either U.S. citizens or permanent residents.

The Graduate Student Research Program (GSRP) is open annually to approximately 100 graduate students holding a bachelor's or a master's degree; GSRP associates must be U.S. citizens enrolled full time at an accredited institution.

The High School Apprentice Program (HSAP) annually selects about 125 high school students located within a twenty mile commuting distance of participating Air Force laboratories.

AFOSR also offers its research associates an opportunity, under the Summer Research Extension Program (SREP), to continue their AFOSR-sponsored research at their home institutions through the award of research grants. In 1994 the maximum amount of each grant was increased from $20,000 to $25,000, and the number of AFOSR-sponsored grants decreased from 75 to 60. A separate annual report is compiled on the SREP.

The numbers of projected summer research participants in each of the three categories and SREP "grants" are usually increased through direct sponsorship by participating laboratories.

AFOSR's SRP has well served its objectives of building critical links between Air Force research laboratories and the academic community, opening avenues of communications and forging new research relationships between Air Force and academic technical experts in areas of national interest, and strengthening the nation's efforts to sustain careers in science and engineering. The success of the SRP can be gauged from its growth from inception (see Table 1) and from the favorable responses the 1996 participants expressed in end-of-tour SRP evaluations (Appendix B).

AFOSR contracts for administration of the SRP by civilian contractors. The contract was first awarded to Research & Development Laboratories (RDL) in September 1990. After

completion of the 1990 contract, RDL (in 1993) won the recompetition for the basic year and four 1-year options.

2. PARTICIPATION IN THE SUMMER RESEARCH PROGRAM

The SRP began with faculty associates in 1979; graduate students were added in 1982 and high school students in 1986. The following table shows the number of associates in the program each year.

YEAR	SRP Participation, by Year			TOTAL
	SFRP	GSRP	HSAP	
1979	70		•	70
1980	87			87
1981	87			87
1982	91	17		108
1983	101	53		154
1984	152	84		236
1985	154	92		246
1986	158	100	42	300
1987	159	101	73	333
1988	153	107	101	361
1989	168	102	103	373
1990	165	121	132	418
1991	170	142	132	444
1992	185	121	159	464
1993	187	117	136	440
1994	192	117	133	442
1995	190	115	137	442
1996	188	109	138	435

Beginning in 1993, due to budget cuts, some of the laboratories weren't able to afford to fund as many associates as in previous years. Since then, the number of funded positions has remained fairly constant at a slightly lower level.

3.   RECRUITING AND SELECTION

The SRP is conducted on a nationally advertised and competitive-selection basis. The advertising for faculty and graduate students consisted primarily of the mailing of 8,000 52-page SRP brochures to chairpersons of departments relevant to AFOSR research and to administrators of grants in accredited universities, colleges, and technical institutions. Historically Black Colleges and Universities (HBCUs) and Minority Institutions (MIs) were included. Brochures also went to all participating USAF laboratories, the previous year's participants, and numerous individual requesters (over 1000 annually).

RDL placed advertisements in the following publications: *Black Issues in Higher Education, Winds of Change,* and *IEEE Spectrum.* Because no participants list either *Physics Today* or *Chemical & Engineering News* as being their source of learning about the program for the past several years, advertisements in these magazines were dropped, and the funds were used to cover increases in brochure printing costs.

High school applicants can participate only in laboratories located no more than 20 miles from their residence. Tailored brochures on the HSAP were sent to the head counselors of 180 high schools in the vicinity of participating laboratories, with instructions for publicizing the program in their schools. High school students selected to serve at Wright Laboratory's Armament Directorate (Eglin Air Force Base, Florida) serve eleven weeks as opposed to the eight weeks normally worked by high school students at all other participating laboratories.

Each SFRP or GSRP applicant is given a first, second, and third choice of laboratory. High school students who have more than one laboratory or directorate near their homes are also given first, second, and third choices.

Laboratories make their selections and prioritize their nominees. AFOSR then determines the number to be funded at each laboratory and approves laboratories' selections.

Subsequently, laboratories use their own funds to sponsor additional candidates. Some selectees do not accept the appointment, so alternate candidates are chosen. This multi-step selection procedure results in some candidates being notified of their acceptance after scheduled deadlines. The total applicants and participants for 1996 are shown in this table.

3

1996 Applicants and Participants			
PARTICIPANT CATEGORY	TOTAL APPLICANTS	SELECTEES	DECLINING SELECTEES
SFRP	572	188	39
(HBCU/MI)	(119)	(27)	(5)
GSRP	235	109	7
(HBCU/MI)	(18)	(7)	(1)
HSAP	474	138	8
TOTAL	1281	435	54

4. SITE VISITS

During June and July of 1996, representatives of both AFOSR/NI and RDL visited each participating laboratory to provide briefings, answer questions, and resolve problems for both laboratory personnel and participants. The objective was to ensure that the SRP would be as constructive as possible for all participants. Both SRP participants and RDL representatives found these visits beneficial. At many of the laboratories, this was the only opportunity for all participants to meet at one time to share their experiences and exchange ideas.

5. HISTORICALLY BLACK COLLEGES AND UNIVERSITIES AND MINORITY INSTITUTIONS (HBCU/MIs)

Before 1993, an RDL program representative visited from seven to ten different HBCU/Mis annually to promote interest in the SRP among the faculty and graduate students. These efforts were marginally effective, yielding a doubling of HBCI/MI applicants. In an effort to achieve AFOSR's goal of 10% of all applicants and selectees being HBCU/MI qualified, the RDL team decided to try other avenues of approach to increase the number of qualified applicants.
Through the combined efforts of the AFOSR Program Office at Bolling AFB and RDL, two very active minority groups were found, HACU (Hispanic American Colleges and Universities) and AISES (American Indian Science and Engineering Society). RDL is in communication with representatives of each of these organizations on a monthly basis to keep up with the their activities and special events. Both organizations have widely-distributed magazines/quarterlies in which RDL placed ads.

Since 1994 the number of both SFRP and GSRP HBCU/MI applicants and participants has increased ten-fold, from about two dozen SFRP applicants and a half dozen selectees to over 100 applicants and two dozen selectees, and a half-dozen GSRP applicants and two or three selectees to 18 applicants and 7 or 8 selectees. Since 1993, the SFRP had a two-fold applicant

4

increase and a two-fold selectee increase. Since 1993, the GSRP had a three-fold applicant increase and a three to four-fold increase in selectees.

In addition to RDL's special recruiting efforts, AFOSR attempts each year to obtain additional funding or use leftover funding from cancellations the past year to fund HBCU/MI associates. This year, 5 HBCU/MI SFRPs declined after they were selected (and there was no one qualified to replace them with). The following table records HBCU/MI participation in this program.

SRP HBCU/MI Participation, By Year				
YEAR	SFRP		GSRP	
	Applicants	Participants	Applicants	Participants
1985	76	23	15	11
1986	70	18	20	10
1987	82	32	32	10
1988	53	17	23	14
1989	39	15	13	4
1990	43	14	17	3
1991	42	13	8	5
1992	70	13	9	5
1993	60	13	6	2
1994	90	16	11	6
1995	90	21	20	8
1996	119	27	18	7

6. SRP FUNDING SOURCES

Funding sources for the 1996 SRP were the AFOSR-provided slots for the basic contract and laboratory funds. Funding sources by category for the 1996 SRP selected participants are shown here.

1996 SRP FUNDING CATEGORY	SFRP	GSRP	HSAP
AFOSR Basic Allocation Funds	141	85	123
USAF Laboratory Funds	37	19	15
HBCU/MI By AFOSR (Using Procured Addn'l Funds)	10	5	0
TOTAL	188	109	138

SFRP - 150 were selected, but nine canceled too late to be replaced.
GSRP - 90 were selected, but five canceled too late to be replaced (10 allocations for the ALCs were withheld by AFOSR.)
HSAP - 125 were selected, but two canceled too late to be replaced.

7. COMPENSATION FOR PARTICIPANTS

Compensation for SRP participants, per five-day work week, is shown in this table.

1996 SRP Associate Compensation

PARTICIPANT CATEGORY	1991	1992	1993	1994	1995	1996
Faculty Members	$690	$718	$740	$740	$740	$770
Graduate Student (Master's Degree)	$425	$442	$455	$455	$455	$470
Graduate Student (Bachelor's Degree)	$365	$380	$391	$391	$391	$400
High School Student (First Year)	$200	$200	$200	$200	$200	$200
High School Student (Subsequent Years)	$240	$240	$240	$240	$240	$240

The program also offered associates whose homes were more than 50 miles from the laboratory an expense allowance (seven days per week) of $50/day for faculty and $40/day for graduate students. Transportation to the laboratory at the beginning of their tour and back to their home destinations at the end was also reimbursed for these participants. Of the combined SFRP and

6

GSRP associates, 65 % (194 out of 297) claimed travel reimbursements at an average round-trip cost of $780.

Faculty members were encouraged to visit their laboratories before their summer tour began. All costs of these orientation visits were reimbursed. Forty-five percent (85 out of 188) of faculty associates took orientation trips at an average cost of $444. By contrast, in 1993, 58 % of SFRP associates took orientation visits at an average cost of $685; that was the highest percentage of associates opting to take an orientation trip since RDL has administered the SRP, and the highest average cost of an orientation trip. These 1993 numbers are included to show the fluctuation which can occur in these numbers for planning purposes.

Program participants submitted biweekly vouchers countersigned by their laboratory research focal point, and RDL issued paychecks so as to arrive in associates' hands two weeks later.

In 1996, RDL implemented direct deposit as a payment option for SFRP and GSRP associates. There were some growing pains. Of the 128 associates who opted for direct deposit, 17 did not check to ensure that their financial institutions could support direct deposit (and they couldn't), and eight associates never did provide RDL with their banks' ABA number (direct deposit bank routing number), so only 103 associates actually participated in the direct deposit program. The remaining associates received their stipend and expense payments via checks sent in the US mail.

HSAP program participants were considered actual RDL employees, and their respective state and federal income tax and Social Security were withheld from their paychecks. By the nature of their independent research, SFRP and GSRP program participants were considered to be consultants or independent contractors. As such, SFRP and GSRP associates were responsible for their own income taxes, Social Security, and insurance.

8.   CONTENTS OF THE 1996 REPORT

The complete set of reports for the 1996 SRP includes this program management report (Volume 1) augmented by fifteen volumes of final research reports by the 1996 associates, as indicated below:

1996 SRP Final Report Volume Assignments

LABORATORY	SFRP	GSRP	HSAP
Armstrong	2	7	12
Phillips	3	8	13
Rome	4	9	14
Wright	5A, 5B	10	15
AEDC, ALCs, WHMC	6	11	16

APPENDIX A -- PROGRAM STATISTICAL SUMMARY

A. Colleges/Universities Represented

Selected SFRP associates represented 169 different colleges, universities, and institutions, GSRP associates represented 95 different colleges, universities, and institutions.

B. States Represented

SFRP -Applicants came from 47 states plus Washington D.C. and Puerto Rico. Selectees represent 44 states plus Puerto Rico.

GSRP - Applicants came from 44 states and Puerto Rico. Selectees represent 32 states.

HSAP - Applicants came from thirteen states. Selectees represent nine states.

Total Number of Participants	
SFRP	188
GSRP	109
HSAP	138
TOTAL	435

Degrees Represented			
	SFRP	GSRP	TOTAL
Doctoral	184	1	185
Master's	4	48	52
Bachelor's	0	60	60
TOTAL	188	109	297

SFRP Academic Titles	
Assistant Professor	79
Associate Professor	59
Professor	42
Instructor	3
Chairman	0
Visiting Professor	1
Visiting Assoc. Prof.	0
Research Associate	4
TOTAL	188

Source of Learning About the SRP		
Category	Applicants	Selectees
Applied/participated in prior years	28%	34%
Colleague familiar with SRP	19%	16%
Brochure mailed to institution	23%	17%
Contact with Air Force laboratory	17%	23%
IEEE Spectrum	2%	1%
BIIHE	1%	1%
Other source	10%	8%
TOTAL	100%	100%

APPENDIX B – SRP EVALUATION RESPONSES

1. OVERVIEW

Evaluations were completed and returned to RDL by four groups at the completion of the SRP. The number of respondents in each group is shown below.

Table B-1. Total SRP Evaluations Received

Evaluation Group	Responses
SFRP & GSRPs	275
HSAPs	113
USAF Laboratory Focal Points	84
USAF Laboratory HSAP Mentors	6

All groups indicate unanimous enthusiasm for the SRP experience.

The summarized recommendations for program improvement from both associates and laboratory personnel are listed below:

A. Better preparation on the labs' part prior to associates' arrival (i.e., office space, computer assets, clearly defined scope of work).

B. Faculty Associates suggest higher stipends for SFRP associates.

C. Both HSAP Air Force laboratory mentors and associates would like the summer tour extended from the current 8 weeks to either 10 or 11 weeks; the groups state it takes 4-6 weeks just to get high school students up-to-speed on what's going on at laboratory. (Note: this same argument was used to raise the faculty and graduate student participation time a few years ago.)

2. 1996 USAF LABORATORY FOCAL POINT (LFP) EVALUATION RESPONSES

The summarized results listed below are from the 84 LFP evaluations received.

1. LFP evaluations received and associate preferences:

Table B-2. Air Force LFP Evaluation Responses (By Type)

Lab	Evals Recv'd	How Many Associates Would You Prefer To Get ? (% Response)											
		SFRP				GSRP (w/Univ Professor)				GSRP (w/o Univ Professor)			
		0	1	2	3+	0	1	2	3+	0	1	2	3+
AEDC	0	-	-	-	-	-	-	-	-	-	-	-	-
WHMC	0	-	-	-	-	-	-	-	-	-	-	-	-
AL	7	28	28	28	14	54	14	28	0	86	0	14	0
FJSRL	1	0	100	0	0	100	0	0	0	0	100	0	0
PL	25	40	40	16	4	88	12	0	0	84	12	4	0
RL	5	60	40	0	0	80	10	0	0	100	0	0	0
WL	46	30	43	20	6	78	17	4	0	93	4	2	0
Total	84	32%	50%	13%	5%	80%	11%	6%	0%	73%	23%	4%	0%

LFP Evaluation Summary. The summarized responses, by laboratory, are listed on the following page. LFPs were asked to rate the following questions on a scale from 1 (below average) to 5 (above average).

2. LFPs involved in SRP associate application evaluation process:
    a. Time available for evaluation of applications:
    b. Adequacy of applications for selection process:
3. Value of orientation trips:
4. Length of research tour:
5   a. Benefits of associate's work to laboratory:
    b. Benefits of associate's work to Air Force:
6.   a. Enhancement of research qualifications for LFP and staff:
    b. Enhancement of research qualifications for SFRP associate:
    c. Enhancement of research qualifications for GSRP associate:
7.   a. Enhancement of knowledge for LFP and staff:
    b. Enhancement of knowledge for SFRP associate:
    c. Enhancement of knowledge for GSRP associate:
8. Value of Air Force and university links:
9. Potential for future collaboration:
10.   a. Your working relationship with SFRP:
    b. Your working relationship with GSRP:
11. Expenditure of your time worthwhile:

12. Quality of program literature for associate:
13. a. Quality of RDL's communications with you:
    b. Quality of RDL's communications with associates:
14. Overall assessment of SRP:

Table B-3. Laboratory Focal Point Reponses to above questions

	AEDC	AL	FJSRL	PL	RL	WHMC	WL
# Evals Recv'd	0	7	1	14	5	0	46
Question #							
2	-	86 %	0 %	88 %	80 %	-	85 %
2a	-	4.3	n/a	3.8	4.0	-	3.6
2b	-	4.0	n/a	3.9	4.5	-	4.1
3	-	4.5	n/a	4.3	4.3	-	3.7
4	-	4.1	4.0	4.1	4.2	-	3.9
5a	-	4.3	5.0	4.3	4.6	-	4.4
5b	-	4.5	n/a	4.2	4.6	-	4.3
6a	-	4.5	5.0	4.0	4.4	-	4.3
6b	-	4.3	n/a	4.1	5.0	-	4.4
6c	-	3.7	5.0	3.5	5.0	-	4.3
7a	-	4.7	5.0	4.0	4.4	-	4.3
7b	-	4.3	n/a	4.2	5.0	-	4.4
7c	-	4.0	5.0	3.9	5.0	-	4.3
8	-	4.6	4.0	4.5	4.6	-	4.3
9	-	4.9	5.0	4.4	4.8	-	4.2
10a	-	5.0	n/a	4.6	4.6	-	4.6
10b	-	4.7	5.0	3.9	5.0	-	4.4
11	-	4.6	5.0	4.4	4.8	-	4.4
12	-	4.0	4.0	4.0	4.2	-	3.8
13a	-	3.2	4.0	3.5	3.8	-	3.4
13b	-	3.4	4.0	3.6	4.5	-	3.6
14	-	4.4	5.0	4.4	4.8	-	4.4

3. 1996 SFRP & GSRP EVALUATION RESPONSES

The summarized results listed below are from the 257 SFRP/GSRP evaluations received.

Associates were asked to rate the following questions on a scale from 1 (below average) to 5 (above average) - by Air Force base results and over-all results of the 1996 evaluations are listed after the questions.

1. The match between the laboratories research and your field:
2. Your working relationship with your LFP:
3. Enhancement of your academic qualifications:
4. Enhancement of your research qualifications:
5. Lab readiness for you: LFP, task, plan:
6. Lab readiness for you: equipment, supplies, facilities:
7. Lab resources:
8. Lab research and administrative support:
9. Adequacy of brochure and associate handbook:
10. RDL communications with you:
11. Overall payment procedures:
12. Overall assessment of the SRP:
13.   a. Would you apply again?
        b. Will you continue this or related research?
14. Was length of your tour satisfactory?
15. Percentage of associates who experienced difficulties in finding housing:
16. Where did you stay during your SRP tour?
        a.   At Home:
        b.   With Friend:
        c.   On Local Economy:
        d.   Base Quarters:
17. Value of orientation visit:
        a.   Essential:
        b.   Convenient:
        c.   Not Worth Cost:
        d.   Not Used:

SFRP and GSRP associate's responses are listed in tabular format on the following page.

Table B-4. 1996 SFRP & GSRP Associate Responses to SRP Evaluation

	Arnold	Brooks	Edwards	Eglin	Griffis	Hanscom	Kelly	Kirtland	Lackland	Robins	Tyndall	WPAFB	average
# res	6	48	6	14	31	19	3	32	1	2	10	85	257
1	4.8	4.4	4.6	4.7	4.4	4.9	4.6	4.6	5.0	5.0	4.0	4.7	4.6
2	5.0	4.6	4.1	4.9	4.7	4.7	5.0	4.7	5.0	5.0	4.6	4.8	4.7
3	4.5	4.4	4.0	4.6	4.3	4.2	4.3	4.4	5.0	5.0	4.5	4.3	4.4
4	4.3	4.5	3.8	4.6	4.4	4.4	4.3	4.6	5.0	4.0	4.4	4.5	4.5
5	4.5	4.3	3.3	4.8	4.4	4.5	4.3	4.2	5.0	5.0	3.9	4.4	4.4
6	4.3	4.3	3.7	4.7	4.4	4.5	4.0	3.8	5.0	5.0	3.8	4.2	4.2
7	4.5	4.4	4.2	4.8	4.5	4.3	4.3	4.1	5.0	5.0	4.3	4.3	4.4
8	4.5	4.6	3.0	4.9	4.4	4.3	4.3	4.5	5.0	5.0	4.7	4.5	4.5
9	4.7	4.5	4.7	4.5	4.3	4.5	4.7	4.3	5.0	5.0	4.1	4.5	4.5
10	4.2	4.4	4.7	4.4	4.1	4.1	4.0	4.2	5.0	4.5	3.6	4.4	4.3
11	3.8	4.1	4.5	4.0	3.9	4.1	4.0	4.0	3.0	4.0	3.7	4.0	4.0
12	5.7	4.7	4.3	4.9	4.5	4.9	4.7	4.6	5.0	4.5	4.6	4.5	4.6
						Numbers below are percentages							
13a	83	90	83	93	87	75	100	81	100	100	100	86	87
13b	100	89	83	100	94	98	100	94	100	100	100	94	93
14	83	96	100	90	87	80	100	92	100	100	70	84	88
15	17	6	0	33	20	76	33	25	0	100	20	8	39
16a	-	26	17	9	38	23	33	4	-	-	-	30	
16b	100	33	-	40	-	8	-	-	-	-	36	2	
16c	-	41	83	40	62	69	67	96	100	100	64	68	
16d	-	-	-	-	-	-	-	-	-	-	-	0	
17a	-	33	100	17	50	14	67	39	-	50	40	31	35
17b	-	21	-	17	10	14	-	24	-	50	20	16	16
17c	-	-	-	-	10	7	-	-	-	-	-	2	3
17d	100	46	-	66	30	69	33	37	100	-	40	51	46

4. 1996 USAF LABORATORY HSAP MENTOR EVALUATION RESPONSES

Not enough evaluations received (5 total) from Mentors to do useful summary.

5. 1996 HSAP EVALUATION RESPONSES

The summarized results listed below are from the 113 HSAP evaluations received.

HSAP apprentices were asked to rate the following questions on a scale from
1 (below average) to 5 (above average)

1. Your influence on selection of topic/type of work.
2. Working relationship with mentor, other lab scientists.
3. Enhancement of your academic qualifications.
4. Technically challenging work.
5. Lab readiness for you: mentor, task, work plan, equipment.
6. Influence on your career.
7. Increased interest in math/science.
8. Lab research & administrative support.
9. Adequacy of RDL's Apprentice Handbook and administrative materials.
10. Responsiveness of RDL communications.
11. Overall payment procedures.
12. Overall assessment of SRP value to you.
13. Would you apply again next year?   Yes (92 %)
14. Will you pursue future studies related to this research?   Yes (68 %)
15. Was Tour length satisfactory?   Yes (82 %)

	Arnold	Brooks	Edwards	Eglin	Griffiss	Hanscom	Kirtland	Tyndall	WPAFB	Totals
# resp	5	19	7	15	13	2	7	5	40	113
1	2.8	3.3	3.4	3.5	3.4	4.0	3.2	3.6	3.6	3.4
2	4.4	4.6	4.5	4.8	4.6	4.0	4.4	4.0	4.6	4.6
3	4.0	4.2	4.1	4.3	4.5	5.0	4.3	4.6	4.4	4.4
4	3.6	3.9	4.0	4.5	4.2	5.0	4.6	3.8	4.3	4.2
5	4.4	4.1	3.7	4.5	4.1	3.0	3.9	3.6	3.9	4.0
6	3.2	3.6	3.6	4.1	3.8	5.0	3.3	3.8	3.6	3.7
7	2.8	4.1	4.0	3.9	3.9	5.0	3.6	4.0	4.0	3.9
8	3.8	4.1	4.0	4.3	4.0	4.0	4.3	3.8	4.3	4.2
9	4.4	3.6	4.1	4.1	3.5	4.0	3.9	4.0	3.7	3.8
10	4.0	3.8	4.1	3.7	4.1	4.0	3.9	2.4	3.8	3.8
11	4.2	4.2	3.7	3.9	3.8	3.0	3.7	2.6	3.7	3.8
12	4.0	4.5	4.9	4.6	4.6	5.0	4.6	4.2	4.3	4.5
Numbers below are percentages										
13	60%	95%	100%	100%	85%	100%	100%	100%	90%	92%
14	20%	80%	71%	80%	54%	100%	71%	80%	65%	68%
15	100%	70%	71%	100%	100%	50%	86%	60%	80%	82%

TESTING THE FROZEN SCREEN MODEL OF ATMOSHPERIC TURBULENCE
AND
AN INTERFEROMETER DESIGN
FOR MEASURING ATMOSPHERIC
TURBULENCE NEAR GROUND LEVELS

Luis M. Amato
Graduate Student
Department of Physics

University of Puerto Rico
Mayaguez campus

TESTING THE FROZEN SCREEN MODEL OF ATMOSHPERIC TURBULENCE
AND
AN INTERFEROMETER DESIGN FOR MEASURING ATMOSPHERIC TURBULENCE NEAR GROUND LEVELS

Luis Amato
Graduate Student
Department of Physics
University of Puerto Rico - Mayaguez campus

Abstract

Atmospheric turbulence is responsible for scattering of the light that makes it's way through the atmosphere and therefore deteriorates the observations being made by any astronomical instrument. This study designs a triple coincidence experiment to test the frozen screen model of atmospheric turbulence and determine if we can put in place an interferometer or equivalent system that will measure the atmospheric turbulence in the near field. Various types of interferometers have been considered including the Fabry - Perot and the Mach - Zehnder arrangements. Other design considerations include the path lengths necessary for detection of small changes in the index of refraction of air, light sources and positioning of the interferometer.

The "frozen" screen model is to be tested to determine if it can be used as a predictive tool. If the turbulent disturbances travel as a frozen screen it should be possible to sample them upstream of a telescope and apply corrections in real time; or if this is not possible then downstream of the telescope for post detection corrections. We propose to build an 'Amato' (one arm in vacuum) Mach-Zehnder type interferometer with physically coupled arms that expand and contract together to null any pathlength changes in the system due to changes in the apparatus. This is to insure that all phase shifts in the fringe pattern are due to changes in the index of refraction of the air in the open arm, see section *. We propose to use two identical setups in an upwind/downwind configuration and check for time delayed coincidences in the fringe patterns. In parallel we propose to run a very high resolution Fabry-Perot Interferometer and very sensitive Microbarograph and do similar coincidence studies to see if any or all methods are useful in detecting and predicting atmospheric fluctuations.

TESTING THE FROZEN SCREEN MODEL OF ATMOSHPERIC TURBULENCE AND AN INTERFEROMETER DESIGN FOR MEASURING ATMOSPHERIC TURBULENCE NEAR GROUND LEVELS

Luis M. Amato

A. Introduction. It is common knowledge that most, if not all, astronomical observations done on earth are affected by turbulence present in the earth's atmosphere. In fluid mechanics the motion of a liquid or gas is considered to be turbulent when it's velocity at any point is fluctuating in magnitude and direction in a chaotic and random manner. Furthermore what distinguishes turbulence from wave action is the fact that turbulence leads to increased rates of transport of heat, momentum and other properties like salt or water vapor [ref. 1]. The stability of density gradients can greatly modify turbulence and the transport that it produces and so can compressibility and electrical conductivity.

Atmospheric turbulence, which is the main concern of this study, is considered by meteorology as small scale motion. It's two major causes are: 1) mechanical turbulence due to the rapid change of large scale wind, and 2) heat convection, caused by heating from below or cooling from above, [ref. 1]. There are three regions in which turbulence is most important, these are: 1) near the ground, 2) in convective air flow, and 3) turbulence occurring in clear air between 25,000-40,000 feet, known as clear air turbulence (CAT). It is also important to notice that atmospheric turbulence is affected by natural factors. For example on a windy day turbulence is stronger near the ground and will therefore be dependent on wind velocity, this type of turbulence is stronger over rough terrain. Convection will increase the turbulence in the daytime and will suppress it at night.

The effects of turbulence are many, first it affects the distribution of the meteorological variables by its ability to produce vertical mixing which is weakest near the ground: therefore we encounter the strongest turbulence gradients immediately above the surface. It also has a marked effect on light that makes it way through the atmosphere, since the index of refraction of the atmosphere, even at a given wavelength, is not constant because the atmosphere's density and temperature are not constant. Some of the reasons why

1-3

atmospheric density is not constant are its decrease with altitude, heating by the sun, and turbulent wind flow. This creates localized changes in the index of refraction for different layers in the atmosphere which causes rays of light to be refracted.. Turbulence also creates irregular patches of temperature and moisture which in turn produce scattering of the electromagnetic and sound waves that go through it. For optical observations this effect creates a lot of trouble. When a telescope looks through an isoplanatic patch (a patch of the atmosphere where the angular size of a single atmospheric coherence cell is determined by the physical size of the cell and its elevation [ref. 2]) within a turbulent region the light is affected more or less uniformly. But if the telescope looks through patches sweeping by the effects of the different patches are combined and the visual image is deteriorated. Although this effect diminishes with increasing wavelength it still affects observations made in the visible and near to mid infrared range of the electromagnetic spectrum.

All of the above effects combine to degrade the image being observed by producing scintillation, "quivering", image motion and scattering. Several modern adaptive optics systems have been created to solve or at least diminish this problem, for example by using a laser beam to create an artificial beacon in the sky that serves as a guide star and measuring the effect of the atmosphere on the light from the guide star to adjust a deformable mirror to conjugate this effects [ref. 3]. The high cost and lack of availability of this system is one of it's biggest constraints. Other systems are available or under development [ref.13] but all suffer from similar drawbacks.

The issue we would like to address is the problem of light starvation. Since our method of correction does not use any light gathered by the telescope or have any elements in common with the telescope it does not use any of the photons available to the system and then lower it's sensitivity.

There have been many studies that have measured atmospheric turbulence at different locations and their findings are reasons to fuel the purpose of this project. For example, one of those used an acoustic echo sounder to measure the turbulence above Air Force Maui Optical Station (AMOS) and found that most of the optical turbulence above this site is in the first 7.5 to 100m above the ground [ref 5]. Another study performed at the Infrared Spacial Interferometer (ISI) located on Mt. Wilson, California

1-4

found that 20% of the fluctuation power observed from a star is caused by close ground turbulence. Furthermore, for t=100 seconds in the observations in that study 12% of the fringe fluctuation (temporal changes in the interference pattern of the light combined from the two telescopes of the interferometer) occurs close to the ground, specifically a few tens of meters from the ground [ref 8]. These among others are all facts that point towards the development of an instrument that can measure the atmospheric turbulence concentrated near the ground, and can do so without damaging the medium being measured or creating more turbulence.

B. Purpose

The purpose of this study is two fold: to determine if the frozen screen model of atmospheric turbulence is valid and, if it is, to design an interferometer, or equivalent system, that will be able to measure the atmospheric turbulence that is present near a telescope and which degrades the irradiance that is being observed. Then the interferometer can relay this information to the telescope so it can correct for the (image) degradation produced by the turbulence. Since 50 to 70 percent of the atmospheric turbulence that affects astronomical observations is located in the first 50 to 100 meters above the ground, a regime known as the surface layer of the atmosphere, the interferometer will be designed with the objective of measuring this part of the atmosphere as it will prove to give the best results for imaging correction. As an adjunct to our consideration of a vertically sampling interferometer we propose to test two other methods that will be simpler to implement The first is telescope level sampling with a Fabry-Perot interferometer of fluctuations in the index of refraction of the air traveling over the telescope and the second is to use a microbarograph that will sample total column variations of pressure over the telescope which we hope to be able to translate into a correction. We will test these methods using coincidence techniques with the dual interferometers; and wind speed and direction monitors.

The most important characteristic that the system should posses is the ability to relay it's information in real (or near real) time so the telescope may benefit from the information nearly instantaneously. This is something that couldn't be achieved by many of the atmospheric turbulence measuring devices seen

before because they needed to gather the information and then analyze it [ref 4,5]; a process which takes too much time for our purpose. However this may prove to be unreasonable and post observation corrections may still be necessary.

C. Considerations for Experimental Design

The atmosphere is a random medium whose behavior is hard to predict but has been studied quite extensively. The Kolmogorov model provides a means of understanding turbulent behavior and tells us that the small scale structure of motion has the property of being locally homogeneous and isotropic [ref6]. Although the details of this hypothesis are not important to us at this time Taylor's "frozen screen" model is. Taylor's hypothesis tells us that for a stationary and homogeneous random field f(r, t) where r is a point in space and t is time, whose time changes are associated with a translation of the spatial field distribution with a constant velocity v, and that this translation does not include any mixing (therefore a "frozen" field), then

$$f (r,\ t + t') = f (r - v\, t',\ t)$$

where v can be taken to be the mean wind velocity with which the field f (r) is being transported [ref 6]. Therefore if we were measuring the atmospheric turbulence in two different points, point A and point B, where B sits downstream from A in terms of wind direction, we would expect to find the same atmospheric turbulence at point A as at point B if the Taylor's hypothesis holds.

The first part of this project will consist of the testing of the "frozen" screen model. This is crucial at this point because if we find out that the "frozen" screen model is not valid, like in other experiments (for example ref. 8), then there is no purpose in building this interferometer because then the turbulence the interferometer measures will not be the same one that is going over the telescope and the corrections that the telescope makes will not be valid. In order to test the "frozen" screen we intend to use two interferometers which will most likely resemble the final design except may be on a smaller scale, and place these interferometers in a similar positions as points A and B in the above example. This will confirm if the atmospheric turbulence we measure with the first one will be the same that we measure

with the second. We will put a Fabry-Perot and a microbaograph at one of these positions to test alternate approaches to the same correction. An important remark is that this experiment will eventually have to be done at the site of the telescope since turbulence varies with surrounding terrain and while on some locations or systems the Taylor model is not valid on others it often is, as seen in ref. 12. This is one reason we have designed a triple coincidence experiment to check the frozen screen model; the Fabry-Perot and microbarographs will be much simpler and more transportable and if we can show that they produce similar results to the larger interferometer testing at observing sites will be much simplified.

The "Amato" Interferometer will initially be built as a bench model to test the null hypothesis of equal arm length changes. Referring to figures 1 and 2; the optics of the open arm of the interferometer will be rigidly coupled to the evacuated light pipe under the assumption that expansion and contraction of both arms will be the same thereby nulling any phase change due to physical dimensional changes in the system. If this proves possible the field model will be constructed with most of the vacuum system, light source and detection system below ground surface level to reduce perturbing the air flow through the second (down wind) interferometer.

A few designs have been theorized and the first of these is shown in fig. 1. [Another can be seen in fig. 2 On page 10] It is a division-of-amplitude interferometer with a very simple design that consists of the light, after passing through the beam splitter, being divided into two rays by the wedge in the middle of the interferometer and then being reflected by the respective mirrors in lines *a* and *b*. The interference pattern being recorded by the detector. The most important part of this design is that line *a* is exposed to the atmospheric turbulence and line *b* is protected by being in a evacuated light pipe. What we hope to accomplish with this design is to have line *b* so well protected that any shift we see in the fringe pattern must be caused by the change in index of refraction of the medium through which line *a* was traveling.
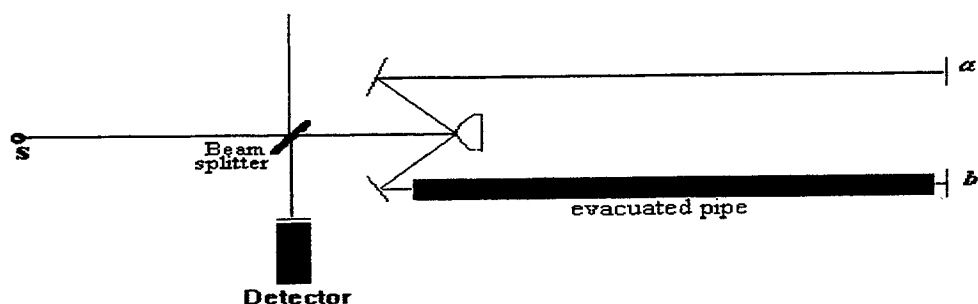
Fig. 1 - General interferometer design for testing "frozen screen" model, where a is the arm that is exposed to turbulence and b is the reference line.

We will need to insure that physical pathlength changes are identical in both arms. We plan to do this, as mentioned above, by making the evacuated pipe the mounting structure for the optics in arm *a*. Subsequently if we measure the fringe shift we can determine the amount of atmospheric turbulence, as represented by the change in the index of refraction of the air, by calculating the change in the light's optical path as a result of the light in line *a* passing through the turbulence. In order to maintain line *b* as controlled as possible a vacuum system will be desirable for thermal and pressure isolation; although a vacuum system introduces many variables of its own. It may even be buried so it is not affected by the wind and temperature variations can be better controlled. If burying the line proves to be successful a vacuum system may not be needed and a sealed (to isolate pressure changes) light pipe may suffice. As we said before since this design is to test the "frozen" screen it will require another interferometer just like this one but further down the wind direction, to make the same measurements and then use a correlation function for the data taken by both. The Fabry-Perot and differential pressure transducer will be run in parallel and similar cross correlations will be done. We will look for similar disturbance patters in each data set with time delays relating to the distance between the instruments and the wind speed.

1-8

Calculations have been made to have an idea of what physical path length the interferometer arms should have in order to see a half or quarter of wavelength change in the fringe pattern. These calculations have been done for different laser sources which include a He-Ne laser at .6328 microns, a CO_2 laser at 11.1 microns and a blue laser at 442 and 488 nm. The index of refraction for a temperature of 15°C and pressure of 760 mm Hg was calculated using the formula [ref 9]

$$(n_{15,760} - 1)\, 10^7 = 2726.43 + 12.288/(\lambda^2 \times 10^{-8}) + 0.355/(\lambda^4 \times 10^{-16})$$

where λ is the wavelength, and the Barrell and Sears equation was used for the change of the index of refraction with temperature and pressure [ref 10]

$$n_{tp} - 1 = (n_{15,760} - 1)\, [p(1 + \beta_{Tp})(1 + 15\alpha)] / 760\, (1 + 760\, \beta_{15})(1 + \alpha T)$$

where T = temperature
   p = pressure
   $\alpha = 0.00366$
   $\beta_T = (1.049 - 0.015\, T)\, 10^{-6}$
   $\beta_{15} = 0.813 \times 10^{-6}$

The physical path length needed according to the wavelength and change in index of refraction is given by the formula $X = 0.5\, \lambda / \Delta n$ where a variation of 0.01°C was used. These calculations resulted in the value of approximately 584 meters for the CO_2 laser, 33 m for the He-Ne laser, 0.624 m for the 442 nm blue laser and 1 m for the 488 nm blue laser. What these results mean is that, for example, if we used a CO_2 laser to see a half wavelength change in the fringe pattern the interferometer arm will have to be 584 meters long. Although this is not impossible it will not be convenient either; a He-Ne laser will be more convenient and then you can make the interferometer arm 5m and have the light bounce back and forth between the mirrors six times. In any case it would be most appropriate in the test phase to have the actual length (as opposed to the folded length) of the exposed arm approximately equal to the isoplanatic patch size at the appropriate wavelength.

This type of arrangement is shown in figure 2 which also demonstrates the other type of interferometer in consideration which is a Mach-Zehnder type of interferometer. As you can see in the figure the beam goes through a beam splitter and is divided into the two arms of the interferometer, one which is shielded

1-9
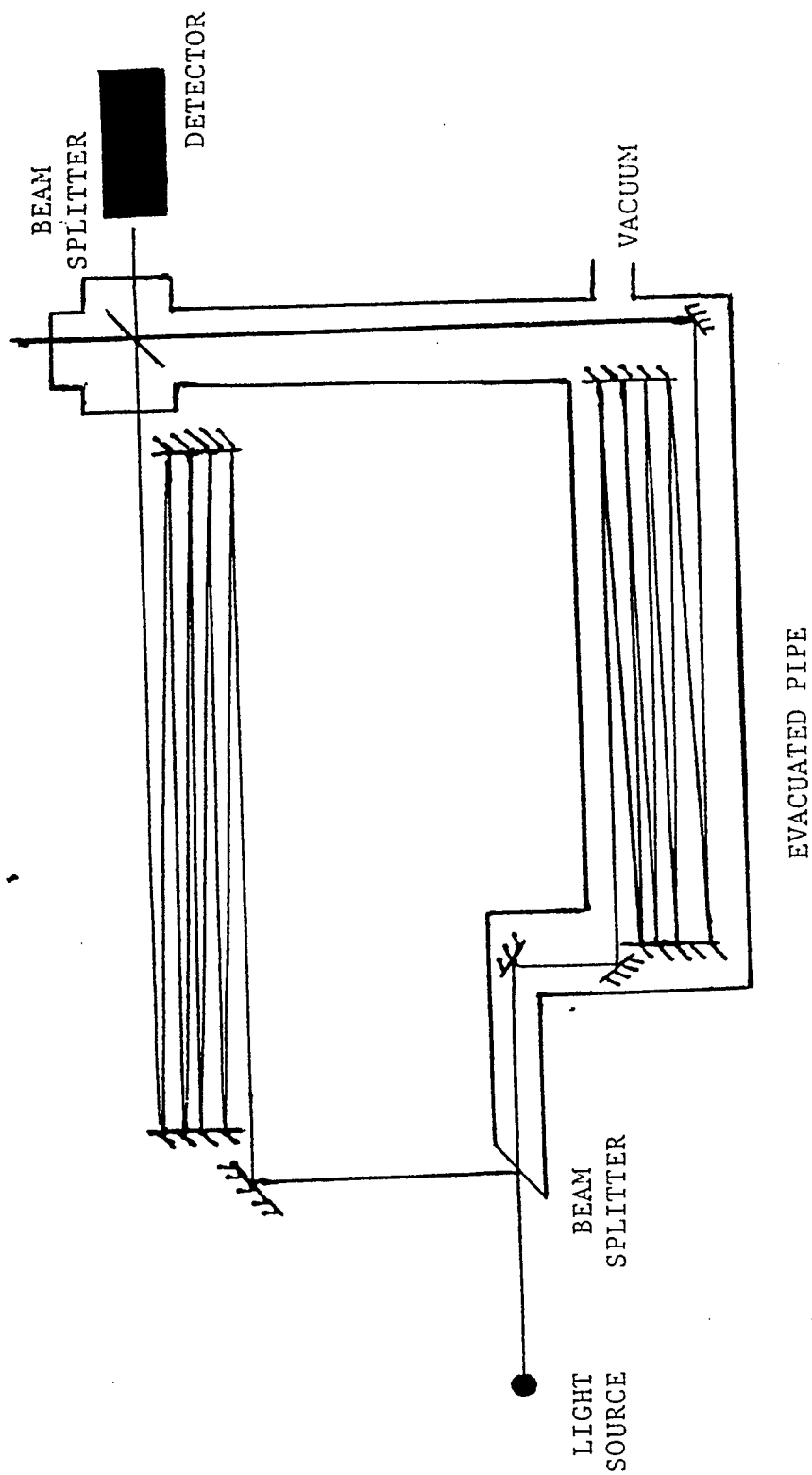
FIG. 2 – Prototype for Mach–Zender type interferometer.

1 –10

by an evacuated light pipe and the other arm that will pass through the turbulence. In both arms you can see the multiple reflections of the light as described above and then the beams recombine at the second beam splitter and the interference pattern is captured at the detector. The arms need be equal only within the coherence length of the light source. With a laser source this is easily accomplished.

Additional experimental considerations address the time scale of the fluctuations which are of order 1 ms. Optical detectors routinely operate at much shorter time scales and consequently will present little problem for either the "Amato" Interferometer or the Fabry-Perot. We have found differential pressure transducers (off the shelf) with response times of 1-2 ms and accuracies of greater than one part in a million (up to 1 part in 10^8) and we feel these will be sufficient for our purposes.

Summary: We have designed an experimental procedure to test the "frozen screen" model of atmospheric turbulence. To do this we have also designed an (Amato) interferometer with one arm under vacuum rigidly coupled to a parallel arm that will sample the air. The interferometer design will be bench tested and then (hopefully) set up in the field as two instruments in an up wind / down wind configuration in conjunction with a microbarograph and Fabry-Perot Interferometer. The data will be cross correlated to see if there is a significant time delayed signal that relates to (distance of separation/wind speed) thus "proving" the frozen screen. If this is proven the experiment will be repeated with a vertical separation of the Amato Interferometers of order 50 meters; once again in coincidence with the microbarograph and Fabry-Perot. This will sample the near earth turbulent layer passing over a hypothetical observing instrument. It will require careful preparation to avoid adding turbulence to the field of view of a telescope, but if the frozen screen model proves correct the vertical sampling can be carried out downwind of the observing instrument. The principal reason for testing the microbarograph and Fabry-Perot is that they are less intrusive more mobile instruments and will cause less interference and prove more versatile in the observatory environment. In consideration of the geometry of observing off vertical one must envision an array of instruments that can sample the air path of the incident light.

References

1) Encyclopedia of Atmospheric Sciences and Astrogeology, edited by Fairbridge, R.W, Reinhold, publishing, New York, 1967.

2) Encyclopedia of Lasers and Optical Technology, edited by Meyers, R.A, Academic Press, California, 1991.

3) Collins, G.P., "Making Stars To See Stars: DOD Adaptive Optics Work is Declassified," Physics Today, pp 17-21, February 1992.

4) Hoover, C.R., Investigation of a Single Point Temperature Probe for Measurement of Atmospheric Turbulence, M.S. Thesis, Naval Postgraduate School , Monterey, California, December 1991.

5) Mattingly, T.S., Measurement of Surface Layer Optical Turbulence Above AMOS, M.S. Thesis, Naval Postgraduate School, Monterey, California, December 1991.

6) Tatarskii, V.I., The Effects of the Turbulent Atmosphere on Wave Propagation, National Science Foundation, Washington D.C. 1971.

7) Steel ,W.H., Interferometry , 2nd edition Cambridge University Press 1983.

8) Bester, M., Danchi, W.C., Degiacomi, C.G., Greenhill, L.J. and Townes, C.H. Atmospheric Fluctuations - Empirical Structure Functions and Projected Performance of Future Instruments, Space Sciences
Laboratory, University of California at Berkeley, 1991.

9) CRC Handbook of Chemistry and Physics, R.C. Weast editor in chief, CRC press, Florida, 1989.

10) American Institute of Physics Handbook, 3rd ed., edited by D.E. Gray, McGraw Hill, New York, 1972.

11) Tolansky, S., An Introduction to Interferometry, Longmans, Green and co., London, 1955.

12) Colavita , MM, Shao, M., Staelin, D.H., Applied Optics, Vol. 26 No. 19, 01 Oct 87, pg. 4106.

13) see for example: Ealey and Merkle, Adaptive Optics in Astronomy; 1994 Kona, SPIE vol. 2201.

STUDY OF PERIOD DOUBLING BIFURCATIONS IN A LOSS AND PUMP MODULATED
SPECIALLY CONSTRUCTED ND:YAG LASER

Colin P. Cahill
Graduate Student
Department of Electrical Engineering

University of Washington
Department of Electrical Engineering
Box 352500
Seattle, WA 98195-2500

August 1996

STUDY OF PERIOD DOUBLING BIFURCATIONS IN A LOSS AND PUMP MODULATED SPECIALLY CONSTRUCTED ND:YAG LASER

Colin P. Cahill
Graduate Student
Department of Electrical Engineering
University of Washington

Abstract

A simple Neodymium-doped Yttrium-Aluminum-Garnet (Nd:YAG) laser was constructed, and its behavior studied. The objective of this project was to drive a solid-state laser, with single longitudinal and transverse modes, into a chaotic state and to map the period-doubling route to chaos. In order to achieve these characteristics, a very short laser cavity was employed, and an acousto-optic modulator was aligned inside the laser cavity. The simplicity of this laser configuration allows comparisons between experimental test results and theoretical models, which are ineffective for laser systems with many modes, due to the required complexity of a model for such a system.

STUDY OF PERIOD DOUBLING BIFURCATIONS IN A LOSS AND PUMP MODULATED SPECIALLY CONSTRUCTED ND:YAG LASER

Colin P. Cahill

Introduction

A recent upsurge in the amount of research conducted toward an understanding of the dynamics of chaotic systems has resulted in many different projects with the aim of harnessing this newfound power of "controlled" chaos. Therefore, it is only natural that lasers would become a part of this quest. To this end, there have been many laser systems constructed and theoretically modeled around the world with several different mechanisms employed to excite chaotic dynamics. However, in order to accurately compare experimental data of this kind to theory, the laser must be simple and its physics understood, so that a reliable model can be developed. The easiest lasers to model are those with single longitudinal and single transverse modes, which is difficult to achieve for certain systems such as gas lasers due to construction constraints. Laser diodes, another system studied for chaotic dynamics, oscillate at very high frequencies, making time-domain analysis impossible. Solid-state lasers, on the other hand, can be built to guarantee single-mode operation with minimal alterations to the basic system, and their dynamics are slow enough to resolve time-domain data. Therefore, this project's objective is to construct a single-mode solid-state Nd:YAG laser that can be driven into a chaotic state, and then to analyze the laser dynamics.

Methodology

General characteristics of Nd:YAG lasers

Neodymium-doped Yttrium-Aluminum-Garnet (Nd:YAG) lasers are the most popular lasers used in commercial markets today due to their versatility, and they are used in many different applications throughout industry. The basic characteristics of Nd:YAG lasers are as follows: (1) a solid-state crystal with good hardness and high thermal stability; (2) primary emission exhibiting Gaussian beam properties at a wavelength of 1.064μm; and (3) capable of being pumped by flashlamps or laser diodes. The last of these qualities is probably the most important because the ability to pump a laser with a laser diode instead of flashlamps decreases the size and increases the efficiency of the entire system, making compact, high power lasers possible.

The absorption of Nd:YAG crystals is the reason why they can be pumped by laser diodes. The crystal has high absorption for wavelengths between 750 and 820nm, so diodes with output wavelengths in that region can be used to pump a YAG system. Fortunately, since laser diodes were first invented, people have been trying to make them powerful enough to pump solid-state lasers, and so today, there are many laser diode options available in the required wavelength and power ranges for YAG lasers.

2-3

There are basically two ways to pump a YAG laser with a laser diode: end-pumping and side-pumping. The latter is usually used in systems where the output power is the most important feature, but end-pumping is much more efficient and straightforward. To end-pump a YAG laser, the diode beam is simply focused onto the end of the laser rod; all of the components, from the laser diode to the output coupler, are consequently aligned together, so the system is stable and easy to set up. However, for those systems in which high power is required, end-pumping is troublesome because it is difficult to get the necessary amount of light into the rod. Hence, side-pumping schemes use many powerful diode arrays encircling the rod, but this type of system is not as efficient as end-pumping because less of the diode light is absorbed by the YAG crystal. In the end, the requirements of the particular application determine how the laser is pumped, and if high power is a necessity, end-pumping just will not work. However, for this project, output power is not a concern, so end-pumping works fine.

Specific Nd:YAG configuration

The laser constructed for this project is composed of a single Nd:YAG crystal rod 5mm long with a diameter of 2mm. The diode laser pump is a 4-watt broad-area emitter with an output wavelength of 808nm, manufactured by SDL (model number SDL-2342-P1). A thermoelectric cooler built into the array package controls the diode's temperature, which is regulated by a laser diode controller, and a precision current source supplies the diode's power. Finally, the other parts within the laser system are: (1) a collimating lens to capture and collimate the laser diode light; (2) a cylindrical lens to round out the diode beam; (3) a focusing lens to focus the diode beam onto the YAG rod; and (4) an output mirror for the YAG laser cavity that is 98% reflective for 1.064μm and has a radius of curvature of 30cm.

There is one more important part included in this system: an acousto-optic modulator (AOM) placed inside the YAG cavity in order to drive the laser into a chaotic state. The AOM works on the principle that a transparent crystal with a radio frequency (RF) wave propagating through it will act like an optical phase grating because of the photoelastic effect, which causes the modulating strain field of the RF signal to couple to the crystal's refractive index. Therefore, modulating the 60MHz RF signal with a frequency on the order of 50kHz introduces a time-dependent change in the refractive index and deflects part of the beam. Ultimately, modulating the losses with the AOM in this manner can be used to make the laser output chaotic. The particular AOM chosen for this project has an additional feature in that the crystal is cut at Brewster's angle for YAG, which causes one polarization to be attenuated when it hits the crystal face—this should ideally result in the laser being linearly polarized in one direction.

The entire system is illustrated in Figure 1. The ultimate length of the YAG laser cavity is determined by the output coupler and the end of the YAG rod facing the laser diode. The input end of the YAG rod is

coated for high reflection at a wavelength of 1.064μm and high transmission at 808nm, so the point at which the diode light enters the laser rod is one of the cavity mirrors.
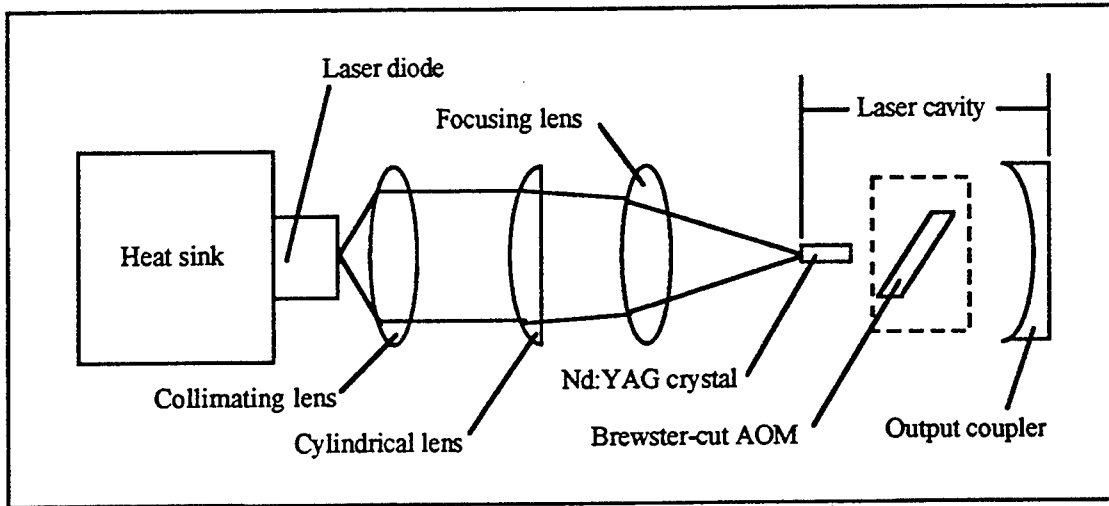
Figure 1: Laser diode end-pumped Nd:YAG configuration.

The length of the final cavity configuration is approximately 2.5 inches (6.35cm) which equates to a longitudinal mode spacing, also called the free spectral range (FSR), of 2.22GHz, as shown below—where c_0 is the speed of light in free space, n_{YAG} and L_{YAG} are the refractive index and length of the YAG rod respectively; and n_{air} and L_{air} are the index and length for the remainder of the cavity.

$$\Delta v_{FSR} = \frac{c_0}{2nL} = \frac{c_0}{2(n_{YAG} L_{YAG} + n_{air} L_{air})}$$

$$\Delta v_{FSR} = \frac{3 * 10^{10} cm / \sec}{2 * (1.82 * 0.5 cm + 1 * 5.85 cm)}$$

$$\Delta v_{FSR} = 2.22 GHz$$

Since the cavity is so short, the longitudinal mode spacing is rather large, which leads to the desirable condition that for pump powers close to threshold, only a single longitudinal mode will oscillate in the cavity. The other requirement of obtaining a single transverse mode is controlled simply by the proper alignment of the diode pump beam and the two YAG mirrors, and usually slight adjustment of only the output coupler is adequate to reduce the YAG beam to the TEM_{00} mode with a Gaussian beam profile.

The alignment of this system was achieved using a Helium-Neon (HeNe) laser mounted so that its beam was collinear with the laser diode beam. Then each of the components was placed into the HeNe beam and adjusted until its reflection was directed back to the HeNe source. This procedure was complicated when the AOM was placed inside the cavity because the Brewster cut of the crystal causes some walk-off of the

beam. However, alignment was achieved by directing the HeNe beam through the AOM to adjust the orientation of the YAG rod, and then aligning the output mirror.

Initial laser performance

One common measure of a laser's performance is its input/output characteristic because it gives the lasing threshold of the system as well as the peak power for the laser. Figure 2 shows this type of graph for the Nd:YAG laser—the input current powering the laser diode versus the output power of the YAG.
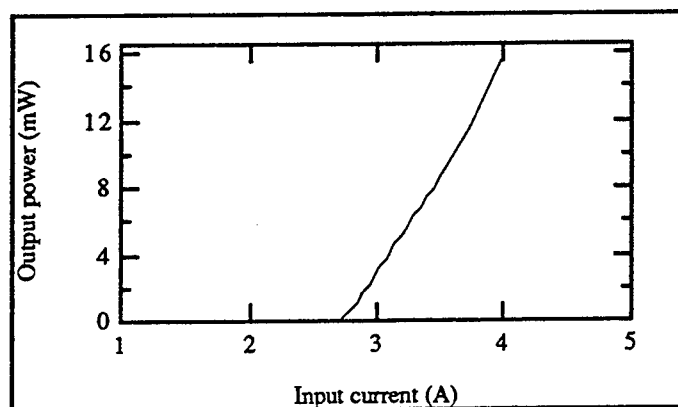
Figure 2: Input/output characteristic for Nd:YAG.

The threshold current value is 2.725A, and the peak power—extrapolating this curve up to 5.2A, the maximum allowable input current for the laser diode—is approximately 35mW. Another measure of the laser's performance for this project is the beam's mode structure.

As mentioned earlier, the transverse modes oscillating in the YAG laser are easily reduced to one by adjusting the cavity alignment, so the only real concern is obtaining a single longitudinal mode. In order to assure that the laser has only one longitudinal mode, the beam is directed into a Fabry-Perot optical spectrum analyzer. The Fabry-Perot cavity is aligned so that the YAG beam enters perpendicular to its mirrors, and its output is examined on a digital signal analyzer. By monitoring the signal from the Fabry-Perot, the current supplied to the laser diode can be adjusted to ensure a single longitudinal mode.

Chaotic behavior of the Nd:YAG laser

The purpose of this project was to build a single-mode laser that could be driven into a chaotic state, and then to analyze its behavior. The system constructed for this project is a diode-pumped, single-mode Nd:YAG laser with an intracavity AOM. This laser system can be driven into periodic and chaotic states by tuning the AOM or by modulating the laser diode input beam. Therefore, this system has two options for controlling and analyzing its chaotic dynamics. In order to prove a dynamic system is actually chaotic, a map to the transition to chaos can be verified. This "route to chaos" is determined by finding a regime

in which the laser output progresses through a series of period-doubling transitions as the modulation of either the AOM or the pump is changed.

For this laser (and probably for most systems), modulating the pump turned out to be much cleaner and less complicated than using the AOM. This occurs because two function generators are needed to modulate the AOM—one for the RF signal, and another to apply the sinusoidal modulation—both of which have two adjustments, amplitude and frequency. In addition, administering the signal to the AOM altered the signal in such a way that the modulation was no longer completely sinusoidal for certain settings, which could be caused by an impedance mismatch between the generator and the AOM. Therefore, while exciting periodic—and eventually chaotic—behavior is possible, modulation with a strange input waveform is undesirable due to its disagreement with theoretical models. However, the laser did perform well enough with this type of modulation to demonstrate a period-doubling route to chaos.

The laser output for two different time series is shown in Figure 3, illustrating the period-doubling effect. These tests were performed with the RF signal at 60MHz and the sinusoidal modulation at 35kHz, which is the measured relaxation oscillation frequency of the YAG laser—usually the frequency of choice for these types of tests. In Figure 3(a), the period 1 orbit for the laser is revealed, with a modulation amplitude of 19mV, and the period 2 orbit is shown in Figure 3(b) with an amplitude of 28mV. These low amplitudes ensure that the modulation is sinusoidal.
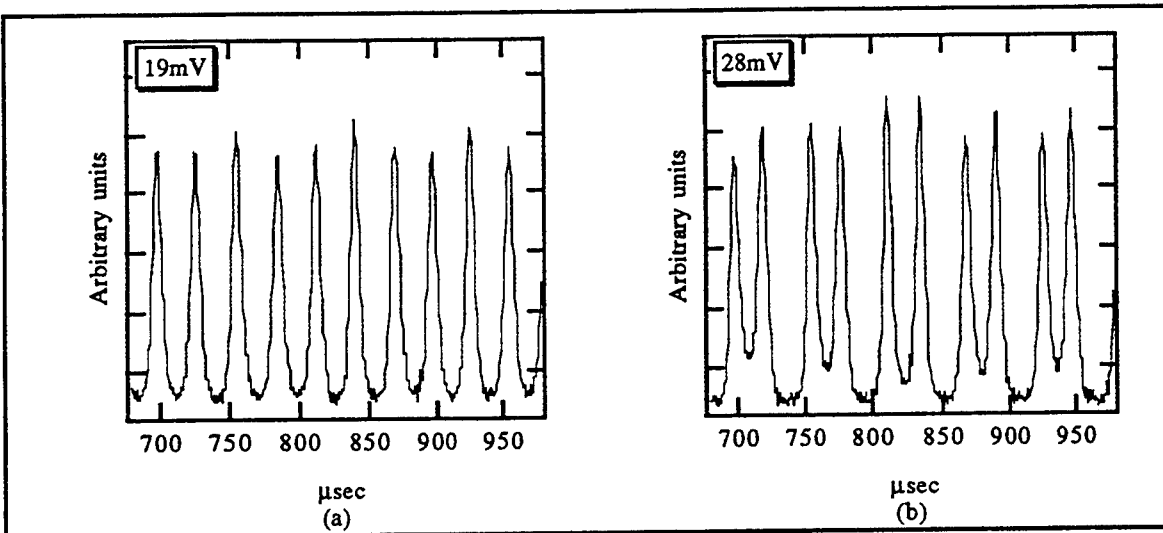
Figure 3: Time series for period-doubling behavior using AOM modulation. Period 1 shown in (a) for amplitude A = 19mV, and Period 2 shown in (b) for A = 28mV.

The frequency spectra for both of these time series are shown in Figure 4, and it is fairly obvious from these plots that period doubling occurs. For the period 1 situation in Figure 4(a), the dominant peak is at 35kHz, and there is a certain degree of harmonics (note the peak at 70kHz—the second harmonic), and as

expected, the period 2 components at 17.5kHz and 52.5kHz are present in Figure 4(b). There is quite a bit of noise in the time series and frequency spectrum—particularly Figures 3(b) and 4(b)—which is attributable to either spontaneous emission noise from the laser, or more likely, the fluctuations of the AOM disrupting the laser's output enough to cause some random noise.
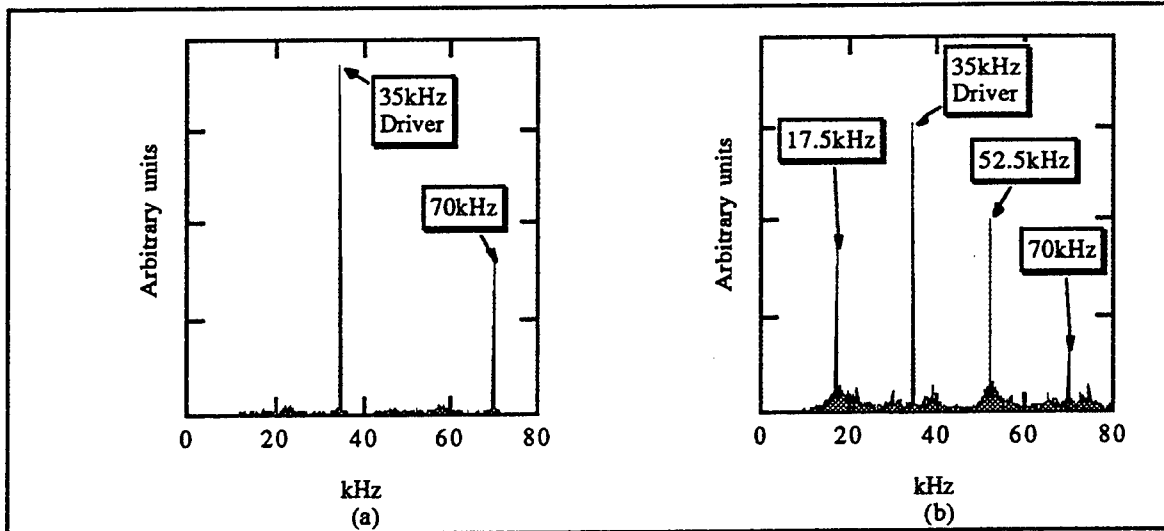
Figure 4: Frequency spectra for period-doubling behavior using AOM modulation. Period 1 shown in (a) for amplitude A= 19mV, and Period 2 shown in (b) for A = 28mV.

In order to illustrate what occurs if the modulation amplitude is increased further, a signal which exhibits chaotic behavior is shown in Figure 5. The time series of Figure 5(a) shows that there is still a component from the period 2 orbit within the signal, but the frequency spectrum of Figure 5(b) contains no distinct peaks and has a broad spectrum. This type of behavior is indicative of chaotic dynamics.
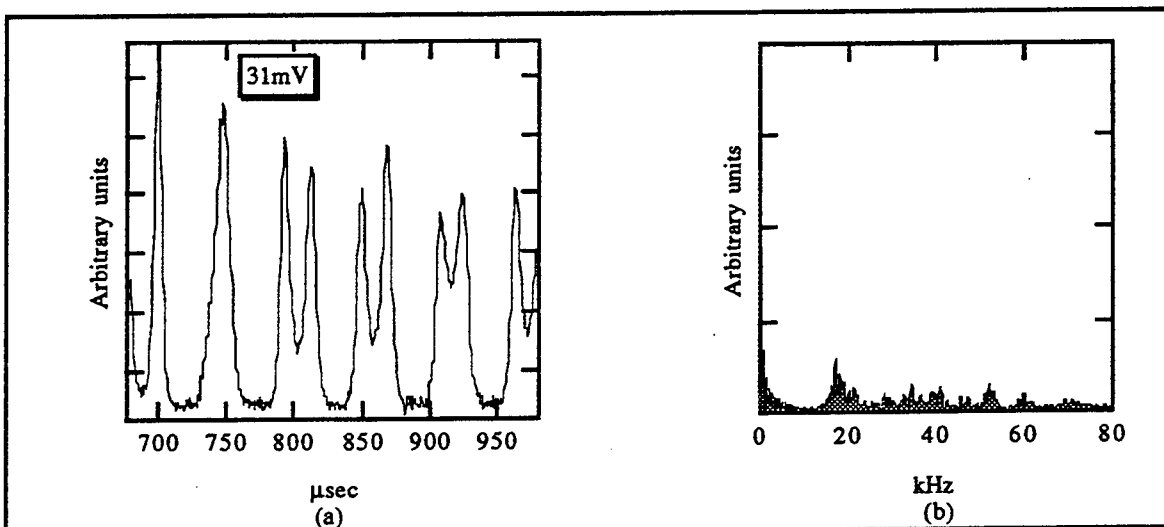
Figure 5: Suspected chaotic behavior using AOM modulation. Time series (a) and frequency spectrum (b) for amplitude A = 31mV.

As stated earlier, modulating the laser diode input current is much less complicated than using the AOM, and it produces a cleaner result. A clear period-doubling regime of the Nd:YAG laser was revealed by this method of excitation. Since only a single sinusoidal input needs to be applied to the current source, only the adjustment of the modulation amplitude is necessary to invoke the period-doubling regime of the laser once the frequency of the modulation is set to the relaxation oscillations. Figures 6 and 7 illustrate the period-doubling effect. Figure 6 shows the time series of the laser output for two different modulation amplitudes, and Figure 7 shows the corresponding frequency spectra.
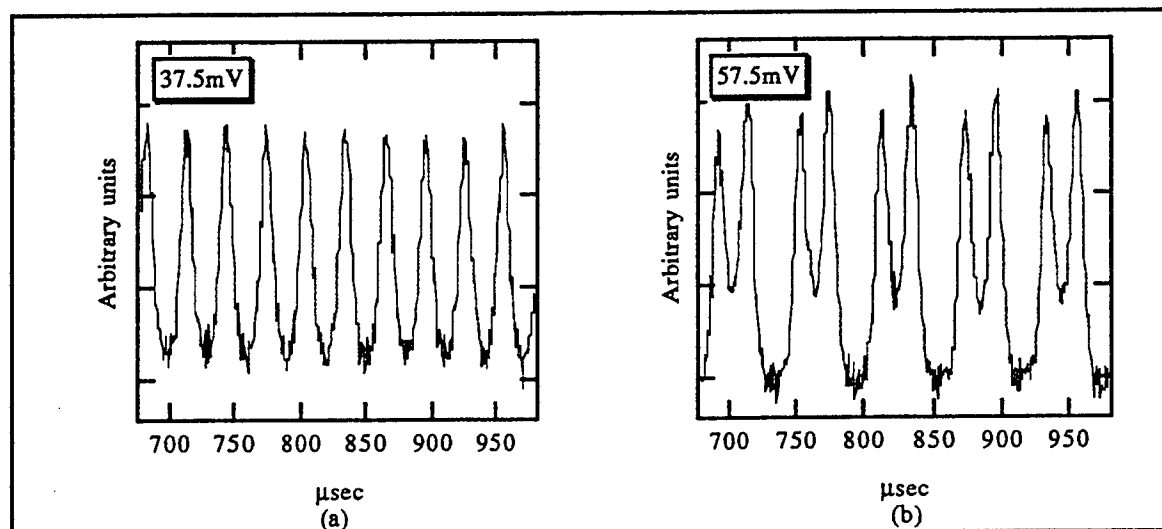
Figure 6: Time series for period-doubling behavior using pump modulation. Period 1 shown in (a) for amplitude A = 37.5mV, and Period 2 shown in (b) for A = 57.5mV.

The period 1 oscillation of the laser, shown in Figures 6(a) and 7(a), has a primary frequency equal to the drive frequency of 33kHz, which is expected, as that is the relaxation oscillation frequency, and a similar degree of harmonics as in the AOM tests (the second harmonic peak at 66kHz). Comparably, the period 2 oscillation shows a dominant peak at 16.5kHz—which is slightly unexpected, but the primary frequency in Figure 6(a) is certainly half that in Figure 6(b)—followed by the other expected peaks at 33kHz, 49.5kHz and 66kHz. This overall behavior clearly indicates a period-doubling situation which reveals the route to chaos for this particular laser system.
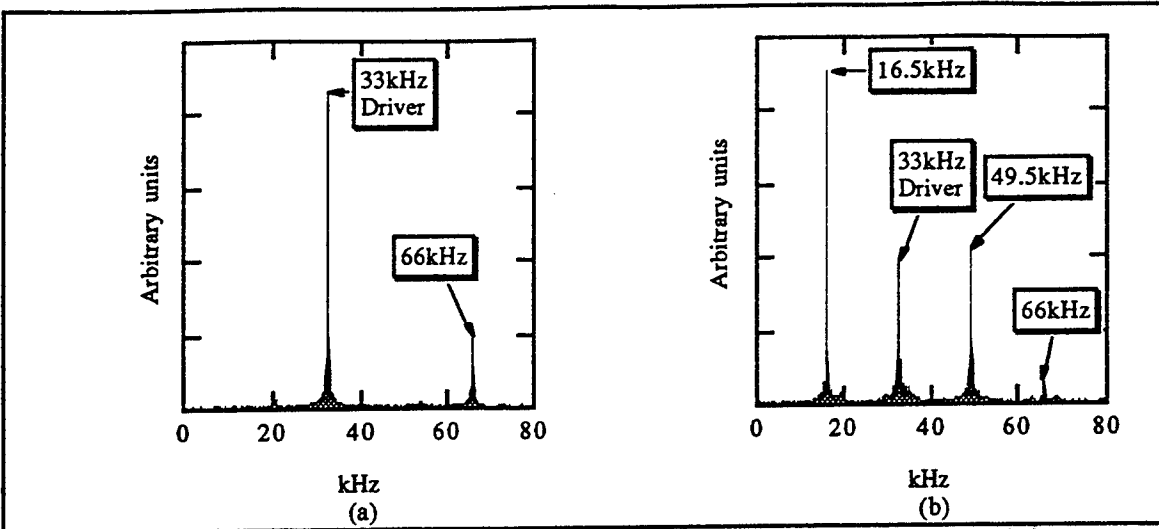
Figure 7: Frequency spectra for period-doubling behavior using pump modulation. Period 1 shown in (a) for amplitude A= 37.5mV, and Period 2 shown in (b) for A = 57.5mV. Note: shading under the curves is a visual aid only.

In order to show the full progression of the dynamics for this pump modulation method, a signal exhibiting chaotic dynamics is shown in Figure 8. This isn't as good an example as shown in Figure 5 for the AOM modulation, but this particular waveform, with its time series in Figure 8(a) and frequency spectrum in Figure 8(b), shows that the laser is on the verge of chaos. There are obviously components of both period 1 and period 2—probably mostly period 2 by looking at the spectrum—but overall the spectrum is very broad, which is a strong indicator of chaotic behavior.
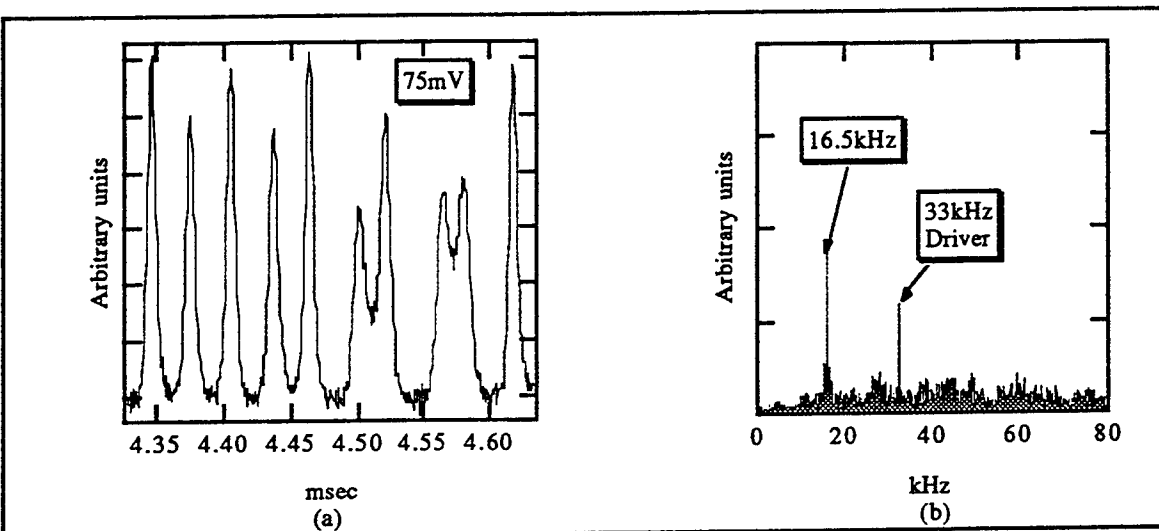
Figure 8: Suspected chaotic behavior using pump modulation. Time series (a) and frequency spectrum (b) for amplitude A = 75mV.

Both of these sets of tests should have also theoretically revealed a period 4 regime, however, the noise of the system obscured this orbit and the system became chaotic. However, by exciting the laser at a frequency of 1/4 of the relaxation oscillation frequency, the period 4 orbit was excited, proving that it is indeed present for this system. However, the simple period-doubling effect illustrated here is sufficient to reveal the route to chaos for this Nd:YAG system.

Conclusion

Overall, this project of building and testing a chaotic, diode-pumped Nd:YAG laser has demonstrated the relative ease of obtaining single-mode operation and two different methods for the excitation of chaos. Creating a very short cavity and verifying the mode structure made single-mode operation trivial, although in the future such a laser could be built with an even shorter cavity, and thus, a larger free spectral range. Both methods for exciting chaotic behavior of the laser—the intracavity acousto-optic modulator and the modulation of the laser diode pump—were successful in revealing a period-doubling route to, and in the end it appears that modulating the input current to the laser diode produces a cleaner result. Since the modulation only involves one signal, instead of two with the AOM, the complexity of the entire system is lessened by modulating the input current, and the complications of building the laser with the AOM are eliminated. The Brewster angle of the crystal face for the AOM made cavity alignment much more difficult, and if this element were eliminated, the cavity could be made much shorter because only a simple Brewster window would need to be placed in the cavity in order to ensure a polarized output. However, both the intracavity AOM and the pump modulation methods of excitation were successful in demonstrating the period-doubling effect, and comparison with theoretical models should eventually determine which method is more effective for exciting chaotic behavior within this type of laser.

THE DESIGN AND CHARACTERIZATION OF NOVEL P-TYPE QUANTUM WELL INFRARED PHOTODETECTOR STRUCTURES BASED ON III-V MATERIALS FOR MID- AND LONG-WAVELENGTH INFRARED DETECTION

Jerome T. Chu
Ph.D. Candidate
Department of Electrical and Computer Engineering

University of Florida
Department of Electrical and Computer Engineering
321 Benton Hall
Gainesville, FL   32611

THE DESIGN AND CHARACTERIZATION OF NOVEL P-TYPE QUANTUM WELL INFRARED PHOTODETECTOR STRUCTURES BASED ON III-V MATERIALS FOR MID- AND LONG-WAVELENGTH INFRARED DETECTION

Jerome T. Chu
Ph.D. Candidate
Department of Electrical and Computer Engineering
University of Florida

Abstract

The design and characterization of a p-type compressively strained-layer (PCSL) InGaAs/AlGaAs/GaAs quantum well infrared photodetector (QWIP) grown on a (100) semi-insulating (SI) GaAs substrate has been performed. The detector is a stacked QWIP which is designed to be sensitive in both the mid- (MWIR) and long-wavelength (LWIR) infrared bands. The MWIR stack is composed of a PCSL $In_{0.2}Ga_{0.8}As/Al_{0.3}Ga_{0.7}As$ QWIP with a detection peak at $\lambda_p = 4.8$ μm, while the LWIR stack is based on a PCSL $In_{0.15}Ga_{0.85}As/Al_{0.1}Ga_{0.9}As$ QWIP with a detection peak at $\lambda_p = 10$ μm. The peak responsivity of the LWIR QWIP was found to be 25 mA/W at $V_b = 2$ V, T = 40 K, and $\lambda_p = 10$ μm. The measured full-width half maximum (FWHM) spectral bandwidth was measured at $\Delta\lambda/\lambda_p = 40$ % and the detectivity was calculated as $D^* = 1.1 \times 10^{10}$ cm-Hz$^{1/2}$/W. Two distinct response peaks were found for the MWIR QWIP at 4.8 and 5.4 μm with maximum responsivities of 12 and 19 mA/W (at T = 77 K and $V_b = 5$ V), and FWHM spectral bandwidths of 21% and 26%, respectively. The detectivity for the MWIR stack at $\lambda_p = 5.4$ μm, $V_b = 1.0$ V, and T = 77 K was found to be $D^* = 5.5 \times 10^{11}$ cm-Hz$^{1/2}$/W. In addition, a novel PCSL QWIP structure was designed for use as a broad band LWIR detector. This new device also uses the InGaAs/AlGaAs/GaAs III-V material system to form an intersubband detector capable of having a relatively flat responsivity throughout the complete LWIR (8-14 μm) band. More innovative and novel device ideas for QWIPs will be discussed in this report, along with a brief summary of other experimental work performed during this research program.

THE DESIGN AND CHARACTERIZATION OF NOVEL P-TYPE QUANTUM WELL INFRARED PHOTODETECTOR STRUCTURES BASED ON III-V MATERIALS FOR MID- AND LONG-WAVELENGTH INFRARED DETECTION

Jerome T. Chu

Recently, a great deal of research has been performed in the area of quantum well infrared photodetectors for application in long-wavelength infrared focal plane arrays (FPAs). Most of the work emphasized the n-doped material [1,2], which uses the electron as the photoinduced carrier, which promised high quantum efficiency and large gain, because of the high mobility and small effective mass of the electron. But because of the quantum mechanical selection rules which prohibit the direct coupling of normally incident photons by the quantum wells, a light coupler of some sort (typically a dielectric or metallic grating) is added on top of the QWIP. This adds a great deal of complexity when it comes to processing these devices into FPAs. P-type QWIPs, on the other hand, have non-zero values for the off diagonal matrix elements which allows direct coupling of normal incidence radiation, which is due to the off zone-center mixing of the light- and heavy-hole states [3]. Because holes exhibit significantly larger effective masses (which corresponds to lower absorption coefficients) and lower mobility when compared with electrons, the performance of p-QWIPs are in general lower than similar n-QWIPs [1,4]. However, if biaxial compressive strain is introduced into the quantum well layers of a p-QWIP, then the effective mass of the heavy holes will be reduced, which in turn can improve the overall device performance [5]. Thus the need to use strained layers in the designs of our p-type quantum well infrared photodetectors.

The Design and Growth of P-type Strained Layer QWIPs

Illustrated in Fig. 1, the IR intersubband transition for the stacked two-color two-band InGaAs/AlGaAs PCSL QWIP occurs from the heavily populated ground bound heavy-hole state (HH1) to the quasi-bound second extended heavy hole state (HH3) for both the MWIR and LWIR bands. This transition was chosen because very thin layers (~25 Å or less) which are required for the more favorable HH1 to HH2 transition, exhibit very low quantum efficiencies. Also shown in Fig. 1, is the schematic energy band diagram for both QWIP stacks. Physically, the multicolor QWIP consists of two distinct multi-

quantum well layers separated by a common ohmic contact layer and sandwiched between the two (top and bottom) ohmic contact layers. The PCSL-QWIP is grown by molecular beam epitaxy (MBE) on a SI (100) GaAs substrate. The bottom, top, and middle contacts consists of heavily Be-doped GaAs layers. Using the substrate as the bottom reference point, the next structure grown on top of the bottom contact is the MWIR $Al_{0.3}Ga_{0.7}As/In_{0.2}Ga_{0.8}As$ PCSL-QWIP stack. The LWIR PCSL-QWIP stack consists of Be-doped $In_{0.15}Ga_{0.85}As$ quantum wells surrounded by $Al_{0.1}Ga_{0.9}As$ barriers sandwiched between the top and middle ohmic contacts and is grown on top of the MWIR QWIP layers. The bound-to-quasi-bound (BTQB) intersubband transition scheme is used to maximize absorption while keeping the thermionic dark current to a minimum, thus allowing the highest possible operating temperatures.

Theoretical Considerations

In order to accurately determine the absorption peak and other device characteristics, we performed theoretical calculations of the energy states in the quantum wells along with the transmission coefficient, $|T^*T|$, by using the multiple layer transfer matrix method (TMM) [6]. Using linearly interpolated values for the heavy- and light-hole effective masses, bandgap energies, and the valence band offset of $\Delta E_v = 35\%$ at T=77 K for GaAs, $In_{0.15}Ga_{0.85}As$, $In_{0.2}Ga_{0.8}As$, $Al_{0.1}Ga_{0.9}As$, and $Al_{0.3}Ga_{0.7}As$ we determined that the HH1 to HH3 LWIR peak would occur at $\lambda_p = 10$ μm, while the HH1 to HH3 MWIR peak would occur at 4.7 μm, with a HH1 to LH2 peak occuring at 5.6 μm, when the effects of biaxial compressive strain were considered. The induced energy band edge shifts for the conduction band, heavy-hole subband, and the light-hole subband are given respectively by [7],

$$\Delta E_c = 2c_1 \frac{C_{11} - C_{12}}{C_{11}} \delta_o$$

$$\Delta E_{hh} = b \frac{C_{11} + C_{12}}{C_{11}} \delta_o$$

$$\Delta E_{lh} = -\Delta E_{hh} + \frac{\left(\Delta E_{hh}\right)^2}{2\Delta_o}$$

where c_I is the combined hydrostatic deformation potential which characterizes the splitting of the Γ_8 valence band under strain, b is the shear deformation potential, C_{ij}'s are the elastic constants, Δ_o is the spin orbit split-off energy, and δ_o is the lattice mismatch or the in-plane strain, which is defined as $\delta_o = (a - a_s/a)$, where a is the lattice constant of the strained material and a_s is the substrate lattice constant.

Another advantage inherent in p-type QWIPs is the naturally larger quantum efficiency when compared with n-QWIPs exhibiting similar absorption characteristics. Since the quantum efficiency is described as

$$\eta = P(1 - R)\left[1 - \exp(-\alpha\,l)\right]$$

when n-type and p-type QWIPs with similar absorption coefficients, α, and well thickness, l, the prefactor P is equal to 0.5 for n-QWIPs and 1.0 for p-QWIPs, which gives us twice the quantum efficiency for p-QWIPs. This is due to the ability of p-type transitions to absorb all polarizations of incoming radiation. Due to the intrinsically low absorption coefficients of p-type materials, and large hole effective masses, biaxial strain must be incorporated into the quantum wells to reduce the effective mass and increase the intersubband absorption.

In the case of our PCSL QWIP, the inclusion of compressive strain of -1.4% for the MWIR layers and -1.0% for the LWIR layers enhances the mobility of the heavy holes by reducing the effective mass [5]. Also associated with the presence of compressive strain is the reduction of the in-plane density of states in the InGaAs quantum well. So that with a significant lowering of the effective mass of the ground heavy holes, an increase in the absorption coefficient and the corresponding quantum efficiency is expected.

Results and Discussion

The performance of the stacked two-color PCSL QWIP was evaluated by forming a 216x216 μm^2 mesa on the MBE grown devices by wet chemical etching. A narrow ring of Au/Cr was deposited by e-beam evaporation to create ohmic contacts for the radiometric and electrical characterization. Note that in this ring type contact, the normal incidence IR illumination is allowed to pass into the QWIP from the top ohmic contact and is allowed on pass through the QWIP stacks. Additionally, three mesa structures were etched for the multicolor QWIP to allow the separate analysis of the LWIR, MWIR, and combined devices.

The LWIR stack was formed by etching down to the middle contact, while the MWIR stack was formed by etching off the LWIR stack and then etching down to the bottom contact. Finally, the combined stack was formed by etching from the top to the bottom ohmic contact.

The dark I-V characteristics for the MWIR, LWIR, and combined stacked QWIP measured at T = 77 K is shown in Fig. 2. As expected, the dark current of the LWIR QWIP stack is several orders of magnitude higher than the MWIR QWIP. This is due to the exponential dependence of the dark current on the barrier height. As clearly seen in Fig. 2, most of the bias is dropped across the MWIR due to the higher dynamic resistance of the MWIR stack. Figure 3 shows the temperature dependent dark I-V curves at T = 40, 60, 77 K for the LWIR QWIP. The asymmetry in the dark I-V curves observed in this device can be attributed to the dopant migration effect [8].

The spectral responsivity of the MWIR QWIP measured at V_b = 5 V and T = 77 K is shown in Fig. 4. The responsivity measurements were performed with the processed device mounted in a cryogenic dewar and illuminated by a chopped blackbody source running through a grating monochrometer and the appropriate filters. The resulting photocurrent is then amplified and detected by a lock-in amplifier. The measurements revealed that two photoresponse peaks were observed in the MWIR band at $\lambda_{p,mw1}$ = 4.8 μm and $\lambda_{p,mw2}$ = 5.4 μm. The 4.8 μm peak is in excellent agreement wwith the ground heavy-hole (HH1) to second bound heavy-hole (HH3) transition calculated by the TMM, which predicted a detection peak at 4.7 μm. The responsivity at the 4.8 μm peak was determined to be 12 mA/W. The calculated detectivity for this peak was found to be 3.3 x 10^{11} cm-Hz$^{1/2}$/W at V_b = 1.0 V and T = 77 K. The measured spectral bandwidth of the first MWIR peak was $\Delta\lambda/\lambda_{p,mw1}$ = 21%, and $\Delta\lambda/\lambda_{p,mw2}$ = 26% for the second, longer wavelength peak. The 5.4 μm peak is due to the intersubband transition from the HH1 states to the first bound light-hole (LH2) states within the quantum well. The calculated responsivity peak for this transition is 5.6 μm, which is in good agreement with the measured value. The higher responsivity of this peak is attributed to the higher absorption coefficient of the HH1 to LH2 transition [4], and to the fact that the LH2 state is a bound state located (energetically) below the barrier edge. The responsivity of 19 mA/W was found for this peak at T = 77 K and V_b = 5.0 V, while the detectivity was found to be 5.5 x 10^{11} cm-Hz$^{1/2}$/W at V_b = 1.0 V and T = 77 K.

The responsivity for the LWIR QWIP stack as a function of the incident IR radiation is shown in Fig. 5. A peak in the responsivity curve was found at $\lambda_p = 10.0$ μm for this QWIP, which agrees exactly with the value predicted from the theoretical TMM calculation. A maximum responsivity of 25 mA/W was measured at T = 40 K and $V_b = 2.0$ V, with a detectivity of 1.1×10^{10} cm-Hz$^{1/2}$/W under the same conditions. It is interesting to note that a very broad response with a FWHM bandwidth of 40% was achieved for this device. Figure 6 shows the relative spectral response of the combined MWIR and LWIR stacks in series, displaying the two dominant peaks in the MWIR band and a much smaller LWIR peak at 10 μm. This has been attributed to the much larger dynamic resistance of the MWIR stack, which causes most of the bias to be dropped across it. If we needed concurrent operation of both stacks in a two terminal configuration, the dynamic resistance must be lowered so that it nearly matches that of the LWIR stack. This can be achieved by reducing the number of periods in the MWIR stack or by making the barriers thinner. This work was presented at the Ninth International Molecular Beam Epitaxy Conference at Pepperdine University, Malibu, CA on August 5-9, 1996.

Additional Work and Possible Future Explorations

In addition to the characterization of the stacked two-color two-band p-QWIP, many other tasks were performed at Phillips Laboratory/VTRP this summer. Most of the tasks were involved with the setting up and testing of the optical and electrical characterization equipment for any future QWIPs. Specifically, these tasks included: configuring the Oriel MS 257 Monochrometer, integrating the monochrometer with the Oriel Merlin Lock-in Amplifier, adding the chopper and filter wheel to the spectrometer assembly, writing LabView code to control the whole setup remotely through the GPIB bus, and testing the system. The work done in the arena of electrical characterization was by writing LabView code, with Mr. Jon Syverson, for the existing Keithley 236 Source Measure Unit (SMU) which allows us a customized system to measure dark I-V characteristics at cryogenic temperatures (T ≤ 80 K), with the existing cryogenic dewars. This system is capable of measuring currents in the femtoamp (10^{-15}) range.

Future collaborations with PL/VTRP and Dr Sheng Li's group at the University of Florida are already in place. Existing agreements with the University and the Department of Electrical and Computer

Engineering involve the design, growth, processing, and characterization of many different p- and n-QWIPs for low background detection in the MWIR and LWIR bands. Several novel and unique QWIP structures have been designed and are currently awaiting growth and processing to validate the usefulness and performance of these cutting edge QWIPs. The first generation of these QWIPs were grown by the University of Florida, but all further growth will be performed in conjunction with PL/VTRP.

In addition to the design and growth of novel QWIP structures, other future work (to be proposed to the AFOSR as a SREP proposal) will explore the possibilities of improving device performance without altering the QWIP structures themselves. This will be achieved by a combination of diffractive anti-reflection (AR) coatings and infrared microlens arrays. Current QWIPs lose approximately 30% of the incoming radiation due to dielectric reflection. A simple way of reducing the loss would be to grow thin ($\lambda/4$) dielectric layers with different refractive indices on the thinned substrate of the QWIPs. The problem with this simple solution is that even with relatively high refractive indices, we would still need to deposit many microns and many layers of materials on the substrate; which will increase the cost and processing requirements. Thus the need for diffractive AR coatings. Another loss common to QWIPs and QWIP arrays is the fill factor. Typically the fill factor of any single device is close to unity. But since the pitch between pixels is always larger than the pixel size, some of the incoming radiation is lost. For example if the pitch between the pixels was 50 μm and the pixel was 40 μm^2, then 36% of the incoming light is lost due to the spacing in between the pixels even if the fill factor is unity. A way of increasing the fill factor (or using the previously lost light) is by using microlenses or microlens arrays. These microlenses can be tailored to focus the incoming radiation completely into the pixel area, effectively increasing the fill factor to greater than unity.

Acknowledgements

References

1. B. F. Levine, J. Appl. Phys. **74**(8), R1 (1993).

2. L. S. Yu, Y. H. Wang, and S. S. Li, Appl. Phys. Lett. **60**(8), 992 (1992).

3. Y.-C. Chang and R. B. James, Phys. Rev. B **39**, 12672 (1989).

4. H. Xie, J. Katz, and W. I. Wang, Appl. Phys. Lett. 56, **3601** (1991).

5. K. Hirose, T. Mizutani, and K. Nishi, J. Crystal Growth 81, 130 (1987).

6. A. K. Ghatak, K. Thyagarajan, and M. R. Shenoy, IEEE J. Quantum Electron. **24**, 1524 (1988).

7. F. H. Pollack, in "Strained Layer Superlattices: Physics," ed. T. P. Pearsall **32**, 17 (1990).

8. H. C. Liu, Z. R. Wailewski, and M. Buchanan, Appl. Phys. Lett. **63**, 761 (1993).
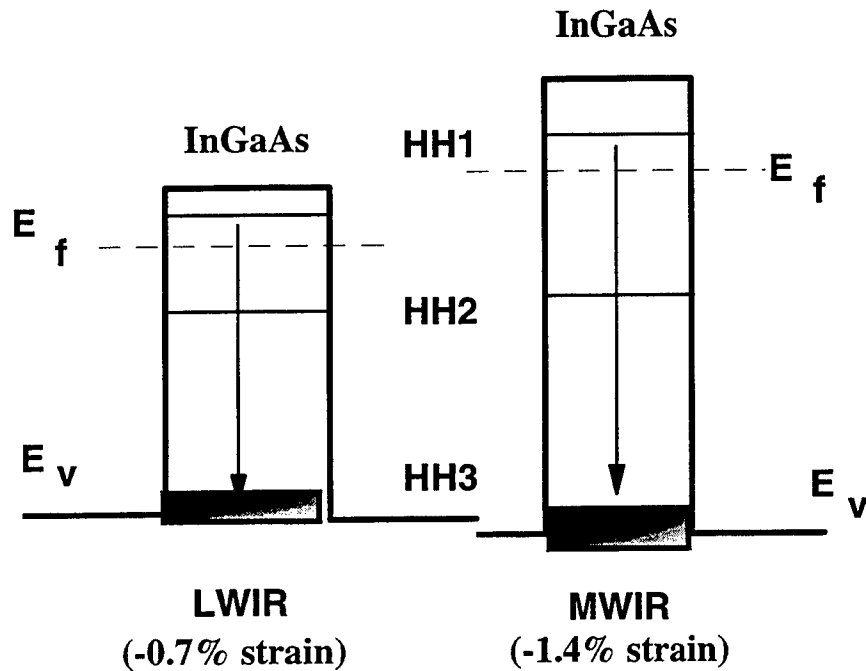
Figure 1. Schematic Energy Band Diagram and the Intersubband Transitions Associated with the 10.0 and 4.8 μm Detection Peaks.
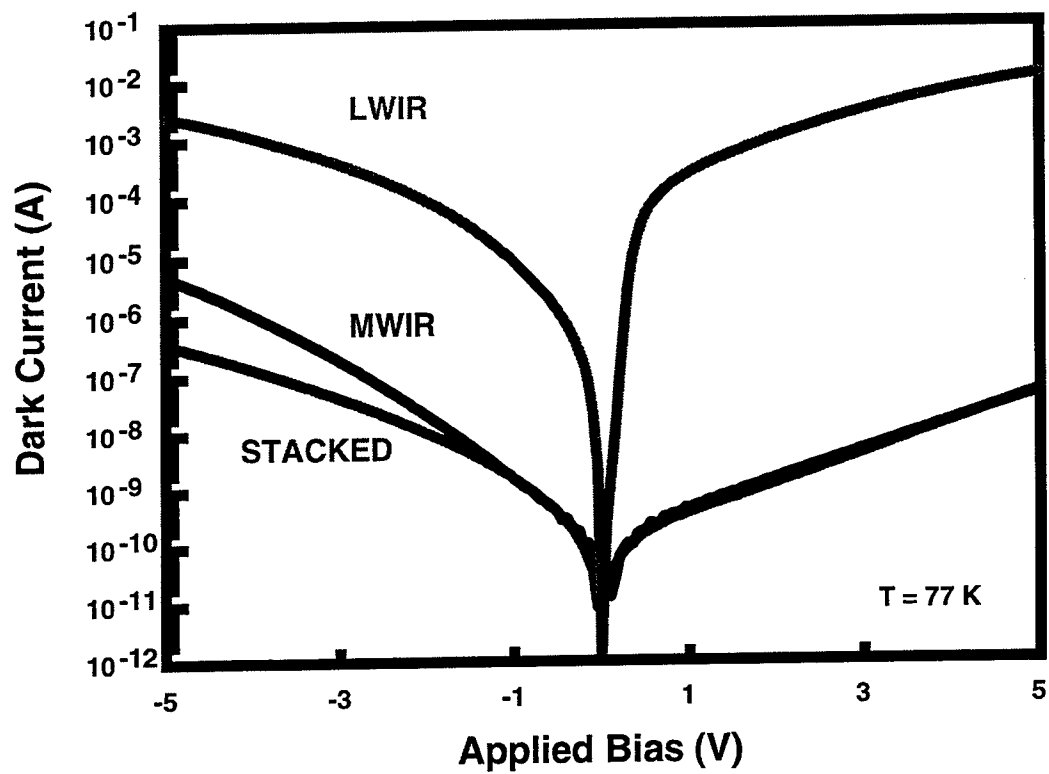
Figure 2. Dark Current as a Function of Bias at T = 77 K for the MWIR, LWIR, and Combined Stacks.
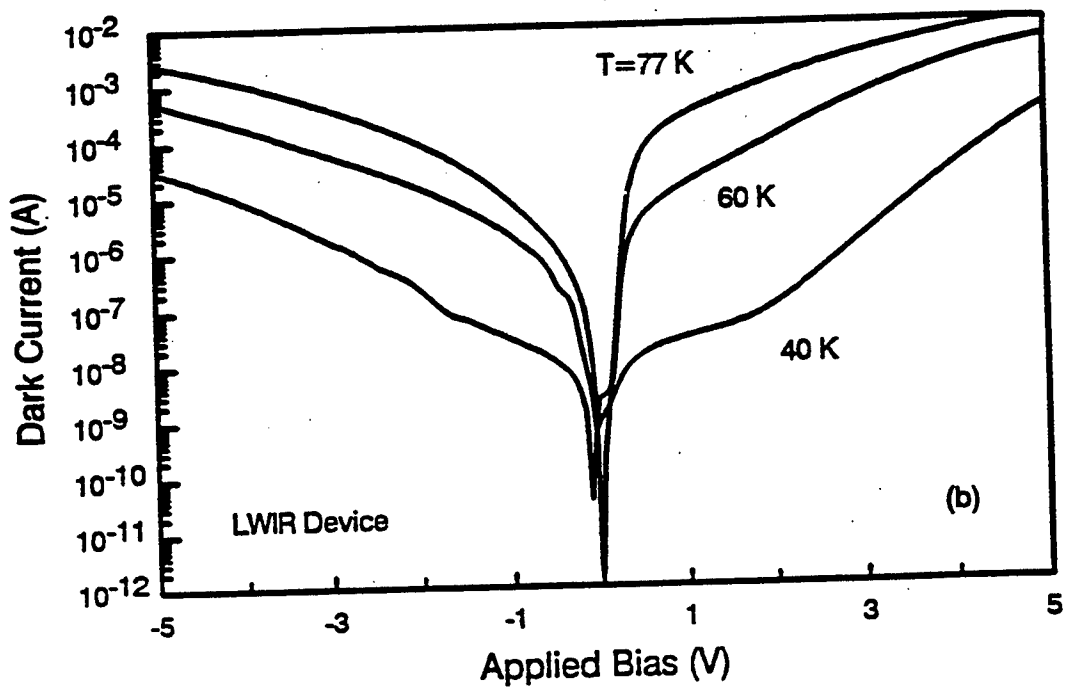
Figure 3. The Dark Current for the LWIR Stack at T = 40, 60, 77 K.
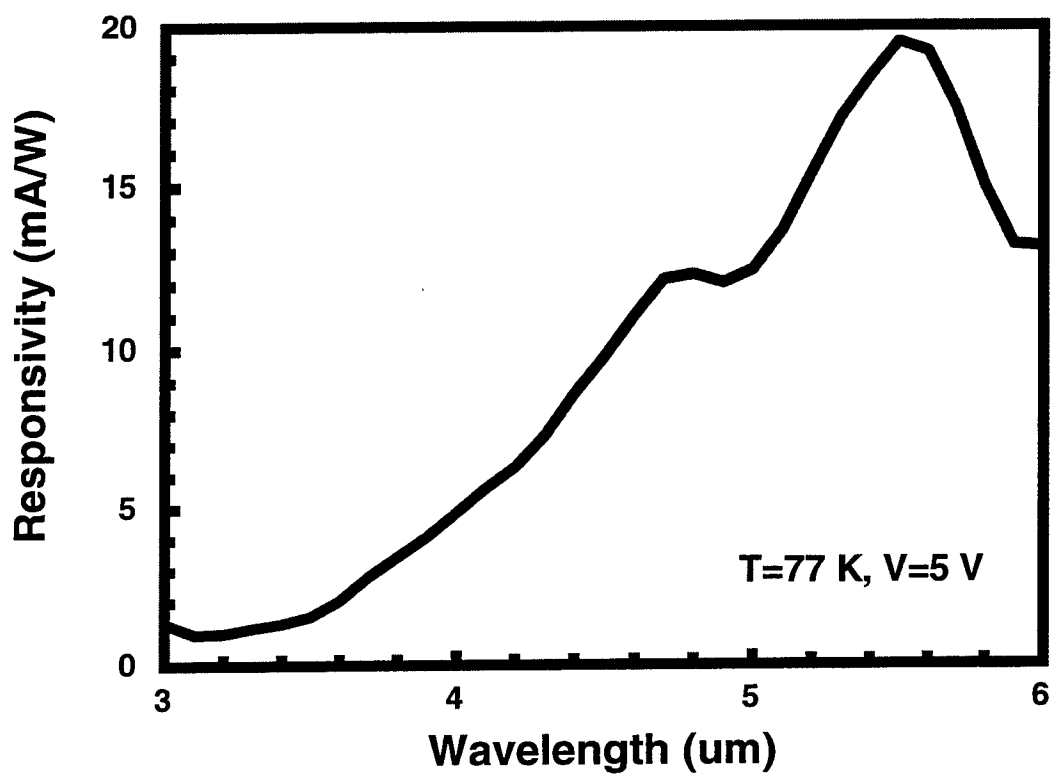
Figure 4. The Measured Responsivity of the MWIR Stack, Showing the Two Responsivity Peaks at 4.8

and 5.4 μm at T = 77 K, V_b = 5.0 V.
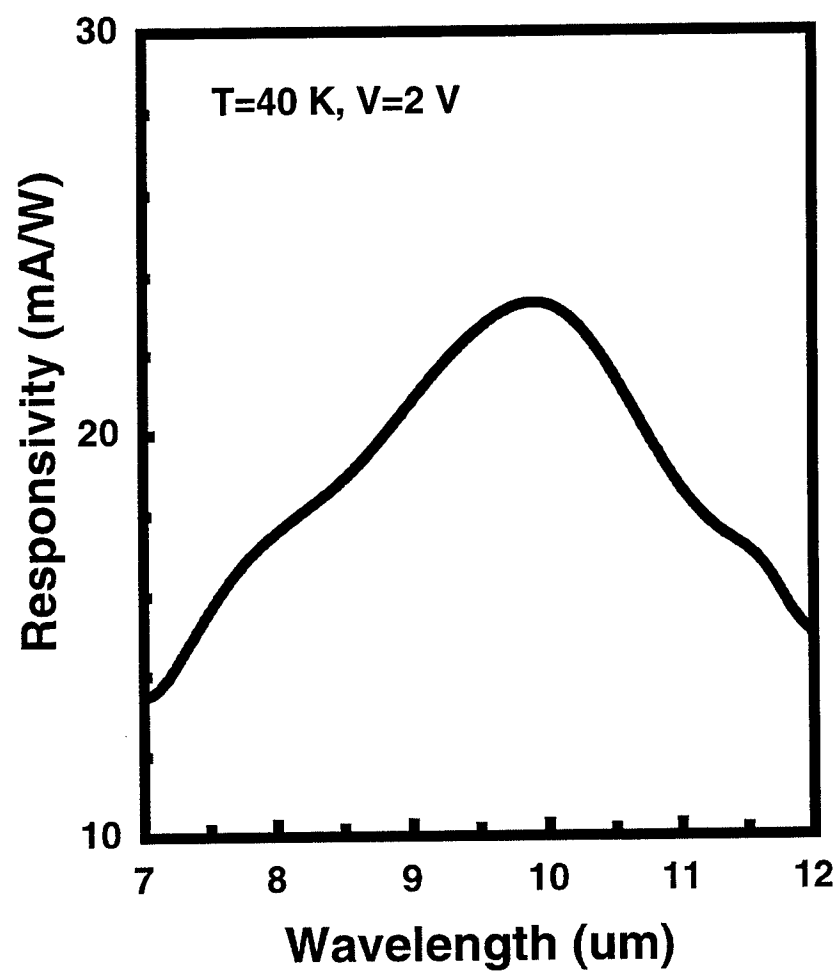
Figure 5. The Measured Responsivity of the LWIR Stack at T = 40 K, V_b = 2.0 V.
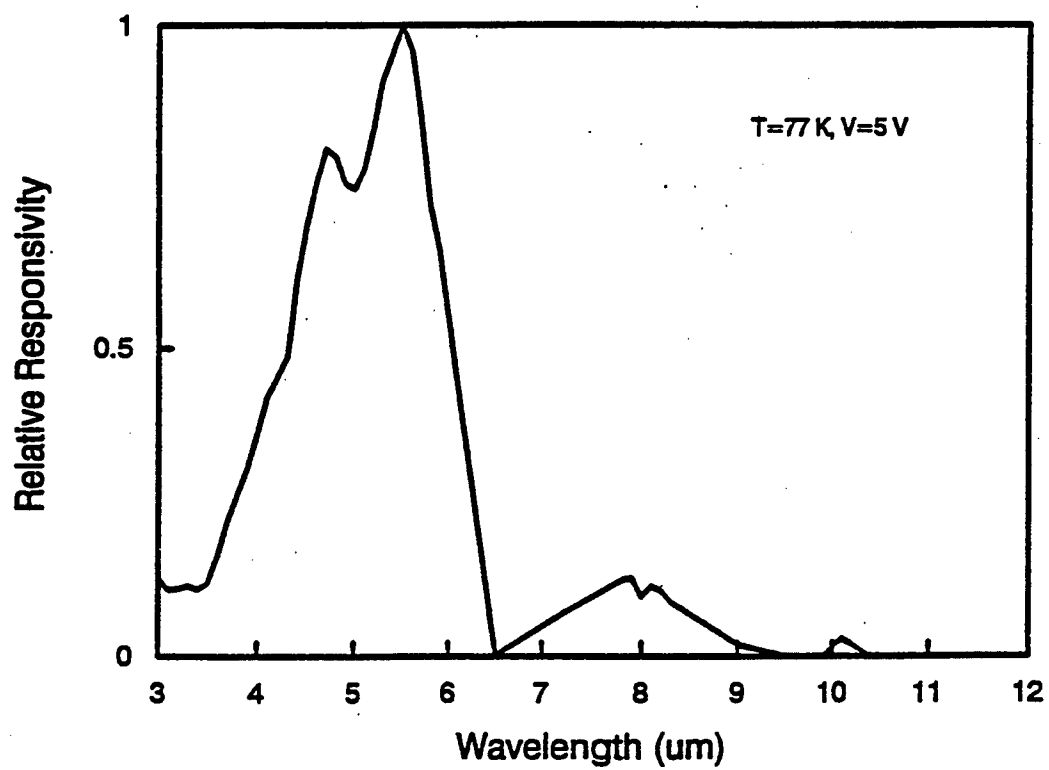
Figure 6. The Combined LWIR and MWIR Stacks Relative Responsivity at T = 77 K, V_b = 5.0 V.

A LABORATORY STUDY OF PLASMA WAVES
PRODUCED BY AN X-MODE PUMP WAVE

Nathan E. Dalrymple
Research Assistant
Department of Nuclear Engineering

Massachusetts Institute of Technology
77 Massachusetts Ave.
Cambridge. MA 02139

A LABORATORY STUDY OF PLASMA WAVES
PRODUCED BY AN X-MODE PUMP WAVE

Nathan E. Dalrymple
Research Assistant
Department of Nuclear Engineering
Massachusetts Institute of Technology

ABSTRACT

An exploratory study of plasma waves produced by an extraordinary-mode pump wave was performed in the laboratory device known as the Versatile Toroidal Facility. Spectral measurements performed *in situ* indicated that resonant modes of the vacuum chamber were obscuring any interesting plasma phenomena that might have been occurring. Modifications that would allow launching of an arbitrary polarization pump wave were conceived. Once implemented, these changes would allow laboratory modeling of a wide range of ionospheric plasmas, including auroral, mid-latitude, and equatorial plasmas. Also, an angularly-scannable probe was designed that would allow extraction of some information about the direction of $\bar{k}$ in future VTF studies.

A LABORATORY STUDY OF PLASMA WAVES
PRODUCED BY AN X-MODE PUMP WAVE

Nathan E. Dalrymple

INTRODUCTION

The purpose of this summer's work was to model ionospheric plasma phenomena in a laboratory setting. Experiments performed in the laboratory have the potential to be cheaper, easier, and more accessible to diagnostics than ionospheric plasma experiments. There are problems with laboratory experiments, however. Boundary conditions imposed by the presence of nearby walls in the laboratory force the plasma phenomena of interest to be smaller than the machine dimensions. Exact matching of ionospheric density, magnetic field, and temperature (assuming this could be done) will produce scale sizes of the same order as those occurring in the ionosphere--up to tens of kilometers. Clearly, this is the wrong approach. We can, however, match position in parameter space, e.g. location on the CMA diagram for wave studies. Another difficulty of laboratory experiments is that the plasmas must be produced as well as probed. This introduces lots of extra hardware that must be maintained and diagnosed before the plasma physics can even begin. Perhaps the best approach is to use the two experimental arenas in concert: laboratory plasmas can be used to cross-check ionospheric experiments in detail. Alternatively, laboratory experimental results can provide guidance to future ionospheric experiments--to reduce the financial risk involved in committing to new ionospheric diagnostics.

This summer I performed an exploratory study of plasma waves produced by an extraordinary-mode pump wave in a laboratory device known as the Versatile Toroidal Facility (VTF). This has not really been pursued in ionospheric studies, mainly because of difficulty of diagnostics (after

disappointing initial results). I also began the design of new diagnostics and experimental configurations for VTF. The following report describes the VTF. the experiments performed using VTF, and the new configurations planned for future studies.

VERSATILE TOROIDAL FACILITY (VTF)

The VTF is a large laboratory plasma device that lives in the Plasma Fusion Center at MIT. It was designed specifically for the purpose of modeling ionospheric plasmas. The VTF is a toroidal device like a tokamak, with major radius (R) of about 1 m and minor radius (a) of about 30 cm. However, unlike a tokamak, the magnetic field is helical. with a strong toroidal component (800 G) and a weak vertical component (20 G). Plasmas are produced inside a stainless-steel vacuum chamber that is evacuated to a base pressure of approximately 10^{-6} torr. The gas of choice (e.g. hydrogen, argon, nitrogen, or oxygen) is leaked in to produce an experiment neutral pressure of about $7*10^{-5}$ torr. There are three main methods of producing plasma. The first is a 3 kW magnetron used for electron cyclotron heating that produces electron densities, n_e. and temperatures, T_e. on the order of $5*10^{16}$ (m^{-3}) and 5 eV, respectively. The second is a set of up to four electron beam emitters mounted on the floor of the chamber that give n_e of up to 10^{18} (m^{-3}) and T_e of up to 10 eV. The third (not used much) is an Ohmic coil in the center of the device that can be driven in a resonant circuit (sometimes called a Taylor discharge). These methods give an ionization fraction of about 10%. A schematic of the machine is shown in Figure 4-1.

Diagnostics can be mounted on the VTF in any of the ports on the top. bottom. or outer circumference. The experiments performed this summer used several radially-scannable potential probes, a radially-scannable Langmuir probe, a dipole antenna. and a loop antenna. All the usual

engineering data was recorded by CAMAC signal conditioning and digitizing modules. The frequency spectra of various probes were measured by 2 to 3 spectrum analyzers and recorded from the plotter outputs of the spectrum analyzers using a CAMAC digitizer. The data were transferred to an Intel-type personal computer for storage and further processing.

MACHINE MAINTENANCE

What I did with the machine can be generally divided into two categories: stuff related to plasma physics (described in the next section), and stuff related to getting the machine in working order so we could do plasma physics. At the beginning of the summer the AC-DC converters that supply the toroidal field current began giving very inconsistent results from shot to shot. Since interpretation of results requires consistency of magnetic field over a large number of shots, this situation was intolerable. In the process of debugging the converters, we discovered that we had almost no documentation for the firing circuits that control them, and that the manufacturer did not exist any longer. Thus we made the decision to install new firing circuits. After installing the new parts, we were able to get sufficient (and consistent) toroidal field current from one converter (instead of two in parallel). However, the two converters would not function in parallel. Deeming the situation workable, we moved on to plasma physics.

X-MODE STUDY

For these experiments, EM waves were produced by a 3 kW magnetron and traveled through standard waveguide to a large pyramidal horn antenna located inside the vacuum vessel of the

VTF. The horn was oriented so that both the direction of propagation and the electric field vector of the linearly polarized radiation were perpendicular to the magnetic field. This extraordinary-mode (x-mode) wave was used both to produce the plasma and to interact with it as a large-amplitude pump wave. Typical density profiles produced using x-mode ECR heating at 2.45 GHz and ECR heating plus electron beam emission are shown in Figures 4-2 and 4-3. Also shown on these figures are the magnetic field and the ordinary-mode (o-mode) and x-mode cutoff (or resonant) frequencies as a function of major radius. The cutoff frequency of the o-mode is just the plasma frequency.

$$\omega_p = \sqrt{\frac{e^2 n_e}{\varepsilon_0 m_e}} \ . \tag{4-1}$$

The right- and left-hand cutoff frequencies of the x-mode are given by

$$\omega_R = \tfrac{1}{2}\left[\omega_c + \sqrt{\omega_c^2 + 4\omega_p^2} \right] \tag{4-2}$$

and

$$\omega_L = \tfrac{1}{2}\left[-\omega_c + \sqrt{\omega_c^2 + 4\omega_p^2} \right]. \tag{4-3}$$

where the electron cyclotron frequency is

$$\omega_c = \frac{eB}{m_e} \ . \tag{4-4}$$

The resonant frequency of the x-mode is just the upper hybrid frequency,

$$\omega_h = \sqrt{\omega_p^2 + \omega_c^2} \ . \tag{4-5}$$

The magnetic field can be written

$$B = \frac{\mu_0 N I}{2\pi R} \ . \tag{4-6}$$

In the case of the VTF, $N = 4 \times 18$ coils and $I = 5800$ A.

High-frequency spectra taken with the dipole antenna for two radii are presented in Figures 4-4 and 4-5. Corresponding low-frequency spectra taken with a potential probe look similar to the one shown in Figure 4-6. The interesting features to note in these figures are the strong pump wave centered near 2.45 GHz and the asymmetric nature of the high-frequency spectra. The amplitude of the plasma spectrum at frequencies just above the pump frequency appears to be enhanced relative to the noise level in the rest of the plot. After these data were taken, it was postulated that the spectral features may have been generated by standing waves in the chamber, rather than any interesting plasma phenomena. Therefore, vacuum (or no toroidal field) spectra were measured. Figure 4-7 is typical of these spectra. Realization: the vacuum (or no-plasma) electric fields set up inside the machine dominated the spectra, probably because of the low electron density produced by the x-mode ECRH. Any plasma waves were obscured by the large-amplitude standing waves in the chamber. This result was disappointing but evidently heretofore unknown. This was fatal to the x-mode study, because higher plasma density causes the pump wave to be cut off and reflected without producing any interesting plasma waves. This avenue of investigation blocked, we sought for other ways we could model the ionospheric plasma.

MACHINE MODIFICATIONS/FUTURE EXPERIMENTS

In the present setup, the VTF has a magnetic field exactly perpendicular to the propagation vector of the incoming heater wave (comparable to the equatorial plasma). To expand the capability of VTF, an antenna was needed that could launch at a variety of angles to the magnetic field. Also, arbitrary-polarization of the launched wave was desired. A short and by no means exhaustive

literature search revealed that such devices have been built in the past. Plans for such a device to be mounted on VTF have begun, but are still in the preliminary planning stage.

While diagnostics available for ionospheric studies (incoherent-scatter radar) give very precise, albeit limited, information about the direction of wave propagation, the *in situ* dipole probes used in the VTF are not nearly as selective. Any wave with an electric field component along the dipole will produce some probe signal. If the amplitudes of the signals measured with the dipole antenna at various angles could be compared, the line of propagation could perhaps be deduced. To this end, an angularly-scannable probe was conceived. When this probe is completed, plasma studies can be conducted with increased diagnostic capability.

CONCLUSIONS

An exploratory study of plasma waves produced by an extraordinary-mode pump wave was performed in the laboratory device known as VTF. Spectral measurements performed *in situ* indicated that resonant modes of the vacuum chamber were obscuring any interesting plasma phenomena that might have been occurring. Modifications that would allow launching of an arbitrary polarization pump wave were conceived. Once implemented, these changes would allow laboratory modeling of a wide range of ionospheric plasmas, including auroral, mid-latitude, and equatorial plasmas. Also, an angularly-scannable probe was designed that would allow extraction of some information about the direction of $\bar{k}$ in future VTF studies.

potential
probe

vacuum vessel

plasma

R

Top View

dipole
antenna

microwave horn
antenna

Section View

dipole
antenna

microwave horn
antenna
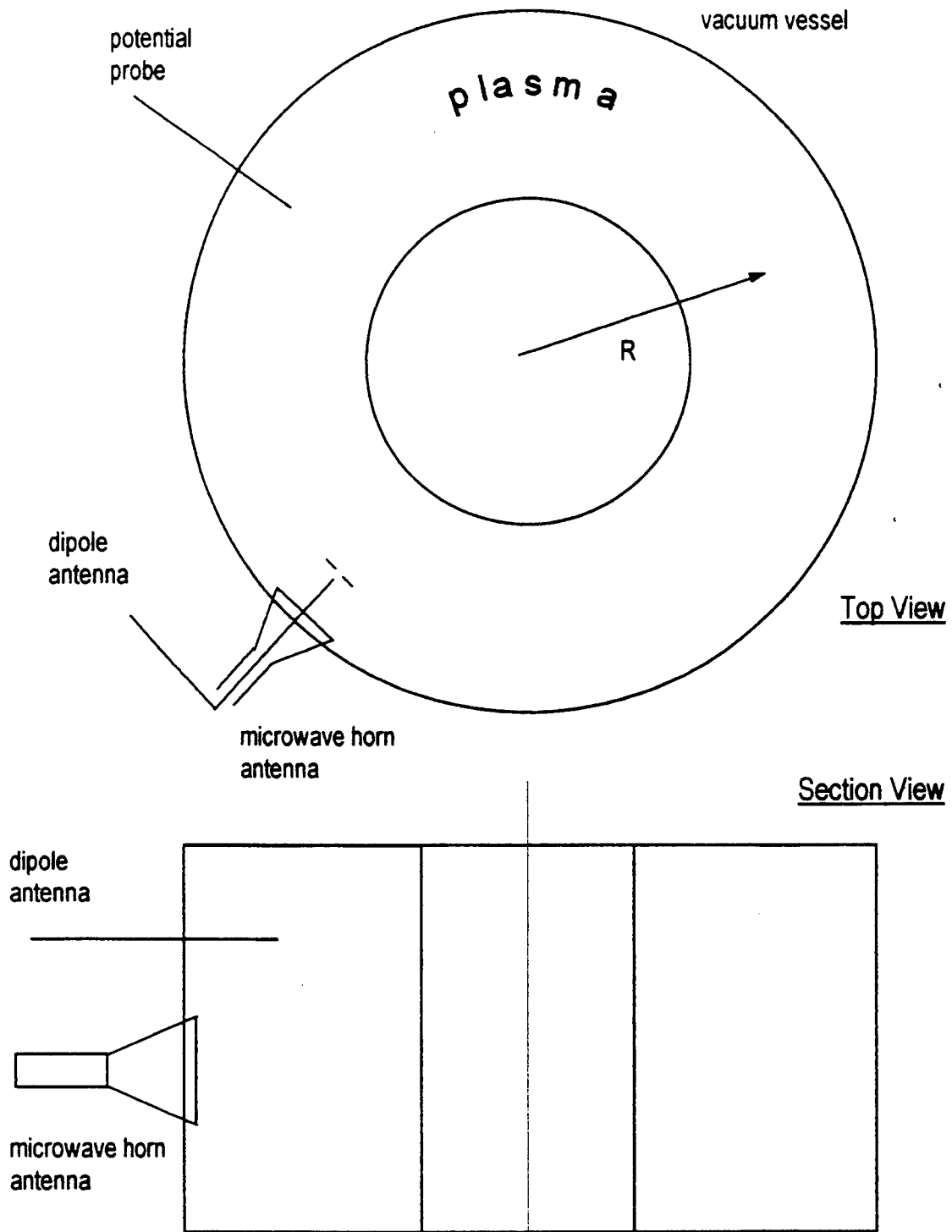
Figure 4-1 Schematic views of the VTF.
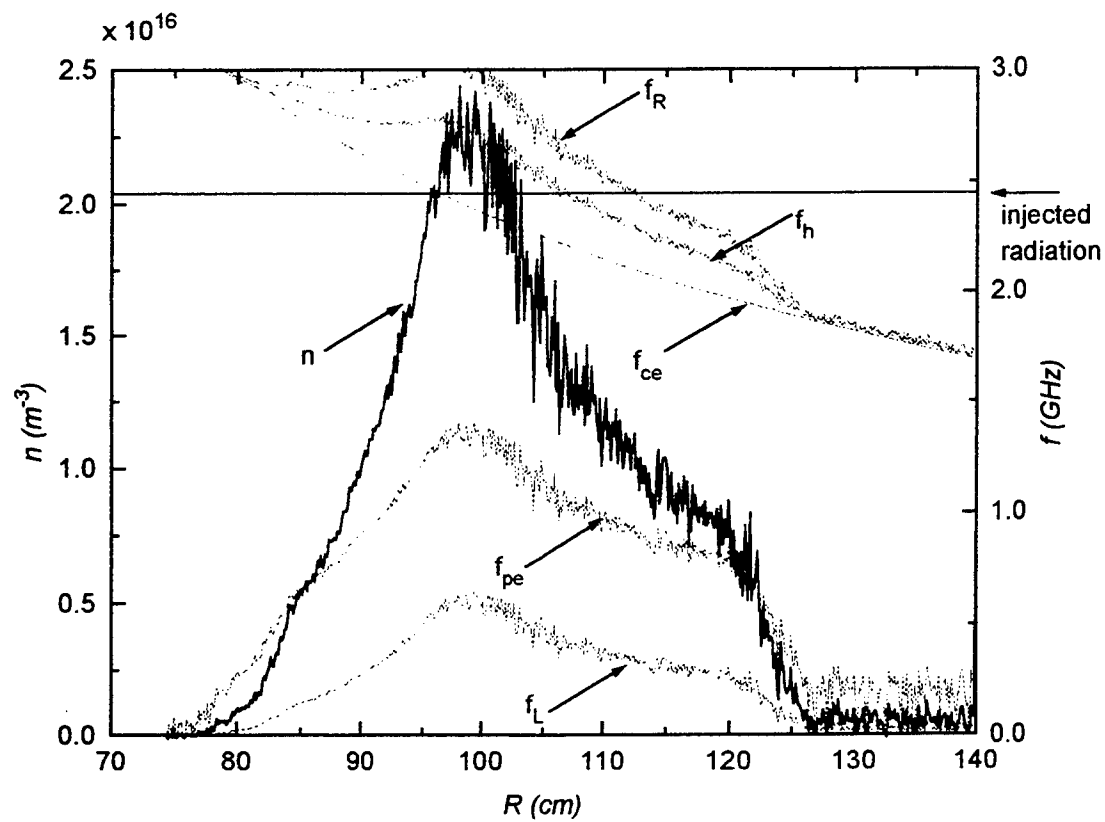
Figure 4-2 Plasma density (Te = 8 eV) in an RF only shot.
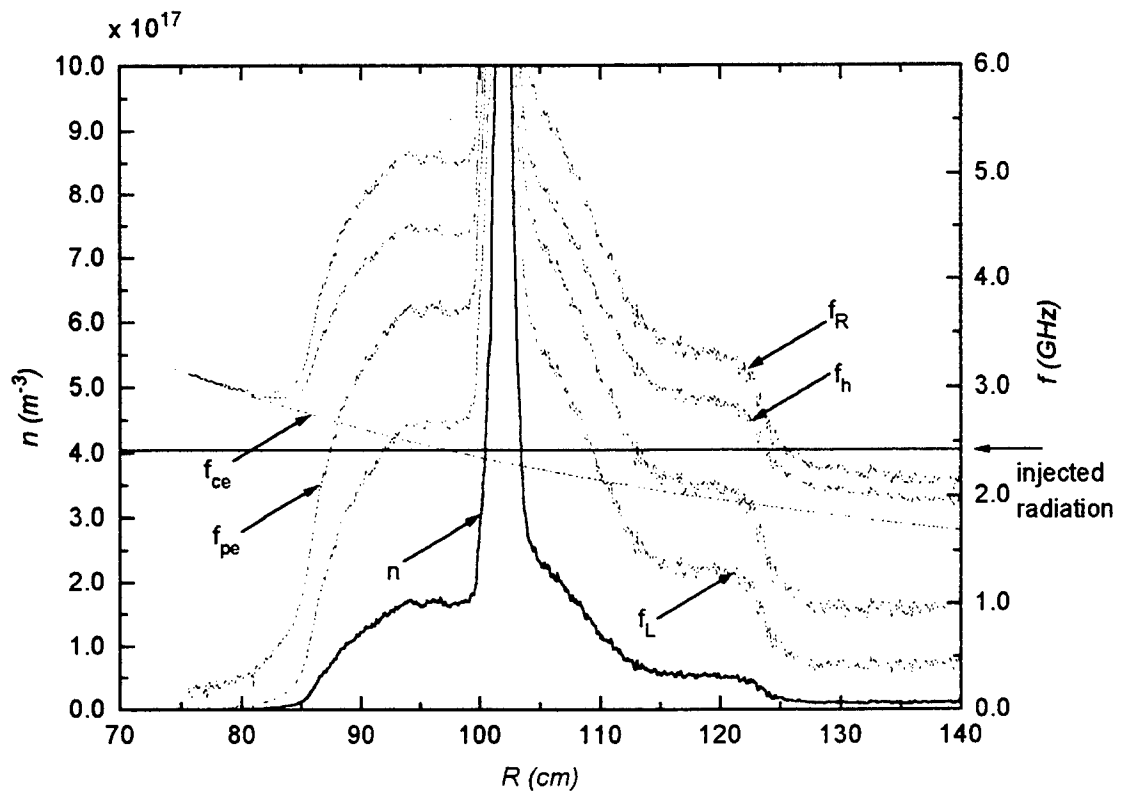
Figure 4-3 Plasma density (Te = 8 eV) in an electron beam plus RF shot.
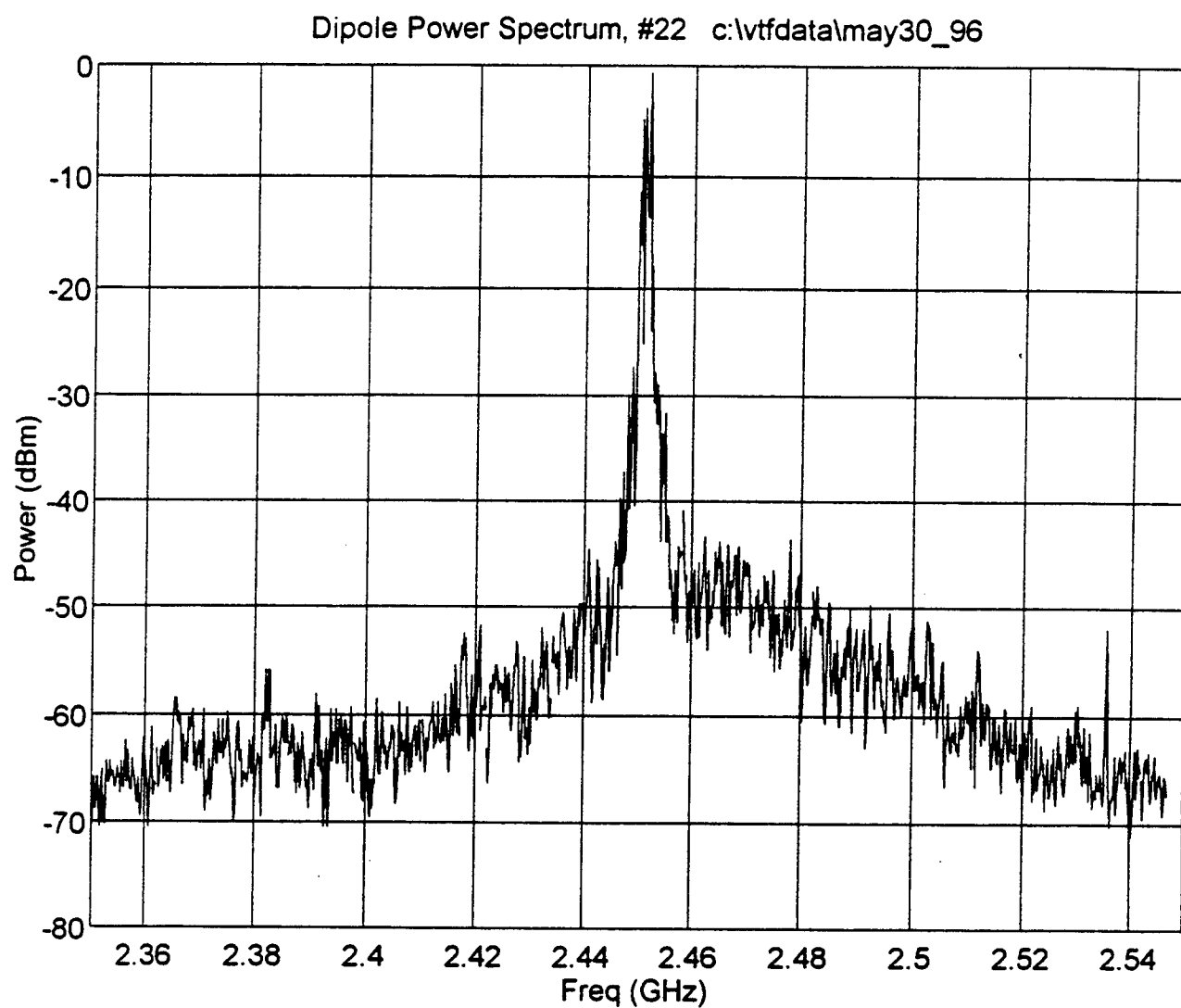
Figure 4-4 High frequency dipole antenna spectrum , R = 110 cm.
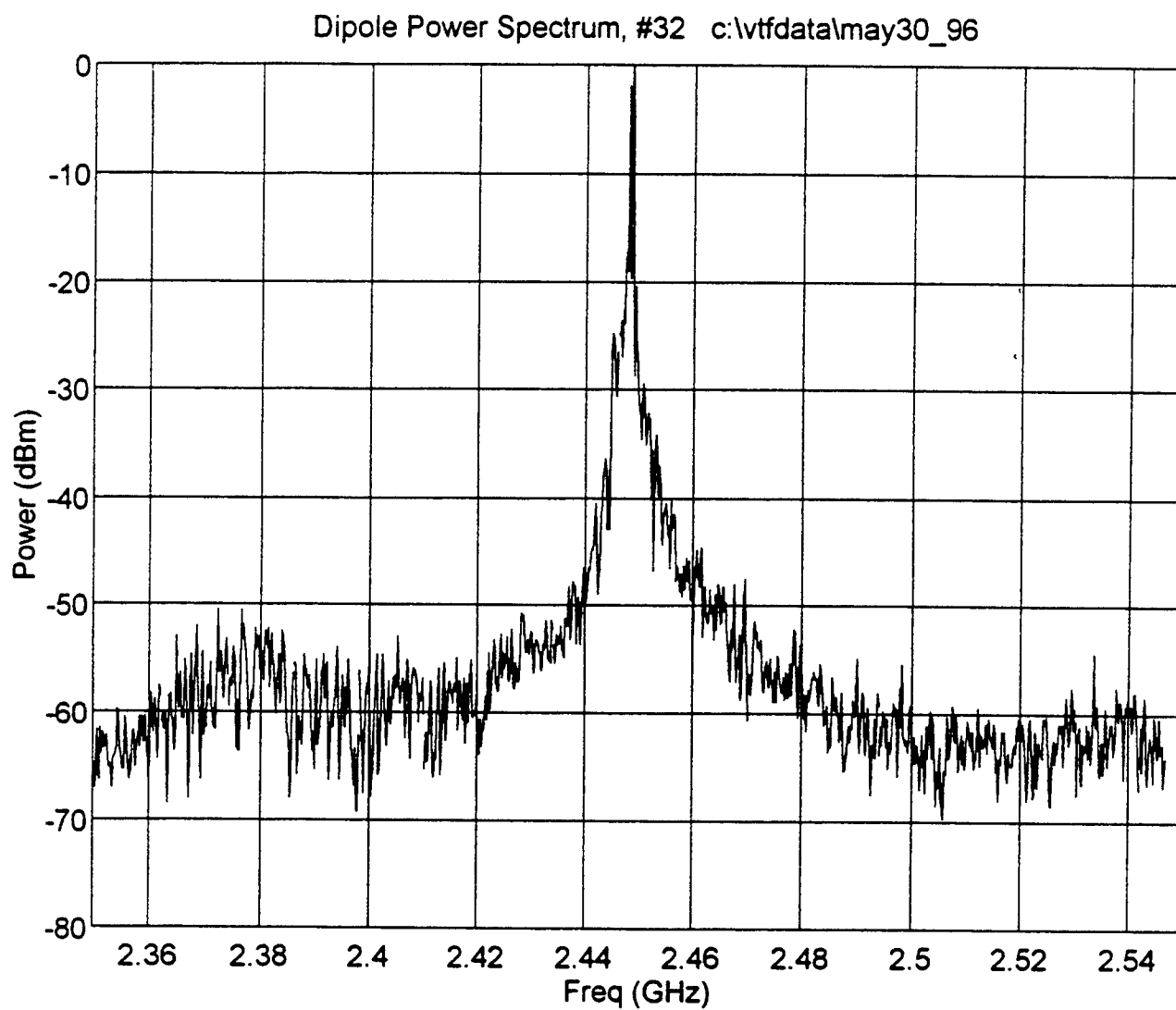
Figure 4-5 High frequency dipole antenna spectrum, R = 120 cm.
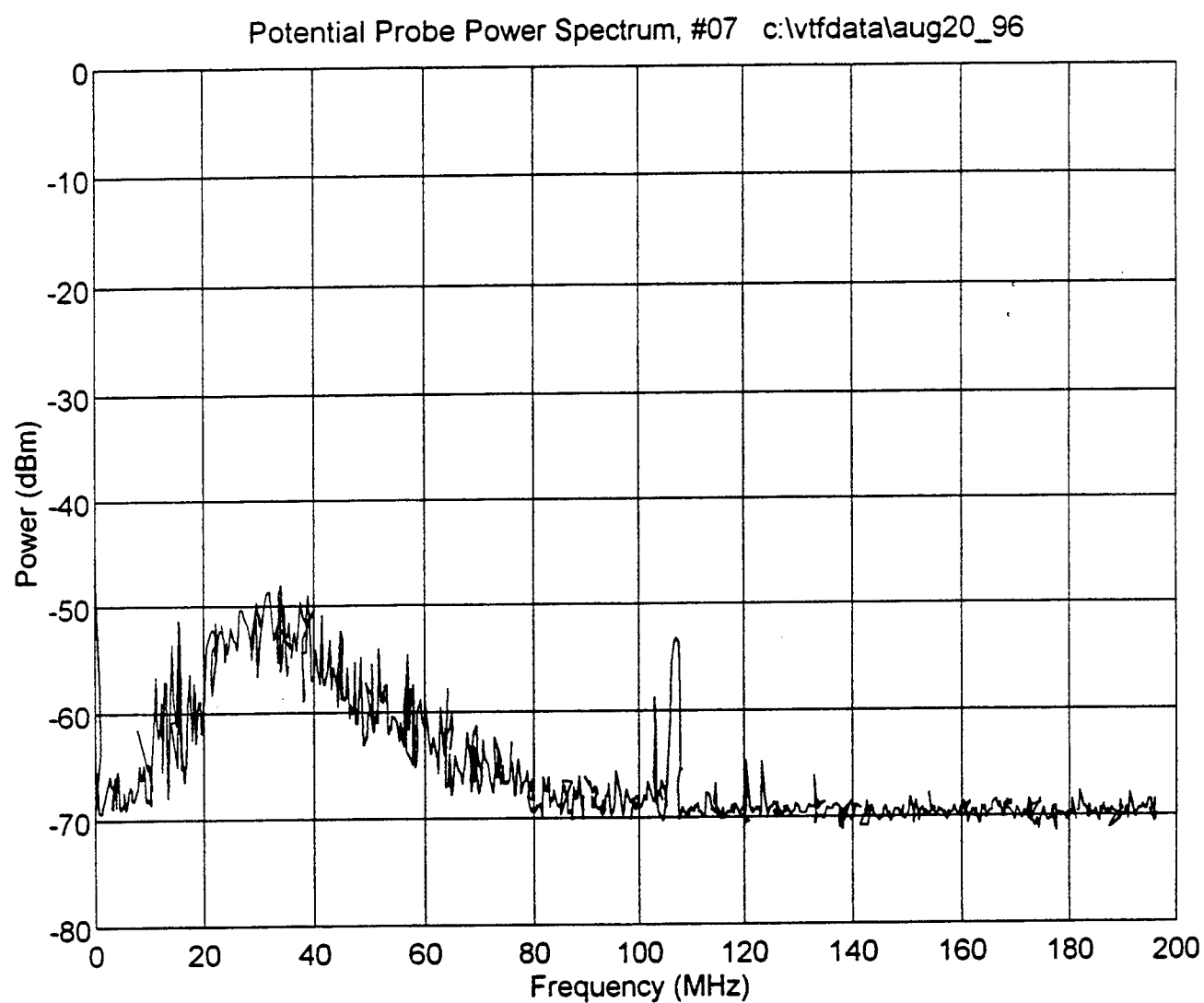
Figure 4-6 Low frequency potential probe spectrum (typical).
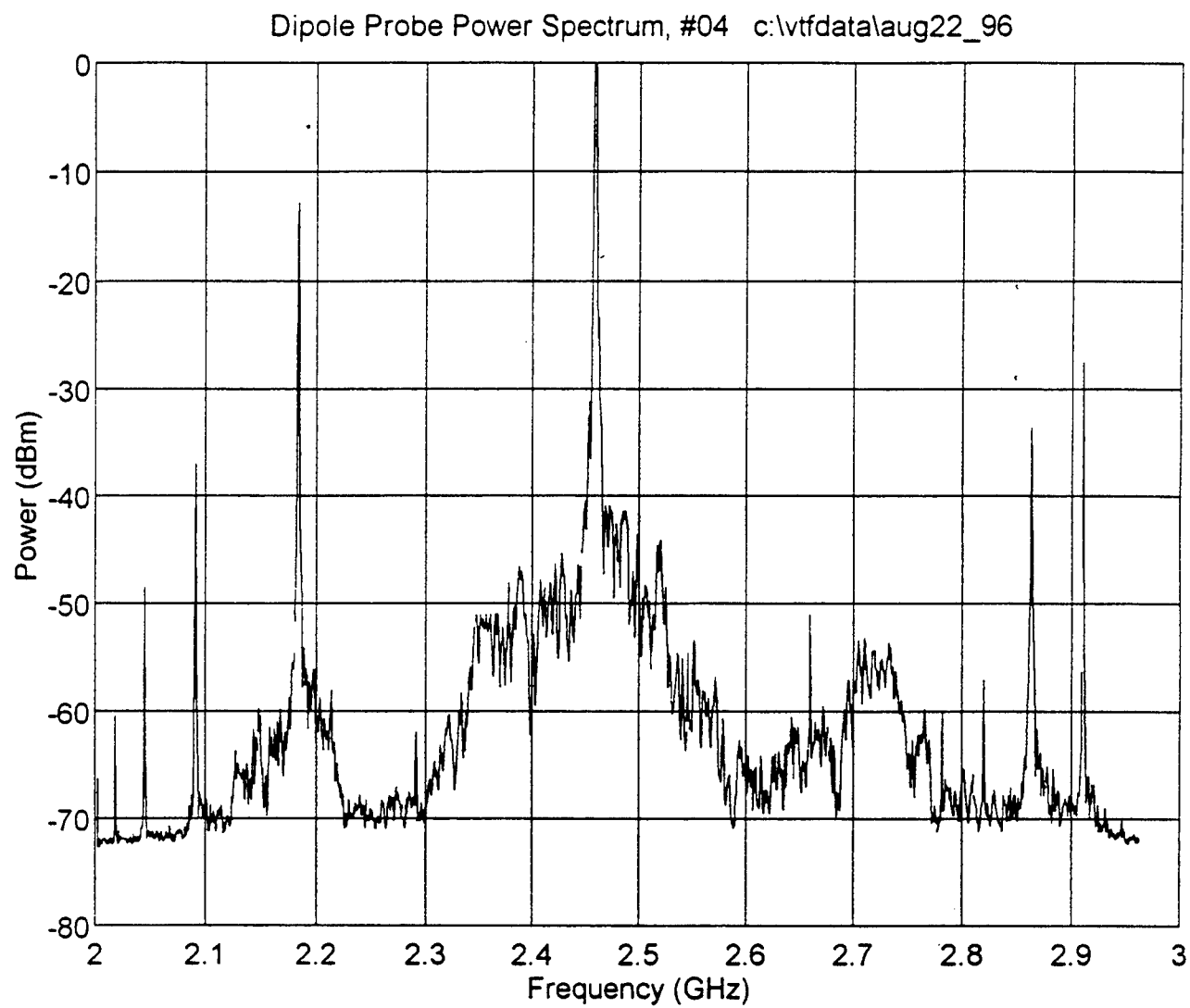
Figure 4-7 High frequency dipole spectrum, vacuum (no TF current).

Michael Doherty's report was not available at the time of publication.

THEORY, MODLING & ANALYSIS OF AMTEC

Matthew Ellis

Master Degree Student

Department of Physics

Texas Tech University

Department of Physics

P.O. Box 41051

Lubbock, TX 79409 - 1051

Introduction

AMTEC, or Alkali Metal Thermal to Electric Conversion, is a power conversion technology based on the properties of the beta alumina'' electrolyte solid[1]. This is a ceramic material with a high ionic conductivity. AMTEC cells work by diffusing sodium ions from a high pressure region to a low pressure region through the beta alumina''. The ceramic has a relatively low electronic conductivity; thus, electrons do not move through with the ions and a potential difference is created between the high pressure side and low pressure side.
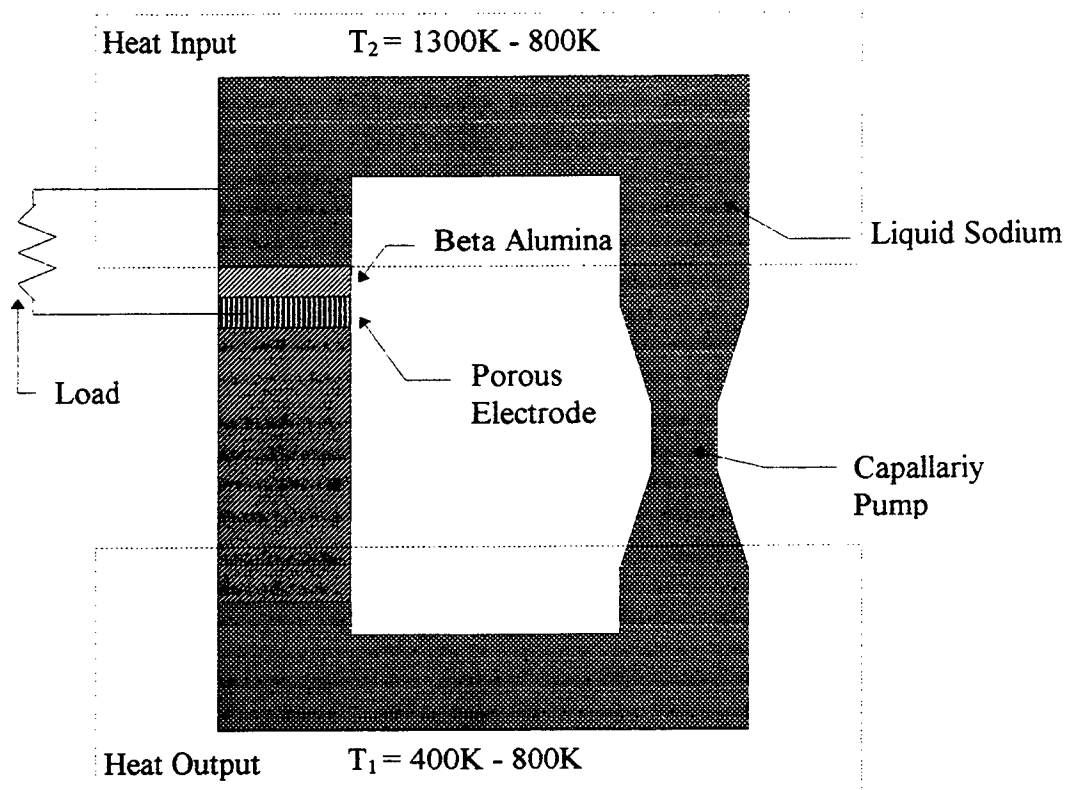
FIGURE 1   **AMTEC Functional Block Diagram**

For space power applications, AMTEC technology has the advantages of high power density, high efficiency and long lifetimes. Efficiencies of approximately 20% have been demonstrated and estimates of efficiencies of 30% - 40% have been predicted.

PL-9A SCP

PL-9A is a single beta tube liquid anode cell with internal heat shields designed to block radiative heat transfer from the evaporator to the condenser. Previous testing of the cell showed poor performance with open circuit voltage lower than normal and minimal carrying capacity of the cell under a load. After discussions with AMPS, it was decided that sodium may have condensed on the heat shields inside the cell. Their suggestion was to heat the entire cell to evaporate any condensed sodium on the heat shields.

After heating the cell with heater tape, the objectives of testing were to first, determine if PL-9A was now functioning correctly; second, test the new single cell package(SCP) with the tantalum element heater; and third, obtain thermal data for modeling the single cell package.

The single cell package consists of several layers of molybdenum and stainless steel. The heat source for the package is two tantalum element heaters each approximately 3.9' feet in length and .02 inch in diameter. The two heaters are connected in parallel with each other to the HP power supply. For modeling purposes, a susceptor was placed on the heater. This susceptor provides a uniform heat source to the cell and simplifies modeling the single cell package. Appendix A shows the single cell package and the location of the each thermocouple in the package and on the AMTEC cell.

After testing PL-9A over a range of operating temperatures from approximately 800K to 1200K the cell produced no significant amount of power under a load. At 400 watts of input power the cell top was at 1180K and the open circuit voltage was approximately .2 volts. Upon loading the cell, the open circuit voltage dropped to zero. Thermal data was successfully obtained with the exception of the susceptor temperatures. These thermocouples measured

abnormally low temperatures compared to the rest of the thermocouples in the package. After

removal of the SCP from vacuum, three of the susceptor thermocouples were removed and

tested with TCs from Omega.

Thermocouple Testing

Three of the susceptor thermocouples were tested along with two TCs obtained from

Omega as well as another TC fabricated in the lab. Ungrounded, isolated TCs from Omega

might have been damaged at the high operating temperatures of the susceptor. Therefore, all

of the TCs used on the susceptor were fabricated in the lab. Figure #1 shows the arrangement

of the thermocouples on the test cylinder. The cylinder is made of stainless steel and the entire

assembly was wrapped with heater tape. Thermocouples number one and five are the isolated

TCs from Omega. Thermocouple number six was fabricated in the lab after testing PL-9A.

Thermocouples two, three, and four were three of the susceptor thermocouples used in the

PL-9A SCP.
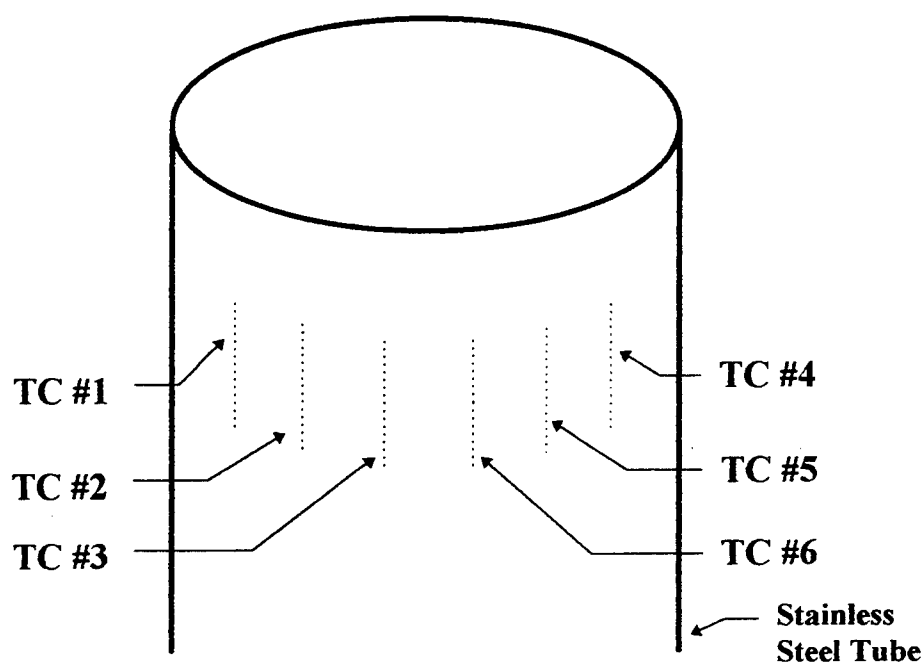
FIGURE 2   **Arrangement of Thermocouples on Tube**

6-4

The entire assembly was heated to a temperature of approximately 600°C. Data from the test is shown in Table #1. The three susceptor TCs began to diverge from the other TCs at approximately 40°C. From that point onward the divergence increases with temperature. The other TC fabricated in the lab does not diverge from the two TCs produced by Omega. This behavior indicates that the erroneous susceptor temperatures were not due to any problems with the TC being ungrounded and it is more likely that the susceptor TCs were fabricated from the wrong material. In any case, with the data obtained from this test the correct susceptor temperatures recorded during the testing of PL-9A may be determined.

Table 1   **Data from Thermocouple Testing**

TC#1 (°C)	TC#2 (°C)	TC#3 (°C)	TC#4 (°C)	TC#5 (°C)	TC#6 (°C)
25.3	24.5	24.8	24.6	25.2	25.3
74.5	57.1	59.5	54.1	73.5	76.6
99.9	70.5	73.1	67.8	98.3	101.9
163.5	107.2	109.7	103.8	161.1	163.3
221.8	146.0	150.4	140.4	218.7	224.2
274.2	181.2	184.3	172.0	270.4	274.7
349.3	227.4	232.2	218.4	345.2	351.8
460.5	294.0	298.7	281.0	456.2	462.9
494.2	317.8	324.1	300.9	490.6	498.1
532.2	332.9	338.2	316.5	528.0	534.2
547.8	341.8	346.5	326.0	544.8	550.0
600.6	367.4	372.2	350.3	598.1	603.0
625.8	379.5	383.5	362.9	624.0	627.9

Calorimeter Experiment

The objectives of the calorimeter experiment are to calibrate the boralectric heater and the boron nitride heater block. Appendix B contains a diagram of the calorimeter experiment setup. Thermocouples placed in the heater block measure the block temperatures as a function of distance from the heater. By calibrating this heater system the actual heat flow to the AMTEC cell can be determined. After determining the conduction heat losses, the

effective Z radiation coefficient for the gap between the cell and the heater can be determined. This data will assist the computer modeling of the AMTEC cells by providing benchmark data for the computer model. A second method for determining the effective Z radiation coefficient for the gap was also employed.

<u>Heater Resistivity Experiment</u>

A second method for determining the effective Z radiation factor for the gap between the heater block and the AMTEC cell was employed with the use of the Accufiber lightpipe probe. This method was based on determining the surface temperature of the heater as a function of heater resistance. The manufacturer of the heater provided a resistivity versus temperature curve for the heater; thus, this test would also verify the manufacturer data. Once the functional relationship between the resistance and surface temperature is established, the heater surface temperature can be determined without a direct measurement. Using the data for the current and voltage input to the heater the resistance can be determined and thus the heater surface temperature can be calculated.
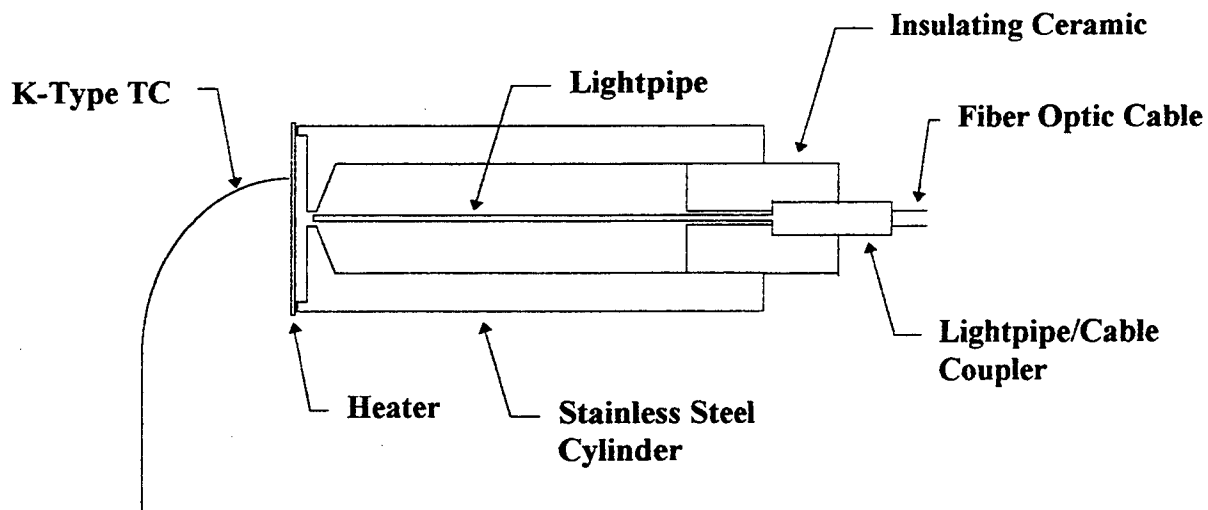
FIGURE 3   **Section View of Test Assembly**

Figure 3 shows the experimental setup for the heater resistivity experiment. Two methods are

used to measure the heater surface temperature. A conventional K type thermocouple is attached directly to the surface of the heater using boron nitride paste. A lightpipe is also used to measure the surface temperature. Due to the expensive and fragile construction of the lightpipe a test assembly was constructed to minimize the chance of breaking the lightpipe. This assembly also allows for the adjustment of the distance of the end lightpipe from the heater surface. The lightpipe works by collecting light emitted from the surface of the heater and transmitting this light to the Accufiber instrument. Then this instrument uses Planck's equation to determine the appropriate temperature[2]. For the lightpipe to function correctly, the fiberoptic cable transmitting the light to the instrument must be calibrated for that particular lightpipe. Furthermore, the emissivity of the surface at temperature must also be known. For our lightpipe test assembly we attached the heater to the end of the stainless steel cylinder. A small hole in the end of the cylinder allowed the lightpipe to see radiation emitted from the surface. This configuration assumed that the gap between the cylinder end and heater was a blackbody cavity and the emissivity could be set to one.

Appendix C shows the data from the heater resistivity experiment. The deviation between the thermocouple measurements and lightpipe measurements at lower temperatures is due to the sensitivity of the lightpipe at longer wavelengths. At shorter wavelengths, errors in the emissivity have a smaller effect on the temperature measurements[3]. Furthermore, the Accufiber setup we used can measure a minimum temperature of 500°C. The data obtained from this experiment provides a resistance versus temperature curve. In comparison, the manufacturer provides a resistivity versus temperature curve. Over the range of temperatures measured (500°C - 900°C) these curves agree within the error of the manufactures data of approximately 13%. By taking the ratio of the resistance to resistivity at the end points of the

measurements, the ratio of the length of the heater element to the area of the element can be found. After numerically fitting the curve provided by the manufacturer, the ratio previously found can be used as a multiplicative constant in determining the heater temperature as a function of resistance.

References

1. Robert K. Sievers, Joesph F. Ivanenok III, Thomas K. Hunt, "Alkali Metal Thermal to Electric Conversion", Mechanical Engineering Magazine, Oct. 1995, pp. 70-75.

2. James W. Knope, "Optical Temperature Measurements in Vacuum Environments with Single and Dual Wavelength Measurement Techniques", 1993 Utah Vacuum Symposium.

3. James W. Knope, "Optical Temperature Measurements in Vacuum Environments with Single and Dual Wavelength Measurement Techniques", 1993 Utah Vacuum Symposium.
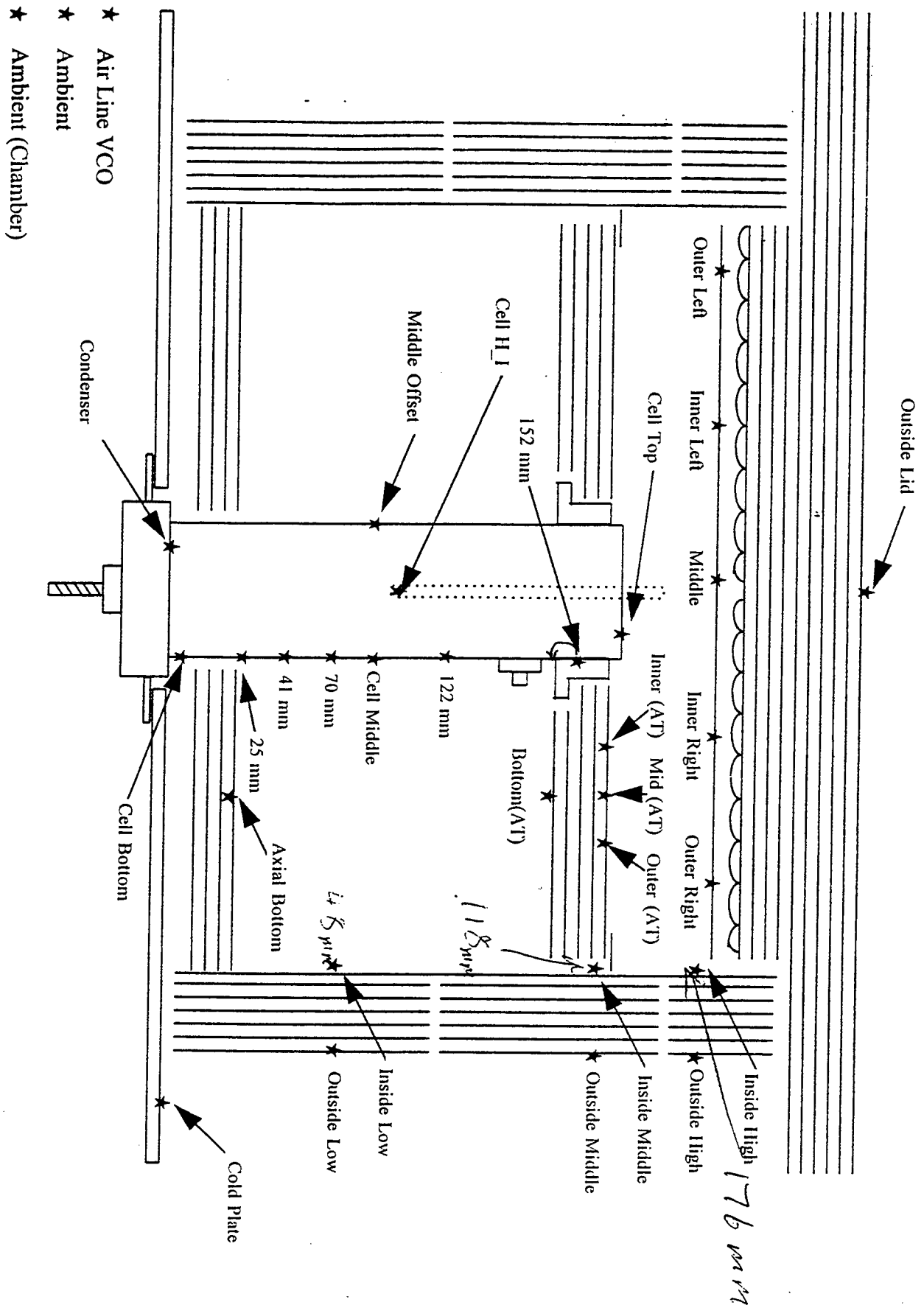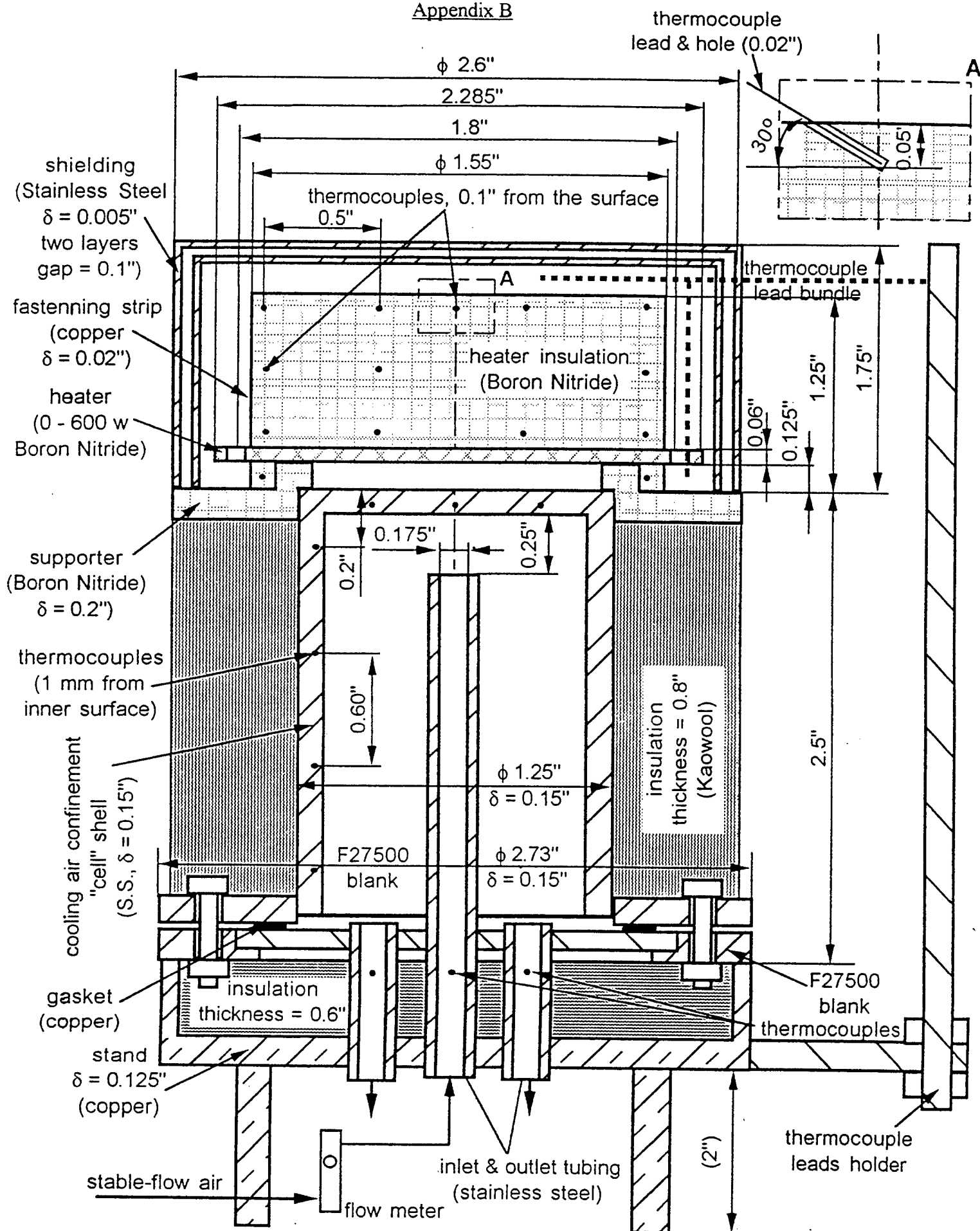
Calibration System for Cell Heating Device (4th Modification)

Voltage	Current	TC temp. (K)	TC Temp (C)	Lightpipe (K)	Lightpipe (C)	Resistance
22	2.16	805.46	532.31	870.82	597.67	10.18519
23.8	2.4	848.21	575.06	919.3	646.15	9.916667
28.1	2.98	943.7	670.55	1023.34	750.19	9.42953
29.1	3.1	962.59	689.44	1046.08	772.93	9.387097
30.3	3.28	987.02	713.87	1071.02	797.87	9.237805
31	3.38	999.05	725.9	1084.42	811.27	9.171598
32	3.51	1026.05	752.9	1100.71	827.56	9.116809
32.7	3.6	1047.36	774.21	1107.54	834.39	9.083333
33.7	3.75	1077.85	804.7	1116.3	843.15	8.986667
34.7	3.88	1094.36	821.21	1127.53	854.38	8.943299
35.7	4	1110	836.85	1137.21	864.06	8.925
36.7	4.11	1104.2	831.05	1116.52	843.37	8.92944
41.5	4.78	1181.87	908.72	1190.93	917.78	8.682008

Resistance Vs. Temperature (Lightpipe)
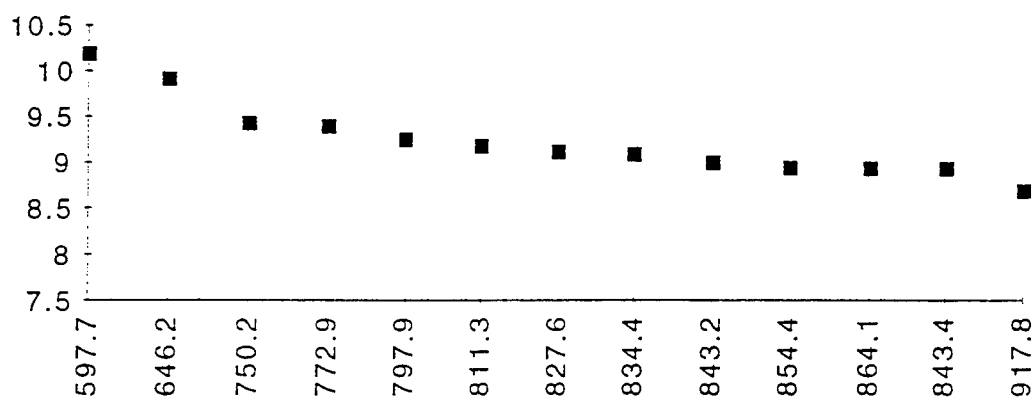
Resistance Vs. Temperature (TC)
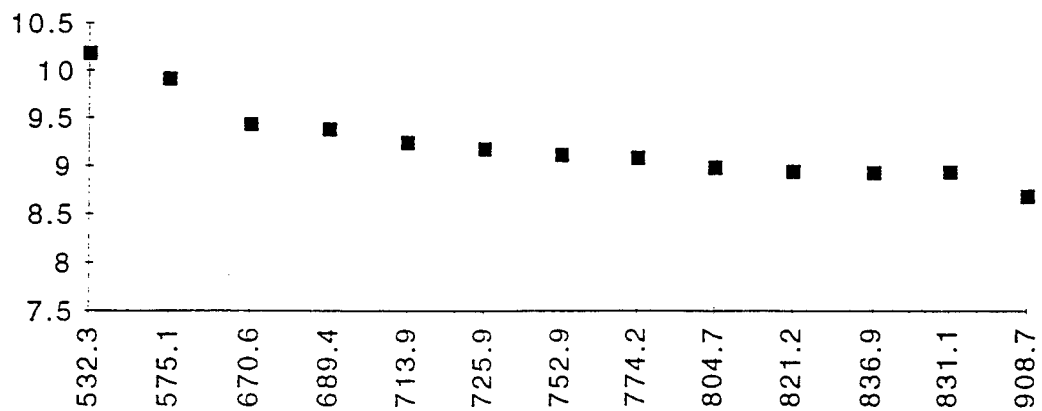
A Quantum Mechanical Investigation of the Structure and Properties of Radiation Induced Defects in a-SiO$_2$

Antonio M. Ferreira

Department of Chemistry

University of Memphis

Smith Chemistry Building

Memphis, TN 38152-6060

Final Report for:

Graduate Student Research Program

USAF Philips Laboratory

Space Electronics Division

September 1996

A Quantum Mechanical Investigation of the Structure and Properties of Radiation Induced Defects in a-SiO$_2$

Antonio M. Ferreira

Department of Chemistry

University of Memphis

Smith Chemistry Building

Memphis, TN 38152-6060

with

Shashi P. Karna

Senior Research Associate

USAF Philips Laboratory

Space Electronics Division

3550 Aberdeen Ave

Kirtland AFB, NM 87117

Abstract

The work presented here represents research conducted at the United States Air Force Philips Laboratory concerning the structure and properties of radiation induced defects in the a-SiO$_2$ lattice. Several proposed structural defects are studied and the nonlinear optical properties of one of these defects have been calculated using *ab initio* quantum mechanical methods. In addition, preliminary work directed toward a method for the calculation of the nonlinear optical properties of resonant interactions is presented and some preliminary results are given and discussed. Suggestions for future work aimed at better descriptions of structural defects in a-SiO$_2$ and associated properties are also discussed.

Calculations

H^+ and SiH_3^+ in a-SiO_2

Background

Silicon dioxide (SiO_2) films are an important part of the metal-oxide-semiconductor (MOS) technology used in radiation hardened electronics. Impurities present in the oxide layer substantially alter both the performance and reliability of any given device. As a result, sophisticated fabrication techniques are currently used for radiation hardening which considerably reduce the presence of defects in the oxide layer. In particular, separation by the implantation of oxygen (SIMOX) has been a very successful technique for the production of SOI materials.

Despite the use of sophisticated techniques, a number of defects, produced either during the processing or by post-processing treatments are still trapped[1] in the insulating oxide layer. Much research has been devoted in the past twenty years to definitively characterize the structure, origin, and radiation-induced physical properties of these defects.[2,3] One of the defects detected in as-grown and radiation-damaged thermally grown oxides as well as those fabricated via SIMOX is a positively charged diamagnetic species.[4]

Traditionally, the structural determination of defects in the MOS structure has relied upon electron paramagnetic resonance (EPR) spectroscopy. For paramagnetic defects in amorphous SiO_2 films, EPR spectroscopy provides a reasonable description of the spin density distribution and the local electronic environment of the magnetic nucleus. From this information, it is often possible to build a reasonably accurate model of the local atomic arrangement surrounding the EPR active centers. Unfortunately, some radiation-induced positively charged centers in SiO_2 films are EPR-inactive indicating that, despite its electrical charge, this species has no unpaired electron in its valence band.[5] Due to the lack of such EPR activity, it has been difficult to identify the local atomic and electronic structure. Recently, Warren *et al.*[4] have proposed a mechanism for the generation and a local atomic structure of the H-induced Positive Charge Defect (PCD) in SIMOX and thermal oxide samples. According to Warren *et al.*, the PCD in H-induced samples are most likely trivalent positively charged oxygen centers.

7-3
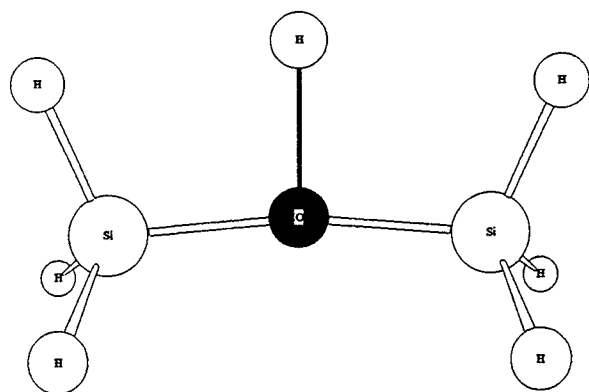
Figure 1

Potential Energy Curve for (SiH₃)₂O–H⁺ Interaction
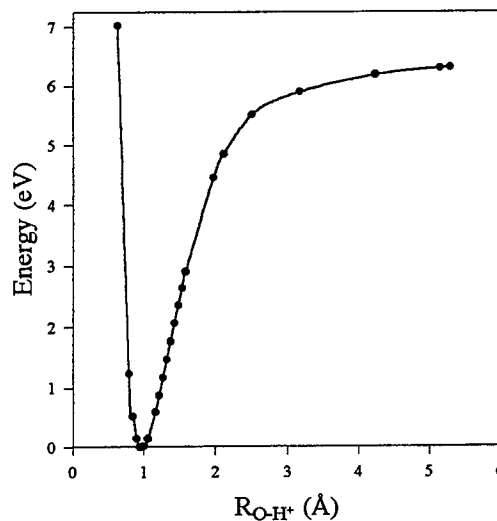
Structure 1

In this study, the structure and stability of over-coordinated O centers has been investigated by *ab initio* quantum mechanical methods. The results of our investigation, indicate that both the Si_2HO^+ and the Si_3O^+ bonded trivalent oxygen
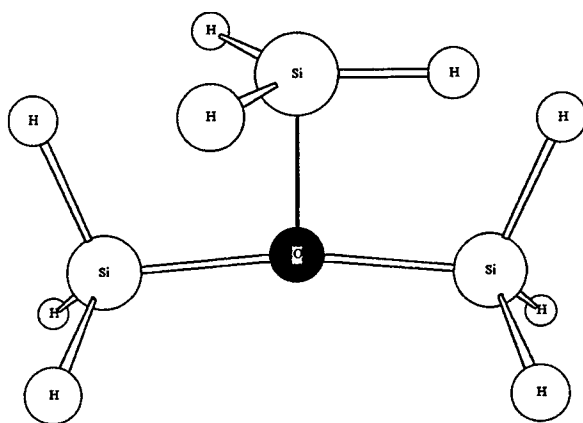
Figure 2

Potential Energy Curve for (SiH₃)₂O–SiH₃⁺ Interaction
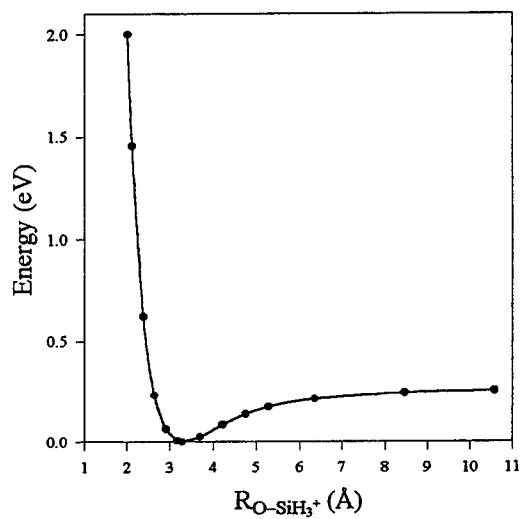
Structure 2

centers are stable with respect to the separated species. However, the binding energy of the Si_2HO^+ coordinated PCD (Structure 1) is much higher than the Si_3O^+ coordinated species (Structure 2) as shown in Figs. 1 and 2.

The potential energy (PE) curves for the interaction of H^+ and SiH_3^+ ions with $H_3SiOSiH_3$ were calculated using an *ab initio* Hartree-Fock (HF) method as implemented in the GAMESS/HONDO computational chemistry package.[6] For the SiH_3^+ ion, a planar geometry was obtained from a HF geometry optimization. The geometry of the neutral precursor ($H_3SiOSiH_3$) was obtained via the same method. In these calculations a double-ζ Cartesian Gaussian basis set, augmented by a p polarization function on the H, and a d polarization function on the Si and O atoms was used.[7,8] The optimized geometries of the precursor and the SiH_3^+ ion were in good agreement with those obtained in previous calculations using similar methods.[9,10]

Results

The calculated PE curves for the interaction of the H^+ ion and the SiH_3^+ with $H_3SiOSiH_3$ are shown in Figures 1 and 2, respectively. As can be seen from the figures, the PE curve for the H^+ coordinated complex (Structure 1) is much steeper in the binding region, with an equilibrium O-H distance of 1.021 Å and a binding energy of 6.764 eV. Although the SiH_3^+ coordinated complex (Structure 2) is also bound with respect to the separated limit, the PE curve has a shallow minimum with a relatively "soft" shoulder. The binding energy of this complex has been determined to be only 0.313 eV. Consistent with this weak binding, the minimum in the PE curve of Structure 2 also appears at a much greater O-Si distance (3.024 Å). This is 1.4 Å (~ 86%) larger than the normal O-Si distance found in bulk SiO_2.

Discussion

The binding energies determined from the *ab initio* calculations confirm the supposition that over-coordinated O centers are thermally stable, however the coordination of the Si_2HO^+ ion is found to be exceptionally strong (~7 eV). This is somewhat surprising given that this entity is similar to that proposed for H^+ motion and which has been characterized by an activation energy of approximately 0.8 eV.[11]

It is quite apparent that mechanistic predictions based on our current calculations and available experimental evidence are not in good agreement. Quantum chemical calculations on radiation induced defect sites have been performed previously making use of the semi-empirical modified intermediate neglect of differential overlap (MINDO/3) model. Previous calculations which are quite similar to the ones presented here are those by Edwards[12] and Robertson[13].

The work presented by Robertson deals with the calculation of over-coordinated Si centers in the formation of valance alternate pair (VAP) defects in bulk SiO_2. However, there are two primary differences between the model used in the Si calculations of Robertson and the model implemented here. Namely, in place of the terminal hydrogen atoms used here (see Structure 2), Robertson used terminal OH groups and the previously mentioned MINDO/3 wave function.

Calculations were also performed using the larger $[(OH)_3Si]_2O$ model cluster at the same *ab initio* level. These results agree very well qualitatively with the results obtained here with only minor changes in the quantitative results. The results of these calculations are given below in the section on H^0 and H^+ migration in a-SiO_2 layers. From the preliminary calculations performed using the larger model cluster it was apparent that the results of the present calculation were sufficiently accurate for the description of the problem at hand.

The calculations of atomic hydrogen coordination to Si–O–Si sites of Edwards suggest that the dissociation energy of atomic hydrogen is approximately 1.5 eV[*] . This difference in calculated dissociation energy can be partially explained in terms of electronic interactions. One would expect that the coordination of atomic hydrogen to an O site would be less stable energetically since the lone pair from the O atom must overlap with the partially filled s orbital of the H atom. This consequent repulsive force would clearly result in a less stable complex and therefore a lower dissociation energy.

In both these earlier calculations, the geometry of the neutral complex was allowed to relax as the coordinating species approached whereas the present calculations do not allow for this relaxation. It was determined that future calculations should include two corrections to these preliminary results. The first of these is the relaxation of the geometries as the two separated species approach to form the final structure. Secondly, electron correlation methods should be introduced into the calculations to account for electron-electron interactions (e.g. MP2 perturbation theory). It should be stressed that although, to our knowledge, the results presented here represent the first *ab initio* calculations on such systems, the work does however provide theoretical evidence for the stability of the proposed over-coordinated O centers.

H^+ vs. H^0 Coordination in a-SiO$_2$

Background

The calculations performed on H^+ and SiH_3^+ binding to O centers raise questions concerning the ramifications of neutral hydrogen (H^0) binding in the same manner. Similar to the H^+ binding proposed by Warren *et al.*, this structure has the potential to be an important defect in the SiO$_2$ lattice. In addition, evidence of H^0 binding would support the work presented by Edwards and Germann which showed that there was clearly a barrier to dissociation for a neutral O–H bond.

It has been suggested that the $(H_3Si)_2O$ cluster used previously is too small to accurately model structural defects in a-SiO$_2$ systems. In order to address this concern, a larger cluster, $[(OH)_3Si]_2O$, was included in this study to examine the nature of the binding of the two species.

Calculations

The calculations performed here were carried out in the same manner as those described above. A geometry optimization was the performed using the same DZP basis set to obtain the precursor (Structure 3). All results were obtained using *ab initio* Hartree-Fock (HF) theory with a double-ζ plus polarization (DZP) Gaussian type basis set. The geometry of the precursor was held constant and the O–H$^+$/H^0 distance was varied to calculate the potential energy curves (See Figures 3 and 4). In addition, MP2 calculations were performed at all points along the PE curve using the same basis set and the initial wavefunction.

Results

The calculated PE curves for H^+ and H^0 coordination to O centers in a-SiO$_2$ are shown in Figures 3 and 4, respectively. It is clear from these curves that the MP2 calculations are consistent with the results obtained using the HF

---

[*] This figure is based on a revised evaluation of the data presented in the original paper.

calculations of the previous study. Clearly, the binding energy is somewhat affected by the inclusion of an additional layer of O atoms. It is interesting to note that the PE curve for the binding of H^0 to the precursor is completely repulsive. It is postulated that this results because the additional electron occupies the π^* orbital of the O–H bond causing an antibonding interaction. Thus we find no equilibrium distance (r_e) for this and the dissociation energy (D_e) is assumed to be zero.

Figure 3

Potential Energy Curve for $[(OH)_3Si]_2O$ — H^+

Figure 4

Potential Energy Curve for $[(OH)_3Si]_2O$ — H
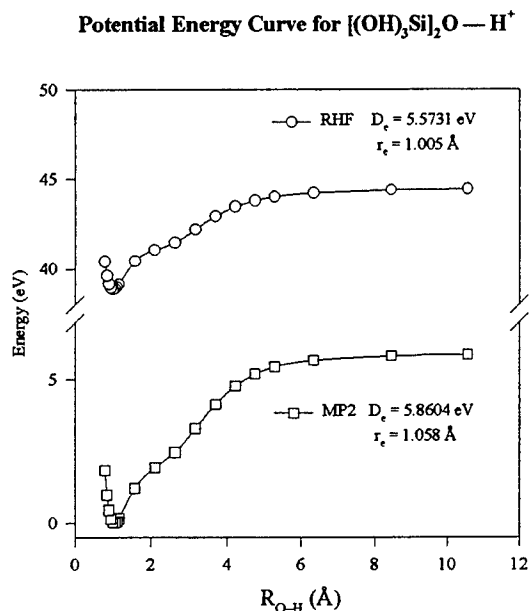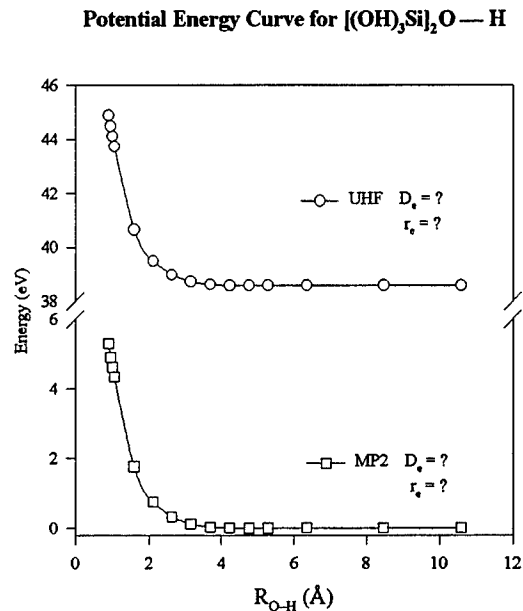
Discussion

Nonlinear Optical Properties of H^+ Defects in a-SiO$_2$

Background

Following the discovery of the second harmonic generation (SHG) of the infrared (IR) light in silica glass fibers a decade ago,[14] there has been considerable interest in the development and applications of photonic components utilizing the NLO effects in a-SiO$_2$ based materials. Recently, Ranon et al.[15] at the former USAF Seiler Research Laboratory have successfully developed an all-optical programmable AND logic gate using the second-order NLO effect in a Ge-doped a-SiO$_2$ planar waveguide. The works of Ranon et al. and others[16] have strengthened the anticipation that novel photonic devices based on silica glasses may soon become an integral part of commercial as well as military technology. Due to Air Force interest in the potential uses of such devices in space applications, there is a need to understand the effects on the NLO response of a-SiO$_2$ based materials in hostile radiation environment. In order to develop such an understanding, we have performed quantum mechanical calculations on the structure and the NLO properties of a model triply coordinated O-hole center believed to be generated in radiation exposed a-SiO$_2$ films.[17,18]

In the presence of an external electric field, E(r,t), the total polarization of a dielectric medium can be written as[19]

$$P = \chi^{(1)}E(r,t) + \chi^{(2)}E(r,t)E(r,t) + \chi^{(3)}E(r,t)E(r,t)E(r,t) + \cdots \qquad (1)$$

where, $\chi^{(1)}$ is the linear susceptibility tensor and $\chi^{(2)}$ and $\chi^{(3)}$ are the first-and second nonlinear optical susceptibility tensors. The $\chi^{(n)}$ tensor in general has $3^{(n+1)}$ components. However, not all components are independent and often only a few elements of the corresponding tensor are required to determine the magnitude of the observables, which are either scalar (for odd-ordered susceptibilities such as $\chi^{(3)}$) or a vector (for even-ordered susceptibilities such as $\chi^{(2)}$). The $\chi^{(2)}$ term determines the strength of the second-order response for various processes, such as second harmonic generation (SHG), electro-optic Pockels effect (EOPE), and optical rectification (OR).

The $\chi^{(2)}$ term for the SHG process is denoted as $\chi^{(2)}(-2\omega;\omega,\omega)$, that for the EOPE is denoted as $\chi^{(2)}(-\omega;\omega,0)$, and for OR, it is denoted as $\chi^{(2)}(0;\omega,-\omega)$. The frequency arguments on the right side of the semicolon represent the input beams and that to the left of the semicolon represent the output beam. A zero in the frequency argument represents a static field. Since we will be mainly concerned with the second-order phenomena such as SHG in this paper, the third-order phenomena and the $\chi^{(3)}$ terms will not be discussed in detail.

The susceptibility tensor, $\chi^{(n)}$, of a dielectric is related to the microscopic polarizability of its constituting units, such as atoms, unit cells, or molecules, as

$$\chi^{(1)} = f^{(1)} \cdot \sum_p \alpha_p \qquad (2),$$

$$\chi^{(2)} = f^{(2)} \cdot \sum_p \beta_p \qquad (3),$$

$$\chi^{(3)} = f^{(3)} \cdot \sum_p \gamma_p \qquad (4).$$

In the above equations, α is the linear polarizability, β is the first-hyperpolarizability, and γ is the second-hyperpolarizability. The $f^{(n)}$ term, known as the local field factor, accounts for the effect of the environment on the linear and the NLO response at the site of the constituting units in the dielectric. Similar to their macroscopic counterparts, the microscopic polarizabilities, α, β, and γ, are tensor quantities of rank 2, 3, and 4, respectively. Thus the α tensor has 9 components, the β tensor has 27 components, and the γ tensor has a total of 81 components. The magnitude of the β and the γ terms determine the strength of the microscopic NLO response of a dielectric. For the second-order effects, $\beta(-2\omega;\omega,\omega,)$ denotes the first-hyperpolarizability for the SHG process, $\beta(-\omega;0,\omega)$ denotes the first-hyperpolarizability for EOPE, and $\beta(0;-\omega,\omega)$ denotes the first-hyperpolarizability for OR process.

As is clear from equations (2)-(4), the macroscopic NLO response of a dielectric is ultimately controlled by the corresponding response of its microscopic units. Any changes in the microscopic structure of a dielectric directly affects its macroscopic NLO response. Therefore, a knowledge of the structure and the NLO properties of the microscopic units of a material provides useful information regarding its bulk NLO response.

In this paper, we are concerned with the changes in the second-order NLO response of a-SiO$_2$ which is quantified the β terms. We report here our calculated values of the components of the β tensor for static field, denoted as $\beta(0;0,0)$ and those for the SHG and EOPE processes at an optical field of IR light ($\lambda = 1.64\mu$m). We also report a scalar quantity, $|\beta|$, which is defined as

$$|\beta| = \left(\sum_i \beta_i^2\right)^{\frac{1}{2}} ; \quad i = x,y,z \qquad (5)$$

where,

$$\beta_i = \tfrac{1}{3}\sum_j \left(\beta_{ijj} + \beta_{jij} + \beta_{jji}\right) \qquad (6).$$

In addition to the NLO coefficient β, we also report the calculated total energy denoted as E, the energy gap between the highest occupied (HO) and the lowest unoccupied (LU) molecular orbitals (MO) denoted as $\Delta\varepsilon$, the dipole moment denoted as μ, and the linear polarizability, α. For the linear polarizability tensor α, the scalar mean polarizability is defined as

$$\langle\alpha\rangle = \tfrac{1}{3}\sum_i \alpha_{ii} ; \quad i = x,y,z \qquad (7).$$

Calculations

The model structures representing the local site of the precursor and the triply-coordinated O-hole center (OHC) in SiO$_2$ used in the present study are shown in Fig. 1 and Fig. 2, respectively. The geometry of the precursor (P) was obtained from *ab initio* Hartree-Fock calculations. The linear and the NLO properties of the precursor and the positively charged species were calculated using the *ab initio* time-dependent coupled-perturbed Hartree-Fock method.[20,21] In all calculations, a double-ζ plus polarization (DZP) Gaussian basis set[22,23] was used. The NLO properties of the POHC were calculated at the theoretically optimized equilibrium geometry of the protonated species.

Results
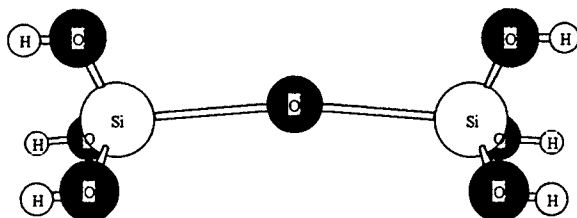
Structure 3
Precursor (P)
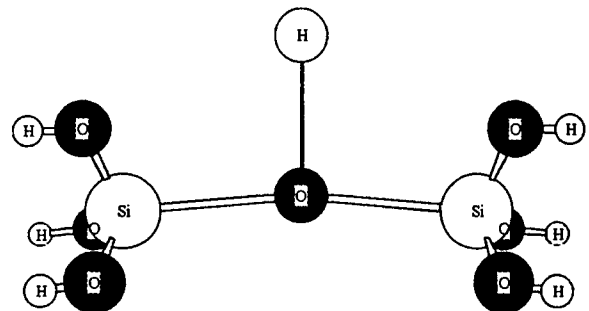
Structure 4
Protonated Oxygen Hole
Center (POHC)

The calculated results for E, $\Delta\varepsilon$, and μ for P (Structure 3) and POHC (Structure 4) are listed in Table 1. The polarizability, α, and the first hyperpolarizability, β, for P are listed in Table 2. The corresponding values for the POHC are listed in Table 3. Although the total energy of the POHC and its unprotonated precursor is not too different from each other, the former being more stable by about 0.0724 eV that the latter, protonation of the species induces substantial changes in the dipole moment and the energy gap between the HOMO and LUMO. Thus, we note from Table 1 that the dipole moment increases by about 0.5 Debye and the HOMO-LUMO energy gap decreases by about 1.014 eV upon protonation of the bridging oxygen. Such a change in the dipole moment is caused by the rearrangement of electron charge around the bridging O atom by protonation. The bare nucleus of H^+ polarizes the lone pair electrons on the O atom along the $O-H^+$ bond. This polarization breaks the nearly-centrosymmetric structure of the charged cloud in the Si–O–Si cluster, thereby leading to an enhanced value of the dipole moment and the second-order NLO coefficient, β.

Table 1. The calculated results for the total energy (E), the HOMO-LUMO energy gap ($\Delta\varepsilon$), and the dipole moment (μ) for the precursor (P) and the protonated oxygen hole center (POHC).

	P	POHC
E (a.u.)	-1105.963990	-1106.160803
$\Delta\varepsilon$ (eV)	17.5232	16.5092
μ (Debye)	0.4235	0.9281

In fact, we note from Table 2 and Table 3 that while the linear polarizability is only slightly affected, the $|\beta|$ coefficient changes by a factor of 4 or more upon protonation. An examination of the various components of the β tensor for the two species (P and POHC) reveals that while the xxz and the yyz component experience only marginal changes upon protonation, the zzz component parallel to the $O-H^+$ bond experiences the largest change.

Table 2. Calculated values for α and β for the POHC (Fig. 2).

α $(10^{-24}$ esu)	$\lambda = \infty$	$\lambda = 1.064\ \mu m$	$\lambda = 0.532\ \mu m$
α_{xx}	7.3066	7.3363	7.4277
α_{yy}	6.8195	6.8450	6.9233
α_{zz}	6.5309	6.5556	6.6314
$\langle\alpha\rangle$	6.8857	6.9122	6.9941

β $(10^{-32}$ esu) $\lambda = 1.064\ \mu m$	$(0;0,0)$	$(-\omega;\omega,0)$	$(-2\omega;\omega,\omega)$
β_{xxz}	-8.8432	-8.9667	-9.2188
β_{yyz}	12.6223	12.7795	13.1091
β_{zzz}	-8.9285	-9.0722	-9.3710
$|\beta|$	5.1495	5.2580	5.4951

Table 3. Calculated values of α and β for the precursor (P) molecule (Fig. 1.).

α $(10^{-24}$ esu)	$\lambda = \infty$	$\lambda = 1.064\ \mu m$	$\lambda = 0.532\ \mu m$
α_{xx}	7.4380	7.4685	7.5622
α_{yy}	6.8185	6.8442	6.9231
α_{zz}	6.3412	6.3654	6.4397
$\langle\alpha\rangle$	6.8659	6.8927	6.9750

β $(10^{-32}$ esu) $\lambda = 1.064\ \mu m$	$(0;0,0)$	$(-\omega;\omega,0)$	$(-2\omega;\omega,\omega)$
β_{xxz}	-10.5186	-10.6296	-10.8725
β_{yyz}	12.2647	12.4137	12.7406
β_{zzz}	-0.6378	-0.6514	-0.6788
$|\beta|$	1.1083	1.1335	1.1865

Discussion

We have presented here the results of our *ab initio* Hartree-Fock calculation on the structure and polarizabilities of a model system representing the precursor and its radiation-induced protonated complex. Our results on the structure reveal that that H^+ binds with a divalent bridging O atom in the Si–O–Si network at an equilibrium distance of about 1.0 Å. The proton binding at the O site accompanies substantial reorganization of the electron charge distribution along the O–H^+ bond, leading to an increase in the dipole moment and the second-order NLO properties of the system.

Method Development

Complex-valued Polarizabilities and Hyperpolarizabilities

Background

Since the first observation of NLO phenomena there has been considerable interest in the theoretical description of the NLO response of materials. Currently, there are two predominant frameworks used for the calculation of the NLO response of a material. These are the time-dependent Hartree-Fock (TDHF) formalism and response theory, which can be classified into density matrix and propagator methods. Response theory offers a more accurate and generally applicable calculation to be performed on any given system. However, the computational methods necessary are very complicated and computationally demanding.

The TDHF formalism is an extension of the well established Hartree-Fock method and is fairly straightforward in both theory and implementation. The primary advantage is that the computational methods required under this approach are straightforward and less computationally intensive. The disadvantage, when compared to response theory, is that TDHF calculations of the NLO properties of materials are only valid for non-resonant frequencies. If the property of interest is calculated near the resonance (or absorption) of the material, the TDHF formalism fails to properly describe the absorption phenomenon and the associated affects on the NLO properties of the material.

The aim of the research presented here is to modify the TDHF theory in order to obtain an accurate description of the NLO phenomenon at or near the absorption of the material. The ability to calculate the resonant NLO properties of a material using this more tractable computational approach will allow for the theoretical study of a much greater range of optical phenomena. In addition, extending the current TDHF method which allows for both *ab initio* and semi-empirical studies, will provide a means for calculating properties for systems which are too large to study with current response theory calculations.

Theory

There are several response theory formulations for the calculation of the (hyper)polarizabilities of molecular systems. For the present discussion, we shall consider the density matrix/equation of motion (EOM) formalism as it offers a straightforward presentation of the problem at hand. In this approach to the problem, we consider the effect of the external

electric field on the electron density of the material. The response of the electron to an applied external field can be considered as that of a damped harmonic oscillator described by

$$\frac{d^2x}{dt^2} + 2\gamma\frac{dx}{dt} + \omega^2 x + ax^2 = -\frac{eE(t)}{m}.$$

In this expression, the applied (optical) field is $E(t)$, the charge of the electron is $-e$, and the damping force is assumed to have the form $\left(-2m\gamma\frac{dx}{dt}\right)$. This expression for the restoring force may be obtained from

$$F_{restoring} = -m\omega_0^2 x - max^2$$

where a is simply a constant related to the nonlinearity of the particular system and ω_0 is the resonance frequency of the system. We take m as the mass of the electron and γ as the damping constant for the harmonic motion of the electron.

For cases of non-resonant phenomena, the damping term is taken to be zero and the equation simplifies. However, in the case of a resonant interaction, this term is clearly non-zero and must be taken into account in order to properly describe the response of the system. The equation used to calculate the polarizability, α, and the first hyperpolarizability, β, under the density matrix/EOM formulation may be written as

$$\alpha_{ij} = \sum_{g,n} \rho_{gg}^{(0)} \left\{ \frac{(r_i)_{ng}(r_j)_{gn}}{\omega + \omega_{ng} + i\Gamma_{ng}} - \frac{(r_j)_{ng}(r_i)_{gn}}{\omega - \omega_{ng} + i\Gamma_{ng}} \right\}$$

and

$$\beta_{ijk}(\omega) = -\sum_{g,n,n'} \rho_{gg}^{(0)} \left\{ \begin{array}{l} \dfrac{(r_i)_{gn}(r_j)_{nn'}(r_k)_{n'g}}{\left(\omega - \omega_{ng} + i\Gamma_{ng}\right)\left(\omega_2 - \omega_{n'g} + i\Gamma_{n'g}\right)} + \dfrac{(r_i)_{gn}(r_k)_{nn'}(r_j)_{n'g}}{\left(\omega - \omega_{ng} + i\Gamma_{ng}\right)\left(\omega_1 - \omega_{n'g} + i\Gamma_{n'g}\right)} \\[3mm] + \dfrac{(r_k)_{gn'}(r_j)_{n'n}(r_i)_{ng}}{\left(\omega + \omega_{ng} + i\Gamma_{ng}\right)\left(\omega_2 + \omega_{n'g} + i\Gamma_{n'g}\right)} + \dfrac{(r_j)_{gn'}(r_k)_{n'n}(r_i)_{ng}}{\left(\omega + \omega_{ng} + i\Gamma_{ng}\right)\left(\omega_1 - \omega_{n'g} + i\Gamma_{n'g}\right)} \\[3mm] - \dfrac{(r_j)_{ng}(r_i)_{n'n}(r_k)_{gn'}}{\left(\omega - \omega_{nn'} + i\Gamma_{nn'}\right)}\left(\dfrac{1}{\omega_2 - \omega_{n'g} + i\Gamma_{n'g}} + \dfrac{1}{\omega_1 - \omega_{ng} + i\Gamma_{ng}}\right) \\[3mm] - \dfrac{(r_k)_{ng}(r_i)_{n'n}(r_j)_{gn'}}{\left(\omega - \omega_{nn'} + i\Gamma_{nn'}\right)}\left(\dfrac{1}{\omega_2 - \omega_{ng} + i\Gamma_{ng}} + \dfrac{1}{\omega_1 + \omega_{n'g} + i\Gamma_{n'g}}\right) \end{array} \right\}.$$

Here, $\rho_{gg}^{(0)}$ is the one-electron density matrix (the one matrix), ω_{ng} is the energy difference between the ground state (g) and an excited state (n), and Γ_{ng} is the population lifetime for the excited state. It is usual to use the Einstein A coefficient as the Γ_{ng} term given by

$$\Gamma_{ng} = \frac{4\omega_{ng}^3 |\mu_{ng}|^2}{3\hbar c^3}.$$

This assumes that the excited state can only decay to the ground state of the molecule, however this approximation has been shown to be useful experimentally. [24]

The implementation of the TDHF solutions in GAMESS is that developed by Karna and Dupuis[25] and alluded to earlier. In this formulation we consider the interaction of monochromatic light and a static electric field with a material. The perturbation is given as

$$\lambda = E(e^{i\omega t} + e^{-i\omega t} + 1).$$

(From this point forward, the shorthand notation $e^{\pm i\omega t} = (e^{+i\omega t} + e^{-i\omega t})$ will be used to represent the oscillating electric field and its complex conjugate.) The perturbation to the Hamiltonian is then defined as

$$H' = \mu \cdot E(e^{\pm i\omega t} + 1)$$

where μ is the dipole moment operator defined by

$$\mu = -\sum_j e \cdot r_j$$

when e is the charge on the electron and r_j is the position vector of the jth electron. Using these relations, the perturbed time-dependent Schrödinger equation

$$H\psi = i\frac{\partial \psi}{\partial t}$$

or

$$\left(H_0 + H' - i\frac{\partial}{\partial t}\right)\psi = 0$$

may be solved.

In order to obtain a solution, Frenkle's variational principle[26] is applied to the time-dependent expression written in matrix form to yield

$$\mathbf{FC} - i\frac{\partial}{\partial t}\mathbf{SC} = \mathbf{SC}\varepsilon$$

with the requirement that S and C satisfy the relation

$$\frac{\partial}{\partial t}\mathbf{C}^+\mathbf{SC} = 0.$$

The spatial orbitals for this system are given by $\phi_n = \chi_n C_n$ where the χ_ns are the basis functions and C is the time-dependent coefficient matrix. The overlap (S) and Fock (F) matrices are given by

$$S_{ij} = \left(\chi_i(1)|\chi_j(1)\right)$$

$$\mathbf{F} = \mathbf{H} + \mathbf{D}[2\mathbf{J} - \mathbf{K}]$$

where $\mathbf{H}$ is the one-electron integral matrix, $\mathbf{J}$ and $\mathbf{K}$ are the two-electron exchange and Coulomb matrices, and $\mathbf{D}$ is the density matrix in terms of the molecular orbitals ($\mathbf{D} = \mathbf{CnC^+}$). Since the S, J, and K matrices are all dependent on the basis functions only, each of these matrices is therefore time-independent. Thus we have,

$$\mathbf{S} \equiv \mathbf{S}^0$$

$$\mathbf{J} \equiv \mathbf{J}^0$$

$$\mathbf{K} \equiv \mathbf{K}^0$$

as the definitions for these matrices. Using the external perturbation and expanding in terms of the energy yields

$$\mathbf{F} = \mathbf{F}^0 + \mathbf{E}^a\mathbf{F}^a + \tfrac{1}{2!}\mathbf{E}^a\mathbf{E}^b\mathbf{F}^{ab} + \tfrac{1}{3!}\mathbf{E}^a\mathbf{E}^b\mathbf{E}^c\mathbf{F}^{abc} + \cdots$$

$$\mathbf{C} = \mathbf{C}^0 + \mathbf{E}^a\mathbf{C}^a + \tfrac{1}{2!}\mathbf{E}^a\mathbf{E}^b\mathbf{C}^{ab} + \tfrac{1}{3!}\mathbf{E}^a\mathbf{E}^b\mathbf{E}^c\mathbf{C}^{abc} + \cdots$$

$$\boldsymbol{\varepsilon} = \boldsymbol{\varepsilon}^0 + \mathbf{E}^a\boldsymbol{\varepsilon}^a + \tfrac{1}{2!}\mathbf{E}^a\mathbf{E}^b\boldsymbol{\varepsilon}^{ab} + \tfrac{1}{3!}\mathbf{E}^a\mathbf{E}^b\mathbf{E}^c\boldsymbol{\varepsilon}^{abc} + \cdots$$

$$\mathbf{D} = \mathbf{D}^0 + \mathbf{E}^a\mathbf{D}^a + \tfrac{1}{2!}\mathbf{E}^a\mathbf{E}^b\mathbf{D}^{ab} + \tfrac{1}{3!}\mathbf{E}^a\mathbf{E}^b\mathbf{E}^c\mathbf{D}^{abc} + \cdots$$

for the remaining time-dependent matrix definitions. Collecting terms of like order and rearranging gives expressions, through first order, of the form

$$\mathbf{F}^0\mathbf{C}^0 = \mathbf{S}^0\mathbf{C}^0\boldsymbol{\varepsilon}^0$$

$$\mathbf{F}^a(\pm\omega)\mathbf{C}^0 + \mathbf{F}^0\mathbf{C}^a(\pm\omega) \pm \omega\,\mathbf{S}^0\mathbf{C}^a(\pm\omega) = \mathbf{S}^0\mathbf{C}^a(\pm\omega)\boldsymbol{\varepsilon}^0 + \mathbf{S}^0\mathbf{C}^0\boldsymbol{\varepsilon}^a(\pm\omega)$$

where $\mathbf{F}^0$ represents the zeroth order solution (*i.e.* the Hartree-Fock case), and $\mathbf{F}^a$ is the first order solution. Imposing the condition $\dfrac{\partial}{\partial t}\mathbf{C}^{0+}\mathbf{S}^0\mathbf{C}^0 = 0$ and collecting like terms yields the zeroth and first order terms

$$\mathbf{C}^{0+}\mathbf{S}^0\mathbf{C}^0 = 1$$

and

$$\mathbf{C}^{0+}\mathbf{S}^0\mathbf{C}^a(\pm\omega) + \mathbf{C}^{a+}(\mp\omega)\mathbf{S}^0\mathbf{C}^0 = 0.$$

The procedure can be applied once more to the equations governing the density matrices to give the related expressions

$$\mathbf{D}^0 = \mathbf{C}^0\mathbf{n}\mathbf{C}^{0+}$$

$$\mathbf{D}^a(\pm\omega) = \mathbf{C}^a(\pm\omega)\mathbf{n}\mathbf{C}^{0+} + \mathbf{C}^0\mathbf{n}\mathbf{C}^{a+}(\mp\omega).$$

Now the quantities for the frequency dependent polarizability (α) may be defined in terms of the dipole moment matrix ($\mathbf{H}^a$) and the first order density matrix ($\mathbf{D}^a$);

$$\alpha_{ab} = -\text{Tr}\left\{\mathbf{H}^a\mathbf{D}^b\right\}$$

and the frequency-dependent expression

$$\alpha(\mp\omega;\pm\omega) = -\text{Tr}\left\{\mathbf{H}^a\mathbf{D}^a(\pm\omega)\right\}.$$

From these, a frequency dependent Fock operator may be written in the form

$$F^a(\pm\omega) = H^a + D^a(\pm\omega)\left[2J^0 - K^0\right].$$

At this point the formulation of the problem is in terms of molecular orbitals, however we prefer to treat the problem in terms of atomic orbitals since these are much more convenient to deal with at the implementation level. We know that a unitary transformation exists between atomic and molecular orbitals, and that it may be written

$$C^a(\pm\omega) = C^0 U^a(\pm\omega).$$

Taking advantage of this, define a transformation matrix, **G**, such that

$$G^a(\pm\omega) = C^{0^+} F^a(\pm\omega) C^0$$

in the MO basis. It is important to note that the **F**, **D**, ε, and **U** matrices are not symmetric for the frequency dependent case, but Karna and Dupuis give certain symmetry conditions which allow us to avoid the calculation all of the matrix elements in certain cases.

Applying the **G** matrix to the first order equation gives

$$\varepsilon^a(\pm\omega) = G^a(\pm\omega) + \varepsilon^0 U^a(\pm\omega) - U^a(\pm\omega)\varepsilon^0 \pm \omega\, U^a(\pm\omega).$$

A fortunate property of the ε matrix is that

$$\varepsilon_{ij}^a(\pm\omega) = 0 \quad \text{if} \quad \begin{cases} i \in \{occupied\} \wedge j \in \{virtual\} \\ i \in \{virtual\} \wedge j \in \{occupied\} \end{cases}.$$

Finally, we have a definition of our **U** matrix;

$$U^a(\pm\omega) = \frac{G_{ij}^a(\pm\omega)}{\varepsilon_j^0 - \varepsilon_i^0 \mp \omega}.$$

The procedure currently used for solving the TDHF problem is an iterative approach. The dipole moment of the molecule is used as an initial guess of the Fock matrix. This Fock matrix is then used to generate the **G** matrix, which in turn is used to create the **U** matrix. Finally, the **U** matrix is used to calculate the density matrix and a new Fock matrix is calculated from the dipole moment of the new density matrix. This procedure is continued until the largest element of the **U** matrix meets the convergence criterion.

Current Developments

The TDHF method described above accurately describes the nonresonant interactions present in NLO phenomena, *i.e.* where the input frequency is far from one of the absorptions of the material. In order to describe resonant processes this method must be extended.

In the description of the damped harmonic oscillator given above, it is important to note that the damping term, γ, is necessarily a complex-valued number. In order to extend the current TDHF method to calculate such resonant phenomena, it is necessary to extend the procedure from real-valued to complex-valued and to obtain a suitable value for the Γ term.

The initial portion of the calculation is carried out in the same manner as in the real-valued formulation. The matrices from the SCF calculation are read in as real-valued data and copied into complex-valued arrays. This is allowable,

since the SCF calculation need not be complex-valued in order to obtain a suitable reference state for the TDHF routine. The calculation of the NLO properties is done with fully complex data since for a complex-valued matrix $\mathbf{C}$, with real-valued matrices $\mathbf{A}$ and $\mathbf{B}$ such that $\mathbf{A} = \text{Re}\{\mathbf{C}\}$ and $\mathbf{B} = \text{Im}\{\mathbf{C}\}$, $\mathbf{C} = \mathbf{A} + i\mathbf{B}$ if and only if $\mathbf{A}$ and $\mathbf{B}$ commute. This property of complex-valued matrices is important since we have no guarantee that $\mathbf{A}$ and $\mathbf{B}$ will commute for any of the matrices involved in the TDHF procedure.

In order to describe the resonant interactions as with response theory, we define a new $\mathbf{U}$ matrix

$$U(\omega)_{ij} = \frac{G(\omega)_{ij}}{\varepsilon_j - \varepsilon_i - \hbar\omega + i\omega\Gamma}.$$

Once the reference state is transformed into complex-valued data, the complex-valued TDHF (CTDHF) calculation is carried out in the same manner as that for the TDHF case. The obvious difference being in the specifics of the mathematical treatment. In order to test the computational details, CTDHF calculations were performed forcing the $i\omega\Gamma$ term in the denominator to be zero. These exactly reproduce the results for the associated real-valued calculations.

Aside from the computational differences between the two methods, the other consideration in calculating resonant interactions is the definition of Γ. In general, we would like this to be the Einstein A coefficient

$$\Gamma_{ij} = \frac{4\omega_{ij}^3 |\boldsymbol{\mu}_{ij}|^2}{3\hbar c^3}.$$

Figure 5

Calculated components for polarizability 6-21G** Basis set
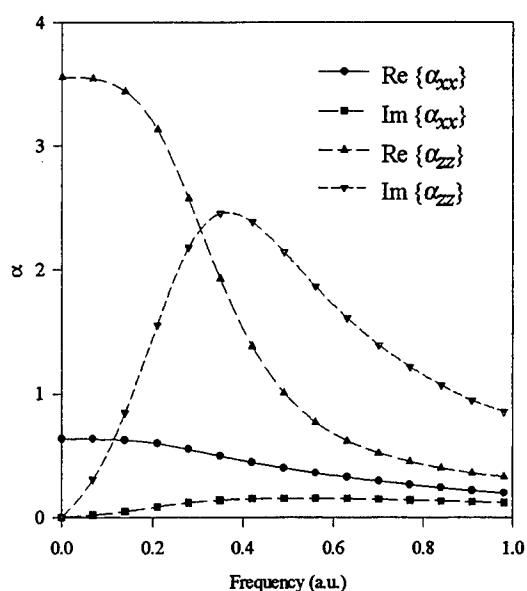
However, the Hartree-Fock method only provides a single state (the ground state) as a reference for the properties calculation. A reasonable calculation of the μ_{ij} term requires knowledge of more than one state of the molecule, as would be provided in a CI (configuration interaction) or MCSCF (multi-configuration self-consistent field) calculation.

A reasonable approximation for the Γ term is needed in order to calculate resonant interactions. We can make use of the fact that the A coefficient is directly related to the population lifetime of the excited state. The lifetime is also directly related to the energy difference between the two states. Therefore, we can approximate the A coefficient by utilizing knowledge of the energy difference between the ground state and the associated excited state.

Using this idea we approximate the energy difference between states by using $\Gamma = \varepsilon_j - \varepsilon_i$ as the definition of the term in our denominator. This is merely the energy difference between orbitals, though as a first approximation it has proven quite useful. For computational purposes there are currently two ways to define Γ in the calculations; 1) enter a constant value to be used or 2) the definition given above. (Note: if the constant is set to zero, we default to this definition.)

The graph below in Figure 5 shows the α_{xx} and α_{zz} components for HF obtained using a 6-21G** basis set with the current method. The Γ term is taken to be the energy difference as defined above. Calculations with larger basis sets were attempted, but convergence could not be achieved. It is obvious that some sort of convergence enhancement is necessary for these calculations. As with the TDHF method, convergence is established when the largest change in any element of the U matrix is below the convergence criterion. For the CTHDF calculation, this is taken to be the maximum of the difference in Real and Imaginary portions of the matrix.

Discussion

The method presented here has been extended to both second and third order properties for both the iterative approach described above (up to second order) and non-iterative based on the $2n+1$ rule. However, it is clear from Figure 5 that there is a problem with the current method.

It is reasonable to expect that the maximum contribution to from the imaginary portion of the polarizability should occur at the resonance of the material. In fact, this is the case experimentally. here we see a maximum in the imaginary part of the polarizability at around 0.4 a.u., which corresponds to the first resonance for hydrogen fluoride. However, the second resonance occurs near 0.8 a.u. Clearly, the current method helps to describe the effects near first resonance, but missed the second resonance of the material entirely.

We can say, however, that the magnitude of the polarizability response predicted by this method up to first resonance agrees with previously published results. In addition, this holds for the second and third order responses up to 1/2 and 1/3 of the first resonance respectively. The results to this point are encouraging for the development of a CTDHF method which will be capable of describing both nonresonant and resonant phenomena. Problems with the convergence and with the description of phenomena at frequencies beyond the first resonance of the material must be addressed before development of this method can be considered reasonably complete. Current research into this computational method is aimed at addressing these problems.

Future Work

Structure and Properties of Radiation Induced Defects

The work presented here represents a short study of the structure and properties of radiation induced defects in a-SiO_2 materials. Clearly, a greater understanding of microscopic properties of such defects is needed in order to further the understanding necessary for the fabrication of improved radiation hard devices for use in Air Force technology.

One such area is the mechanism for H migration in MOSFET devices. It has been shown experimentally[27] that there is a barrier to H motion within the SiO_2 network of approximately 0.8 eV with an associated kinetic isotope effect of $\frac{1}{\sqrt{2}}$ for deuterium. In addition, there is no associated EPR spectrum with systems which exhibit this phenomenon. As yet, no mechanism has been proposed which describes this motion and agrees with all available experimental data.

In light of this, a possible mechanism is proposed for the motion of hydrogen through the SiO_2 lattice based on the theoretical studies presented above. In this model, hydrogen gas (H_2) diffuses through the lattice until it encounters a bridging oxygen site. The lone pair on the oxygen then interacts with the H_2 causing heterolytic bond cleavage yielding a PCD (see above) and an H^- ion. This H^- then diffuses through the lattice and scavenges an H^+ from another PCD. This process can continue indefinitely.

This proposed mechanism, though perhaps too simplistic, may explain the migration of hydrogen under an applied field in SiO_2 layers. The nature of the mechanism provides for random motion of the H through the lattice. Since both the PCD and the H^- are closed-shell systems we would expect no EPR signal from the sample. Finally, this mechanism would exhibit the same kinetic isotope effect as that observed experimentally. In addition, the interaction of the H^- with the PCD may explain the lowering of the energy barrier for $O–H^+$ dissociation from the roughly 6 eV calculated previously. Considering all of the possible advantages of this mechanism, it is clear that a theoretical study into this possibility is warranted.

Theoretical and Computational Methods

In order to address the defects and properties discussed above, novel and improved computational methods need to be developed. Current *ab initio* methods provide a reasonable and accurate description of the defects under consideration for small systems under external fields far from the resonance (absorption) of the material. Future theoretical work aimed at describing these defects under resonant conditions and for larger model cluster sizes require theoretical improvements in the approach. Some important improvements include the effects of the surrounding bulk dielectric on structure and properties and improved methods with better convergence for the calculation of large systems.

The development and implementation of the Time-Dependent Multi-Configuration Self-Consistent Field (TD-MCSCF) theory deserves serious attention. As noted above, the CTDHF method has a drawback in that it provides only a single reference state of the system under consideration. A MCSCF calculation would provide as much or as little information about the various states of the system as we choose. By knowing information of this type, a wide range of phenomena could be easily studied by virtue of the single TD-MCSCF calculation. Specifically, the Einstein A coefficient could be calculated directly by *ab initio* methods eliminating the need for approximations of the type described above. The

ability to perform calculations of this type would have wide implications in the areas of photonics and laser physics, providing the first high-level *ab initio* information on such phenomena.

Acknowledgments

References

1. A. G. Revesz and H. L. Hughes, "The defect Structure of Buried Oxide Layers in SIMOX and BESOI Structures.", *Physical and Technical Problems of SOI Structures and Devices*, J. P. Colinge, *et al.*, Kluwer (Dordrecht), 133 (1995).
2. R. E. Stalbush, A. H. Edwards, D. L. Griscom, B. J. Mrstik, "Post-irradiation cracking of H_2 and formation of interface states in irradiated metal-oxide-semiconductor field-effect transistors", *J. Appl. Phys.* **73**, 658 (1993).
3. P. M. Lenahan, P. V. Dressendorfer, *J. Appl. Phys.* **55**, 10 (1984).
4. W. L. Warren, *et al.*, *Appl. Phys. Lett.* **21**, 689 (1996).
5. R. A. B. Devine, W. L. Warren, J. B. Xu, I. H Wilson, P. Paillet, and J-L. Leray, *J. Appl. Phys.*, **77**, 175 (1995).
6. M. Dupuis, *et al.*, *MOTECC-90: Modern Techniques in Computational Chemistry*, IBM Corporation, Kingston, NY, 1990.
7. T. H. Dunning, Jr. and P. J. Hay, *Methods of Electronic Structure Theory Vol. 2*, H. F. Schaefer III, Ed., Plenum Press (1977).
8. a) T. H. Dunning, Jr., *J. Chem. Phys.* **90**, 1007, 1989.
   b) D. E. Woon and T. H. Dunning, Jr., *J. Chem. Phys.* **98**, 1358, 1993.
9. Shashi P. Karna, John J. Kester, *Photosensitivity and Quadratic Nonlinearity in Glass Waveguides - Fundamentals and Applications*, OSA Tech. Digest Series **22**, 144, 1995.
10. Ian Carmichael, *Chem. Phys.* **116**, 351, 1987.
11. P. S. Winokur, H. E. Boesch, J. M. McGarity, and F. B. Mclean, IEEE Trans. *Nucl. Sci.* NS-24, 2113 (1977).
12. J. Robertson, *Phys. and Tech. of Amorphous SiO_2*, Ed. R. A. B. Devine; Plenum Press: New York, 1988, p. 113.
13. A. H. Edwards and G. Germann, *Nucl. Instr. and Meth. in Phys. Res.* **832**, 238-247 (1988).
14. U. Österberg and W. Margulis, *Opt. Lett.* **11**, 516 (1986).
15. P. M. Ranon, I. Dajani, J. J. Kester, and T. G. Alley, *J. Appl. Phys.* **67**, 3532 (1995).
16. A. M. Glass, in *Photosensitivity and Quadratic Nonlinearity in Glass Waveguides: Fundamentals and Applications*, Vol. 22, 1995 OSA Technical Digest Series (Optical Society of America, Washington DC, 1995), p. 2.
17. W. L. Warren, K. Vanheusden, J. R. Schwank, D. M. Fleetwood, P. S. Winokur, and R. A. B. Devine, *Appl. Phys. Lett.* **68**, 1 (1996).
18. D. A. Buchanan, J. H. Stathis, and P. R. Wagner, *Appl. Phys. Lett.* **56**, 1037 (1990).
19. N. Bloembergen, *Nonlinear Optics* (Benjamin, New York, 1965).
20. S. P. Karna and M. Dupuis, *J. Comp. Chem.* **12**, 487 (1990).
21. S. P. Karna, *Chem. Phys. Lett.* **214**, 186 (1993).
22. T. H. Dunning, Jr., *J. Chem. Phys.* **55**, 716 (1971).
23. T. H. Dunning, Jr. and P. J. Hay, in *Modern Theoretical Chemistry, Vol. 3: Methods of Electronic Structure Theory*, Ed. H. F. Schaefer III (Plenum Press, New York, 1976),p. 1.
24. Boyd,R. *Nonlinear Optics*; Academic Press, San Diego, 1992, Sec. 3.5.
25. Karna, S. P. and Dupuis, M. *J. Comput. Chem.* **12**, 487-504 (1991).
26. Frenkel, J. *Wave Mechanics: Advanced General Theory*; Oxford University Press, Oxford, 1934.
27. Karl Vanheusden, Personal Communication.

A STUDY OF THE GRAIN BOUNDARY
BEHAVIOR OF NANOCRYSTALLINE CERAMICS

Todd C. Hathaway
Graduate Student
Department of Mechanical Engineering

Texas A & M University
College Station, TX   77843-3123

Final Report for:

Summer Faculty Research Program

Phillips Laboratory

Sponsored by:

Air Force Office of Scientific Research

Bolling Air Force Base, DC

and

Phillips Laboratory

August 1996

A STUDY OF THE GRAIN BOUNDARY
BEHAVIOR OF NANOCRYSTALLINE CERAMICS

Todd C. Hathaway
Graduate Student
Department of Mechanical Engineering
Texas A & M University

Abstract

The grain boundary behavior of nanocrystalline ceramics was investigated. To reduce ceramic powder to nanosize, a Union Process HD-01 attritor was used. Research indicates that several controllable factors affect grain growth: initial particle size, sintering temperature and pressure, method of compaction, additives, and degree of contamination/homogeneity. By controlling these factors one can produce materials with superior physical and mechanical properties to those of conventional powders/powder processing techniques.

A STUDY OF THE GRAIN BOUNDARY
BEHAVIOR OF NANOCRYSTALLINE CERAMICS

Todd C. Hathaway
Graduate Student
Department of Mechanical Engineering
Texas A & M University

Introduction

In materials science and solid state physics progress has been made in may cases by one of the following two approaches. Either by developing and applying new methods of investigation or by preparing materials with novel structural features and/or properties(1). Effective production of nanocrystalline ceramics involves three major stages: synthesizing, compacting, and sintering nanosized powders. Silicon carbide was the main material of this investigation. Silicon carbide, a non-oxide ceramic, has excellent mechanical properties at elevated temperatures, but it is very difficult to sinter. It is customary to use sintering aids in the sintering process of silicon carbide(2). However, sintering aids enhance grain growth, especially at the nanoscale level, so other factors must be controlled to retain nanometer size in silicon carbide, as well as other nanocrystalline ceramics.

A STUDY OF THE GRAIN BOUNDARY
BEHAVIOR OF NANOCRYSTALLINE CERAMICS

Todd C. Hathaway

Results/Discussion

Mechanical attrition by high energy ball milling has been developed as a versatile alternative to other processing routes including vapor evaporation, liquid quenching, and chemical synthesis methods. In this process, lattice defects are produced by "pumping" energy into initially single-crystalline powder particles of typically micrometer-size diameter. The internal refining process with a reduction of the average grain size by a factor of 10(3)-10(4) results from the creation and self-organization of dislocation cell networks, small-angle grain boundaries and finally high-angle grain boundaries within the powder particles during the milling process. As a result, increases in atomic level internal strains, excess enthalpy, excess specific heat and Vickers hardness are observed far beyond the levels obtained during conventional deformation processes(3).

75 g of 2-3 micron SiC powder was mixed with 200 mL isopropanol, 95 g SiC media, and 50 g small silicon nitride media. The slurry was placed into a Union Process HD-01 attritor and milled for approximately 80 hours at speeds ranging from 200 rpm to 600 rpm. The tank wall was cooled to 0 degrees centigrade. SEM results taken throughout the milling process show a gradual decrease in particle size, with a final particle size ranging from 0.2-0.3

A STUDY OF THE GRAIN BOUNDARY
BEHAVIOR OF NANOCRYSTALLINE CERAMICS

Todd C. Hathaway

microns. Visual examination of the slurry revealed significant wear on the larger SiC media, while the smaller silicon nitride media was relatively unaffected. The polymer-lined tank showed some wear in the lower portion of the tank, where the attritor arms are closest to the tank wall. The process was attempted with Al powder at the same temperature; however, agglomeration of the Al particles prevented a reduction in particle size from taking place.

Non-oxide ceramics such as silicon carbide and silicon nitride are expected to be useful as structural materials at high temperature because of the high thermal resistance, high chemical stability, and excellent high temperature strength. It is well known that mechanical properties are markedly affected by the presence of grain boundaries; e.g., grain boundary sliding at high temperature should induce stress concentration at triple points and ledges of grain boundaries, resulting in a strength decrease. Such behavior depends strongly on the grain boundary character and extrinsic factors such as additives, impurities, sintering procedure, etc(4). The most common additives in silicon carbide are carbon, boron, aluminum, and their compounds.

A STUDY OF THE GRAIN BOUNDARY
BEHAVIOR OF NANOCRYSTALLINE CERAMICS

Todd C. Hathaway

An amorphous-like layer of 0.5 nm in thickness exists along the grain boundaries in SiC with B+C, and SiC without any sintering aids. Since these materials do not show a remarkable stress decrease at high temperatures, Ikuhara(5) presumed that the amorphous-like layer is not a second phase of sintering aids or impurities, but a relaxed structure formed to reduce its high energy, which is known as an extended boundary. Results of electron energy loss spectrum (EELS) and the energy dispersive X-ray spectroscopy (EDS) verify that the grain boundary layer observed in SiC sintered materials with and without B+C additions is not a second phase mainly composed of sintering aids or impurities, but is of a relaxed structure to decrease the high energy(6).

Additives accelerate the sintering process. Al, AlN, and Alumina were more effective additives than B or C in retaining a small grain size in silicon carbide. The average growth rate of grains during sintering increases in the order Al < B < Be(7). Microstructural observations clearly show that a liquid phase is responsible for the densification of SiC powder when these additives are used as a hot pressing aid(8).

A STUDY OF THE GRAIN BOUNDARY
BEHAVIOR OF NANOCRYSTALLINE CERAMICS

Todd C. Hathaway

Research has also found that strong ceramics in small quantities can strengthen other ceramics. The weak grain boundary phase in silicon nitride has been toughened by forming a nanocomposite grain boundary phase of SiC nanosize particles. The SiC nanosize particles are formed by a reaction between coated carbon and an oxide phase on the surface of silicon nitride powder. The carbon is coated by thermal decomposition of methane gas. By controlling the carbon content, fracture toughness and bending strength are maximized(9).

The addition of nanosized particles into coarser powder of the same composition can improve mechanical properties in some instances. The addition of nanosize SiC powder into conventional SiC powder showed an increased fracture toughness value of 6MPa m(1/2) and compared to 5 MPa m(1/2). Also, the addition of 5 vol% ultrafine SiC to alumina by a ball milling/hot pressing route has resulted in a strength of 1 GPa retained to high temperatures, compared to 600 MPa for pure alumina(10). Similar results may be possible with the addition of ultrafine HfC or TaC into SiC powder.

Hot isostatic pressing (HIP) is a very effective means of sintering ceramics. SiC has been HIPed to near theoretical

A STUDY OF THE GRAIN BOUNDARY
BEHAVIOR OF NANOCRYSTALLINE CERAMICS

Todd C. Hathaway

density without sintering aids. Improved microstructure and minimization of processing flaws are two advantages to HIPing ceramics. Other approaches such as compositing are needed to advance significantly beyond the current state of the art(11). Compositing also assists in retarding grain growth. Smaller particle sizes have a greater tendency for grain growth, especially at the nanoscale level.

Faster consolidation of powders is necessary to retain nanosize particles. Shock consolidation is a method that presents a bright potential but has been limited by inevitable cracking of compacts, especially for ceramics. One objective of dynamic consolidation is to develop a procedure to produce ceramics, such as monolithic SiC, with superior mechanical properties at elevated temperatures. Dynamic densification can be used either alone or in combination with post-shock sintering or hot isostatic pressing (HIPing) in an attempt to produce bulk SiC from powder(12).

Very fast densification of ceramic powders using prior electric discharge before resistance sintering leads to microstructures that retain the particle size of the starting powders. The time taken to achieve near-theoretical density using this method ranges from 5-15 min. The short time is the principal reason for

A STUDY OF THE GRAIN BOUNDARY
BEHAVIOR OF NANOCRYSTALLINE CERAMICS

Todd C. Hathaway

arresting possible grain growth and the electric discharge step may perhaps be responsible for sweeping off impurities from powder surfaces, thus giving clean grain boundaries in the sintered materials(13).

For the compaction of nanocrystalline ceramics, the magnetic pulsed method has also been developed, which is based on converting pulsed electric powder to a mechanical pulse and concentrating that pulse in the compaction zone. By using this technique the major challenges can be met which are encountered in the compaction of nanopowders of hard materials, which difficulties arise from the low bulk density and large specific surfaces of these powders. For the compaction of nanosize alumina powder pressure, pulses in the range from 1 GPa to 5 GPa, lasting 3-300 microseconds, have been applied. Simple-shaped bulk samples maintained a nano-crystalline structure and reached 62 to 83% of the theoretical density(14).

A STUDY OF THE GRAIN BOUNDARY
BEHAVIOR OF NANOCRYSTALLINE CERAMICS

Todd C. Hathaway

Conclusion

The major concern in utilizing ceramics such as silicon carbide in structural materials is improving toughness. The important role of grain boundaries have been widely recognized in designing and processing advances materials with high performance(15). The properties of nanocrystalline ceramics are to a large extent controlled by interfaces, such as external surfaces and grain boundaries. Awareness is growing that the preparation of ceramics with enhanced properties is dependent on better understanding the effect of interfaces on materials properties(16).

Properties of the bulk and grain boundaries of solids are entirely different with respect to chemical composition, structural ordering and resulting electrical properties. Unfortunately, in contrast to much information which has been accumulated on bulk properties of the materials, little is known about interfaces and their impact on processing and properties of nanocrystalline ceramics(17).

A STUDY OF THE GRAIN BOUNDARY
BEHAVIOR OF NANOCRYSTALLINE CERAMICS

Todd C. Hathaway

References

1. H. GLEITER, Progress in Materials Science, Vol. 33, pp. 223-315, 1989.

2. S.-S. SHANG, M. M. MEYERS, Journal of Materials Science, Vol. 31, 1996, pp. 252-261.

3. H.-J. FECHT, Nanostructured Materials, Vol. 6, pp. 33-42, 1995.

4. K. Morita, S. Tsurekawa, H. Nakashima and H. Yoshinaga. Materials Processing and Design: Grain-Boundary-Controlled Properties of Fine Ceramics II, Ceramic Trnasactions, Vol. 44, 1994.

5. Y. Ikuhara, H. Kurishita, and H. Yoshinaga. Grain Boundary and High Temperature Strength of Sintered SiC, Yogya-Kyokai-Shi, Vol. 95, pp. 638-645, 1987.

6. K. Morita, S. Tsurekawa, H. Nakashima, and H. Yoshinaga. Materials Processing and Design: Grain-Boundary-Controlled Properties of Fine Ceramics II, Ceramic Transactions, Vol. 44, 1994.

7. Silicon Carbide Ceramics, Vol. 2, pp. 143-146, 1991.

8. F. F. Lange, Journal of Materials Science, Vol. 10, pp 314-320, 1975.

9.   Tomohiro Yanai and Kozo Ishizaki, Materials Processing and Design: Grain-Boundary-Controlled Properties of Fine Ceramics II, Ceramic Transactions, Vol. 44, 1994.

10.   HIP Densification of Nanophase SiC, Nanoceramics, British Ceramic Proceedings, No. 51, pp 99-105, 1993.

11. Sunil Dutta, High-Strength Silicon Carbides by Hot Isostatic Pressing in Ceramic Materials & Components for Engines, pp. 683-689, 1989(?).

12.   S.-S. SHANG, M. M. MEYERS, Journal of Materials Science, Vol. 31, 1996, pp. 252-261.

13.   Subhash H. Risbud, Chien-Hua Shan.   Materials Science and Engineering A204, pp 146-151, 1995.

14.   V. Ivanov, Y. A. Kotov, O. H. Samatov, R. Bohme, H. U. Karow, G. Schumacher. NanoSturctured Materials, Vol. 6, pp. 287-290, 1995.

15.   Tadao Watanabe, Materials Processing and Design: Grain-Boundary-Controlled Properties of Fine Ceramics II, Ceramic Transactions, Vol. 44, 1994.

16.   J. Nowotny, Materials Processing and Design: Grain-Boundary-Controlled Properties of Fine Ceramics II, Ceramic Transactions, Vol. 44, 1994.

17. J. Nowotny, Ibid.

RAMAN IMAGING AS A TRANSCRITICAL
COMBUSTION DIAGNOSTIC

J. D. Holtzclaw
Research Associate
Department of Aerospace Engineering and Engineering Mechanics

University of Cincinnati
ML # 70
Cincinnati, OH 45221-0070

RAMAN IMAGING AS A TRANSCRITICAL
COMBUSTION DIAGNOSTIC

J. D. Holtzclaw
Graduate Student
Department of Aerospace Engineering and Engineering Mechanics
University of Cincinnati

Abstract

Transcritical liquid injection plays a fundamental role in rocket combustion for the majority of our current (SSME) and future high pressure rocket engines. However, the fundamental physics behind supercritical combustion are barely understood.[1] One reason for this is the difficulty in making quantitative or even qualitative measurements under these conditions. The objective of this research was to develop experimental techniques to provide crucial data for better understanding transcritical phenomena and semi-empirical correlations for use in predictive computational codes. For this experiment, Raman scattering was used to provide a signal based on species concentration in a transcritical environment. Calibration was performed for both the transcritical pressure vessel instrumentation and of the Raman scatter imaging instrumentation. Unfortunately, due to technical difficulties, no actual two phase flow data was taken.

RAMAN IMAGING AS A TRANSCRITICAL COMBUSTION DIAGNOSTIC

J. D. Holtzclaw

Introduction

High pressure liquid injection plays a fundamental role in rocket combustion for current (SSME) and future high-pressure rocket engines. Transcritical injection refers to the case where propellant(s) are introduced into the combustion chamber at supercritical pressures but initially at subcritical temperatures[1]. Once in the hot combustion chamber environment, the injected propellant quickly reaches the supercritical state (supercritical temperature and pressure), but it is uncertain how this transition occurs with respect to propellant atomization and vaporization. Supercritical fluids occur at high pressures and temperatures where distinctions between gas and liquid phases no longer exist. For example, supercritical fluids often posses liquid like densities, but gas like diffusivities. They also posses very complex physical characteristics such as strongly enhanced specific heat and compressibility near the critical point, zero surface tension, and zero enthalpy of vaporization which makes many engineering and scientific calculations difficult. The fundamental physics behind this transcritical process is barely understood especially on the molecular level. One reason for this lack of transcritical knowledge is the difficulty in making quantitative or even qualitative measurements under these conditions. Laser-based diagnostics have yet to be proven under these high-pressure conditions, especially for multi-phase flows. Nonetheless, a few experimental methods seem promising. One such method is the Raman scattering diagnostics.

Methodology

Raman Scattering

"Raman scattering arises from the oscillating dipole moment induced in the medium through the molecular polarizability by the electric field of the incident light wave[2]". It is the inelastic scattering of photons of light from molecules and is termed rotational,

vibrational, or electronic depending on the nature of the energy exchange between the incident light and the molecules[2]. If the molecule gains energy from the radiative field, the resulting lower frequency scattered radiation is called the Stokes component.

Likewise, if the molecule loses energy, the scattered radiation is referred to as the anti-Stokes component. Due to the limited number of molecular energy states for each species molecule, the Raman spectrum resides at fixed frequency separations from the laser and is a characteristic of the molecule from which the scattering emanates[3]. Thus, the Raman scattered signal is species specific and linearly proportional to species number density. Therefore, if a particular species concentration increases, so will its Raman scatter signal intensity. Furthermore, temperature measurements can easily be made from the distribution of the scattering. Unfortunately, Raman scattering produces a very, very weak signal plaguing Raman scattering diagnostics with low signal to noise (S/N) ratios.

Experimental Set-up

All experiments were performed with the Transcritical Droplet Pressure Vessel located at Phillips Laboratory, Edwards Air Force Base. This custom pressure vessel was designed for transcritical cryogenic droplet generation, break-up, and vaporization at high pressures with optical access for laser diagnostics and conventional imaging (see Figure 1).

Since the typically weak Raman signal is proportional to excitation intensity, a high power, pulsed (6 ns, 10Hz) Nd:YAG laser with maximum pulse energy up to 1.65 J at the fundamental wavelength was used to created the Raman scatter. A second harmonic crystal was installed into the Nd: YAG laser to create a 532 nm (max. 800 mJ/pulse) excitation pulse. Due to safety concerns, the laser source was located in a separate room from the pressure vessel which was located in an adjoining test cell as seen in Figure 2. Therefore, the laser beam had to be "steered" by several mirrors into the pressure chamber from another room approximately 40 ft. away from the test chamber. Due to efficiency loses from several beam steering mirrors and flashlamps near the end of their life cycle, average pulse energy delivered to the laser sheet was only 230 mJ.

The circular laser beam was focused through two pairs of cylindrical lenses (200 mm focal length/ 25.4 mm focal length, and 50.2 mm focal length/150 mm focal length) to create a thin laser sheet approximately 25 mm in height and 1 mm in thickness. The laser sheet was

oriented vertically into the test chamber, perpendicular to the droplet orifice, and perpendicular to viewing ports (Sapphire windows, see Figure 1).

Figure 2 shows the instrumentation set-up for the transcritical pressure vessel and imaging systems. Raman signals were collected via an image intensified CCD detector (ICCD) "utilizing a proximity-focused micro channel plate (MCP) image intensifiers fiber-optically coupled to the CCD arrays[4] ". The Raman scatter was filtered through 6 mm thickness of OG570 glass filter placed on the ICCD camera lens (nitrogen Stokes Raman scatter occurs at 607 nm for 532 nm excitation). The ICCD operations was controlled by the "controller" (Princeton Instruments ST-138, see Figure 2) which the user commanded through the imaging system software (IPLab Spectrum by Signal Analytics Corp.) run on a Power Macintosh™. In addition, the detector gate timing was controlled by the PG-200 Pulse Generator which was in sync with the laser pulse. As previously mentioned, the laser pulsed at 10 Hz (6 ns pulse width) while the ICCD was electronically enabled for 5 ms (in which one 200 ns gate pulse containing one laser shot occurred), 500 ms (5 gate pulses and 5 laser shots) and 1 second (10 gate pulses and 10 shots). The oscilloscope was used to check the system signals and timing.

Figure 3 shows the mechanical flow schematic of the test facility. Six flow meters control and measure the flow rates of helium (warm and cool) and nitrogen both into and out of the test chamber. Likewise, eight thermocouples (2 type K, 6 type E) were used to measure propellant temperatures and six type E thermocouples were used to measure temperatures inside the chamber. Finally, two pressure transducers, 0-3000 psig were used to measure the chamber pressure and droplet generator pressure.

Before data could be collected, the Raman imaging system had first to be proven and calibrated. The pressure vessel was filled with ambient nitrogen with pressure ranging from 500 psig to 1500 psig. At each pressure, 15 images were recorded, 5 with a 5 ms exposure and one detector gate (1 laser pulse), 5 at 500 ms exposure and one detector gate (5 laser pulses), and 5 at 1 second exposure (10 laser pulses). Multiply laser pulses were recorded in order to improve S/N ratios and to check credibility of single shot data. For each image, the mean intensity, maximum intensity, minimum intensity, standard deviation, and image area (pixels) were recorded. Then, the average mean intensity and standard deviation were calculated for each gate setting (i.e. 1, 5, or 10 shots) at each pressure setting (i.e. 500, 600, psig, etc). The following equations were used to calculate the average mean intensity (I_{avg}) and standard deviation (sd):

$$I_{avg} = \frac{\sum\limits_{j=1}^{n} I_{mean}}{n} \qquad\qquad\qquad eq.\,1$$

$$sd = \sqrt{\frac{\sum\limits_{j=1}^{n} (I_{mean_j} - I_{avg})^2}{n-1}} \qquad\qquad\qquad eq.\,2$$

where n is the number of images, j is a particular image, and I_{mean} is the mean intensity of image j.

This was done for both a small region of interest (ROI) located in the center of the laser sheet and a large ROI incorporating most of the laser sheet. This was done in order to test the effect on the data of non-uniform intensity in the laser sheet itself. Figures 4 & 5 contain the result of this calibration. Species density increases linearly with pressure. As species density increases, so does the Raman scatter intensity. Therefore, Figures 5 and 6 show excellent correlation between theoretical expectations and experimental results. Furthermore, by comparison, Figures 4 & 5 imply that spatial non-uniformity in the laser sheet did not appreciably effect the calibration results since the spatial distribution was consist in time.

An additional image analysis method was used to check for spatial non-uniformity in the laser sheet. Each image (1, 5, & 10 shot(s)) taken at each concentration (pressure, i.e. 600 psig, 700 psig, etc)) was normalized by the same image (1, 5, & 10 shot(s)) taken at a known concentration (500 psig). Again, this was done using the same ROI. This analysis produced similar results as the above ROI average intensity method. Since normalization method was considerable more time consuming while producing the same results, the ROI average intensity method was preferred.

Next we filled the pressure vessel with helium to 1000 psig, Again, we took several shots at the three different timing schemes (1 shot, 5 shots, 10 shots) and calculated the average mean intensities and stand deviations following the procedure outlined above. Since atomic helium has no rotational or vibrational modes, it exhibits no Raman scattering signal. Therefore, these images will be used as background or noise images and will be subtracted from future images as part of the quantitative analysis of Raman imaging.

Once the background imaging was complete, the transcritical pressure vessel was filled with both GN2 and helium at controlled flow rates to approximately 1000 psig. This produced

a known concentration of GN2 in the pressure vessel. After waiting a few minutes for equilibrium to be established, Raman scatter images were recorded. Again, 5 msec, 500 msec, and 1 sec. exposure times were selected. This process was repeated for different GN2 concentrations. Raman scatter Intensity was plotted versus GN2 molar concentration and the results are shown in Figures 6-8. At concentrations below 25% GN2, the Raman signal intensity varies little. This appears to be the lower Raman scatter signal limit due to the low S/N ratio. However, as later discovered, during testing, the ICCD was receiving spurious light reflected off of the back Lexan™ shield and through the back window of the chamber to the camera. Since some of the light passed through the filters in front of the camera, we realized it had a component that was at a longer wavelength than the laser light. We discovered that the wavelength-shifted light originated from the beam stop at the aft end of the chamber. We reasoned that this spurious signal-generating light was either forward scattered Raman light reflected from the beam stop, or fluorescence or incandescence from the paint on the beam stop due to the intense laser light. Therefore, regardless of GN2 concentration, the ICCD was always receiving some small signal that interfered with our lower Raman signal data points (low GN2 concentration). Hence, we removed the Lexam™ shield and repeated the testing done at GN2 concentrations below 25%. The results which can be see in Figures 9-11. This decrease the lower GN2 molar concentration detection limited to approximately 5%.

Finally, the helium background was subtracted from the images and the results are shown in Figures 12-14. Note that Figures 12-14 do not correlate as well as previous results. Two different helium background were used to calibrate the data, one at high GN2 concentrations that includes spurious background light off the Lexan™ shield, and one at low GN2 concentrations without the shield in place and thus without this spurious background component. This partially explains the poor consistency of the results with background subtraction. Additionally, the data was taken over several days with varying laser output energy (220 mJ to 250 mJ) and with small changes in laser sheet position. (The optics had to be adjusted to correct the laser sheet and camera relative position before helium background experiments were complete. Therefore, the subtracted background will not correspond the same to each image. Image subtraction will void data if pixel-to-pixel correspondence between background and data is lost. Obviously, the background subtraction needs to be consistent for all images in order to expect good results. Data with helium background subtracted should exhibit linear behavior as seen in Figures 9-11. This set of experiments would need to be re-done with helium background images being taken during the same test time as nitrogen Raman data.

Unfortunately, time did not permit this to be done for this report.

Conclusion

Raman scattered signal is species specific and linearly proportional to the nitrogen species number density. Therefore, if nitrogen concentration increases (i.e. pressure), so will its Raman scatter signal intensity. The sensitivity of Raman scatter is approximately 5% nitrogen concentration. Furthermore, from these results, it appears that the nitrogen concentration lower limit for Raman scatter signal is approximately 5% by volume.

Due to technical difficulties (malfunctioning droplet generator tube and broken connector to laser water filter), no actual two phase flow data was taken. However, the pressure vessel, imaging system, and data acquisition are completely calibrated and functional. Testing should began immediately as soon as the current delays are remedy. One should anticipate excellent data results.

ACKNOWLEDGMENTS

REFERENCES

[1] Woodward, R.D & Talley, D.G., "Raman Imaging of Transcritical Cryogenic Propellants", 34th Aerospace Sciences Meeting & Exhibit (AIAA 96-0468), Reno. NV Jan. 1996.

[2] Eckbreth, Alan C., *Laser Diagnostics for Combustion Temperature and Species* Abacus Press, Cambridge, Mass., 1988. pp.12-13.

[3] Chigier, Norman, (Ed). *Combustion Measurements*. Hemisphere Publishing Corporation, 1991, pp.96-102.

[4] Princeton Instruments, Inc. "ICCD Detector: Operation Manual", Feb. 1993, pp 1.
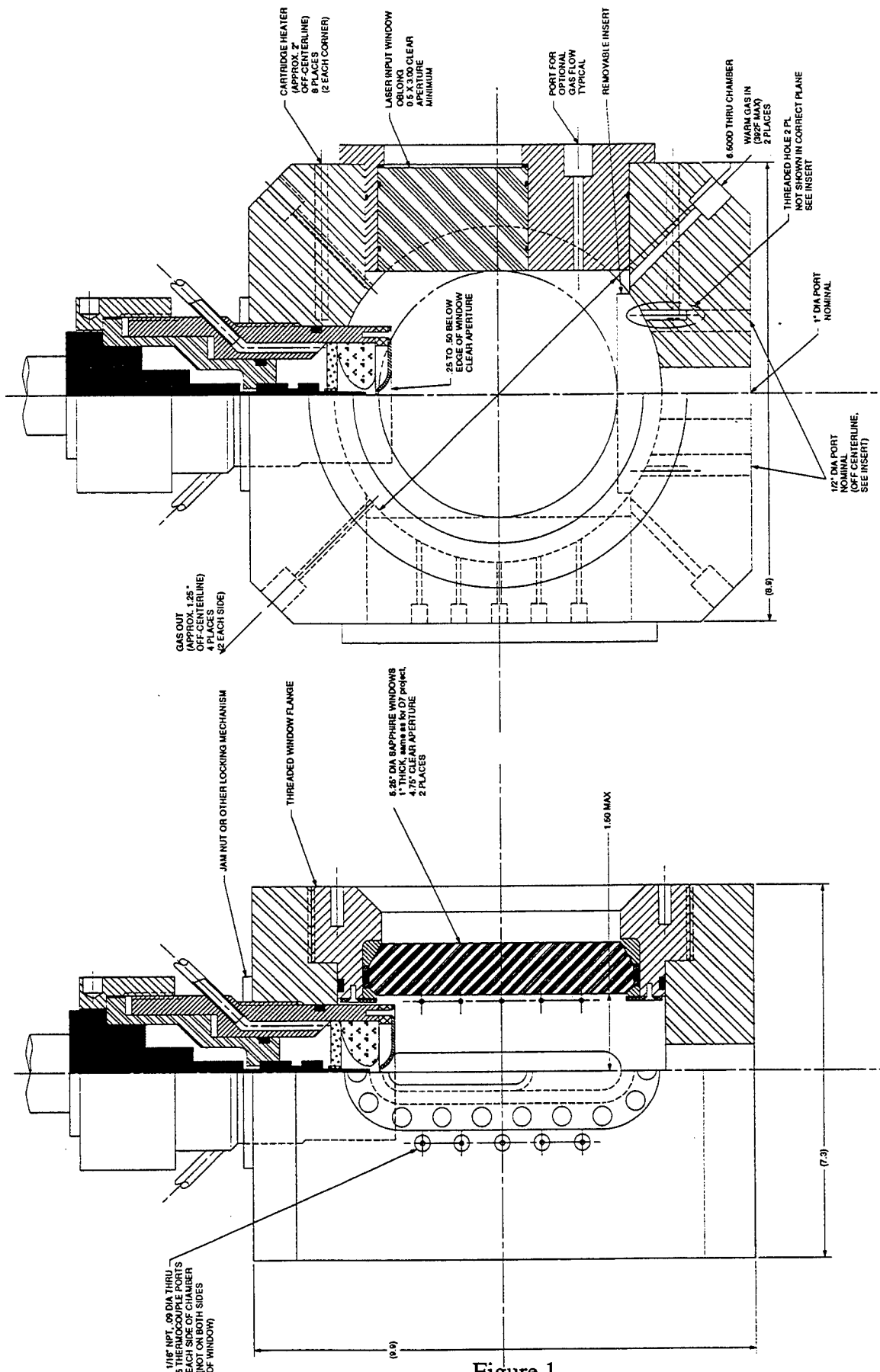
Figure 1
Transcritical Pressure Vessel

CARTRIDGE HEATER
(APPROX. 2"
OFF-CENTERLINE)
8 PLACES
(2 EACH CORNER)

LASER INPUT WINDOW
OBLONG
0.5 X 3.00 CLEAR
APERTURE
MINIMUM

PORT FOR
OPTIONAL
GAS FLOW
TYPICAL

REMOVABLE INSERT

6.500D THRU CHAMBER

WARM GAS IN
(392F MAX)
2 PLACES

THREADED HOLE 2 PL
NOT SHOWN IN CORRECT PLANE
SEE INSERT

25 TO .50 BELOW
EDGE OF WINDOW
CLEAR APERTURE

1" DIA PORT
NOMINAL

1/2" DIA PORT
NOMINAL
(OFF CENTERLINE,
SEE INSERT)

FIGURE 3. FRONT VIEW

GAS OUT
(APPROX. 1.25"
OFF-CENTERLINE)
4 PLACES
(2 EACH SIDE)

(8.9)

JAM NUT OR OTHER LOCKING MECHANISM

THREADED WINDOW FLANGE

5.25" DIA SAPPHIRE WINDOWS
1" THICK, same as kr/ D7 project,
4.75" CLEAR APERTURE
2 PLACES

1.50 MAX

FIGURE 2. SIDE VIEW

1/16" NPT, .09 DIA THRU
5 THERMOCOUPLE PORTS
EACH SIDE OF CHAMBER
(NOT ON BOTH SIDES
OF WINDOW)

(7.3)

(9.6)

9-9

FIGURE 2 INSTRUMENTATION SCHEMATIC
FOR SUPERCRITICAL DROPLET EXPERIMENT

FIGURE 3: MECHANICAL SCHEMATIC
FOR TRANSCRITICAL DROPLET EXPERIMENT
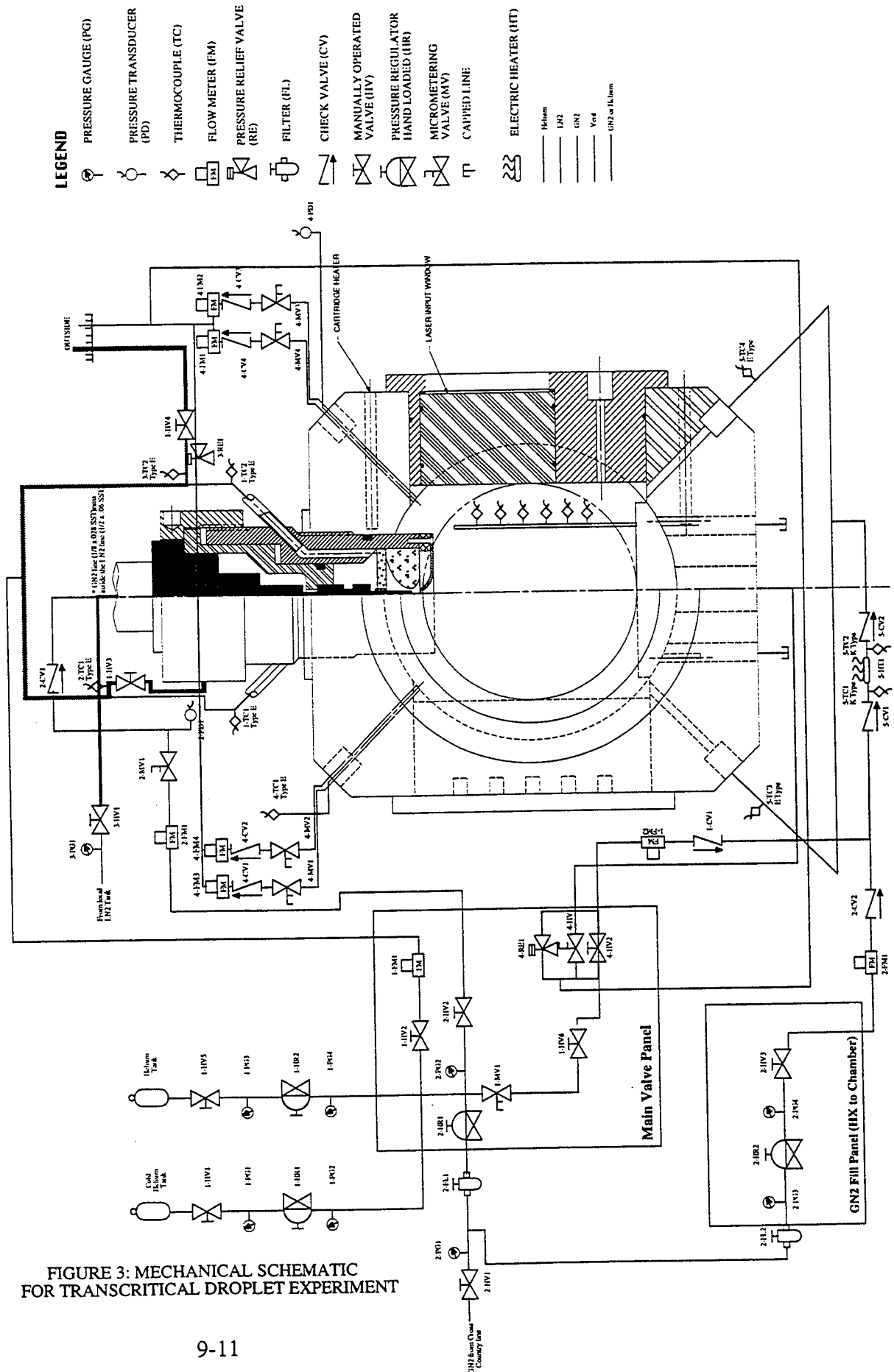
Figure 4: Average mean intensity with standard deviation versus pressure for small ROI
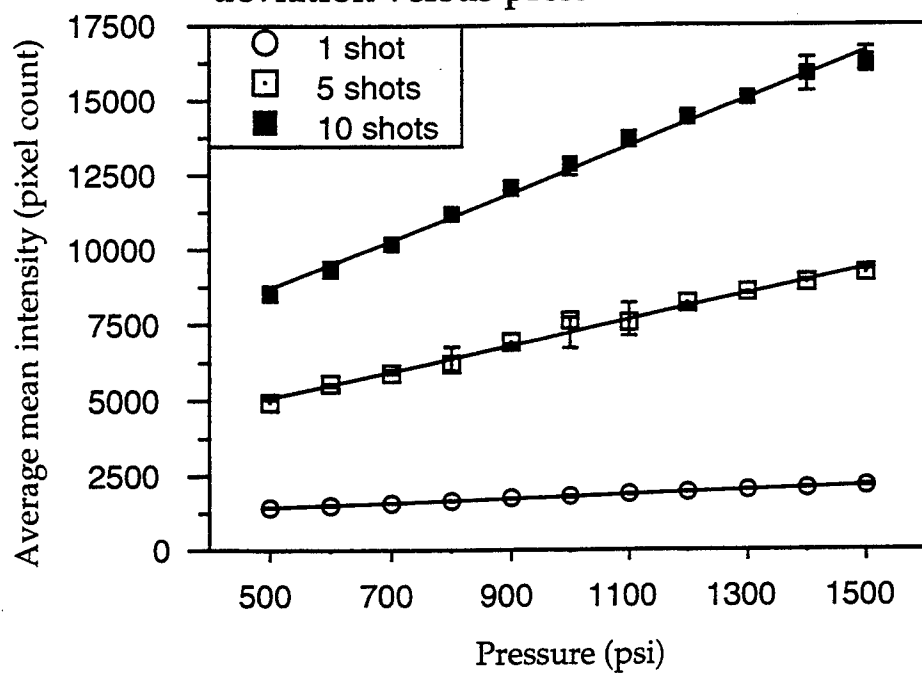
Figure 5: Average mean intensity with standard deviation versus pressure for large ROI
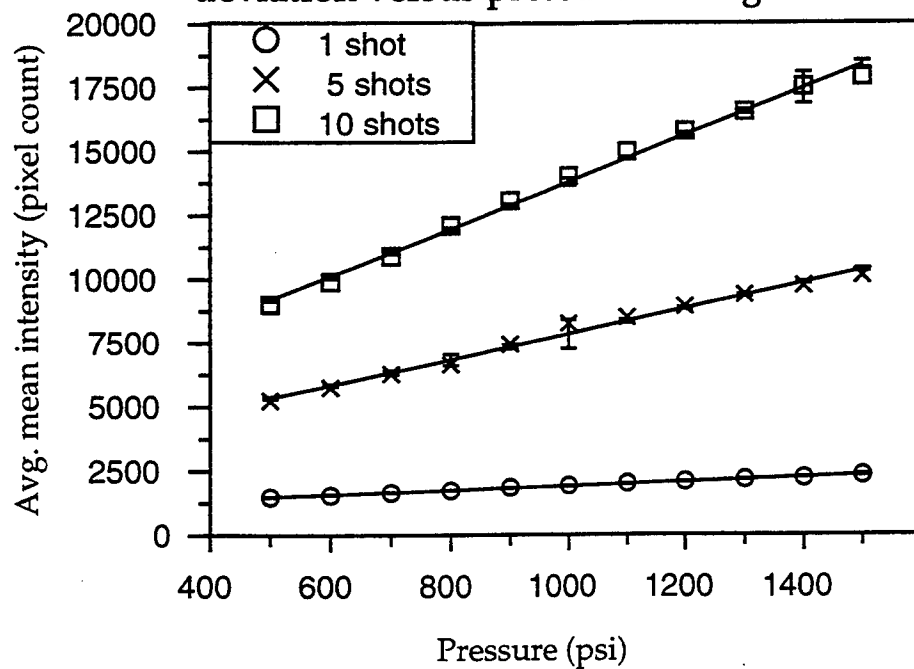
Figure 6: Mean Intensity with standard deviation versus N2 Molar Concentration for small ROI & 1 sho

Mean Intensity (pixel count) vs. N2 Molar Concentration (lb/ft^3)
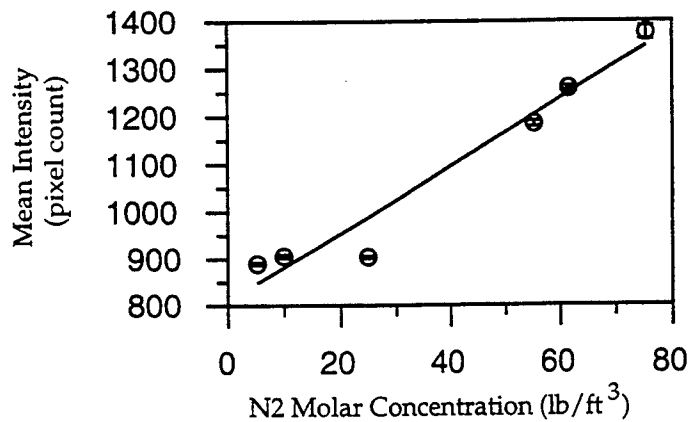
Figure 7: Mean Intensity with standard deviation versus N2 Molar Concentration for small ROI & 5 shots

Mean Intensity (pixel count) vs. N2 Molar Concentration (lb/ft^3)
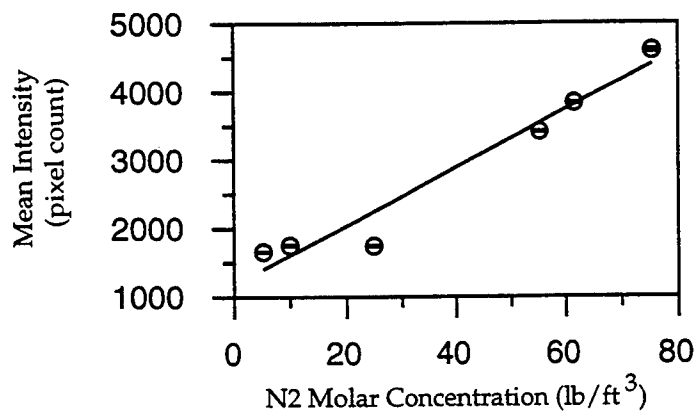
Figure 8: Mean Intensity with standard deviation versus N2 Molar Concentration with small ROI & 10 shots

Mean Intensity (pixel counts) vs. N2 Molar Concentration (lb/ft^3)
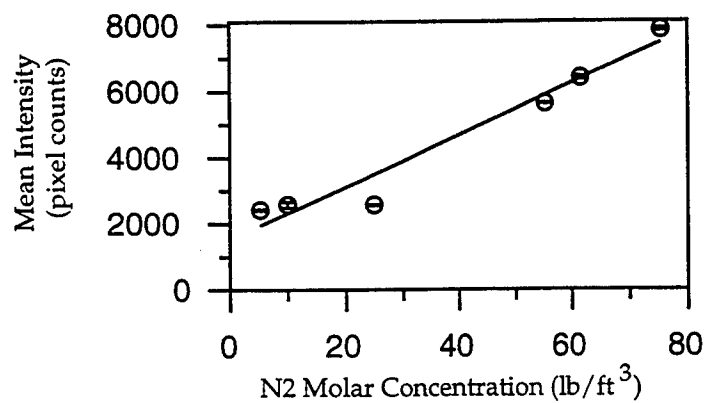
Figure 9: Mean Intensity with standard deviation versus N2 Molar Concentration for small ROI, no reflection & 1 shot
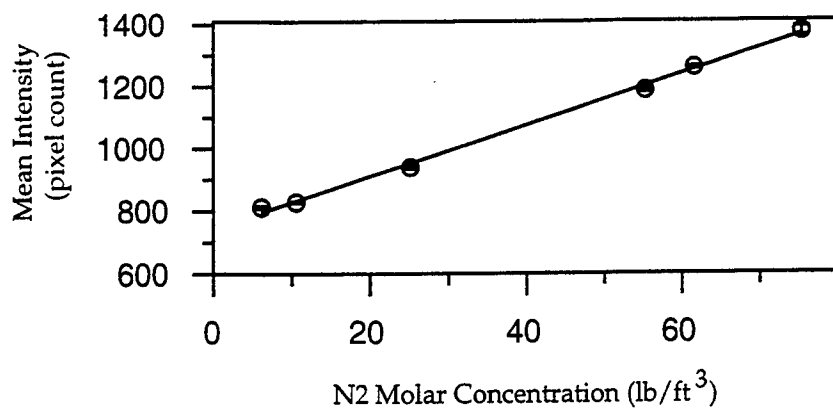
Figure 10: Mean Intensity with standard deviation versus N2 Molar Concentration for small ROI, no reflection, & 5 shots
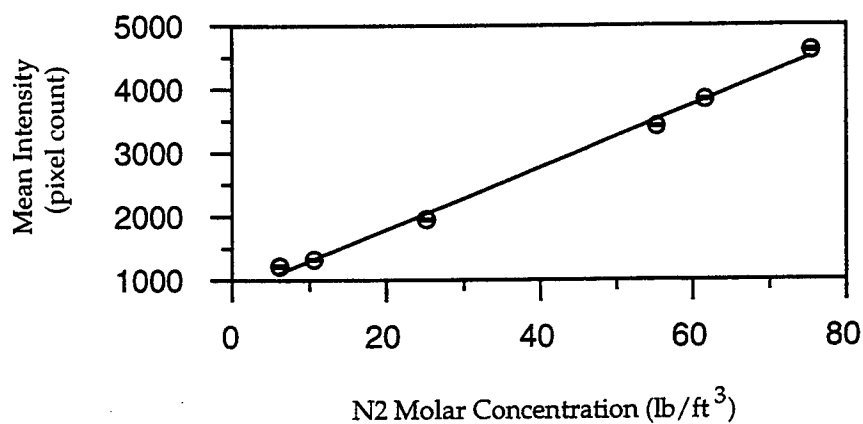
Figure 11: Mean Intensity with standard deviation versus N2 Molar Concentration for small ROI, no reflection, & 10 shots
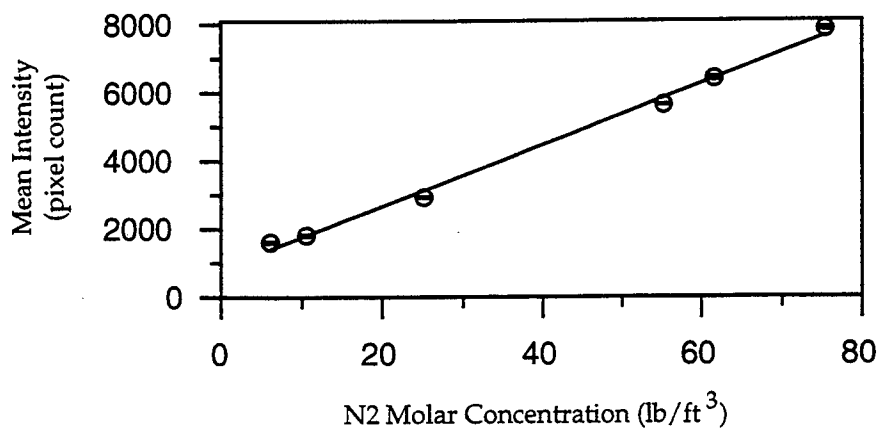
Figure 12: N2 mean intensity versus N2 concentration minus He and noise background for small ROI, 1 shot

Mean intensity (pixel count) vs %N2 Concentration (lbmol/ft^3)
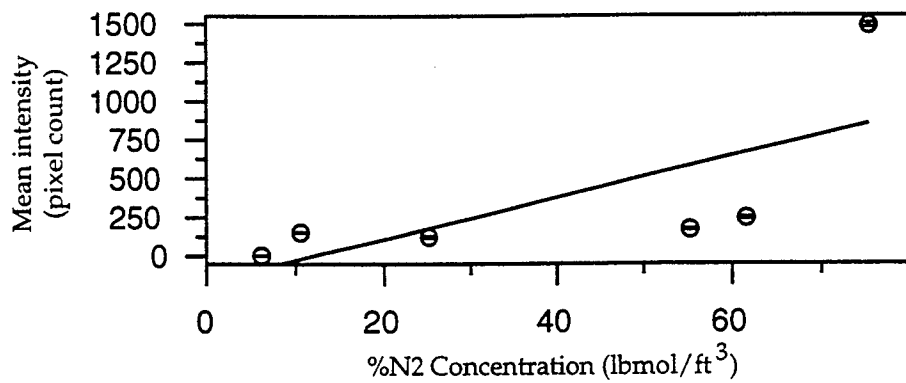
Figure 13: Mean Intensity minus He and noise background versus %N2 concentration for small ROI, 5 shots

Mean Intensity (pixel count) vs %N2 Concentration (lbmol/ft^3)
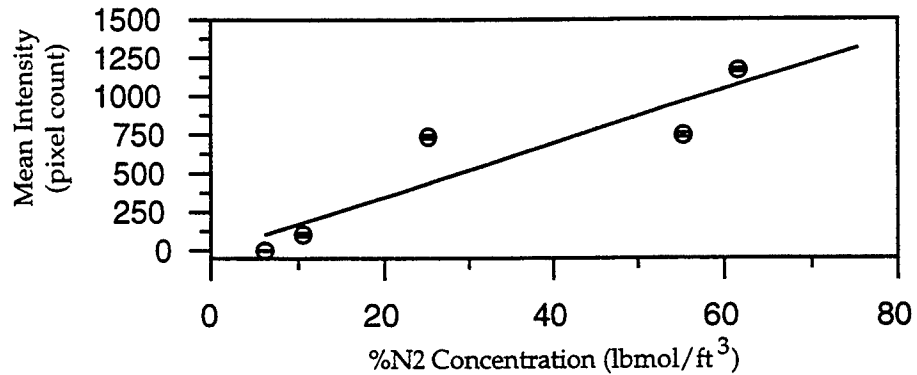
Figure 14: Mean Intensity minus He and noise background versus %N2 concentration for small ROI, 10 shots

Mean Intensity (pixel count) vs %N2 concentration (lbmol/ft^3)
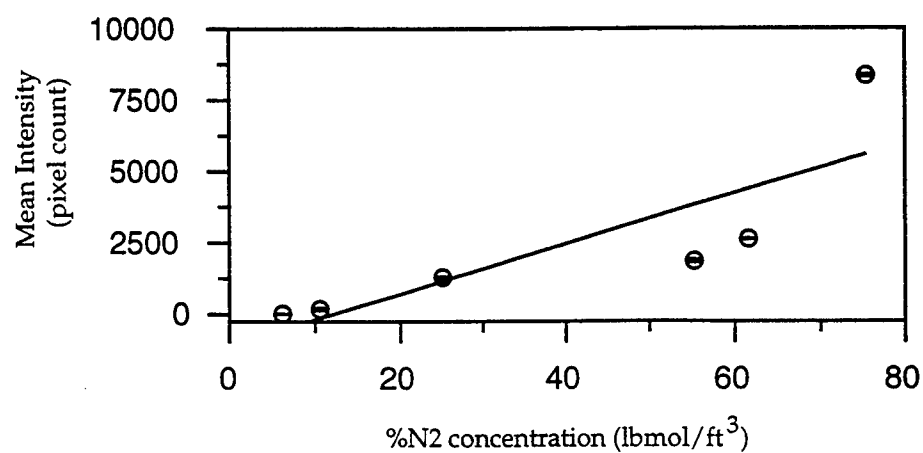
Joy Johnson's report was not available at the time of publication.

MEASUREMENT OF THE SOLID FUEL TEMPERATURE DISTRIBUTION AND ABLATED MASS

OF A PULSED PLASMA THRUSTER

Robert John Leiweke

Graduate Research Associate

Department of Aerospace Engineering, Applied Mechanics, and Aviation

The Ohio State University

2036 Neil Avenue Mall, Room 326

Columbus, Ohio 43210

MEASUREMENT OF THE SOLID FUEL TEMPERATURE DISTRIBUTION AND ABLATED MASS OF A PULSED PLASMA THRUSTER

Robert John Leiweke

Graduate Research Associate

Department of Aerospace Engineering, Applied Mechanics, and Aviation

The Ohio State University

Abstract

The Pulsed Plasma Thruster (PPT) is a low average power (less than 200 W) electric propulsion device used for satellite stationkeeping and drag makeup. Most flight qualified thrusters and laboratory PPT's to date consist of a solid Teflon™ (polytetrafluoroethylene, PTFE) bar placed between two parallel planar electrodes in series with a capacitor charged to a few kV. An arc discharge across the face of the fuel block ablates, ionizes, and accelerates a few micrograms of propellant down the electrode rails. State-of-the-art flight qualified PPT's have low thrust efficiency (<10%) along with low specific impulse (1000 s), presumably due in part to a phenomena called "late-time" ablation. The USAF Phillips (Electric Propulsion) Laboratory at Edwards Air Force Base CA, has recently been investigating the sources of these inefficiencies with the XPPT-1 thruster. The purpose of the present research is to investigate power level effects on ablated mass by measuring the temperature distribution within the fuel and average ablated mass-per-shot. This gives an indication of the net deposited energy, and hence, may illucidate the source of propellant inefficiencies. Although the tests are still incomplete, preliminary results indicate that the Teflon fuel bar experiences a temperature rise up to 40 °C for power levels between 2.5 W and 80 W. Also, average ablated mass-per-shot does not seem to increase with increasing power levels, although again, these measurements are scheduled to be repeated in order to improve experimental accuracy.

MEASUREMENT OF THE SOLID FUEL TEMPERATURE DISTRIBUTION AND ABLATED MASS OF A PULSED PLASMA THRUSTER

Robert John Leiweke

Introduction

The Pulsed Plasma Thruster (PPT) is a low average power (less than 200 W) electric propulsion device used for satellite stationkeeping and drag makeup.[1] Most flight qualified thrusters and laboratory PPT's to date consist of a solid Teflon[TM] (polytetrafluoroethylene, PTFE) bar placed between two parallel planar electrodes in series with a capacitor charged to a few kV. Typical external driving circuits for the main discharge consist of an LRC series network. An avalanche discharge is initiated across the Teflon[TM] fuel face by a low energy spark gap igniter system. A small amount of polymer is ablated (tens of micrograms), and the resulting low density plasma is accelerated towards the exit plane by electromagnetic (Lorentz) and gas dynamic forces. For LRC driving circuits, the discharge and resulting unsteady flow have a characteristic timescale on the order of a few microseconds. State-of-the-art flight qualified PPT's have low thrust efficiency (<10%) along with low specific impulse (1000 s).[1]

The USAF Phillips (Electric Propulsion) Laboratory at Edwards Air Force Base CA, has recently been investigating the sources of these inefficiencies with the XPPT-1 thruster.[2] Mass utilization inefficiencies resulting from neutral vapor emmision of the ablated propellant have been traced to the phenomena of "late-time ablation".[2] It has also been hypothesized[3] that the late-time ablation may be due to an elevated propellant bar average temperature which favors gas dynamical mass evolution through vapor pressure forces, well after the extinction of the arc.

The purpose of the present research is to investigate power level effects on ablated mass. This has significant implications for the MightySat II.1 flight which will use a PPT for orbit-raising. The MightySat flight is a Phillips Laboratory led collaborative effort with Olin Aerospace Corporation (OAC), NASA, and JPL.[4] Initial performance tests[5] at OAC were performed at 0.5 Hz (20 W) with measured performance scaled to the MightSat 100 W power for orbital modeling.

The temperature distribution within the fuel for various power levels gives an indication of the net deposited energy, and hence, may indicate the source of the propellant inefficiencies. Once this source is isolated, one may propose geometrical/electrical changes to future PPT designs.

Experimental Arrangement

XPPT-1 is similar in design to the LES-8/9 PPT, but has increased diagnostic access.[2] It consists of two parallel, PH 17-4 stainless steel electrodes (2.5 cm x 2.5 cm) in series with a 20μF capacitor and a 50 nH stripline. The fuel bar has a 2.5 cm x 2.5 cm fuel face.

Vacuum chamber 5 was used for all experiments.[2] It is 1.2 m in diameter and 1.8 m long, and is evacuated using a 1400 l/s turbomolecular pump backed by a rotary mechanical pump. All of the present experiments were conducted with base pressures beginning at 5.5×10^5 Torr, while the pressures during operation were never greater than 1.0×10^4 Torr. During tests the thruster is affixed to an acrylic plate for electric isolation from the chamber. The chamber is floated electrically to prevent plasma current conduction to the chamber walls.

For these experiments, the XPPT-1 capacitor is charged to 2000 V (40 J) using a laboratory power supply. PPT voltage is measured using a Tektronix 6015 1000X high-voltage probe. The sparkplug is discharged using similar current pulse characteristics as that used in the LES-8/9 PPT.[1,2] A 2μF capacitor charged to 600 V is discharged through a 1:3 voltage step-up transformer to the center pin of the sparkplug. The sparkplug is grounded directly to the PPT cathode. Discharge is alternated between the two sparkplugs using a relay external to the vacuum chamber. Only one of the two fuel bars is discharged during the present measurements.

Temperature measurements were accomplished using ungrounded, 1/16" diameter stainless steel sheath, Type-K thermocouples (Omega). The thermocouple response voltages were converted to Celcius temperatures using a factory calibrated, cold-junction compensated LCD digital (integer) readout (Octa-Scan™ by Electronic Development Labs, Inc.) accurate to within +/- 1 °C. The response time in water of these thermocouples is 0.25 seconds.[6] This scanner is capable of displaying up to eight Type-K thermocouple readings by automatically cycling through each channel at a user-defined speed. Four

thermocouples were inserted into a 4.5 cm long Teflon fuel bar through 1/16" orifices drilled from the back. They were placed symmetrically around the axial centerline of the fuel bar 1/16" apart with each probe tip 0.16 cm, 1.3 cm, 2.5 cm, and 3.8 cm from the fuel face, respectively. In order to insure good thermal contact between the probe tips and polymer fuel, thermal joint compound (Wakefield Engineering, Type 120) was injected into the bottom of each hole using a syringe before insertion. All air bubbles were removed before application of silicone RTV adhesive sealant (Polymeric Systems, Inc., #PSI 601 Clear) securing the probes in place. The scanning time of the digital readout was set to about 16 seconds (4 seconds/channel). This insured that each probe reading would settle to a stationary value. Data was recorded by hand at 30 second intervals during times of rapidly rising temperatures and at 5 minute intervals during slow rates-of-change.

Tests were conducted at 40 J for average power levels of 2.5 W (0.125 Hz), 10 W (0.25 Hz), 20 W (0.5 Hz), 40 W (1 Hz), and 80 W (2 Hz). Additional tests for data repeatability and probe thermal interference were conducted at the 40 W level.

Mass ablation experiments were conducted for 1000 shots using a smaller block of Teflon 0.75" long without thermal probes. Measurements at each of the above power levels were obtained with a Precisa 240A microbalance accurate to +/- 0.1 mg.

Experimental Results

These experiments and subsequent data analysis are not yet complete. Furthermore, it is the intent of the laboratory to supplement this research with interferometric plasma density measurents. For this reason, numerical values will not be presented in this report, but will be submitted to the AIAA Journal of Propulsion and Power for publication at a later date.

Preliminary results show that the Teflon fuel bar does experience a temperature rise between 5 °C and 40 °C for increasing power levels between 2.5 W and 80 W, although this remains to be confirmed by further analysis with one-dimensional heat conduction calculations. Also, average ablated mass-per-shot does not seem to increase with increasing power levels, although again, these measurements are scheduled to be repeated in order to improve experimental accuracy.

Conclusions

Although the Teflon fuel bar does experience a rise of up to 40 °C, preliminary results indicate that there is no significant increase in average ablated mass with increasing average power. Further experiments will be conducted to improve accuracy of the results and will be compared to one-dimensional heat conduction calculations. The final results of these experiments will be submitted for publication in the AIAA Journal of Propulsion and Power.

MACH2 at the Electric Propulsion Lab

The USAF Phillips Electric Propulsion Laboratory has requested MACH2 capability for in-house use via the Maui High Performance Supercomputer Center (MHPCC). MACH2 is a 2-1/2 dimensional Arbitrary (geometry) Lagrangian-Eulerian (ALE) non-ideal magnetohydrodynamics (MHD) code developed by Phillips Laboratory, PL/WSP (Kirtland AFB), for use on Cray supercomputers (XMP, YMP, C90, and Cray2), Sun SparcStations (2, 10, and 20), and IBM RISC 6000 workstations. It is written in FORTRAN 77 and uses the Cray-type pointer and namelist extensions.[7] The code runs under the UNIX and UNICOS operating systems.[8] MACH2 has successfully simulated many complex MHD problems including imploding liners, Plasma Opening Switches, Compact Toroids[9], and an Applied-Field Magneto-Plasma-Dynamic (MPD) thruster.[10] MACH2 has recently been used to investigate the late-time ablation of a PPT.[3]

The first tasks were to set up user accounts at Maui and to establish a software link from the lab using personal computers running MicroSoft[TM] Windows 95[TM]. This was accomplished using a demo program (downloaded from the internet) called XoftWare[TM], by NetManage[TM]. This program allows one to connect to the in-house Hewlett-Packard Apollo workstation and to emulate a Tektronix graphical environment. This was necessary because MACH2 writes post-processed graphical data in a Cray Graphics System (CGS) format, which must be viewed using PSCAN (in Tektronix mode), a program developed by Los Alamos National Laboratory. After successful downloading, un-compressing, and compiling of both XoftWare and PSCAN, the MACH2 subroutine modules and libraries were successfully un-compressed, linked, and compiled on MHPCC under the IBM AIX (Unix) operating system. This was the first time that

the code was compiled on the SP2 processors at MHPCC (the code had been compiled by PL/WSP on the now extinct *SP1 processor*).[11]

After compilation, several one-dimensional, rectangular geometry, ideal gas cases were run to verify the code. These consisted of hydrodynamic inflow boundary condition stability, wall thermal conduction, and external driver circuit tests. These results were verified by comparison to one-dimensional analytic theory.

References

[1]   Vondra, R.J. and Thomassen, K.I., *Flight Qualified Pulsed Electric Thruster for Satellite Control*, J. Spacecraft, Vol. 2, No. 9, Sept. 1974, AIAA 73-1067, 10th Electric Propulsion Conference, Lake Tahoe, NV, Oct. 31-Nov. 2, 1973.

[2]   Spanjers, G., McFall, K.A., Gulczinski, F.S., and Spores, R.A., *Investigation of Propellant Inefficiencies in a Pulsed Plasma Thruster*, 32nd AIAA/ASME/SAE/ASEE Joint Propulsion Conference, Lake Buena Vista, FL, July 1-3, 1996.

[3]   Mikellides, P.G. and Turchi, P.J., *Modeling of Late-Time Ablation in Teflon Pulsed Plasma Thrusters*, 32nd AIAA/ASME/SAE/ASEE Joint Propulsion Conference, Lake Buena Vista, FL, July 1-3, 1996.

[4]   Tilley, D., Pobst, A., Bromaghim, D., Myers, R., Cassady, J., Hoskins, A., Meckel, N., Blandino, J., Brinza, D., and Henry, D., *Advanced Pulsed Plasma Thruster Demonstration on MightySat Flight II.1*, Proceedings of the Utah State Univ./AIAA Conference on Small Satellites, Logan, UT, Sept. 1996.

[5]   Meckel, N.J., Hoskins, A.W., Cassady, J.R., Myers, R.M., Oleson, S.R., and McGuire, M.L.,

        Improved Pulsed Plasma Thruster Systems for Satellite Propulsion, 32nd AIAA/

        ASME/SAE/ASEE Joint Propulsion Conference, Lake Buena Vista, FL, July 1-3, 1996.

[6]   *The Temperature Handbook, Vol. 28,* page Z-44, Omega Engineering, Inc., 1992.

[7]   Peterkin, R.E. Jr., Giancola, A.J., and Sturtevant, J.E., *MACH2: A Reference Manual, Fifth Edition,*

        MRC/ABQ-R-1490, July, 1992.

[8]   USAF Kirtland Air Force Base, New Mexico, Phillips Laboratory, PL/WSP, *MACH2 v.9601 Code*

        Listing, 1996.

[9]   Peterkin, R.E. Jr., Degnan, J.H., Hussey, T.W., Roderick, N.F., and Turchi, P.J., *A Long*

        Conduction Time Compact Torus Plasma Opening Switch, IEEE Trans. Plasma Science,

        No. 21 (5), page 522, 1993.

[10]   Mikellides, P.G., Turchi, P.J., and Roderick, N.F., *Theoretical Model of an Applied-Field MPD*

        Thruster, AIAA Preprint 95-2646, Washington DC, 1995.

[11]   Peterkin, R.E. Jr., *private communication,* USAF Kirtland AFB, Phillips Laboratory, PL/WSP, July,

        1996.

PARTICULATE EMISSION ANALYSIS OF A PULSED PLASMA THRUSTER

Jason Scott Lotspeich
Graduate Research Associate
Department of Mechanical Engineering

Colorado State University
Fort Collins, CO 80523

12-1

PARTICULATE EMISSION ANALYSIS OF A PULSED PLASMA THRUSTER

Jason Scott Lotspeich
Graduate Research Associate
Department of Mechanical Engineering

Abstract

Propellant inefficiency resulting from the ejection of propellant material in particulate form is characterized in a Pulsed Plasma Thruster (PPT). Exhaust deposits are collected and analyzed using a combination of Scanning Electron Microscope (SEM), Energy Dispersive X-ray Analysis (EDAX), and microscopic imaging. Teflon particulates are observed with sizes ranging from over 100 μm down to less than 1 μm. Estimates of the mass entrained in this form show that the particulates may account for up to 40% of the total propellant mass used, indicating that methods of ameliorating this loss mechanism would result in significant improvements in the PPT thrust efficiency.

I. INTRODUCTION

The Pulsed Plasma Thruster (PPT)[1] is an attractive propulsion option for small power-limited satellites. The PPT, shown schematically in Fig. 1, operates at low power levels (<100W) by capacitively storing energy on a long time scale (1 sec), and then discharging the capacitor on a short time scale (10 μs) at high instantaneous power. High reliability is achieved through the use of a solid propellant (typically Teflon) which eliminates the complexity and dry mass associated with gaseous propellants. The only moving part on the PPT is a spring which passively feeds the propellant into the discharge chamber. The solid propellant is converted to vapor and partially ionized by a surface discharge across the propellant face. Acceleration is accomplished by a combination of thermal and electromagnetic forces to create usable thrust. The inherent engineering advantages of the PPT design have enabled the thruster to complete several space missions over the past 30 years with no failures.[1,2,3]

Unfortunately the excellent engineering characteristics of the PPT are coupled with poor performance characteristics. Present designs[4] have achieved thrust efficiencies ($\eta = T^2/2mE$) below 8%. The low thrust efficiency is attributable to both a low energy efficiency and a low propellant efficiency.[5,6] Previous measurements[5,6] have shown that a neutral gas vaporizing from the propellant face long after the current discharge is a significant factor in the low propellant efficiency. Theoretical modeling has also identified propellant inefficiency as a serious impediment to improving PPT performance.[7]

In the present work a second mechanism, particulate emission, is identified as a significant contributor to the low propellant efficiency. Broadband emission indicative of particulates is observed emitting from the PPT long after the current pulse. Scanning Electron Microscopy (SEM) of exhaust deposits shows particulates in agreement with the emission measurements. Energy Dispersive X-ray Microanalysis (EDAX) identifies the particulates as Teflon. Magnified images of the propellant face after discharge show a cratered surface indicative of particle ejection. The propellant mass expended in particulate form is estimated to be up to 40% of the total mass ablated during the PPT discharge. PPT

12-3

design improvements directed at eliminating particulate formation would result in propellant efficiency and concomitant increased thrust efficiency. Recovering 40% of the used propellant mass with minimal .

II. EXPERIMENTAL APPARATUS

The experiments are performed at the Edwards AFB location of the Air Force Phillips Laboratory in Chamber 5 of the Electric Propulsion Laboratory.[5] Surface analysis is conducted using the SEM/EDAX facilities of the Propulsion Directorate Chemistry Department.

A. Pulsed Plasma Thruster XPPT-1

The experiments are performed on the exhaust from XPPT-1 (Experimental Pulsed Plasma Thruster #1). The XPPT-1, shown in Fig. 2, is similar to the LES 8/9 PPT[4,8] electrically and geometrically, however diagnostic access has been maximized in the XPPT-1 design. The stripline (approximately 50 nH), electrode dimensions (2.5 cm x 2.5 cm), electrode separation (2.5 cm), fuel bar geometry (2.5 cm x 2.5 cm), and sparkplugs are identical to that used in LES 8/9. The major difference between the two designs are: (1) the 30° thrust angle in the LES 8/9 has been eliminated in XPPT-1, (2) the housing around the electrodes in LES 8/9 has been removed, and (3) both electrodes in the XPPT-1 are fabricated from 304 Stainless Steel compared to the Mallory 1000 (thoriated tungsten) and 17-4 steel used for the LES 8/9 cathode and anode. The thruster is designed so that a range of capacitances can be easily tested, however 20 μF was used for all of the present tests, approximately equal to the 17 μF used in the LES 8/9 PPT. The interface between the energy storage capacitor and the stripline has been modified in XPPT-1 to allow for a Rogowski coil (Ion Physics CM-1-L) that measures the discharge current. This modification adds approximately 70 nH to circuit inductance.

The thruster is charged using laboratory power supplies. Capacitor voltage is monitored using a Tektronix 6015 1000X high voltage probe connected at a break in the coaxial charging line external to the vacuum chamber. The PPT current is initiated by discharging one of the two sparkplugs fit into the cathode electrode. The spark plug is alternated for each discharge. The experiment is operated automatically using a

Texas Instruments model 405 Programmable Logic Control (PLC) running on a PC computer which also tabulates the number of discharges.

B. Diagnostics

Broadband light emission is digitally recorded using a high-speed framing camera (Stanford Computer Optics 4 QUIK 05). The camera has a minimum 50 ns gate time and an image intensifier for recording low intensity signals. The Charged Coupled Device (CCD) array within the camera is 610 x 488 pixels. For the imaging used in the present work, this corresponds to a spatial resolution of approximately 150 μm. The camera has only single-frame capability so images at different times and shutter speeds are recorded on different PPT discharges. Camera sensitivity increases exponentially with gain.

Exhaust samples are collected on disks of 6061-T6 aluminum, 12.7 mm. dia. and 3.2 mm thick. The aluminum sample substrate is chosen since its composition is well known, and its conductivity helps minimize sample charging during SEM analysis. For SEM/EDAX characterizations, the sample disks are attached to a carbon mount with a silver paste and baked at 200 F for 2 hours to solidify the paste. The SEM/EDAX analysis is conducted with a chamber pressure of 2 x 10^{-7} Torr.

Energy dispersive X-ray microanalysis (EDAX) is used to determine the composition and relative concentration of elements on the sample disks. The electron beam, used for imaging the deposits in the SEM mode, is used at higher energy to excite X-ray transitions within the sample elements. Each element has a critical excitation potential below which its characteristic X-rays will not be generated. This potential should be exceeded by at least a factor of two to detect a sufficiently intense characteristic X-ray peak.[9] To insure excitation of at least one X-ray series (K, L or M) for each of the elements under investigation, an accelerating voltage of 15-20 keV is required. However, these higher energy electrons have decreased resolution for the lighter elements (fluorine and carbon) expected on the sample surface. Thus, lower accelerating voltages (under 10 keV) are optimal for examining lighter elements, and higher accelerating

12-5

voltages are optimal for examining heavier elements, with an expected loss in resolution for X-rays from lighter elements.

The principal materials expected in the EDAX analysis are from the Teflon propellant (33% C, 66% F), 304 Stainless Steel electrodes (.08% C, 69% Fe, 19% Cr, 9% Ni, <2% Mn, <1% Si), and the 6061-T6 aluminum sample disk (97.9% Al, 1% Mg, 0.6% Si, 0.25% Cr, 0.25% Cu). Particles on the sample surface with strong carbon and fluorine X-ray emission are presumed to have been deposited as Teflon (C_2F_4). If the Teflon had disassociated prior to deposition, it is assumed that the gaseous fluorine would have pumped out of the system leaving only a carbon deposit.

III. EXPERIMENTAL RESULTS

Experiments are performed using XPPT-1 configured with a 20 µF capacitor and charged to 1414 V for a discharge energy of 20 J. The thruster is operated at 1/8 Hz corresponding to a power level of 2.5 W. The aluminum sample disk is positioned along the thrust vector 6 cm from the propellant face. A second sample placed at 10 cm, to confirm information discerned from the sample at 6 cm, showed essentially the same deposit characteristics. All data shown is from the sample at 6 cm. Deposits on the sample disks are accumulated over 1000 PPT discharges.

The thruster current and voltage are shown in Fig. 3. At this power level and pulse frequency, XPPT-1 consumes 15.6 µg/discharge of propellant. This mass ablation rate is only 55% of the 28.5 µg/discharge reported for the LES 8/9 PPT operated at similar energy and voltage levels.[4] The difference in mass ablation rates apparently results from the different power levels (which are controlled by the pulse frequency). The LES 8/9 PPT operated at 20 W (1 Hz) as compared to the 2.5 W (1/8 Hz) power level used in the present work. Tests on XPPT-1 operated at 20 W (1 Hz) show 23.3 µg/discharge which is 18% below the LES 8/9 ablation rate.[10] The remaining difference between the mass ablation rates may be accounted for by observing that for XPPT-1 the mass ablation rate increases during the initial 1000 discharges.[10] The mass ablation rate dependence with power possibly results from an increased average temperature in the propellant at increased pulse frequency. The propellant then requires less energy to

12-6

vaporize resulting in increased propellant mass ablation. The increased mass ablation rate with increased propellant temperature has been suggested in PPT modeling work.[7]

Broadband emission from the PPT exhaust is shown in Fig. 4. Figure 4a is recorded during the PPT discharge with a 10 µs shutter and gain of 300 V. The emission is suggestive of a standing arc near the propellant face with streams of plasma accelerated in the thrust direction. The exhaust appears distributed and devoid of particulates. Reduction of the shutter time to 50 ns also shows no evidence of particulates, although the discharge becomes substantially more filamentary. Figure 4b is recorded 100 µs after the discharge with a 10 µs shutter and gain of 800 V. Numerous localized emission sites are apparent. The absence of discharge energy at this time, coupled with previous measurements of a high-density neutral vapor,[5] indicates that the propellant face is continuing to vaporize away propellant. Figure 4c is recorded at the same experimental time as Fig. 4b (albeit on different PPT discharges) but with a longer 100 µs shutter and gain of 450 V. The emission now appears as streaks showing the motion of the emission sites. For the characteristic streak length of 2 cm, a velocity of approximately 200 m/s is inferred. The duration of the streak emission (100 µs) implies a heat capacity incompatible with a single molecule or plasma motion, requiring the higher mass of particulates.

To support the hypothesis of the presence of particulates in the PPT exhaust suggested by the broadband emission, the sample disks were placed in the exhaust and subjected to surface analysis. SEM imaging of the exhaust deposits shows a multitude of material concentrations, attributable to particulates striking the sample, superimposed on a background film. Figure 5 shows an SEM image of a particulate deposit at 1100X magnification. The deposit is approximately 690 µm^2 in area and is surrounded by a circular structure suggestive of the crater formation associated with particle impact.

SEM imaging at reduced magnification (369X), Fig. 6, shows four particle deposits of size similar to that in Fig. 5. The particles appear bright in the SEM photograph which occurs when the electron beam electrically charges the deposit. This indicates that the deposited material is an insulator, unable to conduct excess charge to the substrate, suggesting that the deposits are composed of Teflon. A multitude of smaller sized deposits are also apparent in Fig. 6.

The EDAX Spectra from the particle in Fig. 5 and the background film are tabulated in Table 1. Also listed are the calibration spectra for the propellant (Teflon) and electrode (304 Stainless Steel) materials. Line intensities are normalized to the signal at 700 eV, which is identified as either F or Fe within the resolution of the EDAX, and the intensities are tabulated for both low and high EDAX electron accelerating potential.

The difficulty in separating the critical elements is apparent in the low energy case where the spectral peaks for Teflon and steel both consist primarily of lines at 200 eV and 700 eV. At high energy both materials again share the peaks at 200 eV and 700 eV however the steel also shows large intensity at higher energy transitions corresponding to Cr, Fe and Ni. The Teflon also shows small signals at the Ni transitions attributable to emission from either the EDAX chamber or the sample mount. The small steel transition lines in the background and particle EDAX spectra shows that these components are not principally comprised of steel. The small steel transition signal that is observed implies that some electrode material is deposited, possibly at higher concentration in the background than in the particle. An interesting feature at both energy levels is that the spectra for the particle and for the background film are approximately equal. A possible cause is that a large population of particles are deposited at characteristic sizes less than that detected with the SEM. This would preclude a true EDAX analysis of the background film since a multitude of particulates would always be present thus skewing the results towards the spectra of a particulate. Comparison of the Teflon and particulate spectra for the low energy case shows that the particulate is carbon-rich. This may result from co-sampling background film that has deposited on or below the particle.

A total of 8 particle deposits were identified through SEM and characterized through EDAX. Each of these was concluded to be comprised of Teflon as opposed to 304 Stainless Steel, although all were found to be carbon-rich similar to the EDAX spectra of Table 1.

Images at several magnifications, Fig. 7, illustrate the particle size distribution. These images were obtained using an Olympus AH-2 microscope with magnifications of 5X, 20X, and 100X in Figs. 7a, 7b, and 7c respectively. A full range of particle sizes are observed from a multitude of particles near 1μm in

12-8

the 100X image to two large particles 200 μm long observed in the 5X image. The large particle in the 5X image is part of a streak of several particles that appear to have been deposited as a group. Presumably a relatively large mass struck the sample disk at a slight angle to create several deposits aligned in a single streak. Two such groupings were found on the sample disk.

Figure 8a is a 5X photograph of the face of the Teflon propellant prior to installation in the PPT. Preparation consisted of milling the Teflon to size and cleaning with alcohol. Sandpaper was not used to prevent possible imbedding of the grit material in the propellant, which could later appear as a particulate. The machining marks and various surface imperfections are visible in Fig. 8a. Figure 8b is the same propellant face after 1000 discharges. Two important changes are apparent in the features. First, the machining marks and surface imperfections are absent. This may be a result of the surface repeatedly melting and solidifying between discharges. If the mass is ablated uniformly across the propellant face, 11.2 μm of propellant is vaporized from the front of the Teflon over the 1000 discharge experimental run. This appears to be insufficient ablation to smooth the non-uniformity in the propellant face supporting the hypothesis of repeated melting and solidification between discharges. The second important feature is the appearance of a multitude of craters in the propellant face. The craters are easily distinguishable from being projections by adjusting the focusing depth of the microscope.

V. DISCUSSION

A critical question is whether exhaust in the particulate form accounts for a significant fraction of the propellant usage in the PPT. The total particulate mass can be estimated from Fig. 7a which shows a 2.3 mm x 3.0 mm area of the sample disk magnified at 5X. The particle sizes in Fig. 7a are tabulated by their general size group in Table 2. In the mass calculations for Table 2, the height of each deposit is estimated to be equal to the radius and the volume is calculated as $V=\pi r^2 h$. Density is assumed to be that of Teflon. This analysis estimates a total of 4.06 μg to be in particulate form in Fig. 7a. This mass is scaled by the relative areas of the image to the area of the sample disk to estimate 76 μg of particle deposits on the sample disk, equivalent to 0.55% of the total propellant mass ablated. This estimate ignores particles below 15 μm in

diameter which could have a significant impact on the total mass. Also ignored are the two large streak formations observed on the sample disk. These formations would add approximately 0.5 μg to the total sample disk mass. They are ignored since only two formations on the entire disk surface is a poor statistical sampling.

A conservative estimate of the total mass emitted from the PPT in particle form assumes that the PPT exhaust has zero divergence. The particles are assumed to be emitted in an area equal to area of the propellant face (645 mm^2). Scaling the mass on the sample disk by the propellant area estimates a total particulate mass emitted from the PPT of 390 μg which is 2.5% of the 15.6 mg emitted during the 1000 discharge experiment.

A more realistic estimate, based on the broadband emission, is that the particles are emitted in a 45° cone centered on the thrust axis. Scaling the mass on the sample disk using this estimate predicts a total particle mass emitted by the PPT of 7 mg which is 40% of the total propellant usage in the experiment.

These estimates of the total particle mass emitted by the PPT require significant approximation and the resulting figure may be off by an order of magnitude. What is illustrated is that the most conservative estimate shows the particulate mass to be significant. The more realistic estimate suggests that this propellant inefficiency may be at least as important as late time vaporization,[5,7] and may possibly be the dominant propellant loss mechanism.

Understanding the mechanism behind the creation of the particulates is critical to eventually minimizing this loss mechanism in PPTs. The crater formations apparent in the propellant face after the discharges suggest that particle formation may result from vaporization below the Teflon surface. Embedded vapor would result in high gas pressures that would explosively eject the particulates leaving behind the craters. Energy deposition beneath the front face may be the result of radiation from the plasma arc, particularly soft X-rays which can transmit a short distance into the Teflon. Similar effects have been observed in related work on ablation controlled arcs.[11] Such a mechanism will be independent of the PPT power level and temperature and may account for some of the discrepancy between predicted[7] and measured mass ablation in the PPT.

Emission streaks in Fig. 4 imply that a significant fraction of particles appear to originate from the electrodes. This may be a result of Teflon vapor from previous discharges condensing on the electrode surface. Localized heating from the plasma arc then vaporizes electrode material beneath the condensed Teflon causing particle ejection. Traces of steel in the background film deposits confirm that some electrode vaporization is occurring. The emission images imply that particulate ejection from the electrodes occurs well after the discharge with no detectable particulates during the PPT current. This may be a result of the relatively strong emission from the plasma arc overwhelming the weaker emission from the particulates. The image during the discharge, Fig. 4a, was obtained with a camera gain of 300 V. This gain would be insufficient to record the emission 100 μs after the discharge when particulates are apparent, Fig. 4b. It is also important to note that the streaks apparent in Fig. 4c may not be responsible for the Teflon deposits on the sample disks. The Teflon particles may be emitted at low temperature from the propellant face and never be observable with the camera due to a low emission level.

The experimental design of XPPT-1 compared to the flight-qualified LES 8/9 PPT brings into question whether the particle emission is specific to only the thruster considered in the present work. Similar results have been reported from measurements on LES 8/9 during contamination tests at NASA Lewis.[12] In that work SEM analysis was used to observe a large number of 1 to 5 μm particles superimposed on a base film, in agreement with the present work. Presumably images at other magnifications would have also yielded similar results. The NASA work also reported a few metal particles that may have originated from the electrodes. No such particles were observed in the present work, however this is probably due to the relatively few number of particles that were examined using EDAX.

The present work is concerned solely with sources of propellant inefficiency in the PPT to better guide future thruster designs. No conclusions can be made as to the possible contamination effects of the particles on the spacecraft surfaces. This is because the XPPT-1 is of inappropriate design for contamination studies since it lacks the nozzle around the electrodes that a flight unit would certainly have. In addition, the vacuum facility used in the present work is intentionally small to optimize optical diagnostic access. Contamination study requires a much larger chamber in order to minimize wall interaction. A

dedicated contamination study for the PPT has been performed using a flight-qualified PPT (LES 8/9) in a chamber appropriate for this research at NASA-Lewis.[13] No measurable deposition was observed in the backflow region of the thruster, indicating that contamination is not a major concern for these devices.

V. SUMMARY AND CONCLUSIONS

Surface analysis on exhaust deposits from the PPT reveal a significant quantity of propellant material in particulate form. Estimates of the total mass exhausted in this form show that particulates may account for up to 40% of the total propellant usage indicating that this is a significant, and possibly dominant, source of propellant inefficiency in these devices.

One source of the particulates is believed to be energy deposition below the Teflon surface. This energy vaporizes material behind the propellant face creating a high gas pressure that results in material ejection in the form of particles. This model is supported by the observation of crater formations in the propellant face after PPT discharges. A second potential source results from vaporized Teflon propellant condensing on the electrode. During subsequent PPT discharges electrode vaporization beneath the coating ejects the Teflon material as particulates.

Research directed towards minimizing the particle ejection can have a significant impact on PPT thrust efficiency. Present research at Phillips Laboratory is exploring the use of propellants with reduced soft X-ray transmission in an effort to deposit the arc radiation energy in a minimally thin layer at the propellant face.

The culmination of this research effort is a paper that will be submitted to the Journal of Propulsion and Power under the title "Characterization of Particulate Emission From A Pulsed Plasma Thruster." The authors of this paper will be: Gregory G. Spanjers, Jason Lotspeich, Keith McFall, and Ronald Spores.

Table 1 Normalized spectral line intensities for the background film, a particulate deposit, and calibration spectra of Teflon and 304 Stainless Steel. Intensities are shown using both low (6 -7 keV) and high (15 - 20 keV) energy electrons in the EDAX measurements.

		F or Fe 700 eV	C 200 eV	Cr 450 eV	Cr 5900 eV	Fe 6500 eV	Ni 7100 eV	Ni 7500 eV
Low Energy (6 -7 keV)	Teflon	1	0.29	0	0	0	0	0
	304 SS	1	offscale	0.047	0	0	0	0
	Background	1	1.3	0	0	0	0	0
	Particulate	1	1.4	0	0	0	0	0
High Energy (15 - 20 keV)	Teflon	1	0.31	0	0	0	0.019	0.030
	304 SS	1	offscale	2.4	.38	5.8	0.75	0.46
	Background	1	2.9	.075	0	0.15	0.025	0.075
	Particulate	1	3.3	.037	0	0.11	0.0074	0.074

Table 2: Size distribution and estimated mass for the particle deposits of Fig. 7a.

Diameter (μm)	Number	Total Mass (μg)
15 - 25	105	0.68
25 - 50	20	0.88
50 - 75	4	0.82
75 - 100	2	1.68
Total Particle Mass		4.06

[1] W. J. Guman and D. M. Nathanson, "Pulsed plasma microthruster for synchronous orbit satellite," J. Spacecraft and Rockets **7**, 409 (1970).

[2] Y. Brill, A. Eisner, and L. Osborn, "The flight application of a pulsed plasma microthruster; the NOVA satellite," AIAA-82-1956, New Orleans, LA, (1982).

[3] W. J. Guman and T. E. Williams, "Pulsed plasma microthruster for synchronous meteorological satellite (SMS)," AIAA_73-1066, Lake Tahoe, NV, (1973).

[4] R. J. Vondra, "The MIT Lincoln Laboratory pulsed plasma thruster," AIAA-76-998, Key Biscayne, FL, (1976).

[5] G. G. Spanjers, K. A. McFall, F. S. Gulczinski III and R. A. Spores, "Investigation of propellant inefficiencies in a pulsed plasma thruster," AIAA-96-2723, Lake Buena Vista, FL, (1996).

[6] A. Solbes and R. J. Vondra, "Performance study of a solid fuel pulsed electric microthruster," J. Spacecraft **10**, 406 (1973).

[7] P. G. Mikellides and P. J. Turchi, "Modeling of late-time ablation in Teflon Pulsed Plasma Thrusters," AIAA 96-2733, Lake Buena Vista, FL (1996).

[8] R. J. Vondra and K. I. Thomassen, "Flight qualified pulsed electric thruster for satellite control," J. Spacecraft **11**, 613 (1974).

[9] J. A. Belk, In "Quantitative Scanning Electron Microscopy" (D. B. Holt ed.), p. 389. Academic Press, London, (1974).

[10] J. B. Malak, G. G. Spanjers, K. A. McFall, R. A. Spores, "Power Level Effects in a Pulsed Plasma Thruster," in draft for Journal of Propulsion and Power.

[11] C. B. Ruchti and L. Niemeyer, "Ablation Controlled Arcs," IEEE Trans. on Plasma Science **PS-14**, 423 (1986).

[12] R. M. Myers, L. A. Arrington, E. J. Pencil, J. Carter, J. Heminger, and N. Gatsonis, "Pulsed Plasma Thruster Contamination," AIAA-96-2729, Lake Buena Vista, FL (1996).

12-14
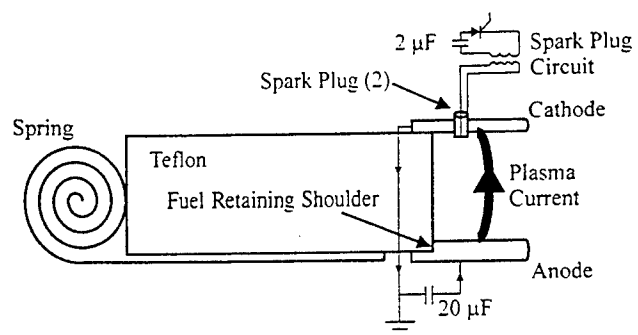
Figure 1. Schematic of a Pulsed Plasma Thruster.
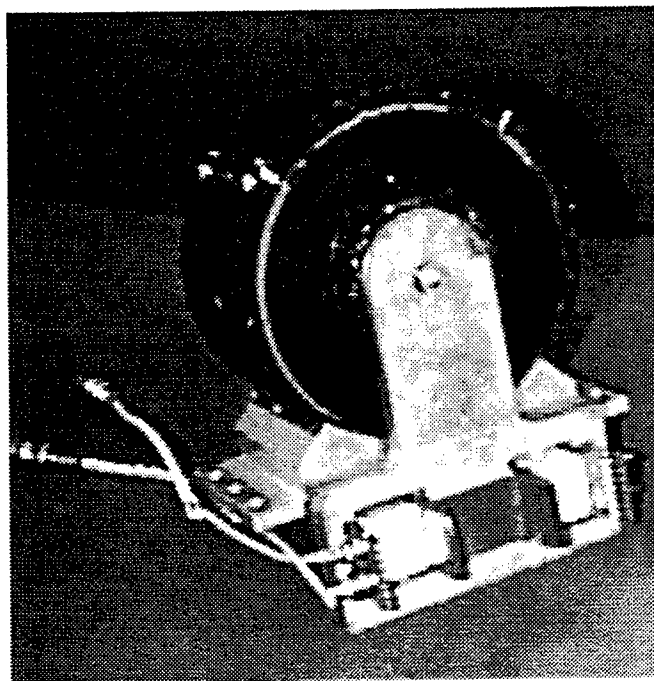
Figure 2. Photograph of XPPT-1 Pulsed Plasma Thruster.
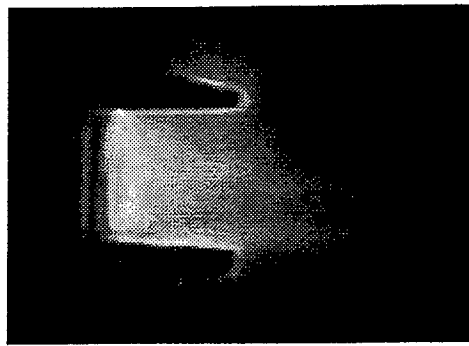
4a)
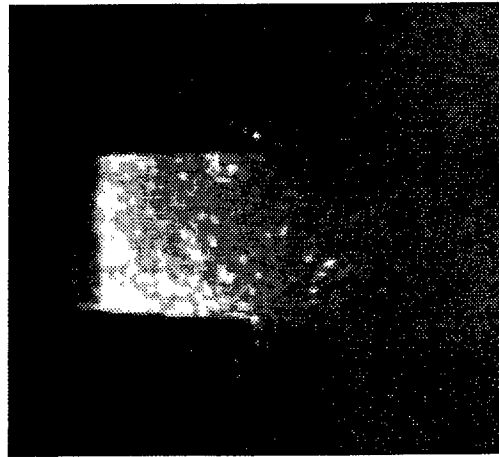
4b)
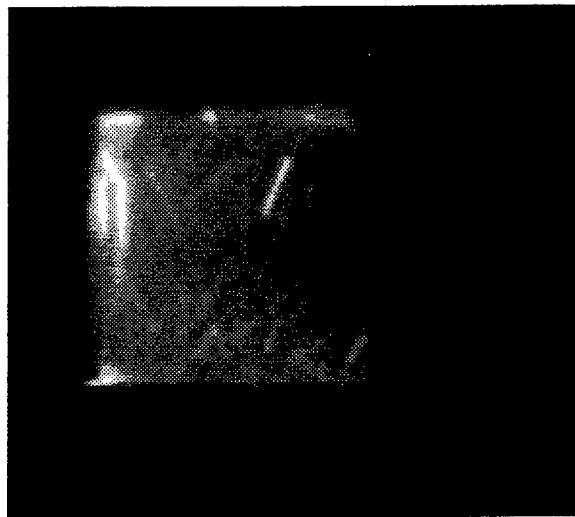
4c)

Figure 4. Broadband emission from the PPT exhaust. 4a) 10 shutter during the PPT discharge, 4b) 10 shutter initiated 100 after the discharge. 4c) 100 shutter initiated 100 after the discharge.
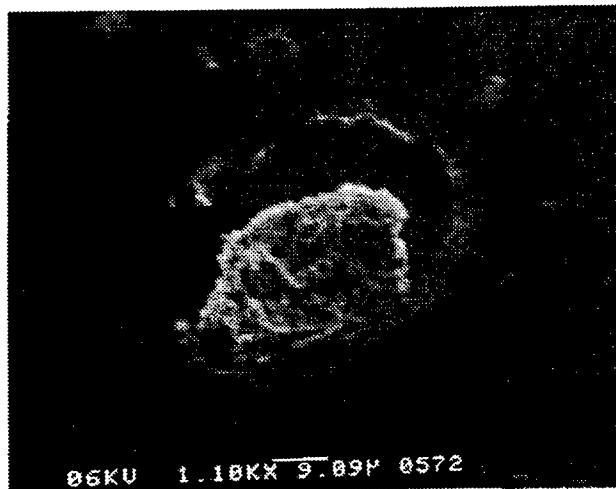
Figure 5. SEM photograph of a sample at 1100X.
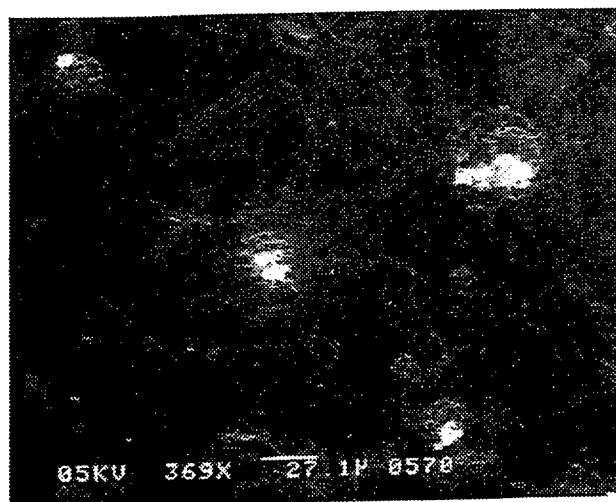
Figure 6. SEM photograph at reduced magnification(369X) shows the relative concentration of 30 μm size particulates and the presence of a multitude of smaller particles.
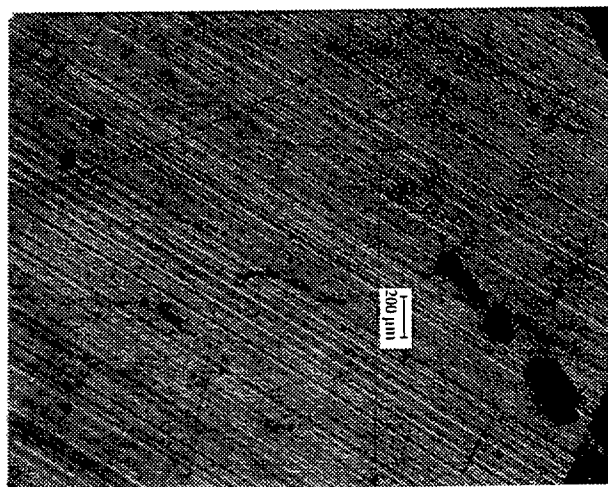
Figure 7a. 5X Magnification.
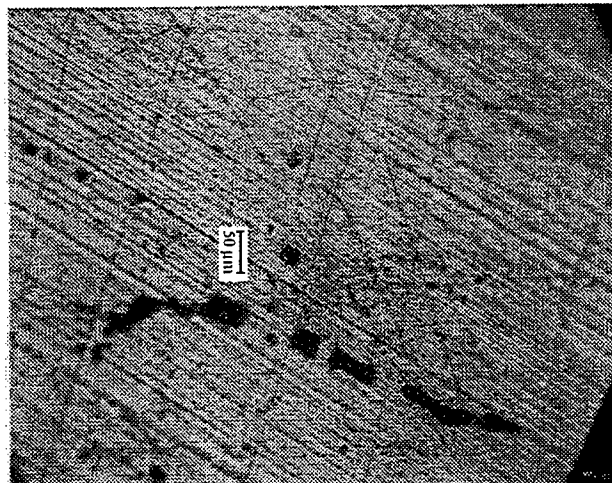
Figure 7b. 20X Magnification.

Figure 7c. 100X Magnification
Figure 7. Microscope Images of a Sample Deposit
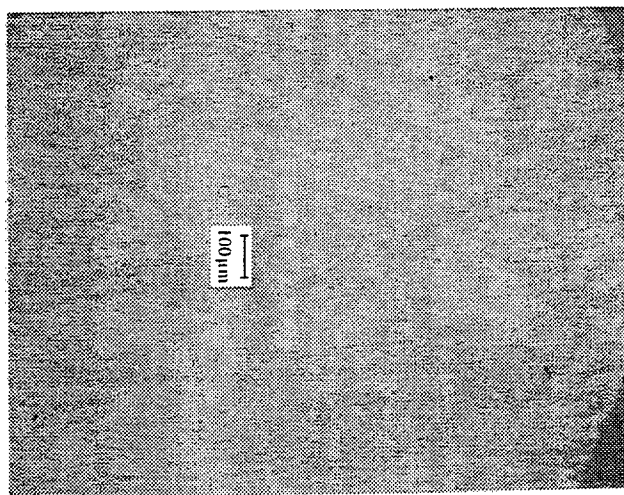
Figure 8a. Teflon Propellant Face Before Firings.
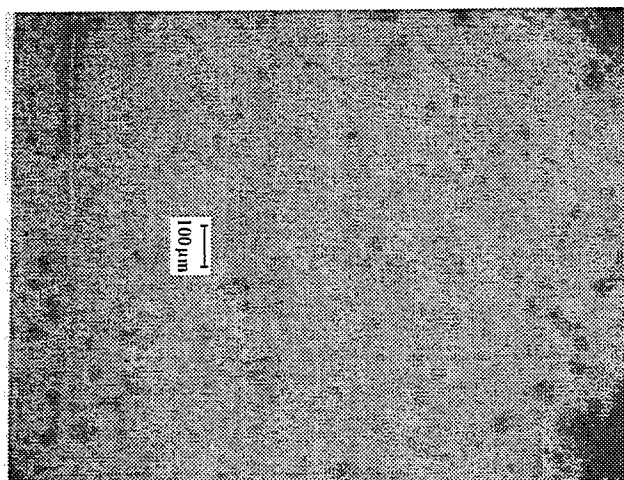
Figure 8b. Teflon Propellant Face After 1000 Shots. Note that pitting has occurred.

THE EFFECT OF BOTTOMSIDE SINUSOIDAL IRREGULARITIES ON A TRANSIONOSPHERIC SIGNAL

Ruthie D. Lyle
Graduate Student
Department of Electrical Engineering

Polytechnic University
Route 110
Farmingdale, NY 11735

THE EFFECT OF BOTTOMSIDE SINUSOIDAL IRREGULARITIES ON A TRANSIONOSPHERIC SIGNAL

Ruthie D. Lyle
Graduate Student
Department of Electrical Engineering
Polytechnic University

ABSTRACT

The scintillation of a transionospheric signal is caused by scattering imposed on the signal in the ionosphere combined with diffraction effect after the signal exits the ionosphere, and the horizontal displacement of this perturbation caused by ionospheric drift. A quasi-particle approach is used to study the phenomenon caused by the bottomside sinusoidal (BSS) irregularities appearing in the equatorial F region of the ionosphere. A three second sample of high-resolution density perturbation data obtained in situ by the low orbiting Atmosphere-E (AE-E) Satellite (orbit 22700, 12/11/79) during its passage through BSS irregularities is modeled by the superposition of three basic functions. The parameters used in the density model of the irregularities capture the realistic spectral information for the present study. Numerical results are presented, and their physical significance discussed.

THE EFFECT OF BOTTOMSIDE SINUSOIDAL IRREGULARITIES ON A TRANSIONOSPHERIC SIGNAL

Ruthie D. Lyle

INTRODUCTION

The scintillation of a transionospheric signal is the result of wave scattering in a drifting inhomogeneous ionosphere followed by diffraction of the wavefront propagating in free space. The investigation of this phenomenon has been a powerful means to remote sensing the condition of the ionosphere.

In the latter part of the 1940's, observation of radio signals received from Cygnus A, a radio star, was noted to fluctuate in intensity irregularly in time. Experimental investigation was conducted to establish the origin of the irregular fluctuations in the received signal. A comparison of data retrieved at three different receiver locations, revealed that there was no correlation between measurements taken a few hundred kilometers apart. However, a correlation between measurements taken a few kilometers apart instead, was found. This indicated that the fluctuations of the radio signals' intensity were a result of their interaction with very localized ionospheric irregularities.

The natural trend of investigation involved determining which part of the Earth's atmosphere influenced the propagating signal. The ionosphere, the section of the Earth's atmosphere ranging from approximately ninety kilometers to slightly more than a thousand kilometers has a bell-like background electron distribution, Fig. 1, with respect to altitude. The index of refraction in this region can differ from one. The peak density occurring between 350 - 400 kilometers, depending on the time of day.

The refractive index which characterizes the ionosphere in terms of the background electron density, as seen by a plane wave neglecting the Earth's magnetic field and ignoring collisions between electrons and neutral particles, is a well known expression,

$$n(\bar{r}) = \sqrt{1 - \frac{\omega^2_{p_o}(\bar{r})}{\omega^2}} \, .$$

(1)

Henry Rishbeth
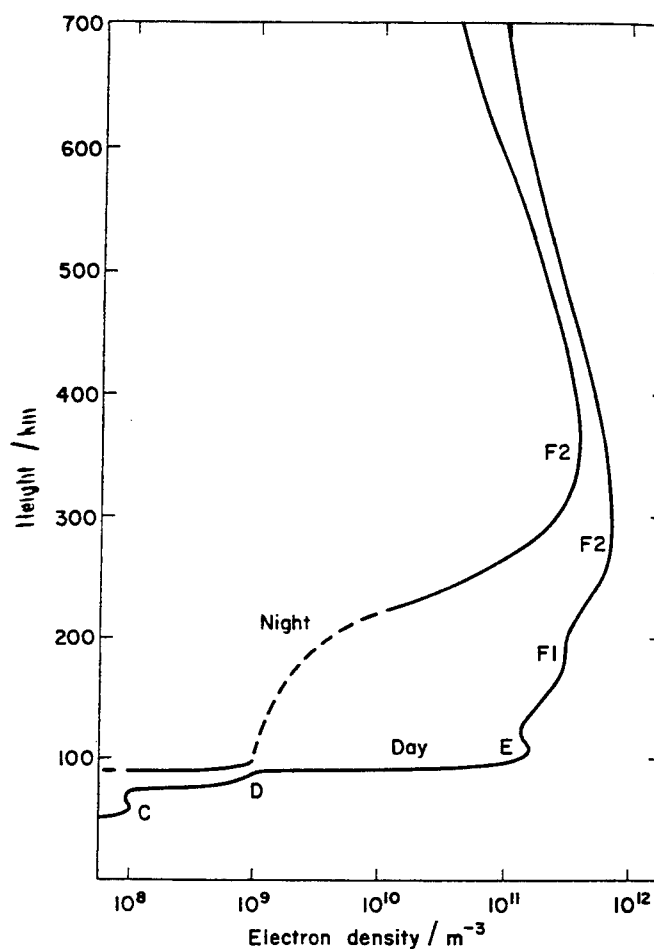
Vertical electron density distributions for typical conditions at mid-latitude. Above 95 km the data are from ground-based and topside observation, Wallops Is., Virginia, June 1968 (*after J. E. Jackson, Goddard Space Flight Center, Greenbelt, Maryland*). Below 95 km the data are from long-wave radio propagation data (Deeks, 1966). The distinct layer at around 65 km is often called the C layer.

Fig. 1. [Rishbeth, 1973]

The plasma frequency in radians, ω_{p_o}, is a function of the background electron density. The frequency in radians of the transionospheric signal is ω.

Eqn. 1 indicates, when $\omega = \omega_{p_o}$, the index of refraction is zero. The signal is reflected. The principle of Ionospheric sounding takes advantage of this feature. The frequency of the sounding signal is typically swept from .5 MHz to 20 MHz. For each respective signal frequency, the index of refraction takes values between one and zero. The time duration from transmitting to receiving is used to determine the virtual height of the reflection layer for a particular signal frequency. In the bottomside sounder experiment a sounding pulse is transmitted vertically from ground into the ionosphere. The reflection heights of the signals are recorded on an Ionogram where the trace denotes the dependence of the virtual height of the reflection layer verses signal frequency. The bell-like variation of the background electron density with respect to altitude, is determined from the Ionograms produced by topside and bottomside Ionosondes.

Therefore the index of refraction governs which signals can propagate through the ionosphere, and which will be reflected. Subsequently if the signal frequency, exceeds the peak plasma frequency, the signal propagates through the ionosphere. When $\omega \gg \omega_{p_o}$, the case for beacon signals, the index of refraction is approximated as,

$$n(\bar{r}) \cong 1 - \frac{1}{2}\frac{\omega^2_{p_o}(\bar{r})}{\omega^2} \qquad (2)$$

In the F region of the ionosphere, Ionosondes occasionally produce a diffused trace in the Ionogram, spread F. Spread F is caused by random fluctuations in the electron density, spread F irregularities, about the background density. In the presence of spread F irregularities a particular signal frequency does not return at a definite time. It is spread over a considerable time duration, indicating the signal is reflected from irregularities, and not a well defined height.

Unpredictable fluctuation of the electron density, ΔN, about the background density results in a corresponding fluctuation in the index of refraction, Δn, and consequently a fluctuation in the amplitude and phase of the transionospheric signal. The associated fluctuation of the index of refraction is given by

$$\Delta n(\vec{r}) = -\frac{1}{2}\frac{\Delta \omega^2{}_p(\vec{r})}{\omega^2} = -\frac{1}{2}\frac{\Delta N e^2}{\omega^2 \varepsilon_o m} \qquad (3)$$

Where $\Delta \omega^2{}_p = \omega^2{}_p - \omega^2{}_{p_o} = \Delta N e^2 / \varepsilon_o m$ and N_o is the background electron density. This perturbation to the transionospheric signal is further enhanced by the diffraction effect in free space and is termed scintillation. Currently, low orbiting satellites conduct high-resolution in-situ measurements of the relative density fluctuations about the background density along known satellite paths (e.g. Valladares et al.).

Recorded beacon scintillation data exhibits a fast oscillatory behavior, with respect to time, with low coherency. In order to extract useful information from the raw data, an averaged quantity called the scintillation index, S_4, is introduced. It is defined as the square root of the normalized variance in the received power. S_4 denotes the severity of the intensity scintillation. An understanding of the physical mechanisms responsible for scintillation and an ability to formulate a theory which characterizes the phenomenon are extremely important to many engineering problems such as, statistical signal fading, and channel modeling. Analysis of scintillation data provides information about the morphological structure, and changes in, the ionosphere.

Experimental observations, in situ and remote, indicate that the electron density in the ionosphere can be highly complex and irregular. Consequently, most scintillation theories consider the problem from a stochastic approach, where the randomness of the ionosphere is described in terms of statistical characteristics such as mean and autocorrelation.

Phase Screen and Rytov theories are applicable for weak scintillation. Weak scintillation occurs when the irregularity region is thin, or the fluctuation in electron density is small such that only the phase of the emerging signal is perturbed. On the other hand, strong scintillation occurs when the fluctuations in electron density is large and/or the irregularity layer is thick. The Parabolic Equation Method, PEM, is applicable for this case. The result of scattering within the irregularity region is to perturb both the amplitude and phase of the beacon signal [Yeh et al., 1982].

The Quasi-particle theory analyzes the effect of ionospheric irregularities on a transionospheric signal from either a stochastic approach [Wu and Marcuvitz, 1983], or a deterministic approach [Ho et al., 1994]. Similarly, it uses the wave equation as a starting point, as done for other stochastic based theories. The wave is, however, viewed as a distribution of particles in the $(\vec{r},\vec{k},t)$ space following a Wigner distribution function. Scattering of the signal by the irregularities is equivalent to the evolution of the quasi-particle distribution. This scheme makes use of the concept of wave-particle duality. Multiple scattering is an intrinsic feature of the derivation, and thus the theory is applicable for strong scintillation.

Experimental measurements have shown that the bottomside sinusoidal (BSS) irregularities can produce moderate to strong scintillation , S_4= 0.1 - 0.8, of a transionospheric signal at 250 MHz (Basu, 1986). Thus in this work, the Quasi-particle theory, based on the deterministic approach, is applied to study the effect of (BSS) irregularities on a transionospheric signal. This type of irregularity is characterized by "quasi-sinusoidal fluctuations" in the electron density about the background density for at least 7000 kilometers in the E-W direction. BSS irregularities occur for up to 300 minutes within a narrow belt approximately ±12 degrees from the dip equator on the bottomside of the equatorial F region of the ionosphere at night [Valladares et al., 1983].

FORMULATION

The wave characteristics including its amplitude and phase can be described by a joint distribution function of the position vector, $\vec{r}$, and the wavevector, $\vec{k}$, known as the **Wigner distribution function** which is defined to be

$$F(\vec{r},\vec{k},t) = \pi^{-2}\int d\vec{r}' \exp(2i\vec{k}\cdot\vec{r}')\psi^*(\vec{r}+\vec{r}',t)\psi(\vec{r}-\vec{r}',t) \qquad (4)$$

where ψ is a wave field component, and the integration is over all space where the field exists. The quasi-particle spatial density and spectral density can be obtained from the Wigner distribution function by the two relations $|\psi(\vec{r},t)|^2 = \int F(\vec{r},\vec{k},t)d\vec{k}$ and $|G(\vec{k},t)|^2 = \int F(\vec{r},\vec{k},t)d\vec{r}$, respectively.

Considering a modeled single-mode type wave equation expressed as

$$i\frac{\partial\psi}{\partial t} = -\left(\nabla^2 + k_0^2\varepsilon_1(\vec{r})\right)\psi \qquad (5)$$

where $\varepsilon_1(\vec{r}) = \varepsilon(\vec{r}) - \varepsilon_o = \varepsilon_{1r}(\vec{r}) + i\varepsilon_{1i}(\vec{r})$ is the perturbed dielectric function due to the presence of the density irregularities, $\varepsilon(\vec{r}) = 1 - \dfrac{\omega^2_p}{\omega(\omega+j\upsilon)}$, and $\varepsilon_o(\vec{r}) = 1 - \dfrac{\omega^2_{po}}{\omega(\omega+j\upsilon)}$ are the total and the unperturbed dielectric function of the ionospheric plasma, and υ is the electron-ion collision frequency, the corresponding transport equation of the Wigner distribution function is derived to be [Ho et al., 1994]:

$$\vec{k}\cdot\nabla F = -(k_0^2/\pi^2)\int d\vec{k}' F(\vec{r},\vec{k}')\int d\vec{s}\{\varepsilon_{1r}(\vec{r}-\vec{s})\sin\left[2(\vec{k}-\vec{k}')\cdot\vec{s}\right]$$
$$+\varepsilon_{1i}(\vec{r}-\vec{s})\cos\left[2(\vec{k}-\vec{k}')\cdot\vec{s}\right]\} \qquad (6)$$

The transport equation is exact for the stationary irregularities and governs the evolution of the quasi-particle distribution along the unperturbed wave trajectory.

In calculating the scintillation index $S_4^2 = [<\rho^2> - <\rho>^2] / <\rho>^2$, only the intensity distribution $\rho = |\psi(\vec{r}, t)|^2$ of the wave is needed, where the average is performed over a spatial period of the dominant BSS irregularity scale length. Thus, the moment equations of (6) are able to service the calculations. The first three moments of the quasi-particle distribution function are: the quasi-particles' number density, current density and energy density, which are defined respectively to be $\rho = \int d\vec{k} F(\vec{r}, \vec{k})$, $\vec{J} = \int d\vec{k} \vec{k} F(\vec{r}, \vec{k}) = \vec{k}_0 \rho + \vec{J}_1$, and $\underline{\underline{s}} = \int d\vec{k} \vec{k} \vec{k} F(\vec{r}, \vec{k}) = \vec{k}_0 \vec{k}_0 \rho + \vec{k}_0 \vec{J}_1 + \vec{J}_1 \vec{k}_0 + \underline{\underline{s}}_1$.

The transport equation (6) leads to a hierarchy of moment equations in the $\vec{r}$ space. Truncating the system of equations to the second moment, it results to

$$k_0 \frac{\partial}{\partial x} \rho + \nabla \cdot \vec{J}_1 = 0$$

$$k_0 \frac{\partial}{\partial x} \vec{J}_1 = \frac{k_0^2}{2} \rho \nabla \varepsilon_{1r} \qquad (7)$$

A three second sample of high-resolution BSS data obtained in situ by the low orbiting AE-E Satellite is shown in Fig. 2. The irregularity spectral maximum occurs near one kilometer scale length and decreases for scale lengths longer than one kilometer [Basu et al., 1986].
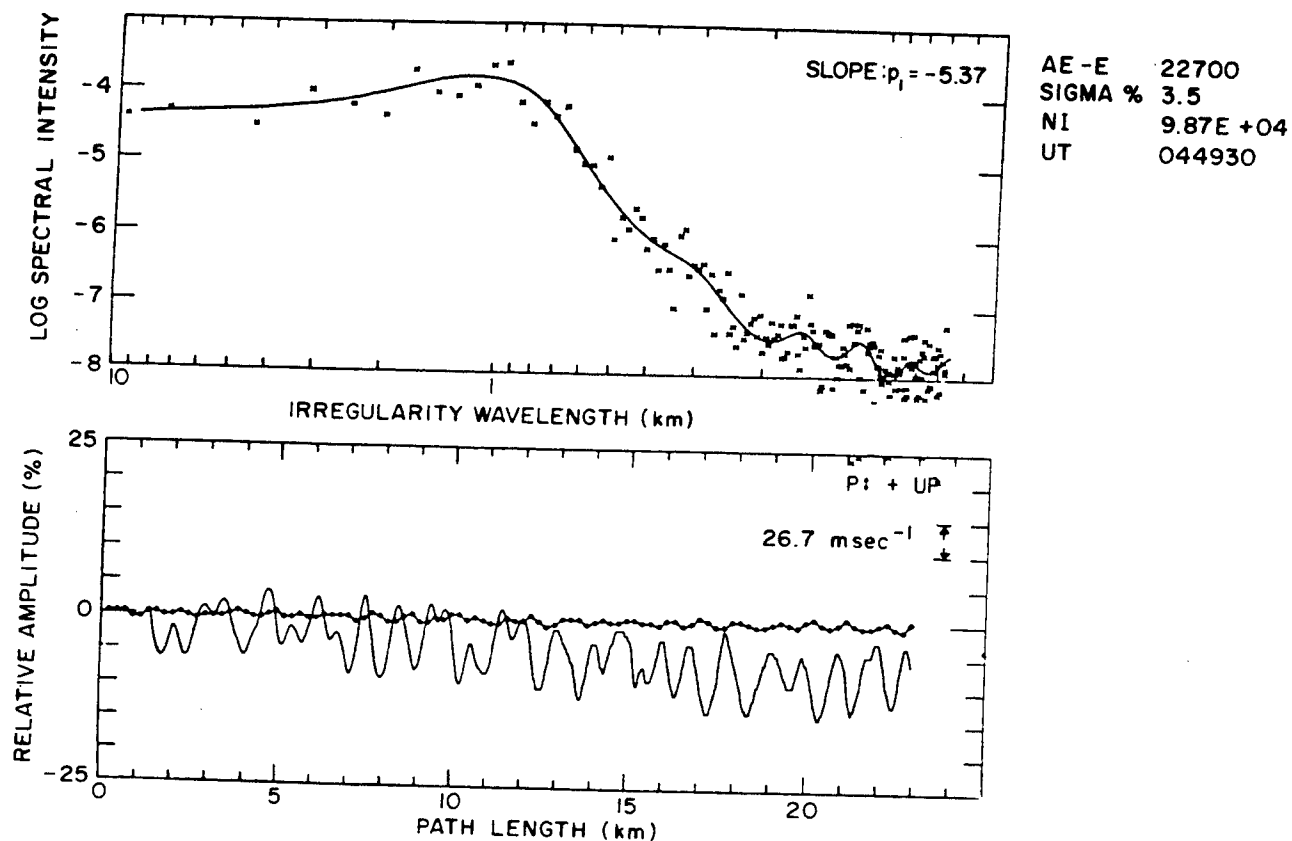
The bottom panel shows the fluctuations of ion density (solid curve) from the RPA during a 3-s interval starting at 0449:30 UT on December 11, 1979, and the pitch or vertical drift (curve with solid circles) from the ion drift meter. The top panel shows the FFT (crosses) and maximum entropy method (solid line) spectrum of ion density fluctuations. The percent irregularity amplitude (sigma), the background ion density (NI), and the power law index (slope) of the roll-off portion of the spectrum are indicated on the diagram. The satellite altitude was 440 km.

Fig. 2. [Basu et al., 1986]

The observed irregularity spectrum shown in Fig. 2, will be modeled analytically in order to specify the perturbed dielectric function $\varepsilon_1(\bar{r})$ in (7). The spectral representation capturing the BSS irregularities' characteristics, is a superposition of three functions, a rectangle, a gaussian and an exponential decay. Its expression is given by

$$\Delta N(k) = C_1 \left[U(k) - U(k - k_2) \right] + C_2 e^{\frac{-(k-k_2)^2}{2\Delta^2}} + C_1 e^{-\gamma(k-k_2)} U(k - k_2)$$

where $U(k)$ is the unit step function; the parameters C_1, C_2, Δ, and γ are chosen to match $\Delta N(k)$ with the observed spectrum as close as possible. The spatial representation, $\Delta N(\xi)$, was determined analytically by performing a one dimensional inverse Fourier Transform of $\Delta N(k)$. The spectrum from the model is shown in Fig. 3 for comparison with the measured spectrum of Fig. 2.

Log Spectral Intensity
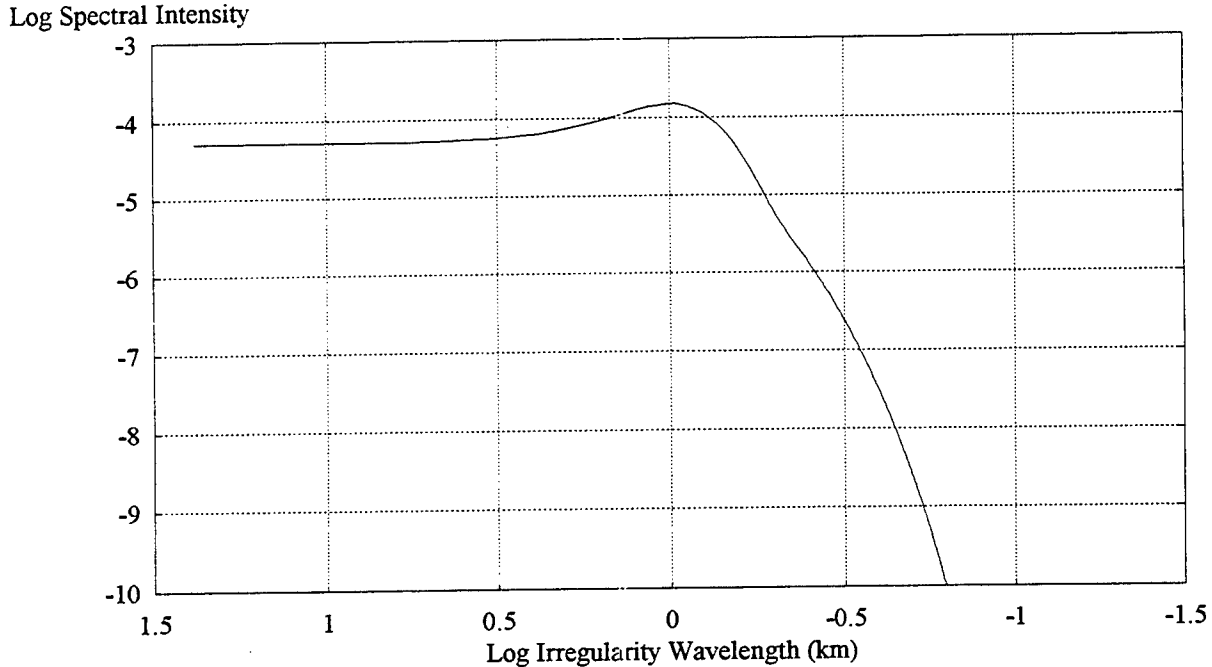
Fig. 3. Model of the Irregularity Spectrum

A beacon satellite signal enters the BSS irregularity layer at an angle as shown in Fig. 4.
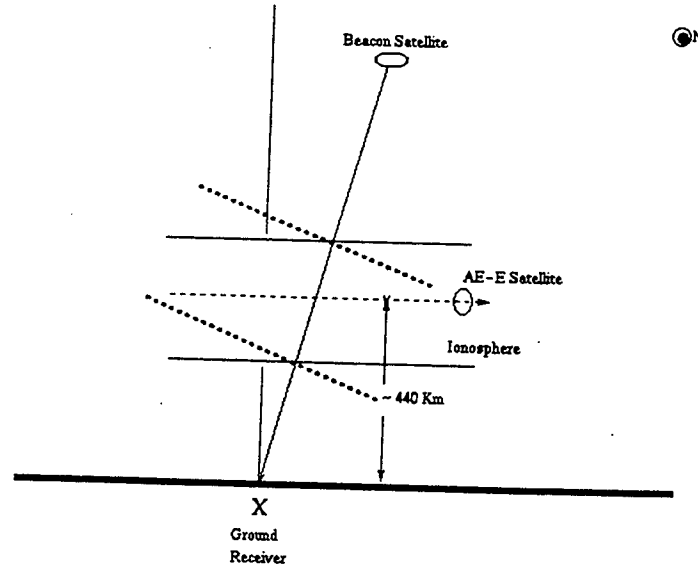
Fig. 4.

Generalizing the expression of the density perturbation, $\Delta N(\zeta)$, into a two dimensional distribution as

$$\Delta N(x,y) = P_\ell(x-\ell)\ \beta/(k_2 + \alpha + 1/\lambda)\ [\sin\eta/y\cos\theta +$$
$$\alpha e^{-(\Delta y\cos\theta)^2/2}\cos\eta + (\lambda\cos\eta - y\cos\theta\sin\eta)/(\lambda^2 + (y\cos\theta)^2)] \qquad (8)$$

where $k_2 = 2\pi/d_2$ and d_2 is the maximum spectral scale-length, α and λ are shaping parameters related to C_1, C_2, Δ and γ, $\eta = k_2\cos\theta(y + x\tan\theta)$, $\beta = \Delta N/N_o$ the percentage of density fluctuation, and the gate function $P_\ell(x-\ell)=1$ for $0\le x\le \ell$ and 0 otherwise, we can now consider the wave scattering within a layer of BSS irregularities, Fig. 5, showing a two dimensional spatial distribution. The layer is assumed to extend to infinity in the transverse direction and have a finite extent along the direction of propagation.
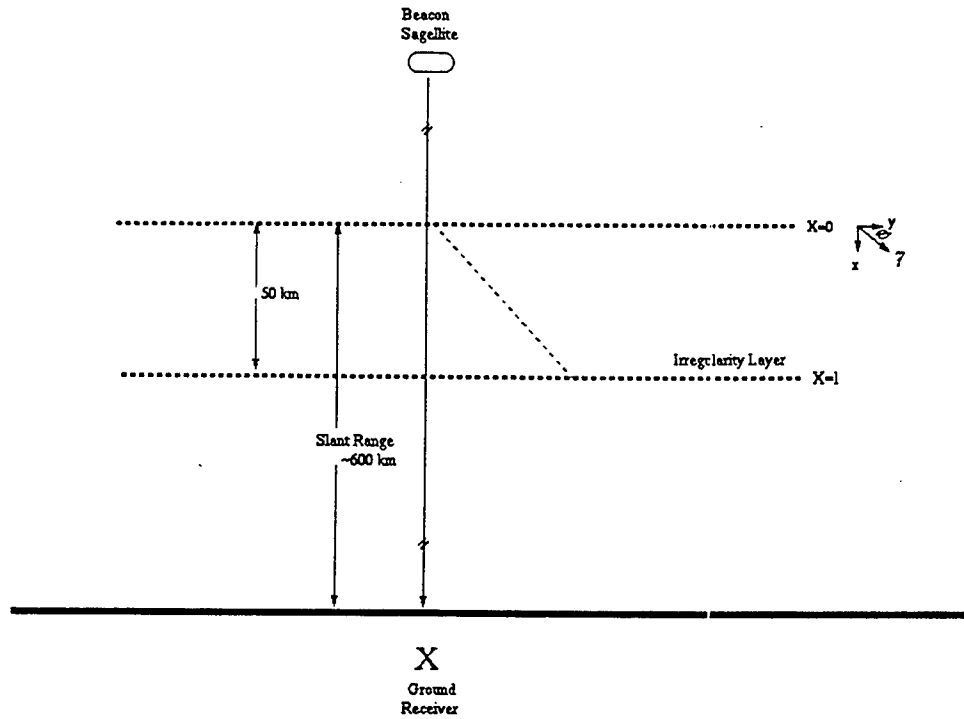
Fig. 5. Incoming plane wave scattered by a two dimension irregularity layer with thickness ℓ

NUMERICAL ANALYSIS

The moment equations are solved numerically to determine the effect of the BSS irregularities on the intensity of a transionospheric signal. The conditions and parameters are chosen in light of experimental observations. A favorable comparison between the numerical results and experimental observations validates the irregularity model and demonstrates the capability of the theory for handling strong scintillation. The theory is aimed not only for explaining the existing irregularities, but also for planning future experiments.

Presented in Figs. 6 and 7, are the dependence of S_4 on propagation distance, with the angle of incidence as a parameter, for signal frequencies of 250 MHz and 350 MHz

respectively. The first part of the curves, up to 50 km, is illustrative of the effect of the BSS irregularities on the beacon signal, followed by diffraction effects in free space. In Fig. 6, the values of S_4 agree with observed values lying in the range $S_4=0.1$-0.8 [Basu et al., 1986]. Fig. 7 shows that the scintillation index decreases with the beacon signal frequency. The dependence of S_4 on beacon signal frequency is further illustrated in Fig. 8.

Presented in Fig. 9 is the dependence of S_4 on the percentage of density fluctuation. The curve shows that S_4 increases with the density fluctuation as shown by observational results.
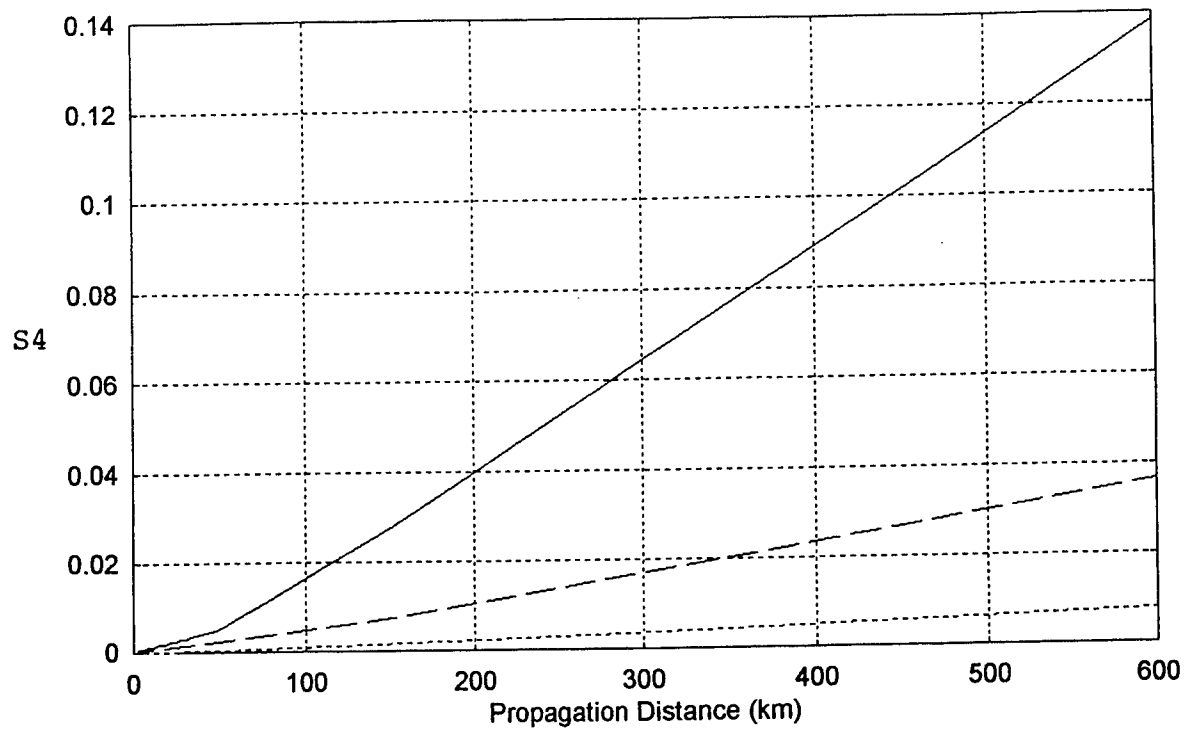
Fig.6. S_4 versus the propagation distance for θ=10 (solid line), 20 (dashed line) and 60 (dotted line) degrees, with β=3.5% and the beacon signal frequency equal to 250 MHz.
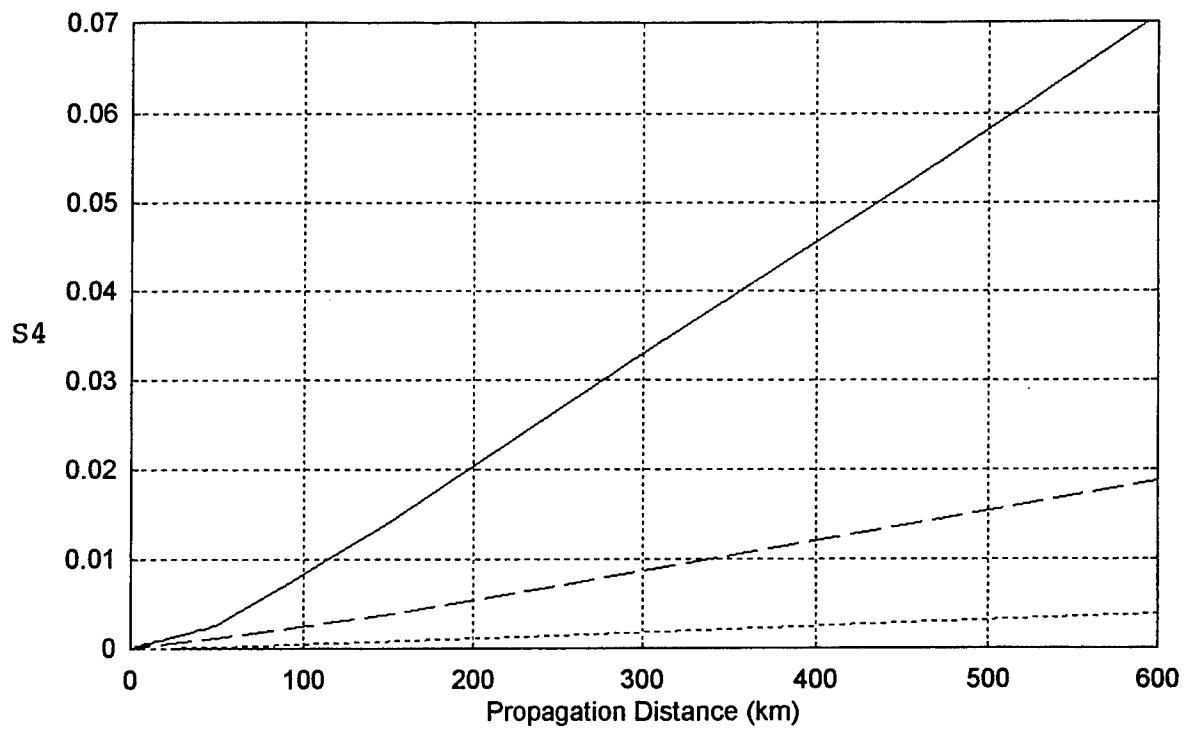
Fig.7. S_4 versus the propagation distance for θ=10 (solid line), 20 (dashed line) and 60 (dotted line) degrees, with β=3.5% and the beacon signal frequency equal to 350 MHz.
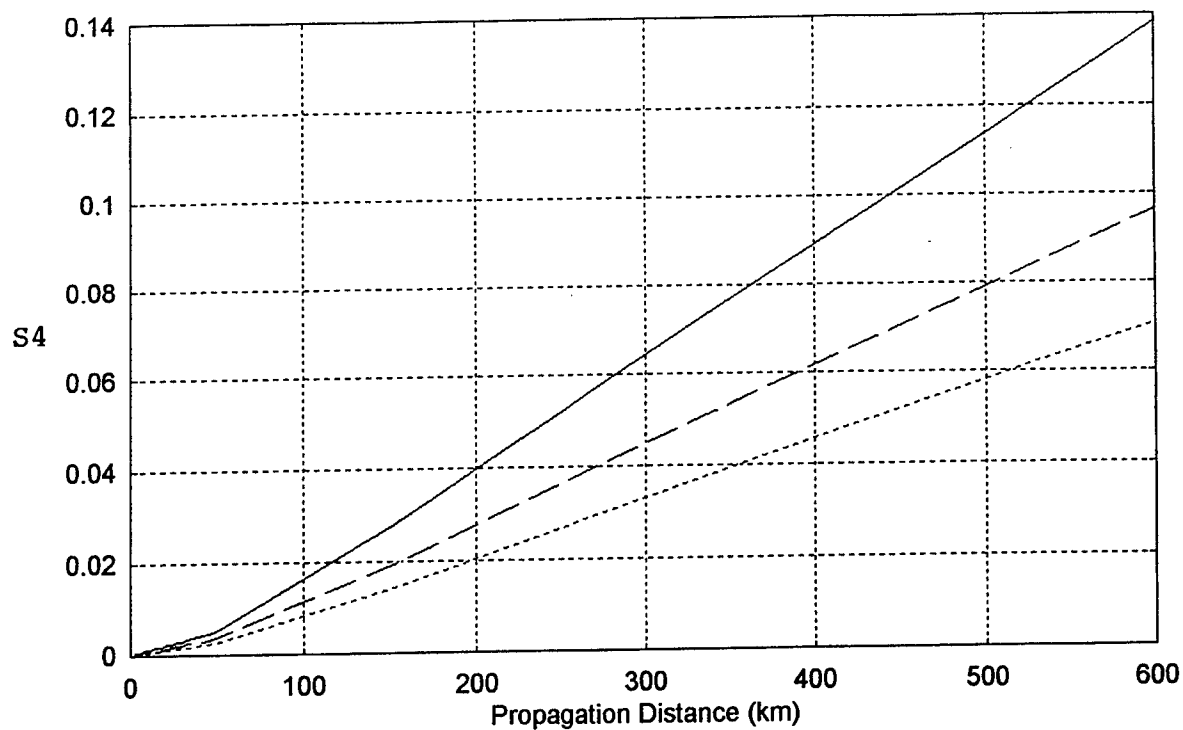
Fig.8. S_4 versus the propagation distance for the beacon signal frequency equal to 250 Mhz (solid line), 300 MHz (dashed line), and 350 MHz (dotted line) with θ=45 degrees, and β=10%.
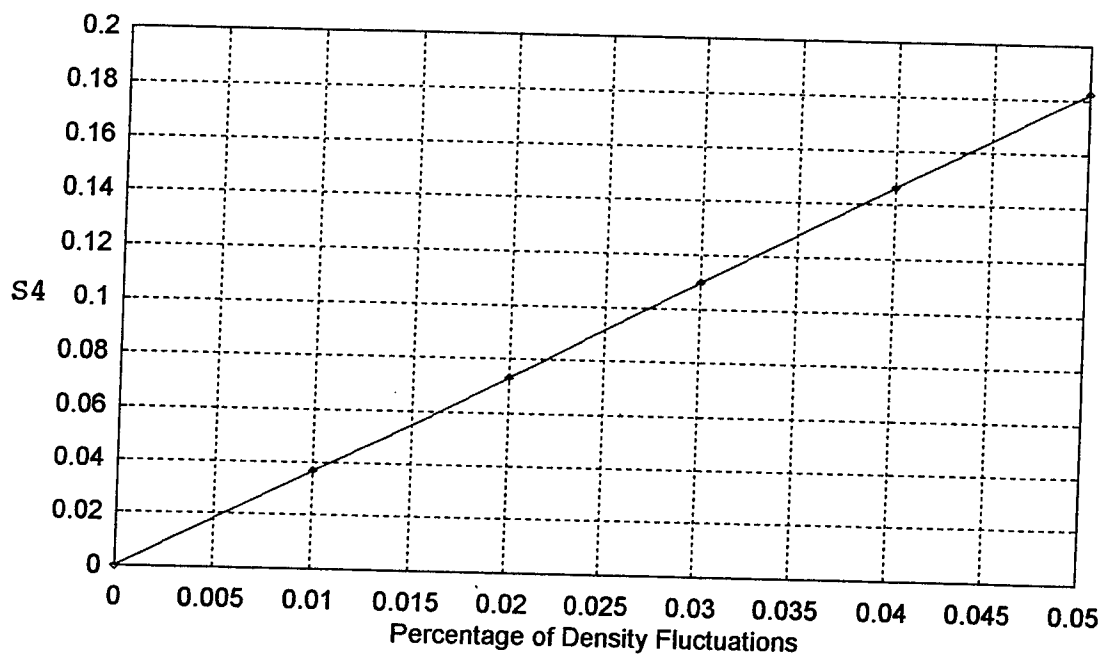
Fig.9. S_4 versus β with θ=10 degrees, at a propagation distance of 500 km and a beacon signal frequency equal to 250 MHz.

ACKNOWLEDGMENTS:

The author is extremely thankful to her thesis advisor, Professor S. Kuo, for his guidance and commitment to excellence.

The author extends sincere thanks to the entire Ionospheric Effects Division at Phillips Laboratory, Hanscom AFB. She is especially grateful to Dr. Basu, and Dr. Weber, for useful discussions, and to Dr. Valladares for providing experimental data.

The author is also grateful to Dr. Joe Huang of Polytechnic University for many useful discussions. This work is supported by the AFOSR.

REFERENCES

Basu, S., Eilleen Martin MacKenzine, Su. Basu, E. Costa, P. Fougere, H. C. Carlson, Jr., H. E. Whitney, 250MHz/GHz Scintillation Parameters in the Equatorial, Polar, and Auroral Environments, IEEE Journal on selected areas in Communications, SAC-5(2), 102-115, 1987

Basu, S., Su. Basu, C. E. Valladares, A. Dasgupta, and H. E. Whitney, Scintillations Associated With Bottomside Sinusoidal Irregularities in the Equatorial F region, J. Geophys. Res., 91(A1), 270-276, 1986.

Bremmer, H., General remarks concerning theories dealing with scattering and diffraction in random media, Radio Sci., 8(6), 511-534, 1983.

Briggs, B. H., Ionospheric Irregularities and Radio Scintillations, Contemp. Phys., 16(5),469-488,1975.

Crane, R.K., Ionospheric Scintillation, Proc. IEEE,65(2),180-199, 1977.

Ho, Antony Y., S. P. Kuo, and M. C. Lee, Analysis of Electromagnetic Wave Scattering by Ionospheric Irregularities, Radio Sci., 29(5), 1179-1186, 1994.

Kelley, M., "The Earth's Ionosphere", International Geophysic Series, Accademic Press, vol. 43, ch.1, 1989.

Rishbeth, H., Physics and Chemistry of the Ionosphere, Contemp. Phys., 14(3), 229-249,1973.

Valladares, C. E., W. B. Hanson, J. P. McClure, and B. L. Cragin, Bottomside Sinusoidal Irregularities in the Equatorial F Region, J. Geophys. Res., 88(A10), 8025-8042, 1983

Wu, D. M., and N. Marcuvitz, Ionospheric scintillations, Radio Sci., 18(4), 589-607, 1983.

Yeh, K., and C. Liu , Radio Wave Scintillations in the Ionosphere, Proc. IEEE, 70(4), 324-259, 1982

COLLISION AVOIDANCE ALGORITHM
FOR SPICE

Dwayne E. McDaniel
Graduate Student
Department of Aerospace, Engineering Mechanics, and Engineering Science

University of Florida
231 Aerospace Building
Gainesville, FL 32611

COLLISION AVOIDANCE ALGORITHM
FOR SPICE

Dwayne E. McDaniel
Graduate Student
Department of Aerospace, Engineering Mechanics, and Engineering Science
University of Florida

Abstract

The Space Integrated Controls Experiment (SPICE) requires the utilization of six linear actuators and six magnetic bearings to drive a six-thousand pound mock-up of a space-based-laser in six degrees-of-freedom. The linear actuators, which do not have fixed lines-of-action, are often required to move through large angles of rotations. Possible contact points between the linear actuators and the test article were studied and an algorithm was developed to determine the minimum distance between each linear actuator and the test article. The algorithm is installed into the computers control software and is designed to terminate operations if the distance between the linear actuators and the test article is too small.

COLLISION AVOIDANCE ALGORITHM
FOR SPICE

Dwayne E. McDaniel

Introduction

The Space Integrated Controls Experiment (SPICE) is an extension of the Space Active Vibration Isolation (SAVI) program. SAVI's objectives were to provide vibration isolation and perform retargeting maneuvers of a mock-up of the front end of a space-based-laser. The vibration isolation and retargeting maneuvers are done through the use of six linear actuators and six magnetic bearings. Figure 1 provides a general picture of the setup for SAVI. The forward body, or test article, is a graphite-epoxy Cassagrin beam expander on which is mounted a dummy segmented primary mirror and a dummy secondary mirror. The aft body is a structure used to represent the host body of the laser generator and is a primary vibration source. Specifications for the retargeting maneuvers require that the beam expander rotate plus or minus two degrees about any axis through its center of gravity. It is through such large rotations that provisions for collision avoidance needs to be addressed.

As seen in Figure 1, the forward body is attached to the Intermediate Gimbal Structure (IGS) via the magnetic bearings. The IGS is attached to the aft body via the linear actuators. When large motions of the beam expander are required, the possibility of collisions is at a maximum between the linear actuators and the three corner pieces of the IGS. In this paper an algorithm, which calculates the minimum distance to touch between the IGS and the linear actuators, is developed and installed into the computer's control software The software is programmed to shutdown operations if the minimum distances reaches a specified value.

Methodology

The calculation of the minimum distance between the linear actuators and the IGS is first formulated as a simple multibody dynamics problem. The bodies of concern are the aft body and
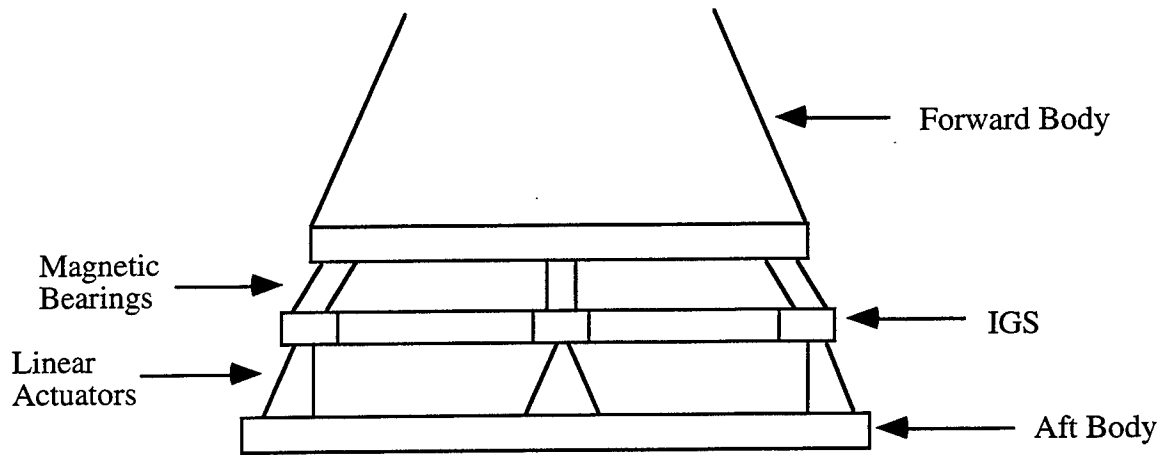
Figure 1

the IGS, which can move in six degrees-of-freedom with respect to the aft body. The information available for the linear actuators is shown if Figure 2. Here, the two frames of reference, F^I and F^H, are the aft body reference frame and the IGS reference frame, respectively. The vector $\underline{V}^I_{OB}$ locates the origin of F^H with respect to F^I and the orientation of F^H with respect to F^I is given by

$$F^H = T^{H/I} F^I \tag{1}$$

where $T^{H/I}$ is a 3x3 rotation matrix. Vector $\underline{V}^I_{OA}$ locates the attachment point of the linear actuator to the aft body in F^I and $\underline{V}^H_{BC}$ locates the attachment point of the linear actuator to the IGS in F^H. For this system, the vectors $\underline{V}^I_{OB}$, $\underline{V}^I_{OA}$, $\underline{V}^H_{BC}$ and the matrix $T^{H/I}$ are known. Note that the superscript on the vectors indicates which frame of reference they are coordinatized in.

The possible contact points between a linear actuator and the IGS are actually a line representing a side of a hole cut out from the lower panel of the IGS corner piece. The problem can then be restated as, "What is the minimum distance between two lines, where one line represents a linear actuator and the second line represents the line of concern on the lower panel of the IGS corner piece?" To properly define the two lines, two vectors locating two points on each line are required. From Figure 2, points A and C are used to define a linear actuator. Points D and E, whose locations are explained in the next paragraph, will be used to define the line of concern on the lower panel of the IGS. Note that point A is fixed in F^I and points C, D, and E are fixed in F^H.

14-4
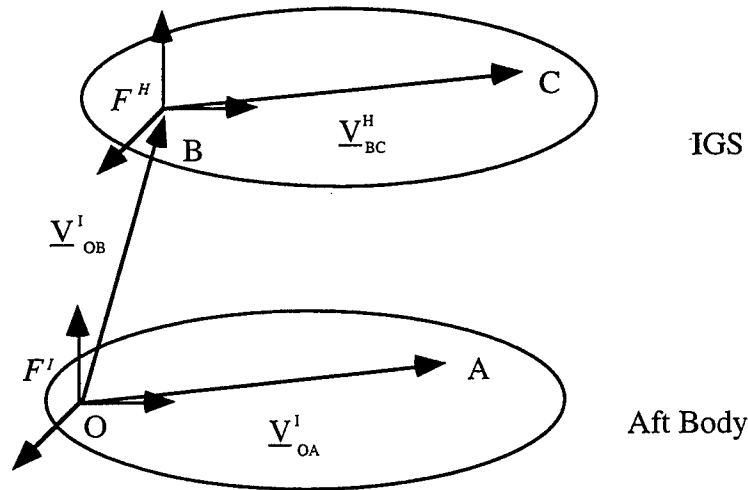
Figure 2

Information locating points D and E on the IGS is not given and has to be obtained. Since the location of the linear actuator/IGS attachment points are known ($\underline{V}^H{}_{BC}$), the location of the points D and E on the IGS in F^H may be determined by

$$\underline{V}^H{}_{BD} = \underline{V}^H{}_{BC} + \underline{V}^H{}_{CD} \qquad\qquad (2)$$

$$\underline{V}^H{}_{BE} = \underline{V}^H{}_{BC} + \underline{V}^H{}_{CE} \qquad\qquad (3)$$

where $\underline{V}^H{}_{BD}$ and $\underline{V}^H{}_{BE}$ are the locations of points D and E on the IGS, $\underline{V}^H{}_{BC}$ is defined above, and $\underline{V}^H{}_{CD}$ and $\underline{V}^H{}_{CE}$ are the vectors from the linear actuator/IGS attachment point to points D and E on the IGS. $\underline{V}^H{}_{CD}$ and $\underline{V}^H{}_{CE}$ can be determined from measurements obtained from the magnetic bearing and IGS blue prints.

The procedure for the minimum distance calculation is quite simple. The two vectors representing the line segments are crossed to form a perpendicular vector. The new vector is then normalized and dotted with a different line vector defined by using one point on each of the original lines. The resulting scalar is the minimum distance between the two original line segments. This procedure is shown in greater detail below for the SPICE structure.

The first step is to coordinatize all the appropriate vectors into one coordinate frame. I chose to do all calculations in F^H, thus, $\underline{V}^I{}_{OA}$ and $\underline{V}^I{}_{OB}$ are transformed into F^H.

$$\underline{V}^H{}_{OA} = T^{H/I}\underline{V}^I{}_{OA} \qquad\qquad \underline{V}^H{}_{OB} = T^{H/I}\underline{V}^I{}_{OB} \qquad\qquad (4)$$

The vectors $\underline{V}^H{}_{AC}$ and $\underline{V}^H{}_{DE}$ are then generated using the following equations

$$\underline{V}^H{}_{AC} = \underline{V}^H{}_{BC} - \underline{V}^H{}_{BA} = \underline{V}^H{}_{BC} - (\underline{V}^H{}_{OA} - \underline{V}^H{}_{OB}) \tag{5}$$

$$\underline{V}^H{}_{DE} = \underline{V}^H{}_{BE} - \underline{V}^H{}_{BD} \tag{6}$$

The perpendicular of $\underline{V}^H{}_{AC}$ and $\underline{V}^H{}_{DE}$, $\underline{P}^H$, is obtained by using the cross product

$$\underline{P}^H = \underline{V}^H{}_{AC} \times \underline{V}^H{}_{DE} \tag{7}$$

and $\underline{P}^H$ can then be normalized to give $\underline{p}^H$. The last vector required is a line connecting one point on line AC and one point on line DE. Here, $\underline{V}^H{}_{CE}$ is used but $\underline{V}^H{}_{CD}$, $\underline{V}^H{}_{AE}$ or $\underline{V}^H{}_{AD}$ would have done just as well. $\underline{V}^H{}_{CE}$ is obtained by

$$\underline{V}^H{}_{CE} = \underline{V}^H{}_{BE} - \underline{V}^H{}_{BC} \tag{8}$$

The distance, S, can be calculated by dotting $\underline{V}^H{}_{CE}$ with $\underline{p}^H$. A last measure is required to account for the radius of the actuator piston and an LVDT sensor which runs parallel to the piston. The scalar distance from the line-of-action of the piston to the farthest side of the LVDT is subtracted from S to give the minimum distance to touch between the IGS and the LVDT sensor.

Results

As mentioned previously, SPICE utilizes six linear actuators. Thus, at every specified time step, the computer software will calculate a minimum distance for each of the six linear actuators. Two important inputs to the software include the quantities $\underline{V}^H{}_{BD}$ and $\underline{V}^H{}_{BE}$ for each of the six actuators. Recall from Eqns.(2-3) that these quantities require values for $\underline{V}^H{}_{CD}$ and $\underline{V}^H{}_{CE}$ which are obtained from blue prints. Values obtained for $\underline{V}^H{}_{BD}$ and $\underline{V}^H{}_{BE}$ are shown in the tables below. Note that the distances are in meters.

Actuator #	X-Coordinate	Y-Coordinate	Z-Coordinate
1	0.3658	3.4667	0.4805
2	-0.3658	3.4667	0.4805
3	-3.1852	-1.4165	0.4805
4	-2.8194	-2.0501	0.4805
5	2.8194	-2.0501	0.4805
6	3.1852	-1.4165	0.4805

Table 1 - $\underline{V}^H{}_{BD}$

14-6

Actuator #	X-Coordinate	Y-Coordinate	Z-Coordinate
1	0.3658	3.396	0.452
2	-0.3658	3.396	0.452
3	-3.1239	-1.3812	0.452
4	-2.7582	-2.0148	0.452
5	2.7582	-2.0148	0.452
6	3.1239	-1.3812	0.452

Table 2 - $\underline{V}^H_{BE}$

Utilizing the values obtained for $\underline{V}^H_{BD}$ and $\underline{V}^H_{BE}$, the algorithm then calculates the minimum

distance to touch for each actuator. As a test case, the actuators were all placed at four inches

below their mid-stroke. Results of the calculations and the measured (approximate) values are

shown below in Table 3. Values are displayed in inches.

Actuator #	Distance to Touch	
	Algorithm	Measured
1	3	3
2	3	2.75
3	3	3
4	3	2.75
5	3	3
6	3	2.75

Table 3

The values from the algorithm agree with what one might expect when the pistons are displaced

equal distances. This is in contrast with the measured values, which are only slightly off but give

the impression that the structure has a slight rotation about its vertical axis. Measurements made at

other various actuator configurations give similar results. It should be noted that the actual

measurements were unavoidably crude and should be treated as approximate values.

Conclusions

A computer algorithm was developed to determine the minimum distance between

SPICE's linear actuators and IGS. Results indicate that a relatively small error does exist, but the

reason for the error is unknown. Symmetric displacements of the actuator pistons should and do

result in equal minimum distances from all six actuators. The slight discrepancy between the measured and calculated values is not understood and should be investigated further.

References

Blankinship, Breakwell, Ninneman, "Space Integrated Controls Experiment (SPICE)", Phillips Laboratory.

Blankinship, Hamilton, Richardson, "The Spice Program", Phillips Laboratory.

Honeywell Inc., "Space Active Vibration Isolation (SAVI), Option Phase Final Report", Phillips Laboratory Contract Number F29601-85-R-0132.

Spiegel, Mathematical Handbook of Formulas and Tables, McGraw-Hill Inc., 1968.

PASSIVE MODULATION OF IODINE LASERS AT GIGAHERTZ FREQUENCIES

Jeff Nicholson
Graduate Student
Department of Physics and Astronomy

The University of New Mexico
800 Yale Blvd. NE
Albuquerque, NM 87131

PASSIVE MODULATION OF IODINE LASERS AT GIGAHERTZ FREQUENCIES

Jeff Nicholson

Graduate Student

Department of Physics and Astronomy

The University of New Mexico

Albuquerque, NM 87131

Abstract

A photolytic iodine laser is shown to have a 13.59 GHz modulation in the laser radiation when simultaneous lasing of two hyperfine transitions is obtained. The necessary gain tuning required to achieve dual line lasing is accomplished through the use of a magnetic field. In addition, we investigate the possibility of using a nonlinear mirror to increase the gain coupling between the two transitions.

PASSIVE MODULATION OF IODINE LASERS AT GIGAHERTZ FREQUENCIES

Jeff Nicholson

Gas lasers have received attention because of their ability to operate at very high cw power levels with good beam quality and possess an active media that is not as susceptible to damage as solid state materials. One example of high power gas lasers, the Chemical Oxygen Iodine Laser (COIL), has been shown to operate at power levels as high as 40 kW [1].

Modulation of these high power lasers at gigahertz frequencies is desirable. Not only does one obtain higher peak intensities in a modulated laser beam, but one can think of a gigahertz modulated laser beam as a radar wave with an optical carrier. Thus, one can envision producing a radar signal that propagates with the qualities of a coherent optical wave. Modulating a laser at gigahertz frequencies with active elements is difficult because of the high bandwidth requirements. In addition, the high intracavity powers of, for example, COIL, impose extreme damage threshold requirements on intracavity elements. An alternative is to force the laser to operate on two transitions of atomic iodine simultaneously. If the radiation in the two transitions is temporally coherent, the intensity of the laser will be modulated at a frequency equal to the frequency separation of the two transitions.

An iodine laser operates on the $^2P_{1/2} -^2 P_{3/2}$ magnetic dipole transition of atomic iodine, with a wavelength of 1.315 μm (see Fig. 1). The strongest of its six hyperfine transitions, and the one that typically lases is the $F' = 3$ to $F'' = 4$. The gain of the second strongest transition, the $F' = 2$ to $F'' = 2$, is more than twice as small as that of the 3-4. The two transitions are separated by 13.59 GHz.
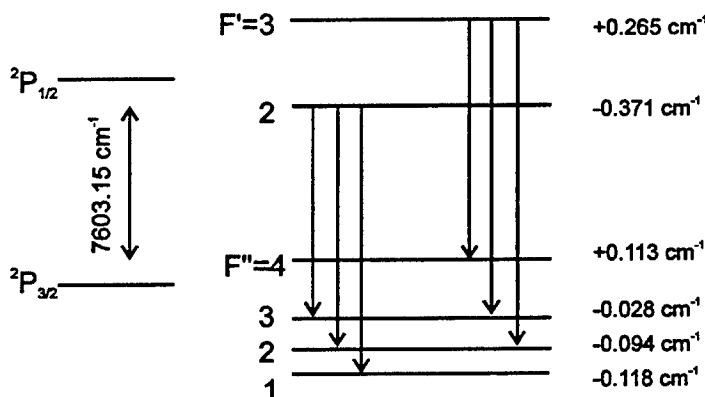

Figure 1: *Energy levels and allowed transitions of atomic iodine.*

Applying a magnetic field to atomic iodine causes Zeeman splitting of the energy levels, removing their
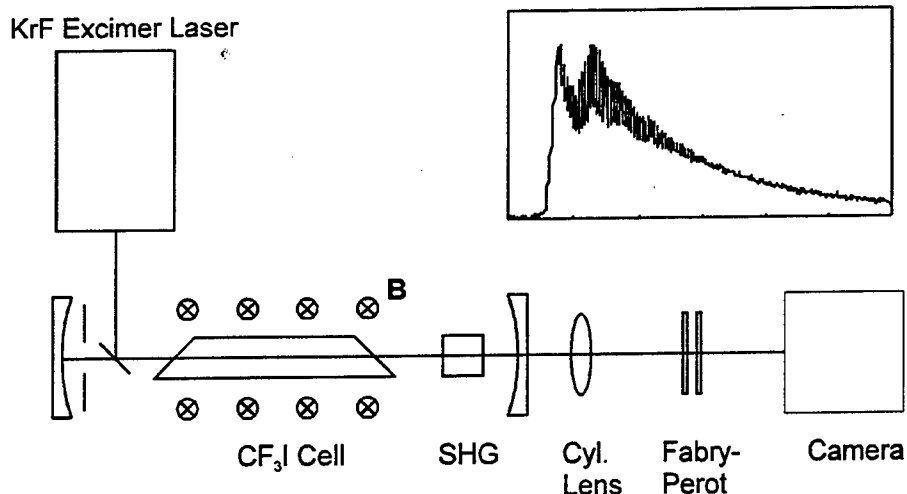
Figure 2: *The experimental setup. Inset: a typical gain-switched iodine pulse showing longitudinal mode beating.*

degeneracies. For small magnetic fields ($<$ kilogauss) the frequencies of the hyperfine transitions are not shifted significantly [2]. For this reason, the transitions are still referred to as the 3-4 and 2-2 transitions, even under the influence of a magnetic field. The gain of the two transitions can be equalized by applying a magnetic field of approximately 350 Gauss perpendicular to the polarization of the laser. [3] With a smaller magnetic field, the 3-4 transition dominates, with a stronger field, the 2-2. Thus the gain of the two transitions can be equalized without the use of intracavity elements.

In this paper, we show the beating that results from the simultaneous lasing of the 2-2 and 3-4 transition in an iodine laser. The experiments were performed with a photolytic iodine laser, a convenient tool for performing small scale experiments which can later be scaled up to the high power COIL. A sketch of the experiment is shown in Fig. 2. The laser consisted of a cell of CF_3I at 8 Torr pumped by a KrF excimer laser producing 250 mJ in 20 ns pulses at 248 nm. As a result of the photolysis at 248 nm, CF_3I dissociates into CF_3 and iodine. 92% of the iodine is produced in the excited state (I^*) [4].

An aperture in the cavity forced oscillation on a single transverse mode. Because the room temperature Doppler width of atomic iodine is approximately 250 MHz [5] and the free spectral range of the cavity was 150 MHz, the laser operated on either one or two longitudinal modes. A typical gain switched pulse is shown in the inset of Fig. 2. The fast beating shown, with a period of approximately 6 ns, is longitudinal mode beating.

A set of ferrite ceramic permanent magnets was used to apply a magnetic field to the gain cell perpendicular to the polarization of the laser. The strength of the magnetic field was tuned by varying the distance between the magnets and the gain cell. This produced a magnetic field of up to a kilogauss that varied less then 10% over the mode volume of the iodine laser.

The single shot spectrum of the iodine pulse was measured with Fabry-Perot interferometer. The free-
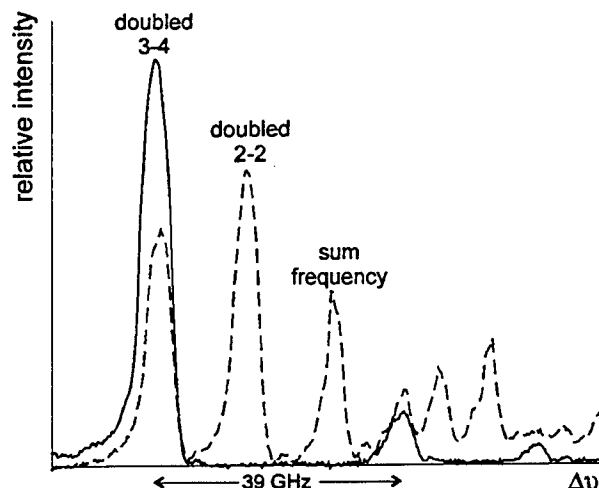
Figure 3: *Fabry-Perot fringes without magnetic field (solid line) and with a 400 G magnetic field (dashed line) applied to the active medium.*

spectral-range of the Fabry-Perot was 39 GHz, and the resolution was approximately 2 GHz at 1.315 μm. Therefore, while the interferometer was capable of distinguishing the hyperfine transitions, it was not able to resolve individual longitudinal modes. A cylindrical lens was used to focus into the Fabry-Perot and produce line fringes.

A streak camera was used to time resolve the iodine laser pulses. When used in conjunction with the Fabry-Perot interferometer, the streak camera was able to time-resolve the spectral content of the laser pulse. This provided details about the temporal overlap of the two different hyperfine transitions.

Because the cameras were not sensitive in the infrared, second harmonic generation was used to frequency double the laser radiation to 657.5 nm. Both intracavity and extra-cavity doubling was investigated. Extra-cavity doubling had the advantage of ease of alignment. Placement of the crystal in the cavity, however, becomes important when considering the effect of the nonlinear crystal in conjunction with the laser resonator outcoupler to create the nonlinear mirror as expalined below.

Fig. 3 shows the Fabry-Perot fringes obtained from the interferometer. The solid curve shows the fringes due to the 3-4 line when there was no magnetic field on the gain cell. The dotted curve shows the fringes obtained when a magnetic field of approximately 400 Gauss was applied to the gain cell, perpendicular to the laser oscillation. Two-line lasing is clearly visible. Because of the second harmonic generation, the doubled 2-2 line appears 27 GHz below the doubled 3-4 line. The sum frequency occurs halfway between the doubled 3-4 and 2-2 lines.

The temporal dependence of the two laser lines for two typical pulses is shown in Fig. 4. The solid curves show the 3-4 line and the dashed curves the 2-2. In Fig. 4a, the 3-4 transition shows beating from multiple longitudinal modes, whereas the 2-2 transition has only a single longitudinal mode. In contrast, both the
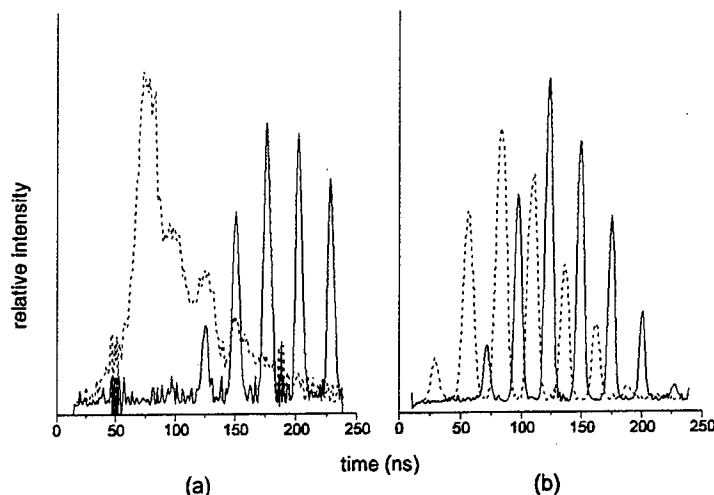
Figure 4: *Temporal dependence of the 3-4 (solid line) and the 2-2 (dashed line) transitions as measured by the streak camera for two different laser pulses.*

3-4 and the 2-2 transitions show longitudinal mode beating in Fig. 4b. Fig. 4 illustrates an inherent problem in producing the desired 13.6 GHz modulation. In order to have a maximum depth of modulation over the entire length of the laser pulse, the two frequencies must overlap temporally and be of equal intensity. In Fig. 4a, the temporal overlap of the 3-4 and 2-2 is only partial. In the case of Fig. 4b, even though the envelopes of the two transitions overlap, longitudinal mode beats in each of the transitions do not. Therefore, this pulse would not show a substantial spectral component at 13.6 GHz.

When the 3-4 and 2-2 transitions have a temporal overlap, and the pulse is viewed with a fast streak camera with a resolution of 5 ps, a clear 13.6 GHz modulation is observed, as is shown in Fig. 5. This data was taken with the second harmonic generation performed extra-cavity.

While the 13.6 GHz modulation is observed without any extra coupling between the 3-4 and 2-2 transitions, the shot to shot variation in the overlap of the two transitions is large. Although the 2-2 and the 3-4 transitions do not share any energy levels (see Fig. 1), there is fast relaxations among the upper and lower hyperfine levels that tends to equalize the populations. Population in the upper hyperfine levels is equalized through collisions with ground state iodine and can take place with a time constant on the order of tens of nanoseconds; relaxation among the lower hyperfine levels proceeds more directly through collisions with any species in the gain cell, and has a time constant of a few nanoseconds [6]. If the gain of the two transitions is not exactly equal, the stronger will build up first, and collisional relaxations will remove the population from the weaker, effectively decreasing the gain of the weaker transition even further. Any small change in the magnetic field away from the crossing point in the gain of the transitions leads to one of the transitions dominating over the other [7]. For this reason an additional coupling between the transitions is desirable.

The possibility of using a nonlinear mirror to equalize the gain of the two transitions was investigated. A
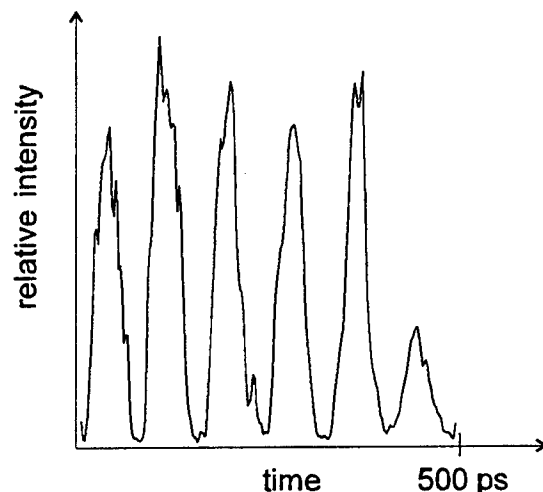
Figure 5: *Intensity profile of the laser pulse showing the Gigahertz hyperfine mode beating.*

schematic of the mirror is shown in the inset of Fig. 6. Such a mirror was first used to modelock a Nd:YAG laser [8]. The nonlinear mirror consists of a second harmonic crystal, and a dichroic mirror as the outcoupler for the resonator. Typical reflectivities for the outcoupler are 90% for the fundamental frequency and 100% for the second harmonics. The distance between the mirror and the second harmonic crystal is such that the difference in the index of refraction for fundamental and sum frequencies introduces a π phase change between the two upon re-entrance into the crystal. The π phase change means that after converting IR to red in the first pass through the nonlinear crystal and reflecting off the outcoupler, the red is converted back to IR in the second pass through the crystal.

A computer simulation was developed in order to investigate the degree of effective gain coupling possible with the nonlinear mirror. The gain media was simulated with rate equations, and the nonlinear mirror with coupled wave equations. Results from this simulation are shown in Fig. 6. The solid lines show the temporal dependence of the 2-2 and 3-4 transitions when there is no nonlinear crystal in the cavity and the gain cross section of the 2-2 transition is 90% of the 3-4 transition. The dashed lines show the profiles when the crystal is placed in the cavity. In both cases, the smaller pulse is the 2-2 and the larger is the 3-4. The case with the nonlinear mirror shows a relative increase in the 2-2 profile with at the expense of the 3-4, demonstrating the coupling ability of the nonlinear mirror.

In conclusion, we have demonstrated an intrinsic gigahertz modulation that occurs in an atomic iodine laser. The gain of two different hyperfine transitions can be equalized through the use of a magnetic field, allowing them to lase simultaneously and beat together. Additional coupling of these transitions is desired to achieve consistent operation and can be achieved through a nonlinear mirror based on intracavity sum frequency generation.

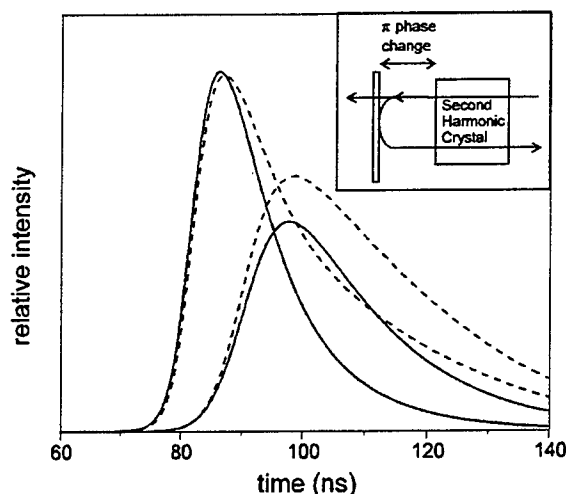The authors would like to thank Dr. Harold Miller for helpful comments.

Figure 6: *Simulation of the nonlinear mirror. Solid curves are the 2-2 and 3-4 (stronger) transitions without the nonlinear mirror. Dashed curves are with the nonlinear mirror. The inset shows a schematic of the mirror. Reflectivities for the dichroic outcoupler are 90% for the IR and 100% for the red.*

References

[1] K. A. Truesdell, S. L. Lamberson, and G. D. Hager, "A history of COIL in the U.S.," *AIAA 23rd Plasmadynamics and Lasers Conference*, 1992.

[2] I. M. Belousova, B. D. Bobrov, V. M. Kiselev, V. N. Kurzenkov, and P. I. Krepostnov, "I^{127} atom in a magnetic field," *Opt. Spectrosc.*, vol. 37, no. 1, pp. 20–24, 1974.

[3] M. A. Kelly, J. K. McIver, R. F. Shea, and G. D. Hager, "Frequency tuning of a cw atomic iodine laser via the zeeman effect," *IEEE J. Quantum Electron.*, vol. QE-27, pp. 263–273, 1991.

[4] G. N. A. Van Veen, T. Baller, A. E. De Vries, and M. Shapiro, "Photofragmentation of CF_3I in the A band," *Chemical Physics*, vol. 93, pp. 277–291, 1985.

[5] G. Brederlow, E. Fill, and K. J. Witte, *The high-power iodine laser*, Springer, Berlin, 1983.

[6] W. Thieme and E. Fill, "Hyperfine relaxation in the iodine photodissociation laser," *Optics Communications*, vol. 36, no. 5, pp. 361–365, 1981.

[7] J. W. Nicholson, W. Rudolph, and G. Hager, "Using laser dynamics to probe the relaxation of an anisotropic velocity distribution of excited iodine," *Journal of Chemical Physics*, vol. 104, no. 10, pp. 3537–3545, 1996.

[8] K. A. Stankov, "A mirror with an intensity-dependent reflection coefficient," *Appl. Phys. B*, vol. 45, pp. 191–195, 1988.

MODELING THERMAL DIFFUSION IN PROBLEMS
WITH SEVERELY NON-MONOTONIC TRANSPORT PROPERTIES

Christopher S. Schmahl
Graduate Student
Department of Aerospace Engineering, Aviation,
and Applied Mechanics

The Ohio State University
328 Boltz Hall
2036 Neil Ave. Mall
Columbus, Ohio 43210

MODELING THERMAL DIFFUSION IN PROBLEMS
WITH SEVERELY NON-MONOTONIC TRANSPORT PROPERTIES

Christopher S. Schmahl
Graduate Student
Department of Aerospace Engineering, Aviation,
and Applied Mechanics
The Ohio State University

Abstract

The modeling of thermal diffusion in problems with non-monotonic thermal conductivity was studied. The chemically reacting thermal conductivity, which exhibited the strong non-monotonic variations was calculated previously (Schmahl, 1996). The data was put into LANL SESAME table form for use with the 2-1/2 Dimensional ALE MHD code called Mach2. Computations were performed to test both the reliability of the unsteady heat transfer problem and to analyze how the code handles the advanced thermal conductivity model. A detailed study of the effects of numerical gridding on the accuracy of the solution was performed. This included modifications to the code for inclusion of the ability to adapt the mesh according to variations in the thermal conductivity. The results indicate that when the advanced conductivity model is used, the accuracy of the solutions is increased.

MODELING THERMAL DIFFUSION IN PROBLEMS
WITH SEVERELY NON-MONOTONIC TRANSPORT PROPERTIES

Christopher S. Schmahl

Introduction

The equilibrium chemical composition, thermodynamic, and transport properties for nitrogen have been calculated (Schmahl). Six possible species were included, which are: N_2, N_2^+, N, N^+, N^{++}, and e^-. The calculations were performed with the inclusion of molecular dissociation and vibrational excitation, single molecular ionization, both single and double atomic ionization. Single electronic excitation was included with a variable electronic partition function cutoff for atomic species. The thermodynamic state range over which the calculations were performed was from 300 K $< T < 30,000$ K and 10^{-3} atm $< P < 10^3$ atm.

One of the most interesting and useful results obtained from these calculations is that the total mixture thermal conductivity exhibites highly non-monotonic variations, especially in state regions where chemical reactions were dominant, see Figure 1. This chemical thermodynamic and transport data is put into LANL SESAME table format for use with the 2-1/2 dimensional ALE MHD code called MACH2 (Peterkin et. al., 1992).

Analyses were performed previously with Mach2 using both the new tabular thermal conductivity and the classical Spitzer-Harm conductivity. The results showed significant differences in the thermal flux calculations, differences as high as 400% in some regions. Aside from these deviations, a number of issues came to light concerning the use of a highly non-monotonic conductivity model in advanced computer simulations. For instance, would adapting the computational grid according to changes in the thermal conductivity increase accuracy?

Would increased grid clustering at thermal conductivity maxima or minima have a significant effect on flow calculations? How does this relate to thermal diffusion length scales?
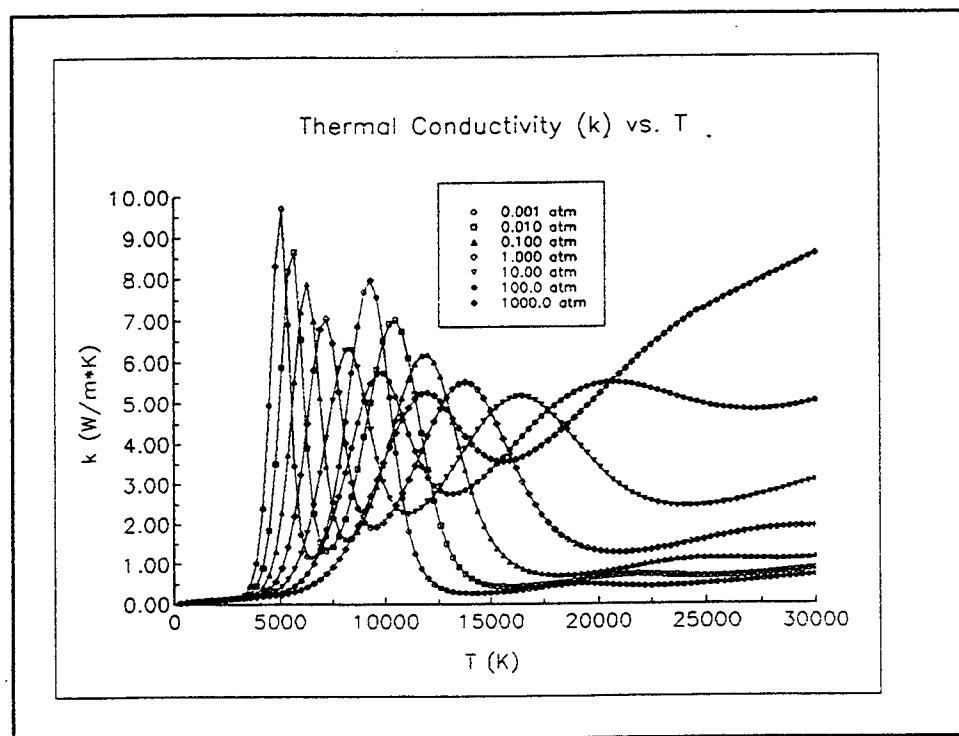

Figure 1. Total mixture thermal conductivity vs. T for nitrogen.

Would adaptive grid clustering, based on thermal conductivity alone, increase accuracy at hot/cold boundaries. Particularly when the initial profile is that of a step function. Answering these questions was the primary motivation for the research performed at the theory/computational physics branch at Phillips Laboratory.

Methodology

The first step in studying the effects of adaptive gridding based on the thermal conductivity is the modification of the 9601 version of the Mach2 computer code to include adaptive grid controls to adapt the computational grid to variations in the thermal conductivity. Two controls are added, one, called TCNDWT, adapts the grid according to the magnitude of the thermal conductivity. The other, called TCNDGRWT, adapts the grid according to gradients in the thermal conductivity. These switches may be used either together or independently of each other. The specific amount of adaptation provided be each switch is determined by the value of that switch, zero being no contribution. The decision to have the ability to adapt the grid on either magnitudes or gradients is based on the assumption that both may be important depending on the physical situation being modeled or the transport model used.

Having the ability to directly adapt according to the thermal conductivity in this manor accomplishes four major things. First, we put enough cells in regions where large amounts of thermal diffusion are important. Second, we capture the full conductivity in descritized space when dealing with highly non-monotonic transport model, thus minimizing the risk of missing important maxima or minima. Third, since the reacting thermal conductivity is a function of both pressure and temperature we can adapt the grid directly on one function instead of two, thus minimizing computational work. And fourth, we can better understand the exact effects that the structure of the transport model has on the behavior of the system.

The Mach2 computations are performed in six phases. The first phase is a two block test problem performed to test the effect of adaptivity weight functions on the computational grid under various conditions. The general conditions include equilibrium reacting equations of state,

16-5

thermal diffusion, heat transfer, and tabular conductivity model. The number of cells per block is 40 x 40. The 1-dimensional thermal boundary conditions are that the wall temperatures are fixed at T = 500 K. Twelve different runs are performed varying the second block gas temperature from 2,000 K to 10,000 K, along with the values of TCNDGRWT and TCNDWT from 0 to 500 in different intervals, respectively. Also the hydrodynamic control is varied to see what the effect of flow movement is on the gridding. These run verified that when TCNDWT is used properly the grid clusters in the block containing the largest thermal conductivity. And when TCNDGRWT is used the grid clusters where the gradient is largest, in this case on the internal block boundaries. The second test problem is a single block, 40 x 40 cell problem to analyze the effects of adaptivity on a 1-Dimensional, wall heat transfer with step function like initial conditions. The general conditions include equilibrium reacting equation of state, thermal diffusion, heat transfer, and tabular thermal conductivity. The wall temperature is kept fixed at 500 K. Nine runs are performed under gas conditions of 10,000 K to 22,000 K and with values of TCNDGRWT from 0 to 1000 and TCNDWT from 0 to 10,000, respectively. These results indicate the best adaptation occurs for values of TCNDGRWT greater than 1000, and for values of TCNDWT from 5,000 to 10,000. But of course the exact values chosen would depend upon the individual physical situation and on the amount of grid clustering required for the particular problem.

The first diffusion analysis is a single block problem to study the effects of both grid adaptation and reduction of scale length on the solution. A 60 x 60 cell block is used with the wall temperature fixed at 500 K. Six runs were performed with the gas temperature held constant at 10,000 K. Computations are performed for three different block lengths: 6.4 cm, 3.2 cm, and

1.5 cm. Three of the runs are done using no grid adaptation and the other three are performed using a value of TCNDGRWT equal to 500. The second diffusion problem is another single block problem, this time of 128 x 60 cells, to compare the effects of the grid adaptation on both the tabular thermal conductivity and the classical Spitzer-Harm thermal conductivity using the three length scales stated previously. The conditions are for equilibrium reacting gas, thermal diffusion, and heat transfer. The wall temperature is kept fixed at 300 K and the gas temperature is kept fixed at 5,802 K. Twenty-four basic runs are performed for this configuration. The first twelve were performed using the classical Spitzer-Harm thermal conductivity. For each of the three length scales the values for TCNDGRWT are varied between three values, which were 0, 500, and 1000, respectively. Only two values for TCNDWT are used, that is 0 and 1000. The next twelve runs are done under the same conditions as above but this time using the tabular conductivity. Four additional runs are done for the 6.4 cm. case to check the accuracy, or sensitivity, of the solution to the timestep used both with and without grid adaptivity. Given that the proper minimum thermal timestep for both cases is approximately 46 ns, these additional runs are performed at 40 ns and 10 ns.

The last calculation performed is a simple unsteady conduction problem to find out if Mach2 gets the right time-dependent solution to a unsteady heat conduction problem by comparison to an existing analytical solution. This is done to verify the physical accuracy of the results from the runs described above, as will be discussed in the next section. We know from previous experience that Mach2 gets the correct steady-state solution (Peterkin). The situation analyzed is a constant property heat conduction problem with the wall temperature fixed at 3,000 K and initial temperature of 300 K.

16-7

Results

The initial runs including both the two block and single block arrangements demonstrate that the modifications to the code to adapt the computational grid on the conductivity work correctly. The results obtained from the classical Spitzer-Harm thermal conductivity for the case of L = 6.4 cm and no adaptivity show the expected step function behavior with a wall flux initially at 1.2×10^6 W/m^2 at t = 0, then gradually decreasing to 1.0×10^6 W/m^2 by 5.1μs. For the L=3.2 cm case the wall flux is at 2.5×10^6 W/m^2 then decreases to 1.2×10^6 W/m^2 by 4.5μs. For the 1.5 cm case, the initial wall flux is at 5.25×10^6 W/m^2 and decreases to approximately 1.5×10^6 W/m^2 by 4.327μs. These results indicate that the decrease of problem size, which of course causes a decrease in zone size, causes a higher initial flux. The differences between them greatly reduce as time increases. For the adaptive case with TCNDGRWT=1000, and for L=6 cm the initial wall flux is 1.25×10^6 W/m^2 and decreases to 1.555×10^6 and is approximately the same value until 3.8μs. For the 6.4 cm case the initial flux is 2.5×10^6 W/m^2 and decreases to 1.7×10^6 by 2μs. for the 1.5 cm case the initial wall flux is 5.25×10^6 W/m^2 and decreases to 2.6×10^6 W/m^2 by 1.135μs.

There is a drastic difference in the solution behavior when using the tabular conductivity. Instead of a consistent step-like function in the flux we see oscillations developing in the solution. The solution at 5.456μs and L=6.4 cm with 128 icells is shown in Fig 2. The oscillation is clearly visible. Looking at the full behavior we see that the oscillation grows with time. And as seen in Figures 3 and 4, with icells = 64 and 32, respectively, the oscillation is still present.
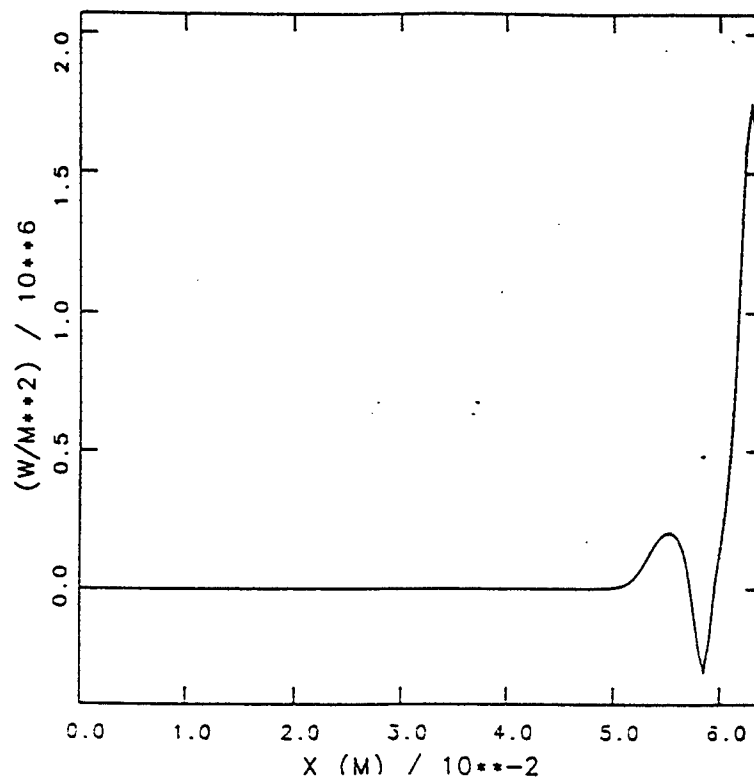
Figure 2. Mach2 solution with 128 icells.
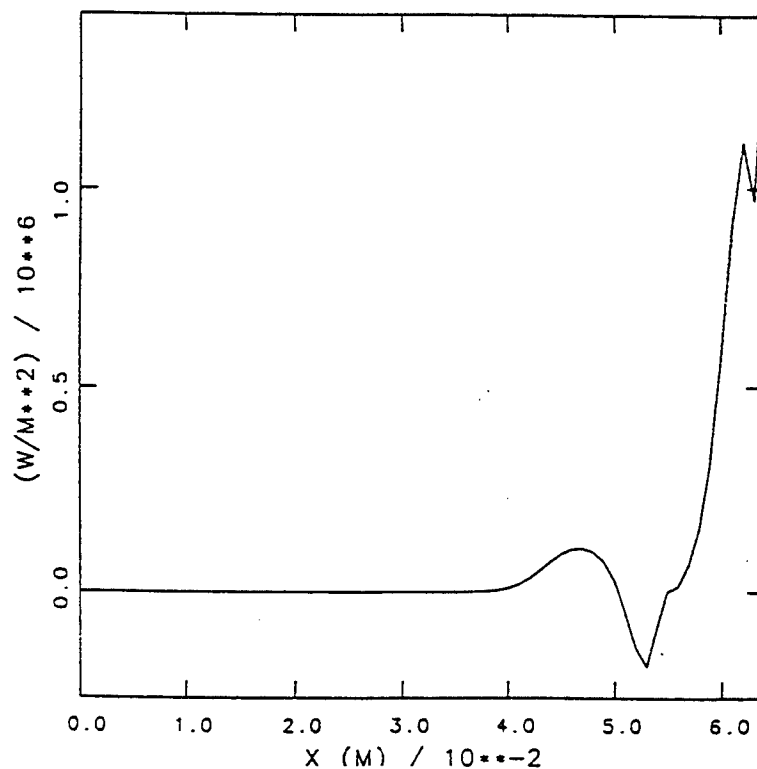
Figure 3. Mach2 solution with 64 icells.
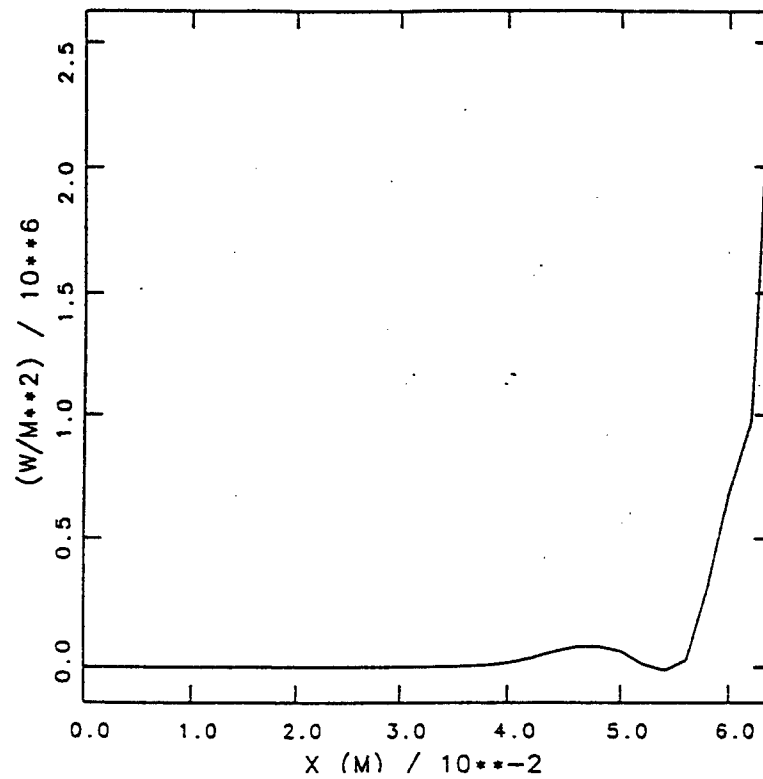
Figure 4. Mach2 solution with 32 icells.

Note that in this case the decision was made to vary the number of cells rather than the problem domain. To make sure this behavior is not due to any timestep errors additional runs were done at different timesteps and the oscillation is still present. The solution at $5.302\mu s$ and for 128 icells with the adaptive grid is shown in Figure 5. Here we see that the oscillation that the oscillation that occurred previously is significantly damped.
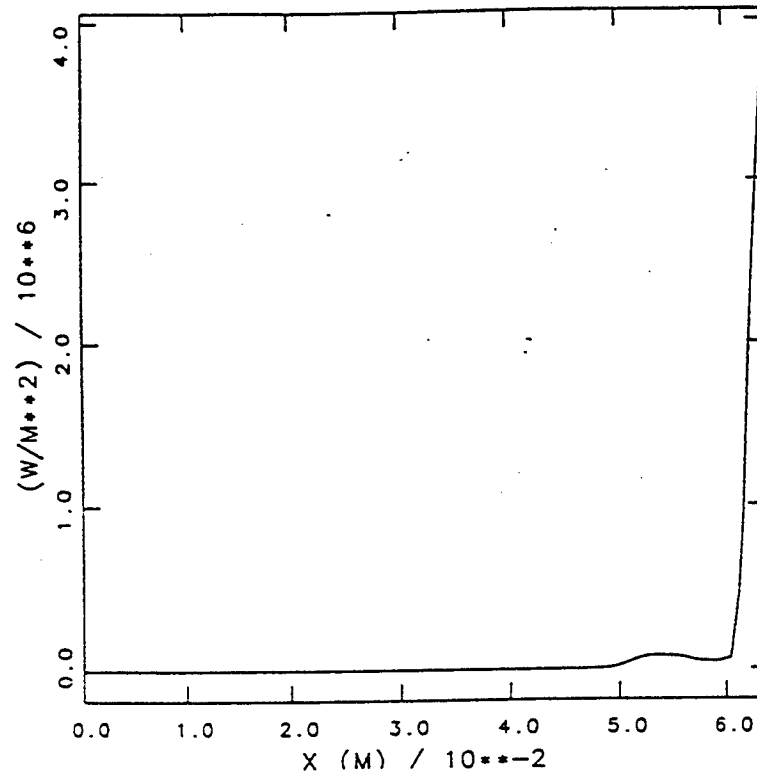
Figure 5. Mach2 solution for 128 icells with adaptive grid.

The same behavior is seen in the solutions for 64 and 32 cells, respectively. The wall stabilization behavior in the thermal flux, as observed in the Spitzer-Harm runs is also present in these cases when looking at the time development of each. Again the runs for different timesteps, smaller that the thermal timestep show similar damping behavior.
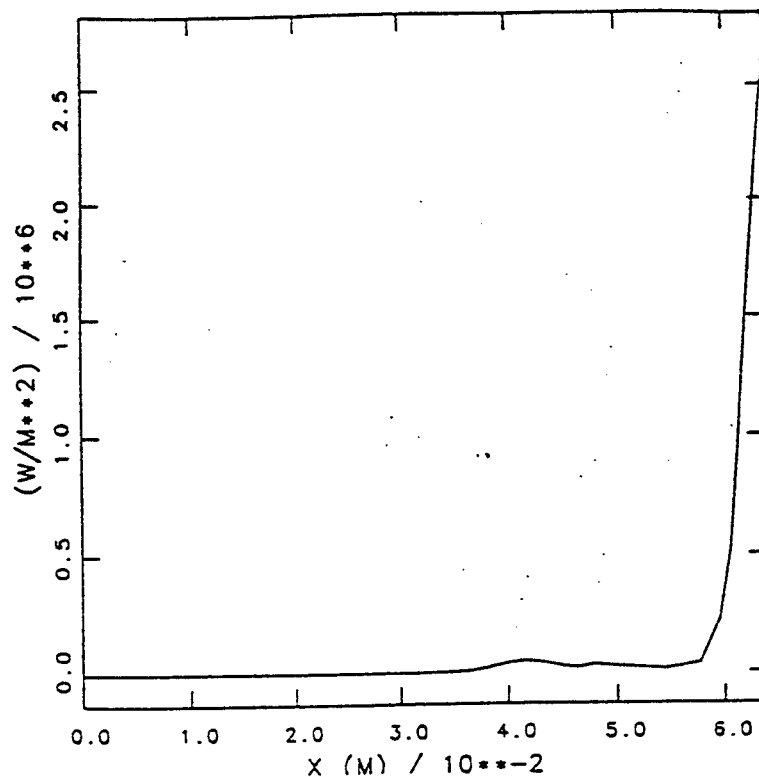
Figure 6. Mach2 solution with 64 icells using adaptive grid.
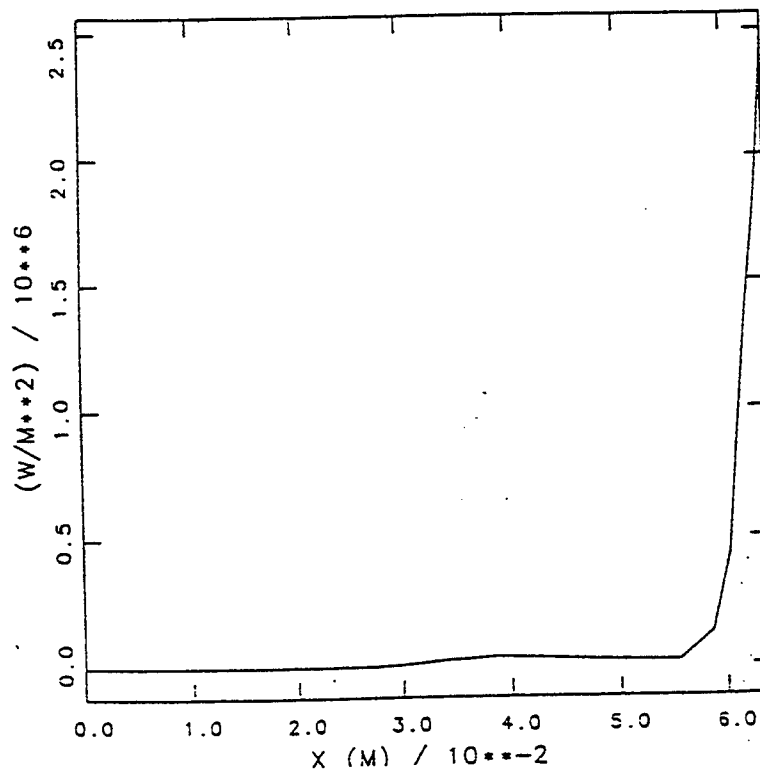
Figure 7. Mach2 solution with 32 icells using adaptive grid.

16-12

Conclusion

The calculation of the multicomponent chemically reacting transport model revealed that in certain state regimes the thermal conductivity exhibits highly non-monotonic behavior. This prompted the modification of the Mach2 computer code to adapt the computational grid to two things. One, to the gradient of the thermal conductivity and two, to the magnitude of the conductivity.

The initial one and two block test problems run demonstrates the effectiveness of the code modifications to adapt the grid according to the thermal conductivity using the two new switches. The first single block diffusion analysis shows that as the problem length decreases, with the number of cells held constant, the initial wall flux increases but equilibrates as time progresses. The second, more detailed analysis reveales the same behavior but as grid adaptation is introduced this tends to stabilize the wall flux, that is, the equilibrium happenes more quickly. When the tabular conductivity is used with no adaptation, oscillatory behavior is observed in the solution. When the grid is adapted according to the thermal conductivity, which in this case means grid clustering near the wall, we see that this oscillation is significantly damped. Runs are performed to omit the possibility that this is a timestep problem or due to some other phenomena other than the grid clustering. These results prove that the inclusion of grid adaptation according to thermal conductivity greatly increases the performance of the diffusion calculations for these cases.

References

Peterkin, Robert E., A. J. Giancola, J. E. Sturtevant. 1992. <u>MACH2: A Reference Manual -</u>

<u>Fifth Edition</u>. Mission Research Corporation. Albuquerque, NM.

Report Number ABQ-R-1490

Peterkin, Robert E. , personal communication

Schmahl, Christopher S., <u>A Computational Study of Shocked Flow Heat Transfer With Improved</u>

<u>Equation of State and Transport Properties - A Case Study For Nitrogen</u>. Master's Thesis.

The Ohio State University. 1996

Jeffrey D. Spaleta's report was not available at the time of publication.

Ducted VLF Transmissions and the
MIT Broadband VLF Receivers

Michael J. Starks

Graduate Fellow

Electrical Engineering and Computer Science

Massachusetts Institute of Technology

77 Massachusetts Avenue, NW16-267

Cambridge, MA 02139

Ducted VLF Transmissions and the MIT Broadband VLF Receivers

Michael J. Starks
Graduate Fellow
Electrical Engineering and Computer Science
Massachusetts Institute of Technology

Abstract

The propagation of whistler-mode signals from ground-based VLF sources in ionospheric ducts is discussed as it pertains to planned experiments at the Arecibo Observatory in September 1993. An experiment to study the effects of HF heating on naturally occurring ducts and conjugate propagation effects is defined, and the design of broadband VLF receivers and antennae for use in the experiment is detailed.

Introduction

It has long been understood that both natural and man-made VLF emissions propagating in the earth-ionosphere waveguide can be coupled into the ionosphere. These transmitted signals may then propagate in the ionosphere and magnetosphere as whistler waves, suffering dispersion along the way. If the signals then emerge from the ionosphere, they can be detected on the ground.

VLF emissions may originate from many sources. One of the most common causes is lightning. Atmospheric electrical discharges generate powerful bursts of broadband noise and the low-frequency components may travel great distances. Man-made sources also emit in the VLF band. The Navy's submarine communication network transmits from several sites and at great intensity.

VLF energy from a sub-ionospheric source will travel in the earth-ionosphere waveguide and can enter the ionosphere continuously along the lower surface (*e.g.*, Helliwell, 1965). Naturally occurring ducts may then convey trapped waves to the opposite hemisphere along the same magnetic line of force, where they emerge from the ionosphere and re-enter the earth-ionosphere waveguide. Wave components that do not enter ducts also follow curved paths through the ionosphere that do not exactly coincide with magnetic field lines. They are not as readily transmitted back out of the ionosphere, however.

Field-aligned density perturbations that may act as ducts are formed naturally in the ionosphere as a matter of course. They are often detected on ground-based sounders by the appearance of spread-F on ionograms. These ducts must exceed sub-kilometer sizes in order to allow propagation of VLF signals in the low-density regions of the magnetosphere. Artificial ducts can also be produced by HF heating, but these density perturbations are typically meter-scale and cannot carry whistlers all the way to the magnetic conjugate point.

Ongoing experiments have shown that HF heating may trigger or amplify natural spread-F events, leading to the formation of viable ducts [Starks, 1995]. Work done previously under the AFOSR Graduate Summer Research Program examined the coupling of VLF transmissions from the Navy's 28.5 kHz transmitter at Aguada, Puerto Rico, into the ionosphere [Starks, 1993]. This work discusses an experiment to verify these processes, and the construction of broadband VLF receivers to carry it out.

Heater-Controlled Spread F and VLF Ducting

Experiments conducted during the summer of 1992 at the Arecibo Observatory suggest the possible involvement of HF heating in the formation of large-scale density perturbations in the nighttime ionosphere. Specifically, during nighttime HF heating experiments in which the ionosphere over Arecibo was heated continuously for some time there rapidly appeared large plasma structures overhead, detected by a Digisonde as significant spread F [M.C. Lee, private communication, 1993]. Apart from appearing quite

some time after the initiation of the modification, this spreading could not be solely attributed to the HF heating for several reasons. First, the perturbations had scale lengths on the order of tens of kilometers (large-scale), while heater-induced spread F is typically the result of small-scale striations. Second, the spreading appeared over a much larger section of the sky than would be expected of heater-induced spread F, extending well out of the center of the heated area. To further confuse the matter, these large-scale field-aligned structures quickly dissipated when the heating was removed. Subsequent attempts to recreate the effect with heating failed, even after long periods of continuous HF transmission.

This apparent formation of large-scale density perturbations in response to HF heating suggests the ability of the heater – under specific conditions – to influence the natural formation of ducts capable of transmitting whistler waves to the conjugate hemisphere. Experiments have long shown that man-made VLF signals are ducted by the ionosphere and can be received at conjugate sites (see, for example, Smith, *et al.*, 1987 and Thomson, 1981), but the effects of HF heating on this ducting are unexplored.

The Ionospheric Research Group at the Massachusetts Institute of Technology is a regular user of the Arecibo Observatory, located in Puerto Rico and supported by the National Science Foundation. One of the group's major experimental goals for the September 1996 heating campaign was to attempt a measurement of VLF signals ducted to the magnetic conjugate point by naturally occurring large-scale density perturbations over the Observatory. During this campaign, the Arecibo HF heater could be operated and the effects on ducted VLF signals observed.

Design of the MIT Broadband VLF Receivers

When the Arecibo experiments were first scheduled, it was assumed that an existing set of superheterodyne VLF receivers would be placed at Arecibo's conjugate point, near Trelew, Argentina, to monitor the strength of VLF emissions. Immediate concerns about the sensitivity of the receivers and their antennae prompted consideration of other instruments. The existing receivers were designed for relatively narrowband operation and incorporate numerous filters other analog signal processing techniques. In addition, the frequency response characteristics of the receivers were not known and their standard antennae would need replaced with a more sensitive design.

In the spring of 1996, it became clear that the best tool for carrying out this experiment would be a broadband receiver capable of monitoring the entire VLF band. By designing new receivers, it would be possible to control important characteristics such as low noise, portability, and a flat frequency response in the band of interest. The MIT Broadband VLF Receiver was designed to meet these needs and facilitate the September 1996 Arecibo-Argentina VLF measurement campaign.

Due to the relatively short span of time available to complete the design, construction and testing of the receiver, the design draws heavily on the 1980-model Stanford Portable VLF Receiver, as

documented in *Paschal* [1980]. The Stanford design is a fully tested production design that has been through the stages of prototyping and revision. Without the luxury of time, a complete ground-up design would have been a monumental task. Even so, several important additions and changes were made to the Stanford design, including correction of several "poor design practices" and the addition of extra features.

The MIT broadband receiver is a magnetic field receiver, and operates in conjunction with air-core loop antennae. The receiver is designed as a two-channel system to permit simultaneous independent measurements with two antennae. This feature is extremely useful in experiments seeking to determine direction of arrival, where orthogonal loop antennae might be used. Additionally, the two channels can be operated from a single antenna but with different filtering and gain settings selected.

There are several vital considerations when designing a broadband receiver:

Frequency Response: It is desirable to achieve a flat frequency response throughout the band of interest. This simplifies the calibration of absolute signal strengths and avoids saturation of the receiver at frequencies where the gain is high. Naturally occurring VLF emissions generally have flat power spectral densities. A flat receiver response makes it easier to identify narrowband VLF transmissions amidst background noise. The MIT design provides flat response from approximately 60 Hz to 60 kHz.

Dynamic Range: Since the sensitivities of antennae and the strength of VLF sources can vary considerably, a design incorporating sufficient dynamic range is important. The MIT design includes switchable gain settings and a continuously adjustable gain setting to provide maximum dynamic range. External amplifier/antennuator modules can be added to increase the dynamic range in extreme situations.

Noise Immunity: The benefits of a sensitive system are lost if spurious signals from interference sources are not reduced sufficiently. The MIT VLF receivers are enclosed in aluminum cases to provide an electrostatic shield against noise. The input transformers are carefully designed to avoid capacitive noise coupling as well. The portability of the receivers permits use in areas distant from power lines to minimize 60 Hz hum.

The MIT Broadband VLF Receiver is built around three printed circuit boards. The first two are identical *signal stages*, providing two independent channels of operation. The third is a *control stage*, where the final signals are handled and certain other receiver functions are carried out.

RECEIVER STAGE

Input Stage

The MIT design incorporates two identical receiver stages. Each has a differential common-base input stage made of discrete bipolar transistors. Construction of the input amplifier from discrete

components allows complete control over noise characteristics, bias currents, and feedback configuration. This stage is identical to the Stanford design. A low-impedance differential design is chosen to obtain good noise figures and high bias stability. In addition, the bifilar winding in the transformer secondary (discussed later) makes a differential design a good choice. There is better common mode rejection; DC currents in the transformer secondary are balanced, reducing microphonics; and even-harmonic distortion is reduced.

The amplifier (*figure 18-1*) consists of a differential common-base amplifier followed by a differential common-emitter gain stage and emitter-follower buffers. Transistors Q1 and Q2 form the common base stage, operating at about 100 μA quiescent current. This yields about a 520 Ω input resistance, emitter to emitter. The outputs are amplified by Q3 and Q4, which comprise a differential pair. The diff-pair bias current is 31 μA to keep their noise current below that of Q1 and Q2. R5 and R6 set the stage's gain and provide the feedback that reduces the input impedance. Q5 and Q6 provide output buffering for the gain stage.

Q7 is the current source for the diff-pair, and includes common-mode feedback through R11, R12, and R15. DC common-mode feedback is also applied through R17 to the emitters of Q1 and Q2 through the transformer secondary. A small amount of differential DC feedback is applied to the bases of the input pair through R9 and R10 to equalize their emitter currents, and the potentiometer R35 allows fine adjustment of the input circuit balance. These methods combine to dramatically increase the common-mode rejection of the input amplifiers. D3 provides first-order temperature compensation to the bias circuit.

Frequency Compensation Stage

Frequency compensation (*figure 18-2*) in the receiver is also taken from the Stanford design, and includes two components. The first is a high-stability IC amplifier that equalizes the receiver gain below the input turnover frequency (about 350 Hz), where the reactance of the loop antenna equals the input resistance. If the panel switch is in the *flat* position, this circuit flattens the frequency response down to about 60 Hz. With the switch in the *350 Hz* or *1 kHz* positions, the compensation is deactivated.

The second component of this stage is a switchable 1 kHz fourth-order Butterworth high-pass filter. It is built around a dual-741 op amp chip. This filter is intended for use in extremely noisy conditions, where 60 Hz hum and its harmonics need to be filtered out. It is activated when the panel switch is in the *1 kHz* position, and inactive otherwise.

Variable Gain Stage

The filtered signal is next passed to the variable gain stage (*figure 18-3*), where the high-speed operational amplifier U101 adds the signal gain indicated by the setting on the front panel gain switch. Switchable gains of 0, 20, or 40 dB are possible through the use of the analog switches in U102.

CONTROL STAGE

Adjustable Gain Stage

It is expected that this receiver will be used in a variety of situations and environments. In situations where the output signal should match a desired amplitude as closely as possible, it is convenient to have a continuously variable gain setting. The adjustable amplifiers (*figure 18-4*) in U103 provide the variable gain desired. Another 10 dB of gain is obtainable from this amplifier through the potentiometer in the feedback path. The Stanford design puts the potentiometer in the input signal path as a resistive divider. This is an undesirable configuration, as it adversely affects input impedance, directly couples noise into the stage, and requires running the signal to the front panel. The MIT design avoids all of these problems.

Alternatively, if a situation calls for precise signal strengths to be measured, the adjustable amplifier has a switch on the potentiometer that locks the gain at 1, thus introducing no uncertainty into the measurement.

Two identical adjustable amplifiers are included to process the two signal channels independently. The outputs of these amplifiers are presented on the front panel as the final signals.

Audio Amplifier

To allow the user to aurally monitor the signals being received, U104 is included as an on-board audio amplifier. The amplifier receives its input from the outputs of the variable gain amps and provides an output suitable for headphones or a small speaker. The gain of the stage is set with a simple input resistive divider controlled from the front panel. This single IC solution replaces the more complex Class-AB amplifier stage in the Stanford design.

Calibration Oscillator

U105 (*figure 18-5*) forms the receiver's gain calibration oscillator. It is a multivibrator running at 5 kHz, creating a differential square-wave signal. When the front panel switch is set to calibrate a receiver channel, power is applied to the oscillator and injected into the input transformer of the receiver input stage. This allows calibration of the receiver output to an absolute scale.

Battery Monitor

The receiver runs on 10 D-cell alkaline batteries. It is capable of operating at voltages from 10 to 15 volts. The simple battery test circuit of the Stanford design has been replaced with a low-power battery indicator circuit that provides some idea of the battery condition prior to a complete discharge. The system measures the voltage on one side of the split supply and compares it with several stable trip points generated

by a zener diode and resistive dividers. High impedance comparators light the battery indicator lamps according to the current bus voltage.

INPUT TRANSFORMER

The VLF receiver requires an input transformer to achieve the low input impedances desired. The system is designed to be a 1 Ω input impedance, but the common-base configuration only achieves an input impedance of about 520 Ω. To correct for this difference, we require a transformer with a turns ratio squared $m^2 = 520$. Therefore we have a turns ratio of about 22.8.

Transformers tend to have frequency responses that roll off both at the high and low ends. The low rolloff is primarily due to the inductance of the primary while the rolloff at the high end stems from the shunt capacitance of the transformer windings. For good performance, we want a large primary inductance, and small winding resistances and capacitances. These are conflicting requirements. That is, we may increase the inductance by winding more turns of smaller wire, but this increases the winding resistance and may increase the distributed capacitance.

Fortunately, our relatively small value of m allows a good design from all angles. Our design calls for a center-tapped primary and a center-tapped secondary. The center-tapped primary balances the input circuit for common mode signals from the antenna, such as those caused by electrostatic pickup of interference. The center-tapped secondary is necessary to accommodate the differential input design. To obtain the good common-mode rejection, the fields from each half of the primary must be equally coupled into each half of the secondary. We accomplish this by using bifilar winding, where two wires are wound simultaneously in each the primary and the secondary. They are connected to form the center tap, and we are guaranteed to have equal numbers of turns in each half of the winding. This increases the distributed capacitance of the transformer, as it places high- and low-potential windings in close proximity, but this is mitigated somewhat by our low-impedance input design.

The MIT input transformers are pot-core designs. The secondary is wound first on a bobbin, consisting of 251 turns (bifilar) of #32 enameled copper wire. Then a 3-mil copper ribbon is wound around the secondary to act as an electrostatic shield. This prevents electrostatic coupling between the primary and secondary. The ends of the shield are insulated to avoid having a shorted turn in the transformer. The primary is then wound on top of the secondary, consisting of 11 turns (bifilar) of #18 enameled copper wire. The bobbin is then placed into two precisely-machined ferrite cups that shield the transformer from external magnetic fields. This ensures there will be no stray pickup of signals directly by the transformer.

RECEIVER ANTENNAE

The component of the VLF receiving system that is equal in importance to the receiver itself is the antenna. Without a quality antenna, the effort spent on good receiver design is wasted. An antenna must be sensitive enough to detect the weakest expected signal, yet must match the input impedance of the receiver as closely as possible. Another consideration is the portability of a design. In general, the sensitivity of an antenna depends on the product of the antenna mass and the antenna area. More sensitive antennae must therefore be larger, heavier or both.

The Arecibo heating campaign experiment calls for two antennae of widely differing requirements. Since one receiver will be located at the Observatory to directly monitor the VLF transmissions of the Navy system, a small loop antenna is sufficient. For this need, the Stanford standard loop was chosen. This is a 56.7 cm square loop antenna consisting of 21 turns of 18 gauge wire. It is a 1 Ω, 1 mH antenna design to match the input impedance of the Stanford receiver (the MIT receiver has the same input impedance). This small loop has a sensitivity of about 900 μV-Hz$^{1/2}$/m.

The second antenna is to be erected at Trelew, Argentina, to monitor VLF signals exiting the ducts overhead. Since the expected absolute strength of these signals is not known, we must construct the most sensitive antenna practical. This requires size, and triangular loops become a good choice. The final antenna design calls for a 6-turn 14 gauge equilateral triangle, 7 m on a side. It is also a 1 Ω, 1 mH antenna. By contrast to the smaller loop, it has a sensitivity of about 50 μV-Hz$^{1/2}$/m. This is almost a factor of 20 better. This antenna must be hoisted by its apex onto a tower and its two other corners guyed to the ground using non-conductive tethers.

The main difficulty in loop antennas is avoiding distributed capacitance. This capacitance affects the low-frequency performance of the system if it becomes too large. Fortunately, the use of a low-impedance input design shunts the antenna capacitance so that it is not a serious problem. The small loop has a distributed capacitance of about 800 pF, while the larger loop has only about 9 pF.

Data Processing

The Arecibo-Argentina campaign was expected to last five days in September 1996. During this time, about 40 hours of data from the VLF receivers located at the Observatory and in Trelew would be recorded. The largest problem to overcome is that of the very strong sub-ionospheric signal dominating the ducted signal received in Argentina. Separating the two signals in the Argentina data is very difficult, because the signal transmitted by the MSK-modulated Navy VLF system is, for our purposes, a pseudo-random sequence of frequency shifts.

It was for this reason that the second VLF receiver was to be located at Arecibo. It would directly monitor the transmissions of the Navy antenna, providing a baseline with which to compare the Argentina

data. A signal train that has traversed an ionospheric duct will have a definite phase delay with respect to the signal that has followed the earth-ionosphere waveguide. By cross-correlating the Arecibo record of the transmission with the signal received in Argentina, the presence of the ducted signal can be revealed.

Another important factor is that the Navy transmitter is not truly mono-chromatic. Instead, it transmits two distinct frequencies spaced around the 28.5 kHz suppressed carrier. These two frequencies will travel at slightly different velocities in the duct, and it may be possible to calculate the length of their path from the phase shifts. The presence of two frequency samples provides the ability to double-check the result.

Conclusions

This work is another step in the process of understanding the process of VLF coupling into, and ducting by, the earth's ionosphere. Previous efforts considering the coupling process have been supplemented by theoretical analysis of instability processes that may form density perturbations capable of ducting VLF emissions. Experiments have been defined for September 1996 to measure the effects of HF heating on the natural instability processes and the resulting ducting action. Broadband radio receivers to carefully measure the ducted VLF emissions as they emerge at the magnetic conjugate point have been designed and are being constructed.

Epilogue

The Arecibo heating campaign for September 1996 was canceled due to high water levels in the basin where the heater antenna array is located. The experiment defined in this document has been postponed until at least January 1997.

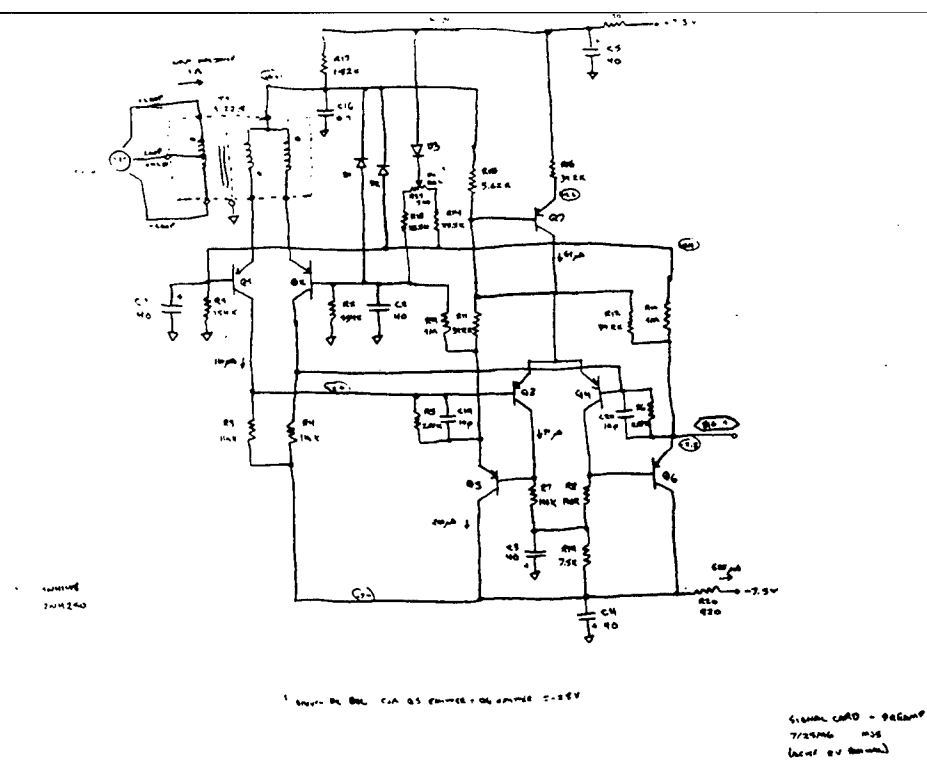## Acknowledgments

Figure 18-1

Figure 18-2

Figure 18-3

Figure 18-4
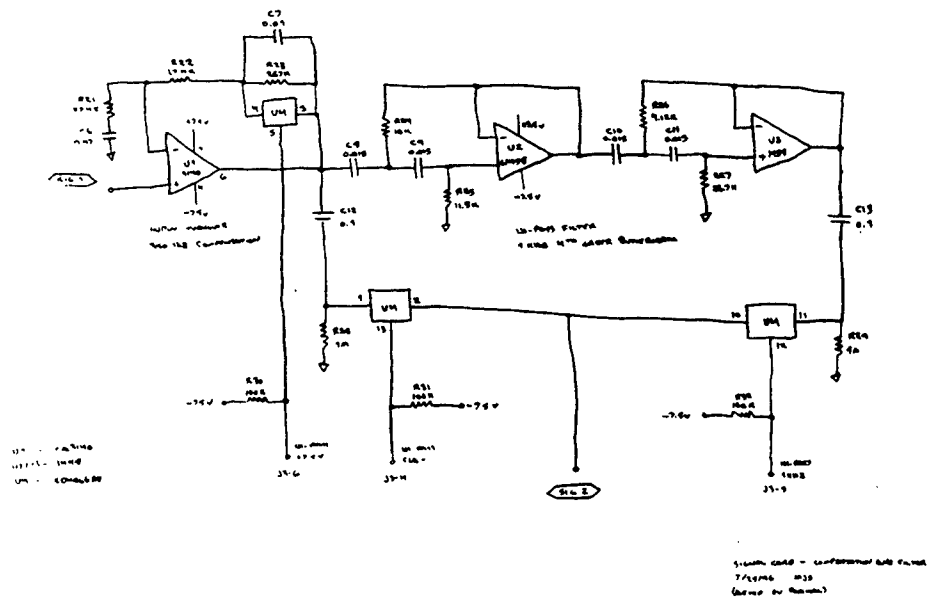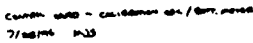
Figure 18-5

References

Helliwell, R.A., *Whistlers and Related Ionospheric Phenomena.* Stanford: Stanford University Press, 1965.

Paschal, E.W., Design of broad-band VLF receivers with air-core loop antennas. Stanford University Internal Report, September 1980.

Smith, A.J., Yearby, K.H., Bullough, K., Saxton, J.M., Strangeways, H.J., Thomson, N.R., Whistler mode signals from VLF transmitters observed at Faraday, Antarctica. Memoirs of National Institute Polar Research, Special Issue No. 48, p. 183.

Starks, M.J., Transmission of VLF Waves into ionospheric ducts at Arecibo, Puerto Rico. Summary report to AFOSR, September 1993.

Starks, M.J., Gravity wave seeding of Perkins' instability and HF-amplified spread-F over Arecibo, Puerto Rico. Boston University Master's Thesis, 1995.

Thomson, N.R., Whistler mode signals: spectrographic group delays. *J. Geophys. Res.,* 86, 4795.

Watt, A.D., *VLF Radio Engineering.* Oxford: Pergamon Press, 1967.

Balloon Launch Retromodulator Experiment

Clark Steed
Graduate Student
Utah State University

Charles M. Swenson
Assistant Professor
Utah State University

Final Report for:
Summer Faculty Research Program
Phillips Laboratory

Sponsored By:
Air Force Office of Scientific Research
Bolling Air Force Base, DC

and

Phillips Laboratory

October 22, 1996

19-1

Balloon Launch Retromodulator Experiment

Charles M. Swenson
Assistant Professor
Utah State University

Clarke Steed
Graduate Student
Utah State University

ABSTRACT

Under the AFOSR summer research program researchers from Utah State University / Space Dynamics Lab spent 12 weeks at the Phillips lab preparing and flying a retromodulator laser communication package on a high altitude balloon. The package was a prototype system for a low-power laser communications system for small low earth orbiting satellites. The work was divided into preparation of the ground station at Starfire Optical Range, assembly and testing of the retromodulator control electronics, micro controller programming and the actual balloon flight of September 15, 1996. All technical objectives of the experiment were met during the 1 1/2 hour flight of the balloon which reached a float altitude of 103,000 ft. The ferroelectric liquid crystal based retromodulator design of Utah State provided test patterns for modulation rates up to 20 kilo bits. Data was successfully down linked using a 1200 bps RS232 format and a simplistic receiver. This report outlines some of the reflected laser communications activities conducted under this summer research program.

Reflected Laser Communication Systems

Charles M. Swenson
Assistant Professor
Utah State University

Clark Steed
Graduate Student
Utah State University

1 Introduction

Satellite laser communications concepts have been under development for many years. Laser communications from ground to low earth orbit is relatively simple because most of the hardware is on the ground and the satellite need only be provided with a relatively simple sensor. However, conventional approaches to laser communication from satellite to ground require sophisticated hardware aboard the satellite such as a reliable laser subsystem and a capable subsystem for optical acquisition, tracking, and pointing to the receiver. The complexity of this hardware introduces concerns about cost, added weight, power consumption and reliability; the efforts needed to resolve these concerns have significantly delayed the implementation of laser communications systems on operational satellites. An example of the effects of this problem is the recent cancelation of the DSP Laser cross link program after 10 years of development and approximately $600 million spent.

An alternate approach to laser communications which does not require extensive hardware on the satellite makes use of a retromodulator. The
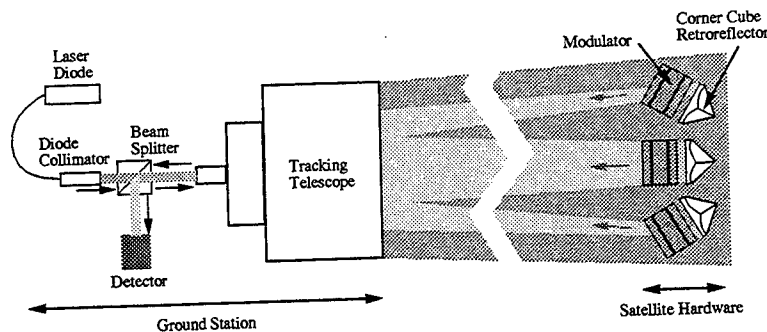
Figure 1: Conceptual diagram of a retromodulator communications system

alternate concept is as follows: First a laser site on the ground illuminates the satellite with either a continuous beam or a uniform train of pulses. On board the satellite is a corner cube, which reflects the incident laser light back to the transmitter on the ground. Associated with the corner cube is a modulation mechanism which reacts rapidly to change the intensity or the polarization of individual reflected pulses. By appropriately controlling this retromodulator the laser light pulses reflected back to the ground station are encoded with the communications signal (see Fig. 1).

Retromodulated commmunictions offers the potential advantage of significantly reducing the size, power, and weight of hardware required aboard the satellite for laser communications while maintaining many of its advantages in general. This relatively new concept has many potential applications and may be appropriate where:

- The remote part of the communications link must be *very low power*.
- The remote site is inaccessible except by free space transmission.
- Weight and volume at the remote sight are a concern.
- There is a need for a "secure" data link.
- RF jamming is a concern.
- Simplicity at the remote site is desirable.
- A moderate data rate is required.

- Occasional delayed access to communications are acceptable.
- There is a need for simultaneous communications access to the remote sight.

A few specific applications that could benefit from such a technique are:

- Communications during atmospheric re-entry.
- Communications to/from downed pilots.
- Satellite to satellite links.
- Satellite to earth links:

  - Redundant or backup communications link.
  - Fly along noninterfering link.
  - Primary communications link.

Perhaps the most compelling reason for developing this type of communications system is to meet the sever power constraints of very small or micro satellites. This class of statellites typically do not have extensive deployable solar panels. The limited surface area of micro satellites for solar cells makes power a primary concern and techniques for conserving spacecraft power need to be explored.

Utah State University / Space Dynamics Lab has been involved in reflected laser communications research since 1992. Internal funding at USU allowed Dr. Swenson to initially study the concept with graduate students [1]. Dr. Charles Swenson and a graduate student spent 12 weeks during the summer of 1994 testing retromodulator concepts at Phillips Lab under the Air Force Office of Scientific Research Summer Research Program [2]. A flight opportunity was identified for a proof of concept test at the end of the summer. The Space Experiments directorate at Phillips Lab would be flying a high altitude balloon with an experiment for the Department of Energy in the spring of 1995. The primary mission is atmospheric sampling

but there was room for an additional payload providing it was small and can be easily mounted on the existing package. Development of the test hardware began in the fall of 1994 and successful ground testing of some of the retromodulators occured at the Starfire Optical Range in December of 1994. Shortly after this testing the balloon flight for the DOE was cancelled ending the flight opportunity for the retromodulator experiment.

The Air Force Academy, through Mr. Gill Moore, became interested in this potentially low power communications technology and offered a test flight for hardware on one of the small "Falcon" satellites being built by Academy students. The Falcon satellites are to be placed into low Earth orbit by a launch system being devloped from surplus minuteman missile assets by the Space and Missle Test and Evaluation Directorate at Kirtland Airforce Base. As step to the final satellite and good practice for ground based operations it was decided to conduct a test of the retromodulator laser communications package and as much of the Falcon sat spacecraft as possible on a high alitude balloon over the Starfire Optical Range (SOR). Much of the hardware for the previously planned balloon test of 1995 could be used. Preparation for this new balloon test and the test itself were carried out during the 12 weeks of this years Air Force Office of Scientific Research Summer Research Program.

This report presents an overview of the balloon launched retromodulator laser communications experiment activities conducted under this summer research program. This summers successful balloon launch was a joint effort involving researchers from Utah State University working in PL/VTRA, the Starfire Optical Range (PL/LIG), the Air Force Academy, the Space and Missle Test and Evaluation Directorate, PL/SX, and Laurence Livermore National Labs.

2 Balloon Retromodulator Experiment

The balloon reteromodulator experiment consisted of three principal parts. The first part is the actual the retromodulator experiment consisting of an array of retromodulators, drive electronics, an optical receiver, and a micro controller for operating the experiment. This portion of the experiment was built and tested by USU/SDL working out of PL/VTRA during the summer. The second part of the experiment is the ground station consisting of a laser transmitter, an optical receiver, and the pointing and tracking system. This was provided by SOR with some componets from USU/SDL and was also setup during the summer. The final component was the balloon system for carrying the retromodulator experiment to 105,000 ft altitude over the ground station. This portion was provided by the Air Force Academy with help from Norm Kjome of the University of Wyoming and Kjome Research. It consisted of a high altitude research balloon (approximately 70 feet in diameter and 50 feet tall at the float altitude) and support hardware for safty, tracking, and cut down.

A balloon at 24 km altitude is probably the next closest platform to an actual satellite for free space optical communications as most of the turbulent effects of the atmosphere would be observed. This program provided an ideal opportunity for a quick and relatively inexpensive demonstration of the reflected laser communications concept as well as a good "dry run" for a potential satellite demonstration. A brief outline of some of the objectives of the balloon test were:

1. Develop a working relationship between USU/SLD and the Air Force on reflected laser communications.
2. Demonstrate the basic principles and hardware of retromodulated laser

communications in a way that shows scaleability to a satellite.

3. Validate the communications link budget for retromodulated communications including atmospheric effects (scintillation, backscatter, etc) with vertical propagation through the atmosphere.

4. Test an assembly of FLC based retromodulators for parallel operation, temperature effects, speed, and modulation depth.

2.1 Ground Station

The 1.5 meter telescope at Starfire Optical range was used as the ground station consisting of a laser trasmitter and a optical receiver. The trasmitter consisted of A 5 watt 810 nm diode laser that was fiber coupled to a optical system mounted on the belly of the 1.5 meter telescope. These optics colimated the output of the fiber into about a 14 centimeter diameter beam with a half angle divergence of 1.5 mRad. The optical receiver consisted of the 1.5 meter telescope and a USU/SDL photomultiplier tube detector and pre-amp. SOR integrated all of these elements and developed new tracking capabilities for the 1.5 meter mount for high altitude balloons. Data from the photomultiplier tube was low-pass filtered at 10 kHz and digitized at 20 kHz for the experiment. Snatches of data were stored for post flight analysis.

2.2 Link Budget

Radio frequency communication links are typically described by engineers in terms of power, power gains, and power losses in decibel notation. Most engineers and scientists working with optical systems describe their systems in terms of number of photons, divergences, absorptions, and effective areas. The field of laser communications is mixed and we have chosen the latter system.

A detailed link budget was developed in spread sheet form for the balloon launch retromodulator experiment. This budget accounted for both signal and noise sources in the communictions link and was based on a variety of measued and expected values. Signal to noise ratios were calculated for two types of detectors, a simple threshold system and an integrating system.

2.2.1 Radar Equation

The number of photons received, N_{rx}, by a ground station from a retrore-flector at distance R with effective area A_{ret} obeys the well known radar equation [3]. A modified form of this equation which is descriptive of a retromodulator communication system is given by (1).

$$N_{\mathrm{rx}} = \frac{N_{\mathrm{tx}} A_{\mathrm{ret}} A_{\mathrm{rx}}}{\Omega_{\mathrm{tx}} \Omega_{\mathrm{ret}}} \tau_a \tau_o \tag{1}$$

Where N_{tx} is the number of photons transmitted into solid angle Ω_{tx} and received with effective area A_{rx}. The quantity Ω_{ret} describes the solid angle into which photons are returned from the retroreflector and accounts for intentional spoiling of the retroreflector and/or diffraction spreading. The global transmittance of the atmosphere and of the optics are accounted for by τ_a and τ_o respectively.

2.2.2 Link Calculations

The link budget calculations were made using a spread sheet on a PC. These calculations were made pre-flight and validated in sections using bench measurements, background observations, and ground based measurements of signal returns over a 5.4 km range. We present synopsis calculations for look angles of 45° from the ground station which corresponds to the longest

range and smallest crossections for the retromodulators and for 0° (directly overhead), the best case condition.

Transmitter

Design Element	Units	Value
Link Wavelength	nm	810
Transmitter Power	Watts	5.000
Transmitter Photons Generated	photons/s	2.04E+19
Transmitter Divergence Half-Angle	Rad	1.5E-3
Solid Angle of Transmitter	Str	7.07E-6
Transmitter Optics Losses	transmittance	0.657
Transmitter Photons Emitted	photons/s	1.34E+19

Receiver

Design Element	Units	Value
Antenna Diameter	m	1.5
Global Efficiency		0.8
Effective Area	m^2	1.75

Retro-reflector

Design Element	Units	45°	0°
Reflector Diameter	cm	2.54	
Look Angle to Array	Deg	45	0
Array Factor	unitless	0.167	2.082
Effective Area	cm^2	0.85	10.55
Optical Transmittance	transmittance	0.40	0.40
Spoiling half-angle	Rad	4.79E-4	
Solid Angle	Ster	7.21E-7	

Radar Equation

Design Element	Units	45°	0°
Maximum Altitude	m	32000	
Look Angle to Payload	Deg	45	0
Range to Retromodulator	m	45255	32000
Atmospheric Loss Outgoing	transmittance	0.7	
Atmospheric Loss Returning	transmittance	0.7	
Photons Received	photons/s	1.46E+7	7.25E+8

Noise

Design Element	Units	Value
Dark Noise Photons	photons/s	4.86E+4
Background Photons	photons/s	1.34E+5

Backscatter Photons	photons/s	1.53E+8	
Total Non-signal Photons	photons/s	1.53E+8	

Signal

Design Element	Units	Value
Modulation ratio	unitless	0.025
Sample Period	s	5E-5
Bit Period	s	5E-4
Noise Factor	unitless	5

Detector

Design Element	Units	45°	0°
High Level Rate	photons/s	1.68E+8	8.79E+8
Low Level Rate	photons/s	1.54E+8	1.71E+8
Expected Std	photons/s	9.16E+6	2.10E+7
Signal/Noise (Threshold)	unitless	1.55	33.75
Samples/Bit		10	
Photons/Bit (High)	photons	8.39E+4	4.39E+5
Photons/Bit (Low)	photons	7.68E+4	8.57E+4
Signal/Noise (Integrating)	unitless	4.91	106.71
Error Rate	s^{-1}	7.04E-3	~ 0

2.3   Balloon System

A 141,000 cubic ft polyethylene-film research-balloon was used to loft the retromodulator experiment and associated support and recovery equipment as illustrated in Fig. 2.3. The payload string included three strobe lights for detection by aircraft and SOR, radar transponders for the FAA, and GPS receivers and data links for position information. The balloon system was provided by the Air Force Academy with technical and equipment support from Norm Kjome of Kjome Research. The balloon and instrument string were launched from a site 2 miles west and 1 mile south of the Starfire Optical Range at the south end of Kirtland Air Force Base. Careful analysis of wind profile data, prior to launch, predicted that the balloon would travel east and north about 24 miles from SOR and then above 60,000 ft would move
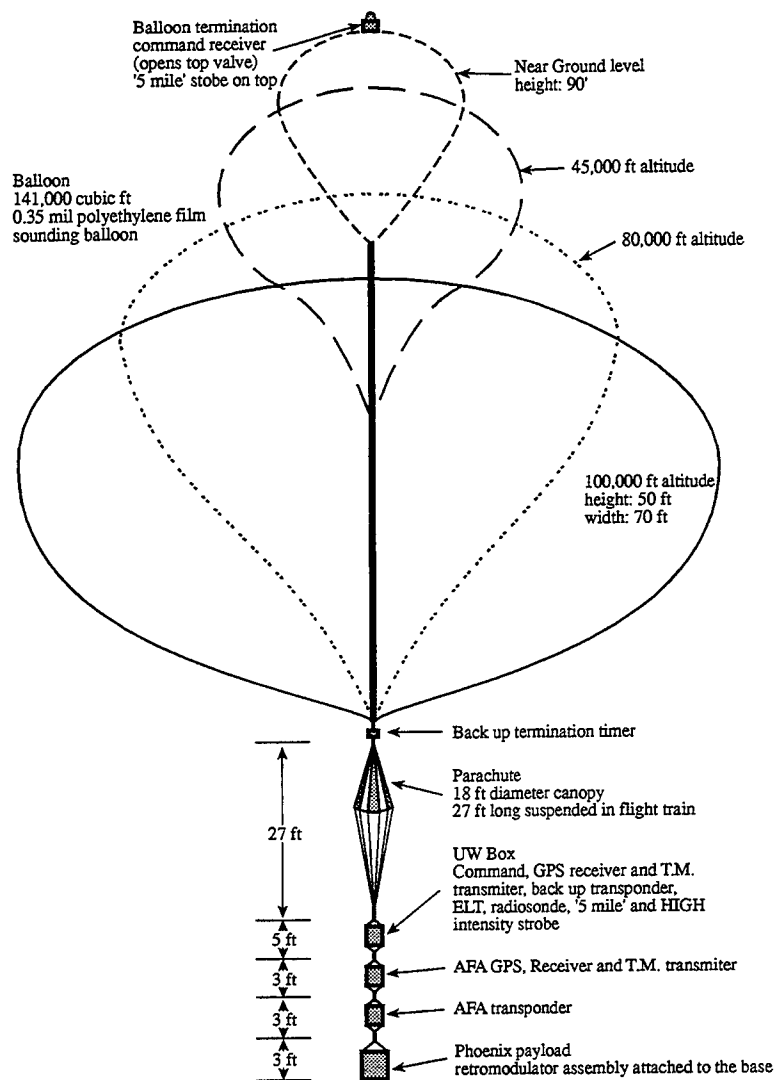
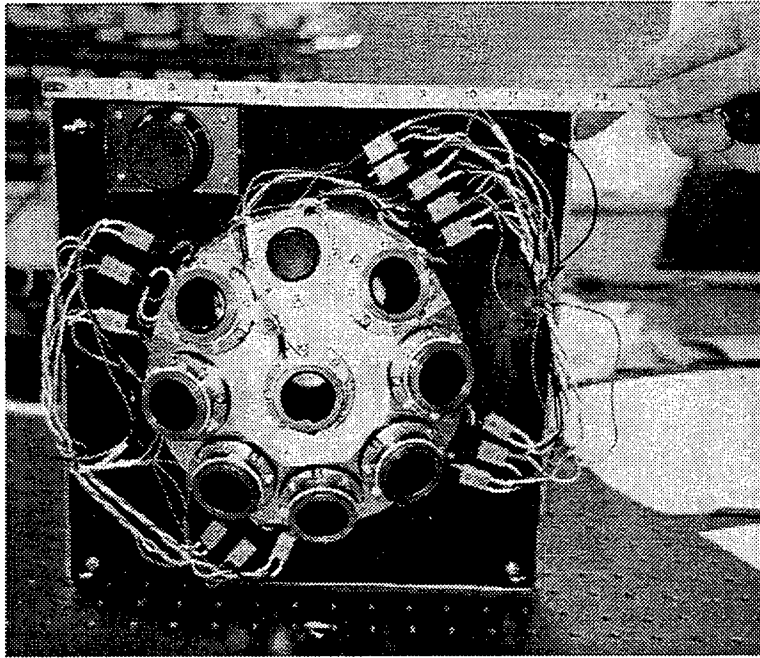Figure 2: High altitude balloon and payload train.

Figure 3: Preflight photograph of the retromodulator assembly

west, back over the ground station. The balloon followed this trajectory passing within about 10 degrees of vertical over SOR and continued about 30 miles west before it was brought down. This was the first high altitude balloon flight at SOR and was an important demonstrated of their tracking capability of this platform for near-space optical experiments.

3   Retromodulator Instrumentation

The retromodulator instrumentation consisted of an array of retromodulators as pictured in Fig. 3 along with control electronics. The electronics within the payload executed and monitored several tasks during the balloon flight. The on board micro controller provided modulating signals for the FLCs while measuring and controlling the temperature of each of the nine

individual retro assemblies. The hardware also contained the capability to receive optical uplink data sent from the ground station. A Tattletale model 8(TT8), from Onset Computer Corporation, managed these tasks. All of the electronic subsystems needed to operate the experiment interfaced with this advanced microcontroller. The flexibility, compact size and rich features of the TT8 made it a good choice for a on-board flight computer. The TT8 provided a Motorola 68332 microprocessor integrated with the following features: eight 12-bit analog to digital inputs, RS232 serial communication lines, high speed Queued Serial Module, multiple Time Processing Units, digital I/O lines. This computer consumes little power and operates off of a single power supply(7-15 V). A printed circuit board (PCB) was fabricated to interface the TT8 to the other modules. This board also implemented additional tools needed to run the experiment such as a 4 channel 12-bit and a 8 channel 8-bit digital to analog converters to drive the FLCs, high current switching transistors to control the heaters, an analog MUX to switch between temperature probes, and amplification circuitry for the optical uplink. A simple block diagram of the system can be seen in Fig. 3.

3.1   Retromodulator

The electrical components of the retromodulator assembly include the FLC, temperature probe, and heater. The balloon payload contained nine of each. The FLCs require a $\pm 5V$ square wave signal to drive them. This was accomplished by using one of the 12-bit D/A channels to produce the drive signal. Mixing this signal with nine other offset voltages, from the D/A chips, produced separate controls for each of the FLCs. This compensated for the offset biases of the op-amps and individual personalities of the liquid
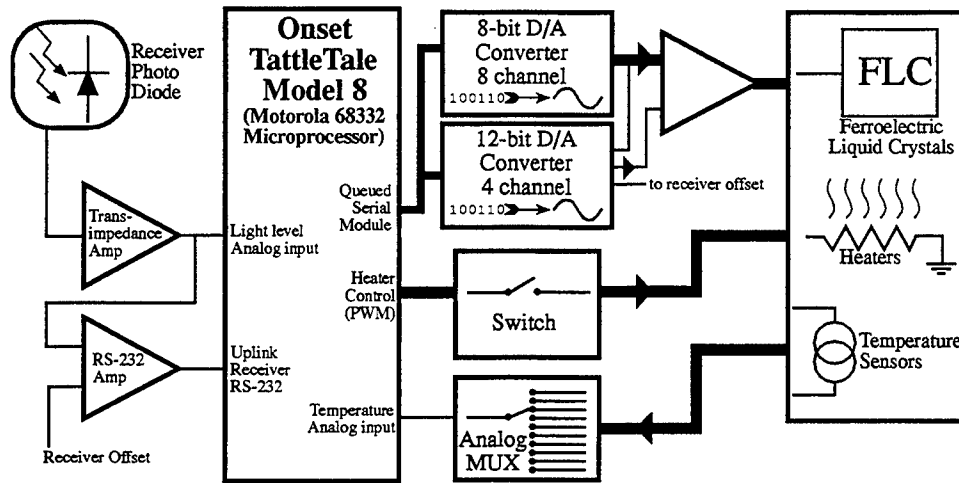
Figure 4: Block diagram of the electronics for the retromodulator communications experiment

crystals. Analog Devices AD590 temperature probes monitored the assemblies. The AD590 produces a current proportional to the temperature of the device. One microamp per degree Celsius ($1\mu A/^\circ C$). Dropping this current across a $10k\Omega$ resistor yielded ten millivolts per degree Celsius ($10mV/^\circ C$). To accommodate the nine temperature sensors an analog multiplexer was used. The output voltage of the MUX was input into one of the A/D channels on the TT8.

3.2 Optical Receiver

An optical detector system provided the balloon payload with the capability of receiving optical uplink data. A large active area silicon PIN photodiode was mounted on the bottom of the experiment. The two terminals of the unbiased diode fed up to the printed circuit board via a coaxial cable. Because of the low signal levels, careful considerations were made to reduce the additions of noise into the receiver system. The small currents from

the photo diode were input into a high gain transimpedence amplifier. The output of this stage connects to an A/D input of the TT8 and to another stage of gain. The A/D input allows the software to determine the level of light illuminating the experiment. This level is used to set the offset level in the next stage of gain. This light level is also valuable data because it can be used to verify part of the link analysis. The second stage of the receiver gain generates an RS-232 compatible signal. A simple level detection system coverts the analog light level signal into a digital communications signal. An offset from one of the 12-bit D/A converter channels is used to determine the transition level. The gain of this stage is set high enough to ensure a strong RS-232 output even at low light levels. Basically this op-amp is operating as a comparator, driving the output to the rails of the device. The output connects to one of the RS-232 receiver ports on the TT8.

3.3 Programming/Data Logger port

The payload electronics implement an interface to other computers using either a RS-232 or RS-422 communication standards. This allows easy access to the microprocessor for the purpose of programming and debugging the hardware and software. During the balloon flight this port connected to a data logger that recorded system health information.

3.4 Software

During the balloon flight the on board computer ran software that controlled the experiment. This software was developed in C on a desktop PC and then cross compiled using the Aztec C compiler and then loaded into the flash memory of the Tattletale model 8. The main functions of the software were

to modulate the FLCs, control the temperatures of the retromodulator assemblies, receive uplink data optically from the ground station, and maintain a system timing so that the system would be synchronized with computers and clocks at the ground station. The FLCs were modulated through several test patterns in order to better prove the concept of a passive optical communications system. The majority of the data needed could be obtained by modulating the FLCs at a 500Hz square wave. Short bursts of higher frequency modulations also were tested. Because of the lack of an RF uplink or down link while the balloon was in fight, the software performed these tasks optically. Several times during each ten minute cycle, the computer would send down system health information by modulating the FLCs using a RS-232 like communications scheme. Using this method, it was possible to monitor system health information real time.

System Timing Schedule The system repeats every ten minutes Starting on the hour, ten past, twenty past, etc. The schedule is as follows:

2 Minutes 500 Hz Square wave modulating the FLCs on the balloon

30 Seconds System health down link (temperature, light level, etc.) This information is sent five times along with other test patterns during this thirty second period.

30 Seconds Higher Frequency tests. Six five-second bursts of high frequency square waves are modulating the FLCs on the balloon. The frequencies sent are 1k, 5k, 10k, 1k, 5k and 10k Hertz.

2 Minutes Stage 2, System health down link, is repeated four times. (i.e. the system health is sent 20 times during this stage.)

19-17

5 Minutes FLCs open. This allows for scintillation studies on the reflected laser beam.

Also written into the software but not used in flight was the ability to uplink data to the experiment. Information is sent to the balloon by modulating the outgoing laser. This data is received by the balloon payload and echoed by the FLCs on the balloon. Further development of this code will lead to the ability of real time uplink commands to be sent using only an optical link.

4 Flight and Preliminary Results

On Sunday night September 15, 1996 at 11:14 PM the balloon retromodulator experiment was successfully launched. One aborted attempt, due to high ground winds, had been made earlier in the week. The payload was illuminated by the 810 nm IR laser and optically tracked by telescopes at SOR though out the flight. Returns from the retromodulator were observed when the payload entered a 45° cone above the SOR. Data on-board the payload were transferred to the ground using only the passive retromodulators. Some preliminary of the data has been made and is shown in Fig. 4. A clear 500 Hz square wave can be observed with scintillation varying the amplitude in addition to some high frequency noise due to shot processes.

All technical objectives of the experiment were met and the researchers involved were very satisfied. The payload was available for data collection and experiments at the float altitude for over 1.5 hours. During which time snap shots of the received waveform were recorded for latter analysis. Approximately 140 M bytes of data is yet to be reduced and compared with the theoretical performance of this compunctions link.
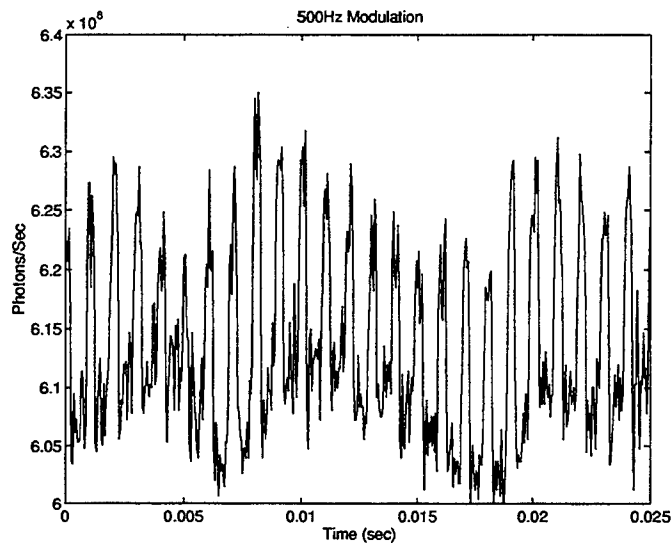
Figure 5: Sample data from a retromodulator at about 24 km range

5 Summary

The twelve weeks of the AFOSR summer research program have been very productive in developing and actually flying hardware for a retromodulator communications link. The tests achieved several firsts; The first retromodulator communications system to near space, the first laser communications experiment on a high altitude balloon, and the first high altitude balloon tracked by Starfire Optical Range. This project kept to an aggressively short time line and minimal budget. It involved a large number of people and several organizations including Utah State University/Space Dynamics Lab, the Air Force Phillips Lab (LI, VT, and SX), the Air Force Academy, and The Air Force Space and Missile Systems Center (TEB). All technical objectives of the experiment were met and the researchers involved were very satisfied. Considerable data has been generated that will help in the development of retromodulator communications systems. The AFOSR summer

research program is a very important and effective program in promoting cooperative research between Universities and the Air Force labs.

References

[1] Gary Jensen and Charles Swenson. A laser downlink for small satellites using an optically modulated retroreflector. In *Proc. 6th Annual AIAA/USU Conf Small Sat.*, 1992.

[2] Charles M. Swenson and Stephen Clarke. Reflected laser communication systems. Technical report, Air Force Office of Scientific Research / Phillips Lab, 1994.

[3] Charles M. Swenson and Gary L. Jensen. Low-power optical tranceiver for low earth orbit. In *SPIE Proceedings Vol 2553*, page 58, July 1995.

A STUDY OF COAXIAL VIRCATOR GEOMETRIES

Kevin Woolverton
Research Assistant
Department of Electrical Engineering

Pulsed Power Laboratory
Texas Tech University
Lubbock, TX 79409-3102

A STUDY OF COAXIAL VIRCATOR GEOMETRIES

Kevin Woolverton
Research Assistant
Department of Electrical Engineering
Pulsed Power Laboratory
Texas Tech University

Abstract

A study of efficiency improvement for a coaxial virtual cathode oscillator is presented. The coaxial geometry has many physical parameters that can be changed to alter the performance of the system. The parameters of interest include the placement of a ring cut in the anode base, and the polarity of the pulsed system. The ring is varied in width and in position from the center line. 43 variations were simulated and results normalized to the original configuration without a notch given. Comparisons of frequency, efficiency and particle dynamics of geometries with the pulsed system positive and negative is given. MAGIC, a 2-$\frac{1}{2}$ dimension particle-in-cell code, is used to simulate the different geometries.

A STUDY OF COAXIAL VIRCATOR GEOMETRIES

Kevin Woolverton

Introduction

Vircators are high-power microwave sources based on the bremsstrahlung radiation of relativistic electrons oscillating in electrostatic fields and are important microwave sources due to their simplicity and the fact that no external magnetic field is required for their operation. They require no heavy external coils or high-current power supplies. Vircators have been shown to be tunable and able to be phase-locked. Yet, vircators are not very efficient with typical efficiencies on the order of 2% for vircators with axial extraction and 0.6% for vircators with transverse extraction [1]. Hence, improvement in efficiency is an important area that has been extensively studied and which little is known about. Many different geometries have been studied to increase efficiency, including the reflex triode, the reditron and more recently the virtod [2].

The virtual cathode is formed by the space charge limiting current being exceeded, resulting in a depressed electrostatic field which overcomes the kinetic energy of incoming electrons. The electrons decelerate giving up energy to the microwave field. Then the electrons are accelerated away from the virtual cathode back towards the anode and towards the real cathode in a process called reflexing. This reflexing continues and produces microwaves at a frequency which is proportional to the square-root of the applied potential and inversely proportional to the anode-cathode gap spacing. But this is not the only mechanism for microwave production. When the virtual cathode forms, it is highly unstable and it changes in magnitude and position which is another mechanism for microwave production. This frequency with the reflexing frequency, is the plasma frequency of the virtual cathode.

Efficiency can be improved by trying to match the two frequencies or by eliminating one source of microwave production to let the other dominate, thus eliminating competition resulting in higher efficiency. The geometry under consideration is a coaxial vircator in which the microwaves are axially extracted perpendicular to the electron beam. Figure 1 shows the coaxial geometry. The anode is positively pulsed and a toroidal virtual cathode is formed. MAGIC, a 2-$\frac{1}{2}$ dimension particle-in-cell code, is used to simulate the different geometries.
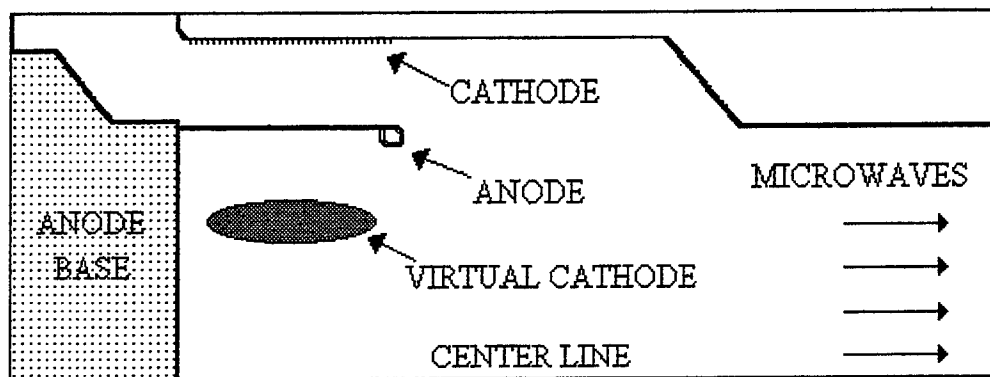
Figure 1: Coaxial Vircator Geometry

It has been put forward that efficiencies for the coaxial geometry are dependent upon a mechanism known as electron phase separation [3]. Phase separation is a mechanism that contains what are termed wrong-phased electrons and right-phased electrons. The wrong-phased electrons are the electrons that are accelerated at the expense of energy from the microwave field. The right-phased electrons are the electrons that are trapped in the potential well between the real and virtual cathodes. In the coaxial geometry, the right-phased electrons oscillate in the potential well and the wrong-phased electrons move towards the center axis where they are repelled by Coulombic forces. This process of electron movement has been observed in animated phase-

space plots from MAGIC. Thus, the wrong-phased electrons are caught in the interaction space, stored there, and radiate their own microwaves out of phase with the right-phased electrons. To eliminate these wrong-phased electrons, it has been suggested to place a center conducting rod down the center and placing a center rod is believed to increase efficiency [3], [4].

MAGIC simulations were run to determine the effect of placing a rod down the center of the system. In the determination of the rod's effectiveness, the input power, output power and efficiency is calculated at the dominant frequency. Most geometries studied here have the dominant frequency and direct comparison is only meaningful if this is the case. If the dominant frequency is different, then total power is used for comparison. Generally, the spectrum desired is a highly coherent signal with few peaks at multiple frequencies. Yet, in certain circumstances it might be desirable to have a wide range of frequencies at high power. Figure 2 shows the efficiencies of the different geometries at the dominant frequency. The rods have the following radii: 1 corresponds to a 4 millimeter radius, 2 corresponds to a 7.8 millimeter radius and 3 corresponds to a 11.5 millimeter radius. Also, a surprising result occurred when a hole was placed in the anode base instead of a rod, efficiency then increased significantly, both in the power at the main frequency and in the overall signal power.

The calculation of the efficiency was performed by taking a Fourier transform of the output signal to find the dominant frequency of the signal and the magnitude at the dominant frequency. Then, with an assumed mode, the power could be calculated. Similarly, the entire power in the signal was calculated where all frequencies were taken into account. Figure 3 shows the total output power, again normalized to the no-rod case.
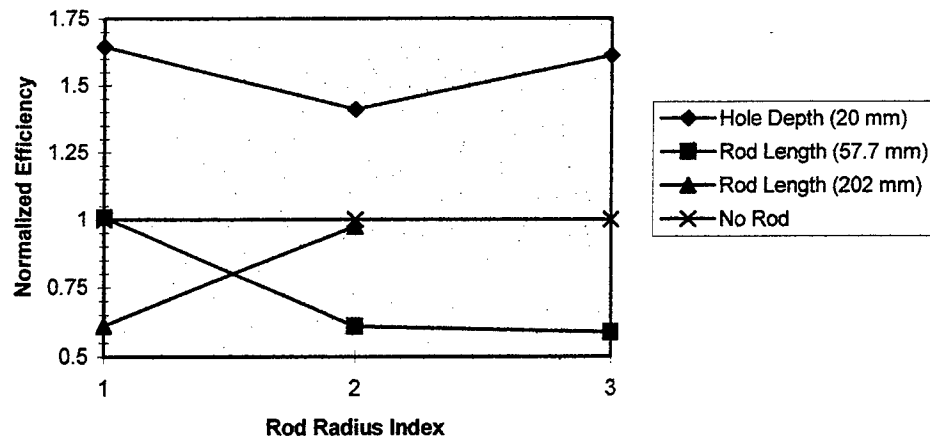
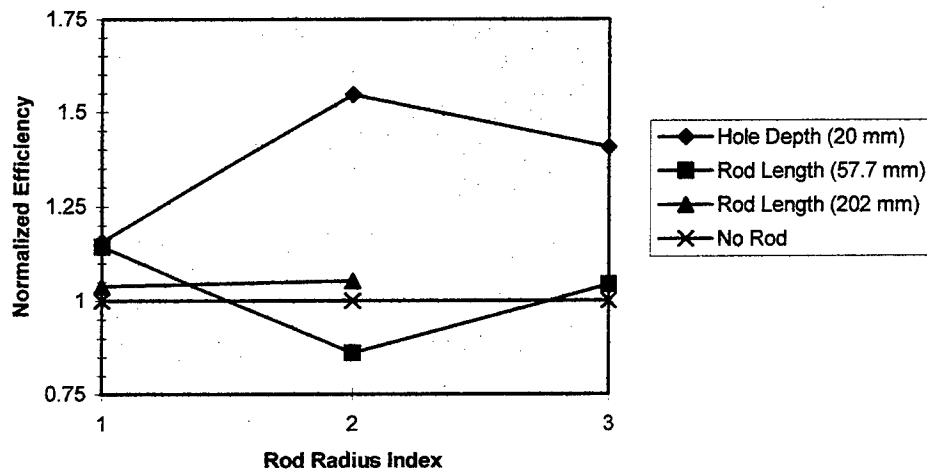Figure 2: Efficiency at the Main Frequency Normalized to no Rod

Figure 3: Efficiency Using Total Power Normalized to no Rod

Matching the diode impedance to the transmission line impedance is important for a maximum output power [3]. Making changes in the geometry resulted in little changes in impedance and was eliminated as the cause for the increased output. What appeared to occur is that the hole in the anode created a radial electric field, all along the axis, that discuraged

electrons from entering the region of wrong-phased electrons. It was also thought that a ring culd be used instead of a hole and this might better match the retarding field with the reflexing and increase efficiency further [5].

Simulations

Vircators are highly unstable devices and the fields in the interaction region are difficult to predict. It was found that a hole placed in the center of the anode base produced a higher efficiency than without the hole. The reason is that a radial electric field was produced that discouraged electrons from entering the wrong-phased region. With a ring cut into the anode base, at the appropriate radius, it might be more likely to match the reflexing mechanism. An additional effect from cutting a ring in the anode base that could also further increase the efficiency is that both sides of the ring produce fields that tend to keep electrons in the right-phased region and efficiencies are expected to increase in some cases as compared to the case where a hole is placed in the center. Figure 4 shows the geometry of the simulations performed.
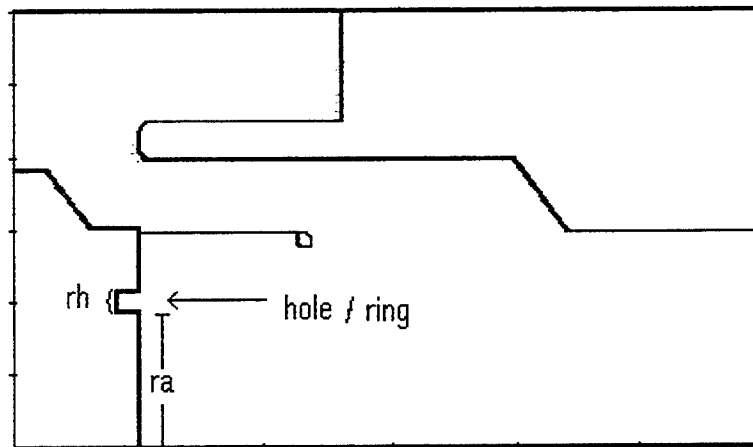
Figure 4: Coaxial Vircator with a hole

The variable "ra" is the distance from the center line to the beginning of the ring and "rh" is the

width of the ring. Figures 5 and 6 show the efficiency at the dominant frequency of the various parameters normalized to the no rod case. The ring depth is 0.2 cm. In the figures, the indexes on the horizontal axis represent the distance from the center line to the start of the ring. The index distances are: 1 corresponding to 3.1825 cm, 2 corresponding to 3.8485 cm, 3 corresponding to 4.5145 cm, 4 corresponding to 5.1805 cm, 5 corresponding to 5.8465 cm, 6 corresponding to 6.5125 cm, 7 corresponding to 7.1785 cm, 8 corresponding to 7.8445 cm, and 9 corresponding to 8.5105 cm.
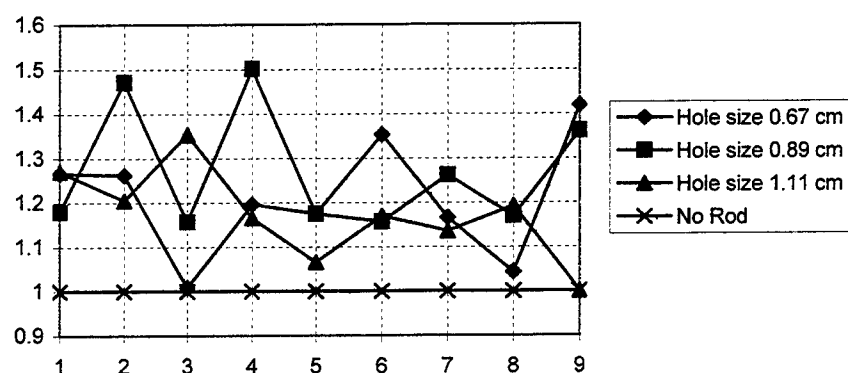
Figure 5: Efficiency at the Main Frequency Normalized to no Rod
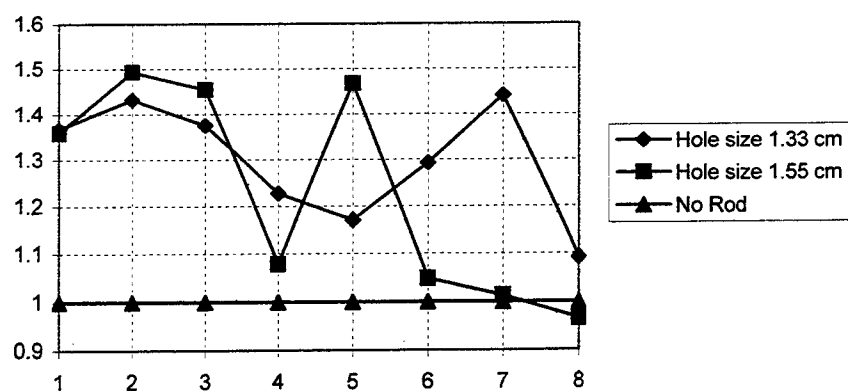
Figure 6: Efficiency at the Main Frequency Normalized to no Rod

Figures 7 and 8 show the efficiency of the overall power of the various parameters normalized to the no rod case.
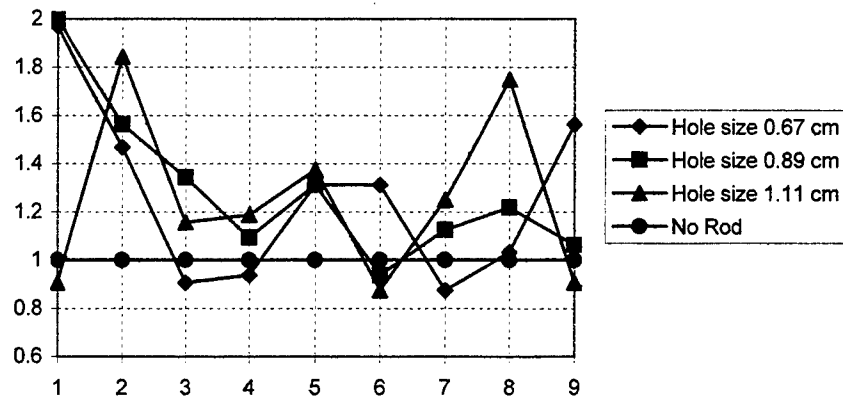
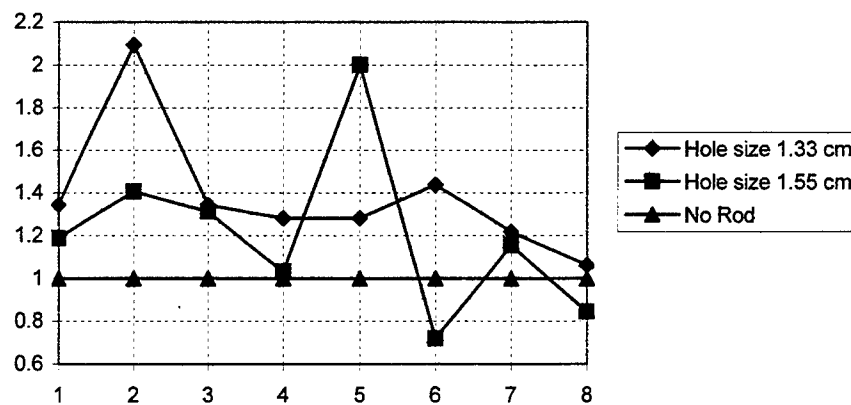Figure 7: Efficiency Using Total Power Normalized to no Rod

Figure 8: Efficiency Using Total Power Normalized to no Rod

All of the previous geometries were conducted with the inner conductor, the anode base, pulsed positively and the outer conductor grounded. Russian systems typically have the outer conductor grounded with the inner conductor being pulsed negatively, so a geometry was tested where the inner conductor was pulsed negatively like the Russian systems. The system was designed to be implemented in the current system with little modification and is shown below.
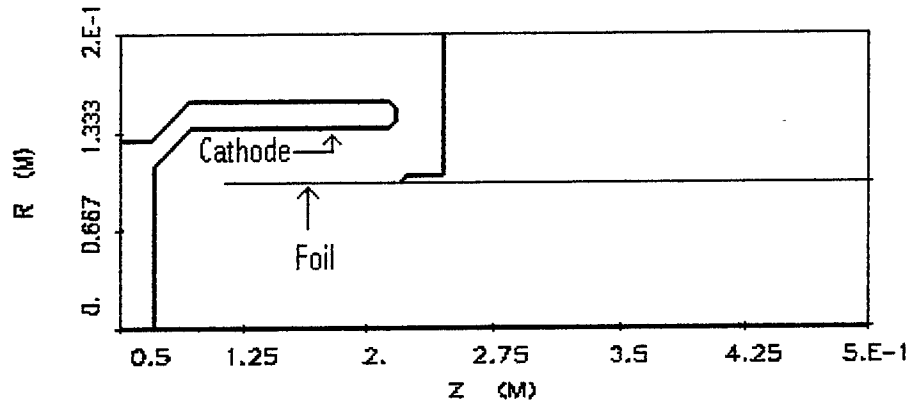
Figure 9: Negatively pulsed geometry

The negatively pulsed system's a-k gap was modified until the dominant frequency was comparable to the positively pulsed system's a-k gap. The original system had an a-k gap of 3.11 cm and the negatively pulsed system had an a-k gap of 3.77 cm. Even with the dominant frequency of the negatively pulsed system matching the positively pulsed system, it was still not set to maximize the output power since the incoming impedance did not match the diode impedance. Yet, the efficiency still increased. The normalized efficiency at the dominant frequency for the negatively pulsed system was found to be 1.9127 that of the positively pulsed system. The total normalized output power efficiency of the negatively pulsed system to that of the positively pulsed system was found to be 1.3438.

It was found that bunches of electrons get transmitted down the waveguide. These transmitted electrons, due to the negative potential of the negatively pulsed system, were significantly larger in number than those in the positively pulsed system where the electrons are drawn towards the positive potential. Hence, a natural mechanism existed to get rid of electrons in the virtual cathode region allowing new electrons to enter into the region and give up their energy to the microwave field. Figure 10 shows the phase-space plots of the two systems. The

positively pulsed system's phase-space plot is shown in figure 10A and the negatively pulsed system's phase-space plot is shown in figure 10B. Figure 11 shows the FFT of the systems. The positively pulsed system's FFT is shown in figure 11A and the negatively pulsed system's FFT is shown in figure 11B.
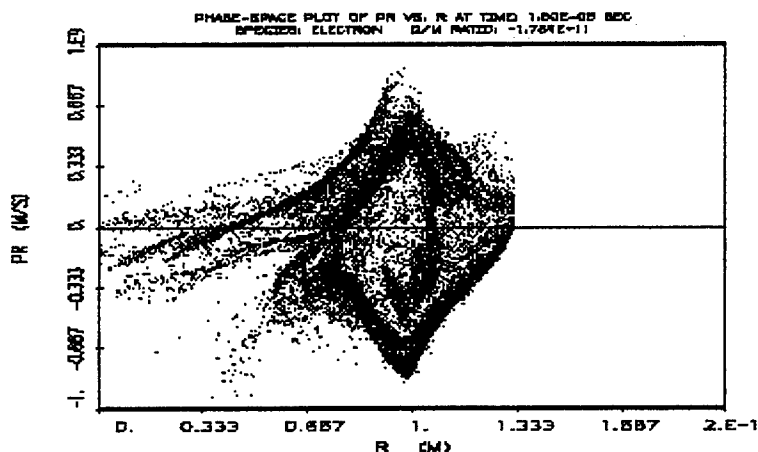

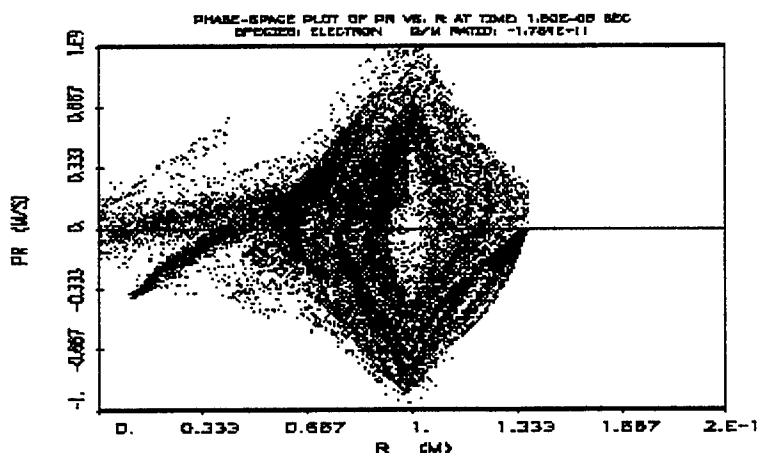Figure 10A: Phase-space Plot of Positively Pulsed System

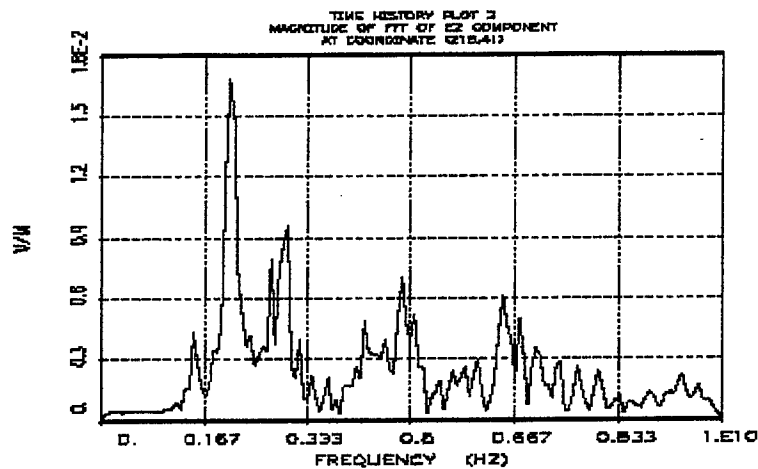Figure 10B: Phase-space Plots of Negatively Pulsed Systems
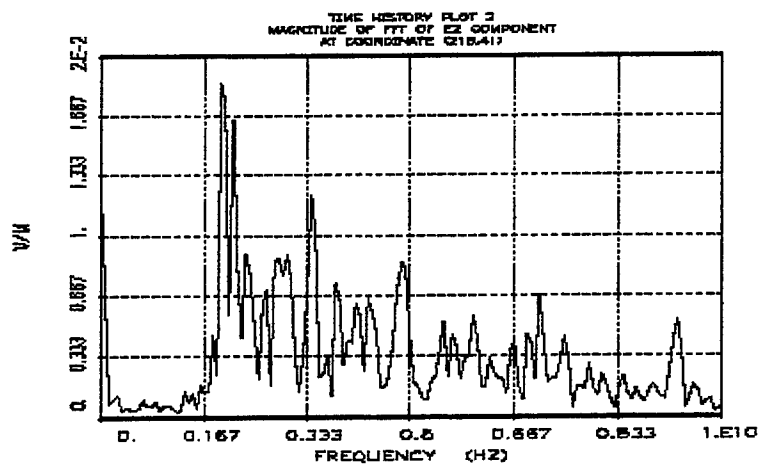
Figure 11A: FFT of Positively Pulsed System

Figure 11B: FFT of Negatively Pulsed System

Conclusion

The purpose of this study was to investigate geometries that increased the vircator's efficiency. It was put forward by the Russians that efficiency could be increased by placing a rod down the center to collect the wrong-phased electrons [3]. It was found that placing a rod down

the center only drew more electrons into the wrong-phased region, decreasing the efficiency, and placing a hole in the center increased the efficiency by producing a field that kept more electrons in the right-phased region [5]. By changing the hole in the center into a hole offset from the center producing a ring can increase the efficiency further. Finally, changing the system from a positively pulsed system into a negatively pulsed system created a mechanism for electrons to be eliminated from the virtual cathode region. This elimination also eliminated electrons in the wrong-phased region and significantly increased efficiency. Further improvements might be made by combining the two effects, placing a hole a distance from the center, producing a ring notch, in a negatively pulsed system.

Acknowledgements

[1]   Benford, J., Swegle, J., "High-Power Microwaves", Boston: Artech House, Inc. 1992.

[2]   S. B. Bludov, N. P. Gadetskii, K. A. Kravtsov, et. al., "Generation of High-Power Ultrashort Microwave Pulses and their Effect on Electronic Devices", Plasma Physics Reports, vol. 20, no. 8, 1994, pp. 712-717.

[3]   Selemir, V. D., Alekhin, B. V., et. al., Plasma Physics Reports, 1994, vol. 20, no. 8, ppl 621-639.

[4]   Crawford, Mark, Ph.D. Dissertation, Texas Tech University 1994.

[5]   Woolverton, Kevin, Kristiansen, M., Hatfield, L. L., "Coaxial Vircator Source Development", Beams 1996 Transactions.

EXACT POLE LOCATIONS OF DIELECTRIC GEOMETRICAL OBJECTS IN VARIOUS DIELECTRIC MEDIUM

Mark C. Worthy
Graduate Student
Department of Environmental Engineering

University of Alabama in Huntsville
Huntsville, AL 35899

21-1

EXACT POLE LOCATIONS OF DIELECTRIC GEOMETRICAL
OBJECTS IN VARIOUS DIELECTRIC MEDIUM

Mark C. Worthy
Graduate Student
Department of Environmental Engineering
University of Alabama in Huntsville

Abstract

The problem of buried ordnance detection is introduced. Specific discussion of the buried ordnance problem as it pertains to range cleanup efforts and its' financial future is presented. The dielectric properties of soils and plastic targets are given. The approach for finding exact pole locations from a dielectric infinite slab, a dielectric sphere, and a dielectric infinite cylinder is presented (and applied). The exact poles for the slab and sphere are found for various sizes and dielectric properties. There is a discussion (and use) of Carl E. Baum's perturbation formulas for dielectric slabs and spheres. George Hanson's results (formulas, from using Carl's same approach) are given (and used) for an infinite dielectric cylinder. The poles found from the perturbation formulas are compared with the exact poles and an "effective" region for using the perturbation formulas is established.

EXACT POLE LOCATIONS OF DIELECTRIC GEOMETRICAL OBJECTS IN VARIOUS DIELECTRIC MEDIUM

Mark C. Worthy

Introduction

As I discussed in my final report to RDL in 1993 the problem of removing unexploded ordnance on (and under) government land is a technical and financial nightmare. "As a result of decades of neglect, the American taxpayer will be saddled with billions of dollars in cleanup cost," said Rep. George Miller, D-Calif. [Associated Press, 1993]. According to the Department of Defense there are approximately nine million acres of past and present test ranges that contain ordnance [MMWG, 1996]. As a civilian what is perhaps most disturbing is that there are between 1200 and 1700 Formerly Used Defense Sites (FUDS, now public or private land) which are believed to be contaminated [MMWG, 1996]. The composition of the unexploded ordnance (UXO) ranges from plastics to various metals and ores (for instance: the UXO at Aberdeen Proving Ground in Maryland includes 82,000 kilograms of depleted uranium rounds) [Beamish, 1993]. Approaches to find the buried ordnance have included airborne sensors, IR imaging, magnetic sensors, ground penetrating radars (GPR's), and even a few attempts at acoustic imaging.

In December 1992 a Federal Advisory Committee to Develop On-Site Innovative Technologies (the DOIT Committee) was formed and (more importantly) funded to address this problem (and others). By late 1993 DOIT had set up four working groups that would specifically address the most important problems. As such the Military Munitions Working Group (MMWG) was one of these four and it would deal with ordnance contamination problem.

This is where I left this problem in 1993. There was a newly funded working group armed with a list of experienced scientists that, I thought, would surely tackle this problem. Unfortunately, I was wrong.

The biggest obstacle appears to have come from the DOIT Committee itself. In order to fund a project the DOIT Committee requires (and rightly so) that the technology be proven to work. Each year (1993, 94, 95, and 96), however, the MMWG's final report to the DOIT Committee says that there is still no proven technology.

As a result it is now August 1996 and very little lead-way has been made on this problem. One of the reasons has to do with MMWG's idea of proven technology. MMWG wants something that can tell the user whether or not the underground object that is being detected is in fact ordnance (and perhaps what type of ordnance it is) as opposed to just being an old soup can, plastic toy, or ordnance that has exploded and is now environmentally inert. Well if these things were in the air we might be able to do this; however, distinguishing objects underground can be an electromagnetic nightmare.

There are other funding considerations. One is what the DOD considers the standard of performance for detecting ordnance. This standard was developed years ago by the U.S. Army Corps of Engineers (USACE) using old technology (the Mark 26 Forester FEREX 4.021 magnetometer) [MMWG, 1996]. It is this low standard of performance that the DOD still bases its contract decisions on (for military base work). Because this standard is so low there has been no incentive for private industry to develop better technology (they only are required to use the old magnetometer specifications in there proposals). It is now the opinion of the MMWG itself that the standards be re-established [MMWG, 1996].

Another important consideration involves environmental regulations. In December of this year the EPA is supposed to issue new regulations specifically addressing the ordnance problem [MMWG, 1996]. This is a case where regulations could be good news because until now what laws there were on this problem were so vague that the government wasn't being forced to remove the ordnance. For instance, one way military ranges have been getting around declaring the UXO as waste has been to say that unexploded ordnance lying beneath or on the surface is considered to be the "ordinary use" of the object (not a "waste," if it were a waste they would have to find and remove the UXO's). The new regulations will, supposedly, require the removal of UXO's on FUDS as well as military ranges.

As far as future funding goes there is good news here as well. On June 22, 1996 officials from the DOD, DOI, DOE, and EPA signed a 235 billion dollar 10-year pact with the DOIT Committee for finding and implementing new technologies. So if these problems that I've addressed here are cleared up then the MMWG should see some of this funding.

As for improving the technology it would appear that the best approach involves developing a library of what the electromagnetic pole signatures of the various ordinance looks like. With such a library a user could know if what has been detected is of interest. Developing this library, however, is no simple task. In 1994 Carl E. Baum developed an approach for using perturbation formulas (much more condensed mathematical formulas) to find the signatures of basic dielectric geometrical shapes in a dielectric medium [Baum, 1994]. It is the purpose of this report to establish the effectiveness of these formulas by comparing them to the exact cases. If their effectiveness is proven then the same approach could be used in creating our library.

Dielectric Properties of Soils and the Ordnance

Scattering of electromagnetic waves occur when there is a difference between the dielectric properties of the target and the medium [McCann et al., 1988]. Dielectric targets of interest in the ordnance problem typically have a permittivity, ε, of about $2.5\varepsilon_o$. The earth, unfortunately, is not as predictable.

The dielectric properties of soil not only depend upon the type of soil but also the amount of moisture (and minerals) in the soil. For clays as the water content rises from 0 to 40% ε rises quickly from 3 to $\cong 20\varepsilon_o$ [Wang, 1978]. For sandy soils ε rises from 3 to $\cong 30\varepsilon_o$ [Wang, 1978]. The conductivity, σ, of the soils rises from $\cong .001$ to $\cong .1$ S/m for a rise in water content.

For the results found in the following pages I will use a target permittivity, ε_2, of $2.5\varepsilon_o$ and will look at soil permittivities, ε_1, ranging from 4 to $20\varepsilon_o$ and conductivity's, σ_1, ranging from .001 to 1 S/m. I will also look at the case where the target is in water $\varepsilon_1 = 81\varepsilon_o$ (and salt water $\varepsilon_1 = 81\varepsilon_o$, $\sigma_1 \cong 4$ S/m), as well as the case when $\varepsilon_1 >> \varepsilon_2$.

The Exact Approach

The signature differences of the scattered waves from a target not only depend upon these dielectric differences but also upon the various shapes and sizes of the targets. The scattered wave-forms for basic geometric shapes have been derived from many different physicist. The poles of these waves can be found by solving for the poles of the scattering coefficients. In the

following section I will present these derived wave-forms and there coefficients for a dielectric sphere, infinite slab, and infinite cylinder.

Before I present these three cases, however, I should define a few important terms. The relative dielectric constant, ε_r, will be defined as

$$\varepsilon_r \equiv \frac{t \arg et}{medium} = \frac{\varepsilon_2}{\varepsilon_1}$$

The propagation constants for the medium, γ_1, and the target, γ_2, are

$$\gamma_1 = s\sqrt{\mu_o \varepsilon_1}\left[1 + \frac{\sigma_1}{s\varepsilon_1}\right]^{\frac{1}{2}}$$

and

$$\gamma_2 = s\sqrt{\mu_o \varepsilon_2}$$

where $s = \Omega + j\omega \equiv$ the complex frequency.

Finally, the ratios of these propagation constants, ξ, will be defined as

$$\xi \equiv \frac{\gamma_1}{\gamma_2} = \varepsilon_r^{-\frac{1}{2}}\left[1 + \frac{\sigma_1}{s\varepsilon_1}\right]^{\frac{1}{2}}$$

Sphere:

The series solution for a plane wave falling upon a sphere was first introduced by Mie in 1908. In 1941 Julius Adams Stratton provided a more extensive and complete model of the problem in his infamous book entitled <u>Electromagnetic Theory</u>. For derivations of the following equations I refer you to Stratton, 1941 or the Laplace form in Baum, 1992.

The scattered electric, E, and magnetic, H, waves from a dielectric sphere are

$$E_{sc} = E_o f(s)\sum_{n=1}^{\infty} (-1)^n \frac{2n+1}{n(n+1)}\left[-a_n M_{n,o}(\gamma_1 r) + b_n N_{n,e}(\gamma_1 r)\right.$$

$$H_{sc} \equiv \frac{\sigma_1 + s\varepsilon_1}{\gamma_1} E_o f(s)\sum_{n=1}^{\infty}(-1)^n \frac{2n+1}{n(n+1)}\left[b_n M_{n,e}(\gamma_1 r) + a_n N_{n,o}(\gamma_1 r)\right.$$

Where r is the radius of the sphere and a_n and b_n are the scattering coefficients. These scattering coefficients are functions of $\gamma_1 r$ and $\gamma_2 r$, and they depend upon Bessel functions. Where here I will be using the modified spherical Bessel functions:

$$k_n(x) = \frac{e^{-x}}{x} \sum_{p=0}^{n} \frac{(n+p)!}{p!(n-p)!}(2x)^{-p}$$

$$i_n(x) = \frac{1}{2}\left[-k_n(-x) + (-1)^{n+1} k_n(x)\right]$$

The scattering coefficients have been derived as

$$a_n = \frac{-\left[\dfrac{1}{\xi}\left[\gamma_2 r i_n(\gamma_2 r)\right]' i_n(\gamma_1 r) - \gamma_2 r i_n(\gamma_2 r)\dfrac{\left[\gamma_1 r i_n(\gamma_1 r)\right]'}{\gamma_1 r}\right]}{\left[\dfrac{1}{\xi}\left[\gamma_2 r i_n(\gamma_2 r)\right]' k_n(\gamma_1 r) - \gamma_2 r i_n(\gamma_2 r)\dfrac{\left[\gamma_1 r k_n(\gamma_1 r)\right]'}{\gamma_1 r}\right]}$$

$$b_n = \frac{-\left[\left[\gamma_2 r i_n(\gamma_2 r)\right]' i_n(\gamma_1 r) - \gamma_2 r i_n(\gamma_2 r)\dfrac{\left[\gamma_1 r i_n(\gamma_1 r)\right]'}{\xi\gamma_1 r}\right]}{\left[\left[\gamma_2 r i_n(\gamma_2 r)\right]' k_n(\gamma_1 r) - \gamma_2 r i_n(\gamma_2 r)\dfrac{\left[\gamma_1 r k_n(\gamma_1 r)\right]'}{\xi\gamma_1 r}\right]}$$

In solving for the poles of the scattered waves, a_n will correspond to the H-modes, and b_n will correspond to the E-modes. Therefore, the exact poles, s_α, of the H-modes for a dielectric sphere can be found from the equation

$$\frac{1}{\xi}\left[\gamma_2 r i_n(\gamma_2 r)\right]' k_n(\gamma_1 r) - \gamma_2 r i_n(\gamma_2 r)\frac{\left[\gamma_1 r k_n(\gamma_1 r)\right]'}{\gamma_1 r} = 0$$

and the exact poles of the E-modes for a dielectric sphere can be found from the equation

$$\left[\gamma_2 r i_n(\gamma_2 r)\right]' k_n(\gamma_1 r) - \gamma_2 r i_n(\gamma_2 r)\frac{\left[\gamma_1 r k_n(\gamma_1 r)\right]'}{\xi\gamma_1 r} = 0$$

Slab:

We will now consider the case of the infinite dielectric slab, with thickness l, in a dielectric medium. Technically there would not be natural frequencies since the pole locations depend upon the direction of the incident wave [Baum, 1994]. However, since we are really interested in

finite size targets we will assume normal incidence. Making this assumption the scattering coefficient R_o, has been derived as [Baum, 1994]

$$R_o = \frac{\left[\xi^2 - 1\right]\sinh(\gamma_2 l)}{2\xi\cosh(\gamma_2 l) + \left[\xi^2 + 1\right]\sinh(\gamma_2 l)}$$

Note that there is only one scattering coefficient here. This is because the magnetic field is polarized (parallel to the electric field, so the E and H poles are the same). This implies that the exact poles, s_α, for the dielectric slab can be found from the equation

$$2\xi\cosh(\gamma_2 l) + \left[\xi^2 + 1\right]\sinh(\gamma_2 l) = 0$$

Cylinder:

For the dielectric infinite cylinder the we do not have the spherical wave-forms that we had in the case of the sphere. Therefore, the Bessel functions in the scattering coefficients will be the standard first and second order Bessel functions (not spherical or modified spherical). These Bessel functions in the integral form are

$$J_n(x) = \frac{1}{\pi}\int_0^\pi \cos(x\sin\theta - n\theta)d\theta$$

and

$$H_n(x) = J_n(x) - iY_n(x)$$

where

$$Y_n(x) = \frac{1}{\pi}\int_0^\pi \sin(x\sin\theta - n\theta)d\theta - \frac{1}{\pi}\int_0^\infty \left[e^{n\phi} + (-1)^n e^{-n\phi}\right]e^{-x\sinh\phi}d\phi$$

The scattering coefficients a_n, and b_n derived in the ω form (s = jω) are [Balanis, 1989]

$$a_n = \frac{J_n'(\gamma_2 r)J_n(\gamma_1 r) - \xi J_n'(\gamma_1 r)J_n(\gamma_2 r)}{\xi J_n(\gamma_2 r)H_n'(\gamma_1 r) - J_n'(\gamma_2 r)H_n(\gamma_1 r)}$$

$$b_n = \frac{\xi J_n'(\gamma_2 r)J_n(\gamma_1 r) - J_n'(\gamma_1 r)J_n(\gamma_2 r)}{J_n(\gamma_2 r)H_n'(\gamma_1 r) - \xi J_n'(\gamma_2 r)H_n(\gamma_1 r)}$$

In the case of the dielectric cylinder the a_n coefficient corresponds to the E-modes and the b_n coefficient corresponds to the H-modes. Therefore, the exact poles, ω_α ($s_\alpha = j\omega_\alpha$), for the infinite dielectric cylinder can be found by

$$\xi J_n(\gamma_2 r)H_n'(\gamma_1 r) - J_n'(\gamma_2 r)H_n(\gamma_1 r) = 0$$

for the E-modes and

$$J_n(\gamma_2 r)H_n'(\gamma_1 r) - \xi J_n'(\gamma_2 r)H_n(\gamma_1 r) = 0$$

for the H-modes.

Perturbation Formulas

To the casual observer these exact formulas probably don't look so bad. However, anyone who has ever had to expand Bessel functions will tell you that finding the poles of functions that contain multiples and derivatives (and multiples of derivatives) of Bessel functions would be a cumbersome task. Recall also that these exact formulas are for nice geometrically shaped objects. Pole functions for real ordnance cases would be even more busy (much more). With this in mind Carl E. Baum made some approximations that would make these functions easier to work with for the slab and the sphere. The hope is that these perturbation functions will give results so close to the exact functions that others will be able to apply similar approximations to the exact pole functions for the real ordnance cases. The following paragraphs will show Baum's results for the slab and the sphere from his July 24, 1994 interaction note (IN 504).

Slab:

For the slab we will define the natural frequencies as

$$s_\alpha = s_{\alpha,0} + \Delta s_\alpha$$

where $s_{\alpha,0}$ is found from the limiting case when $\xi \to \infty$ giving

$$\sinh(s_{\alpha,0}\sqrt{\mu_o \varepsilon_2}\, l) = 0$$

note that this number will be imaginary. For Δs_α I refer you to Baum's work where

$$\Delta s_\alpha \approx -\frac{2\varepsilon_r^{\frac{1}{2}}}{\sqrt{\mu_o \varepsilon_2}\, l}\left[1 + \frac{i}{2}\frac{\sigma_1}{s_{\alpha,0}\varepsilon_1}\right]$$

Sphere:

The same method applied to the sphere has similar results where the poles are still

$$s_\alpha = s_{\alpha,0} + \Delta s_\alpha$$

Now, however, we will have different $s_{\alpha,0}$; one for the H-modes and one for the E-modes. For the H-modes as $\xi \to \infty$ we see that the exact formulas can reduce to

$$i_n(\gamma_2 r) = 0, \text{ or in other words: } i_n(s_{\alpha,0}\sqrt{\mu_o \varepsilon_2}\, r) = 0,$$

For the E-modes as $\xi \to \infty$ we can see that the exact formulas can reduce to

$$\left[\gamma_2 r i_n(\gamma_2 r)\right]' = 0, \text{ or in other words: } \left[s_{\alpha,0}\sqrt{\mu_o \varepsilon_2}\, r i_n(s_{\alpha,0}\sqrt{\mu_o \varepsilon_2}\, r)\right]' = 0$$

Again, $s_{\alpha,0}$ is a purely imaginary number. The Δs_α term for the sphere is nearly identical to the slab where

$$\Delta s_\alpha \approx -\frac{\varepsilon_r^{\frac{1}{2}}}{\sqrt{\mu_o \varepsilon_2}\, r}\left[1 + \frac{i}{2}\frac{\sigma_1}{s_{\alpha,0}\varepsilon_1}\right]$$

for the H-modes and

$$\Delta s_\alpha \approx -\frac{\varepsilon_r^{\frac{1}{2}}}{\sqrt{\mu_o \varepsilon_2}\, r}\left[1 + \frac{i}{2}\frac{\sigma_1}{s_{\alpha,0}\varepsilon_1}\right]\frac{(s_{\alpha,0}\sqrt{\mu_o \varepsilon_2}\, r)^2}{(s_{\alpha,0}\sqrt{\mu_o \varepsilon_2}\, r)^2 + n(n+1)}$$

for the E-modes.

Cylinder:

A fellow SRP worker (for RDL) George Hanson used Carl's same approach for an infinite dielectric cylinder. The results again, were very similar. Where $s_{\alpha,o} = j\omega_{\alpha,o}$, for the E-modes $s_{\alpha,0}$ can be found from $J_n(\gamma_2 r) = 0$, or in other words: $J_n(\omega_{\alpha,0}\sqrt{\mu_o \varepsilon_2}\, r) = 0$, and for the H-modes $s_{\alpha,0}$ can be found from $J_n'(\gamma_2 r) = 0$, or in other words: $J_n'(\omega_{\alpha,0}\sqrt{\mu_o \varepsilon_2}\, r) = 0$. For Δs_α George found

$$\Delta s_\alpha \approx \frac{-\varepsilon_r^{\frac{1}{2}}}{\sqrt{\mu_o \varepsilon_2}\, r}\left[1 + \frac{i}{2}\frac{\sigma_1}{s_{\alpha,0}\varepsilon_1}\right] \qquad \text{for the E-modes, and}$$

$$\Delta s_\alpha \approx \frac{-\varepsilon_r^{\frac{1}{2}}}{\sqrt{\mu_o \varepsilon_2} \, r} \left[1 + \frac{i}{2} \frac{\sigma_1}{s_{\alpha,0} \varepsilon_1} \right] \frac{(s_{\alpha,0} \sqrt{\mu_o \varepsilon_2} \, r)^2}{(s_{\alpha,0} \sqrt{\mu_o \varepsilon_2} \, r)^2 - n^2} \qquad \text{for the H-modes.}$$

The Results

The results were found with great assistance from the Mathcad 6.0 Plus software using the root finder function. However, in order to find the exact (and perturbed) function's poles for the first three E-modes and H-modes the functions had to be greatly simplified before they could be put into Mathcad. This meant analytically expanding, multiplying, and taking the derivatives of the first three Bessel, Hankle, modified spherical Bessel, and modified spherical Hankle functions (then reducing them). Reducing them was a tedious but necessary task (Mathcad's root finder wouldn't work with the functions in their expanded form). The root finder itself uses the secant method (similar to the Newton method). It was still necessary to make some adjustments to the software before it would work, and anyone who has ever used this root finder knows that it is highly dependent on good initial guesses.

In the case of the cylinder I was unable to find the exact poles. The problem revolved around the standard Newman functions (and their derivatives). The software could calculate values for the exact functions, but to set them equal to zero to find the roots would cause the software to lock up. I had to truncate part of the integration involved in the Newman functions in order to get results. Therefore, what poles were found for the dielectric cylinder were not "exact." These poles did, however, provide a "check" for the poles from the perturbation formulas. Note that I could find poles from the perturbation formulas for the cylinder but not from the exact formulas (hence, the perturbation formulas are already proving their usefulness).

In order to show all of my results for this project I would need to far exceed my 20 page limit guideline (or else use an unreadably small font). Therefore, I will instead list all of the cases that I found poles for (for the sphere and the slab), show a few examples of the exact verses perturbed poles, present a graph showing the most effective regions of the perturbed functions, and give an example of the perturbed function's poles for the infinite cylinder.

The following is a list of the 42 different cases that poles were found for both the exact and the perturbed functions for the dielectric slab and sphere.

$\varepsilon_1/\varepsilon_o$	σ_1	$\varepsilon_2/\varepsilon_o$	r, L
4	0, .01, .1	2.5	10cm
5	0, .01, .1	2.5	10cm
5	0, .01, .1	2.5	50cm
6.25	.094, .15	2.5	10cm
10	0, .001, .01, .1, .17	2.5	10cm
10	.2, .235, .27, .3	2.5	10cm
10	0, .01, .1	2.5	50cm
20	0, .01, .1, .2, .3, .4	2.5	10cm
81	0, .01, .1, 1, 1.36, 2.6, 4	2.5	10cm
1E+09	0, .1, 1.0	1	10cm
1.00E+09	1.0E+07	1	10cm
1E+09	1.5E+09	1	10cm
1E+09	2.1E+09	1	10cm

Now I will present 3 examples of these 42 different cases.

For $\varepsilon_1/\varepsilon_o = 20$, $\sigma_1 = 0.1$ S/m, $\varepsilon_2/\varepsilon_o = 2.5$, and r = L =10cm the poles are:

Dielectric Slab:

Exact Pole Locations	Poles From Perturbed Functions
S = -1412707635 ± 5885016898j Rad/s	S = -1404263208 ± 5956625173j Rad/s
S = -1404042987 ± 11877057377j Rad/s	S = -1372487458 ± 11913250346j Rad/s
S = -1402450255 ± 17845701316j Rad/s	S = -1361895541 ± 17869875519j Rad/s

Dielectric Sphere:

H-modes:

Exact Pole Locations (n = 1)	Poles From Perturbed Functions
S = -702802199 ± 8494151033j Rad/s	S = -692572049 ± 8519741048j Rad/s
S = -701335900 ± 14632677053j Rad/s	S = -683277959 ± 14647484452j Rad/s
S = -700963871 ± 20664312364j Rad/s	S = -679510783 ± 20674789103j Rad/s

Exact Pole Locations (n = 2)	Poles From Perturbed Functions
S = -703774677 ± 10907785129j Rad/s	S = -687676435 ± 10927822261j Rad/s
S = -701862369 ± 17232015601j Rad/s	S = -681331825 ± 17244620616j Rad/s
S = -701281840 ± 23355662653j Rad/s	S = -678456717 ± 23364945263j Rad/s

Exact Pole Locations (n = 3)	Poles From Perturbed Functions
S = -2149393851 ± 7684455686j Rad/s	S = -1910671582 ± 7610165973j Rad/s
S = -703229571 ± 14280728878j Rad/s	S = -683575371 ± 14317938563j Rad/s
S = -701507619 ± 20459222977j Rad/s	S = -679599668 ± 20475984445j Rad/s

E-modes:

Exact Pole Locations (**n = 1**)	Poles From Perturbed Functions
S = -945474120 ± 5208046179j Rad/s	S = -962437415 ± 5202213524j Rad/s
S = -739813302 ± 11580719706j Rad/s	S = -725455032 ± 11597707281j Rad/s
S = -716946825 ± 17652958869j Rad/s	S = -697133855 ± 17664794039j Rad/s

Exact Pole Locations (**n = 2**)	Poles From Perturbed Functions
S = -1142426611 ± 7407776310j Rad/s	S = -1161347249 ± 7338176235j Rad/s
S = -784516407 ± 14100717019j Rad/s	S = -766817313 ± 14112485162j Rad/s
S = -738624749 ± 20302712560j Rad/s	S = -717166945 ± 20312433204j Rad/s

Exact Pole Locations (**n = 3**)	Poles From Perturbed Functions
S = -725610376 ± 11527141264j Rad/s	S = -1019745178 ± 11495148305j Rad/s
S = -730930664 ± 17499599769j Rad/s	S = -792861036 ± 17499828530j Rad/s
S = -718255854 ± 23531418977j Rad/s	S = -735691318 ± 23536182094j Rad/s

For $\varepsilon_1/\varepsilon_o$ = 5.0, σ_1 = 0.1 S/m, $\varepsilon_2/\varepsilon_o$ = 2.5, and r = L =10cm the poles are:

Dielectric Slab:

Exact Pole Locations	Poles From Perturbed Functions
S = -3366739206 ± 11387158523j Rad/s	S = -2935629419 ± 11913250346j Rad/s
S = -3352533035 ± 17525889101j Rad/s	S = -2850894084 ± 17869875519j Rad/s
S = -3347929821 ± 23570193197j Rad/s	S = -2808526417 ± 23826500692j Rad/s

Dielectric Sphere:

H-modes:

Exact Pole Locations (**n = 1**)	Poles From Perturbed Functions
S = -1634852502 ± 8153523761j Rad/s	S = -1518441276 ± 8519741047j Rad/s
S = -1659911355 ± 14438608468j Rad/s	S = -1444088494 ± 14647484456j Rad/s
S = -1665623781 ± 20527555920j Rad/s	S = -1413951142 ± 20674789104j Rad/s

Exact Pole Locations (**n = 2**)	Poles From Perturbed Functions
S = -1669986985 ± 10636884958j Rad/s	S = -1479276363 ± 10927822269j Rad/s
S = -1671129698 ± 17065639153j Rad/s	S = -1428519373 ± 17244620615j Rad/s
S = -1671194846 ± 23233996050j Rad/s	S = -1405518616 ± 23364945263j Rad/s

Exact Pole Locations (**n = 3**)	Poles From Perturbed Functions
S = -3691185912 ± 8109486893j Rad/s	S = -2750875426 ± 7637320345j Rad/s
S = -1676580259 ± 13995667729j Rad/s	S = -1446467845 ± 14317938560j Rad/s
S = -1670581700 ± 20299955652j Rad/s	S = -1414662236 ± 20475984444j Rad/s

E-modes:

Exact Pole Locations (n = 1)	Poles From Perturbed Functions
S = -2137829857 ± 4785927350j Rad/s	S = -2222159291 ± 5202213524j Rad/s
S = -1733425231 ± 11338919712j Rad/s	S = -1554360857 ± 11597707281j Rad/s
S = -1696026337 ± 17493802291j Rad/s	S = -1460073289 ± 17664794039j Rad/s

Exact Pole Locations (n = 2)	Poles From Perturbed Functions
S = -2553827566 ± 7319835451j Rad/s	S = -2580872335 ± 7338176235j Rad/s
S = -1844107480 ± 13906854986j Rad/s	S = -1623880445 ± 14112485162j Rad/s
S = -1747380786 ± 20165137979j Rad/s	S = -1493327496 ± 20312433204j Rad/s

Exact Pole Locations (n = 3)	Poles From Perturbed Functions
S = -1607432764 ± 11429608048j Rad/s	S = -2186173588 ± 11495148305j Rad/s
S = -1718891503 ± 17377228736j Rad/s	S = -1661258074 ± 17499828530j Rad/s
S = -1702235153 ± 23425320722j Rad/s	S = -1523709239 ± 23536182094j Rad/s

For $\varepsilon_1/\varepsilon_o$ = 1000000000, σ_1 = 0 to 1 S/m, $\varepsilon_2/\varepsilon_o$ = 1, and r = L =10cm the poles are:

Dielectric Slab:

Exact Pole Locations	Poles From Perturbed Functions
S = -189605 ± 9418251357j Rad/s	S ≈ same
S = -189605 ± 18836502714j Rad/s	S ≈ same
S = -189605 ± 28254754071j Rad/s	S ≈ same

Dielectric Sphere:

H-modes:

Exact Pole Locations (n = 1)	Poles From Perturbed Functions
S = -94802 ± 13470893394j Rad/s	S ≈ same
S = -94802 ± 23159706436j Rad/s	S ≈ same
S = -94802 ± 32689711857j Rad/s	S ≈ same

Exact Pole Locations (n = 2)	Poles From Perturbed Functions
S = -94802 ± 17278404105j Rad/s	S ≈ same
S = -94802 ± 27266139265j Rad/s	S ≈ same
S = -94802 ± 36943222210j Rad/s	S ≈ same

Exact Pole Locations (n = 3)	Poles From Perturbed Functions
S = -94802 ± 22638648625j Rad/s	S ≈ same
S = -94802 ± 32375374089j Rad/s	S ≈ same
S = -94802 ± 41938997315j Rad/s	S ≈ same

E-modes:

Exact Pole Locations	(n = 1)	Poles From Perturbed Functions
$S = -100156 \pm 18337585322j$ Rad/s		$S \approx$ same
$S = -97038 \pm 27930491780j$ Rad/s		$S \approx$ same
$S = -96034 \pm 37431872789j$ Rad/s		$S \approx$ same

Exact Pole Locations	(n = 2)	Poles From Perturbed Functions
$S = -158153 \pm 11602675385j$ Rad/s		$S \approx$ same
$S = -106317 \pm 22313798279j$ Rad/s		$S \approx$ same
$S = -100032 \pm 32116776872j$ Rad/s		$S \approx$ same

Exact Pole Locations	(n = 3)	Poles From Perturbed Functions
$S = -140756 \pm 18175425338j$ Rad/s		$S \approx$ same
$S = -110347 \pm 27669658409j$ Rad/s		$S \approx$ same
$S = -102809 \pm 37213971421j$ Rad/s		$S \approx$ same

Condensing all 42 different cases into a graph that would establish an effective region for the perturbation functions required two jobs. First I found the percent errors for all 42 cases between the exact verses perturbed poles. Then I established two dimensionless parameters, τ and ε_r, for graphing. Where:

$$\tau = \frac{r\sigma_1\sqrt{\mu_o\varepsilon_2}}{\varepsilon_1} \quad \text{and} \quad \varepsilon_r = \frac{\varepsilon_2}{\varepsilon_1}$$

In the following graphs everything inside the curves represents a "good" region. In the first graph the perturbed functions were less than 6% off for the region inside the curve, and in the second graph (next page) the perturbed functions were less than 2% off.
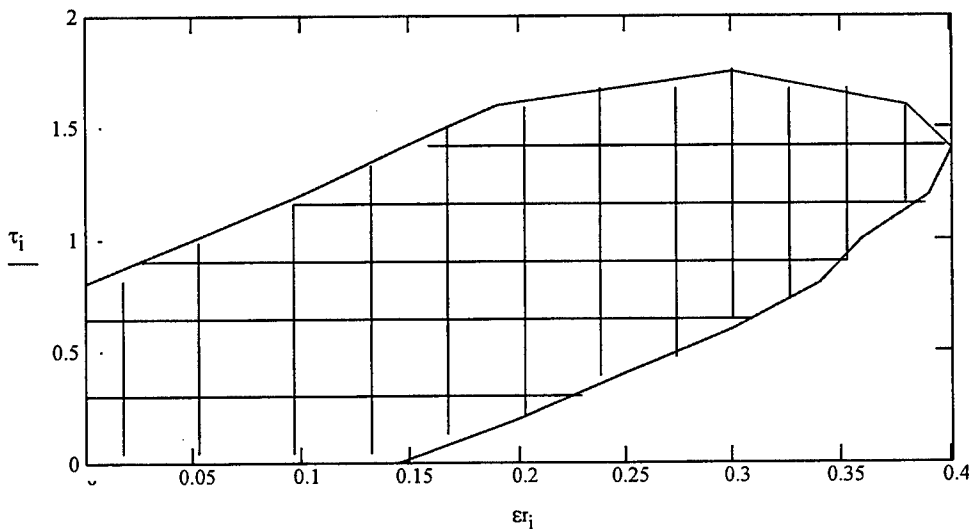
Graph 1: < 6% error for perturbed functions
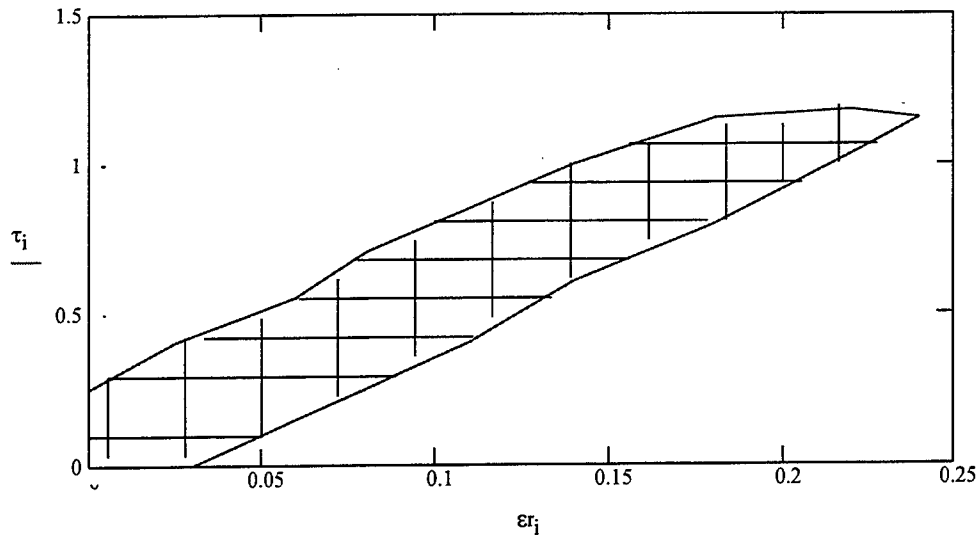
Graph 1: < 2% error for perturbed functions

For some idea of what the poles look like for a dielectric infinite cylinder in a dielectric medium I will present one of the eight cases that I looked at (for the perturbation functions). For $\varepsilon_1/\varepsilon_o = 10$, $\sigma_1 = 0.1$ S/m, $\varepsilon_2/\varepsilon_o = 2.5$, and $r = L = 10$cm the poles are:

Dielectric Cylinder:

H-modes:

Poles From Perturbed Functions (**n = 1**)   Poles for the Perturbed Functions (**n = 2**)

S = -1344697098 ± 3273462241j Rad/s   S = -1659709311 ± 5629149005j Rad/s
S = -982595207 ± 10053805484j Rad/s   S = -1040579416 ± 12668967842j Rad/s
S = -961217428 ± 16151768747j Rad/s   S = -987779919 ± 18873126920j Rad/s

Poles From Perturbed Functions (**n = 3**)

S = -1934413437 ± 7828540854j Rad/s
S = -1102472693 ± 15156345008j Rad/s
S = -1019288657 ± 21485713812j Rad/s

E-modes:

Poles From Perturbed Functions (**n = 1**)   Poles for the Perturbed Functions (**n = 2**)

S = -948026340 ± 7191428082j Rad/s   S = -948026340 ± 9682431336j Rad/s
S = -948026340 ± 13261675545j Rad/s   S = -948026340 ± 15925993861j Rad/s
S = -948026340 ± 19261677782j Rad/s   S = -948026340 ± 22007531888j Rad/s

21-16

Poles From Perturbed Functions ($n = 3$)

$S = -948026340 \pm 12052868409j$ Rad/s

$S = -948026340 \pm 18478487610j$ Rad/s

$S = -948026340 \pm 24655812211j$ Rad/s

Discussion

The first point that I would like to make is about the nature of the poles themselves (exact or perturbed). Note that the closer ε_1 gets to ε_2 the more shift to the left for the real components (with very little change in the imaginary terms). I should also point out that for the exact poles there was a non complex pole that doesn't show up using the perturbed functions. However, since real roots don't oscillate they wouldn't show up on radar anyway. Notice also the "layering" effect for the poles of the sphere and slab.

The effect of the conductivity term, σ_1, is not shown in the results. Basically its effect is

Sphere/Slab Poles for $\sigma_1 = 0$ Sphere/Slab Poles for increasing σ_1
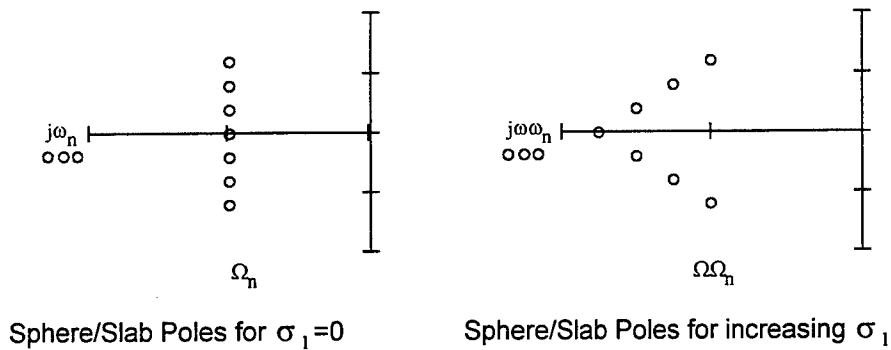
The greater the conductivity of the soil the more acutely angled shaped the pole-layer became. Where the perturbation formulas usually had greatest errors for the most damped of those poles (poles that were furthest left).

As for the size of the target usually being 10cm, generating poles for other size targets would simply involve the following: if the target is increased in size by some factor, k, then the poles would be decreased by this same factor and vice-versa (for $\sigma_1 = 0$; this is only an approximation for other σ_1).

For cases where $\varepsilon_1 \gg \varepsilon_2$ increasing ε_1 by a factor of 100 decreased the real part of the poles by a factor of 10 (for $\varepsilon_2 = 1$). The imaginary term remained the same.

21-17

There were some unexpected results in comparing the poles for the exact verses perturbed functions. Notice from the graphs (in the result section) that there are many cases where some εr would contain "good" values but for $\sigma_1 = 0$ ($\tau = 0$) the percent errors were to large to be considered "good." I noticed when compiling the percent errors that as σ_1 is increased (hence, as τ is increased) the error decreased until it reached some minimum, then the error would begin to increase until it was too large to be considered "good." This explains the reason for the similar shapes of the two graphs ("<6% error," verses "<2% error").

The effectiveness region established for the perturbation functions would be applicable to many different soils. Where for soils (with plastic targets) τ ranges between 0 and 1 and ε_r ranges between 0.1 and 0.6. The "<6% error" graph shows "good" results for τ ranging (nonlinearly) from 0 to 1.75 and ε_r ranging (nonlinearly) from 0 to 0.4. The **best** results from the perturbed functions correspond to low-moisture soils.

As for the dielectric cylinder, notice that poles for the H-modes and the E-modes have "switched" roles as compared to the dielectric sphere. Evidence for this happening can be found by comparing the pole functions of the sphere with the cylinder (in previous sections). Again, the poles in the result section were found from the perturbation formulas. Notice that the "layering" effect occurs with the cylinder's poles as well. However, with the cylinder it seems that increasing the conductivity of the medium causes a decrease in the imaginary terms (not the large increase in the magnitude of the real terms like with the slab and sphere).

In comparing the poles from the perturbed formulas for the cylinder with the poles from the "near" exact formulas I was able to get low percent errors. In fact the results seemed to show basically the same effectiveness region that was found for the sphere and slab case. However, since I was unable to get the "exact" poles (due to the computer limitations discussed earlier) I will not be presenting these results.

Conclusions

The buried ordnance problem was introduced. The present financial state of the UXO problem was discussed.

The exact approach for finding the natural signatures for a dielectric sphere, and an infinite dielectric slab and cylinder were presented. This approach was used to find these poles for various size targets and different dielectric mediums.

An approximate approach for finding these same results was presented. The results found from these approximation formulas were compared to the exact poles. A region of effectiveness was established for these approximating formulas. This region varied with for τ ranging (nonlinearally) from 0 to 1.75 and ε_r ranging (nonlinearally) from 0 to 0.4. The effective region theoretically contains many different types of soils. The approximation formulas showed the best results for low-moisture soils.

The approximation formulas proved their usefulness when the "exact" poles could not be found for a dielectric infinite cylinder. Although, "nearly" exact poles for the cylinder showed that the effectiveness region is close to that of the dielectric slab and sphere.

With these three very different shapes having basically the same effectiveness region, I feel fairly confident that this effectiveness region will be the same for any of the specific buried plastic ordnance cases. Therefore, the approximation approach made by Carl E. Baum will be of great assistance in developing a library of the natural frequencies of different plastic ordnance.

References

Associated Press release (unauthored), Dozens of former U.S. military sites may be sitting on ordnance, The Huntsville Times; Huntsville, Alabama; April, 1993.

Balanis, C.A., Advanced Engineering Electromagnetics, John Wiley and Sons, Inc., New York, 1989.

Baum, C.E., Concerning the identification of buried dielectric targets, Phillips Laboratory's Interaction Note 504, July, 1994.

Baum, C.E., Representation of surface current density and far scattering in EEM and SEM with entire functions, Phillips Laboratory's Interaction Note 486, February, 1992.

Beamish, R., Taxpayer-owned land full of hazards, report finds, Albuquerque Journal; Albuquerque, NM; A7, July 9, 1993.

Federal Advisory Committee To Develop On-Site Innovative Technologies (unauthored), Military Munitions Working Group - final report, Western Governors Association, Denver, CO, June, 1996.

McCann, D.M., P.D. Jackson, and P.J. Fenning, Comparison of the seismic and ground probing radar methods in geological surveying, Proc. IEE, 135(F-4), 380-389, 1988.

Stratton, J.A., Electromagnetic Theory, McGraw-Hill Book Company, New York, London, 1941.

Wang, J., T. Schmugge, and D. Williams, Dielectric constants of soils at microwave frequencies-II, NASA Technical Paper 1238; Goddard Space Flight Center; Greenbelt, Maryland; 1978.

A Preliminary Study for Computer Simulations of Plasma-Filled Backward Wave Oscillators

Douglas T. Young
Department of Physics

Texas Tech University
Department of Physics
Lubbock, TX 79401-1051

A Preliminary Study for Computer Simulations of Plasma-Filled Backward Wave Oscillators

Douglas Young
Graduate Research Assistant
Department of Physics
Texas Tech University

Abstract

In this report, the results of preliminary work for the study of plasma-filled Backward Wave Oscillators (BWO) using the Particle-in-Cell (PIC) code MAGIC is described. After briefly discussing the operating principle of a BWO, the effect of grid heating in MAGIC is illustrated and MAGIC's ability to suppress grid heating is demonstrated. The effects of grid heating suppression on a standard BWO simulations are presented. The primary effect of grid heating suppression on a standard BWO simulation observed is the reduction of the simulated microwave output power. This reduction in output power is mostly likely due to the suppression of space charge waves in the electron beam when grid heating suppression is used. These results suggest that grid heating suppression in MAGIC should not be used in the simulation of plasma-filled BWOs.

A Preliminary Study for Computer Simulations of Plasma-Filled Backward Wave Oscillators

Douglas Young

Introduction

In recent years, a resurgence of interest has occurred in high power microwave (HPM) generation and sources. This recent interest is fueled by the need for high power microwaves in science, industry and in the military.

The Backward Wave Oscillator (BWO) is one particular high power device in which a renewed interest has occurred. This recent interest in the BWO focuses on several novel schemes for increasing their output power. One such scheme uses ripples with increasing amplitude, known as non-uniform slow wave structures. Another method fills the wave guide with plasma. A combination of the two methods mentioned above is also being explored to increase the output power.

Discussion of Problem

Several experiments have been conducted in which the waveguide of a BWO is filled with plasma.[1,2] In these experiments, the presence of the plasma increased the output power of the microwaves generated. PIC simulations of plasma filled BWOs would improve our understanding of why this increase occurs. In this report, preliminary work for studying plasma filled BWOs with the Particle-in-Cell (PIC) code MAGIC, which stands for Magnetic Insulation Code, is presented.

Methodology

This report will begin with a brief review of the theory on BWO microwave generation. The ability of MAGIC to simulate plasmas of the type that will be used in actual experiments is then discussed. The effect of grid heating on MAGIC plasma simulations is examined and MAGIC's ability to suppress grid heating within a typical plasma simulation is demonstrated. Results of additional MAGIC simulations of a typical BWO with the grid heating algorithm are presented to illustrate the effects of the use of grid heating suppression on BWO simulations. For these simulations, a geometry

similar to that used by the UNM BWO Experiment is used.[3] The report will conclude with a summary of the results, a discussion of future work, and a section of acknowledgments.

Results

A. Review of BWO Theory

The geometry of a typical BWO is shown in Figure 1.

BWO WITH Sinusoidal SWS
SWS period = 2.5 cm   Bmax = 3.0 T

Currents = LCC NO NO 0.0 1.0
Electron Phasespace Plot
at t = 1.50E-09 s
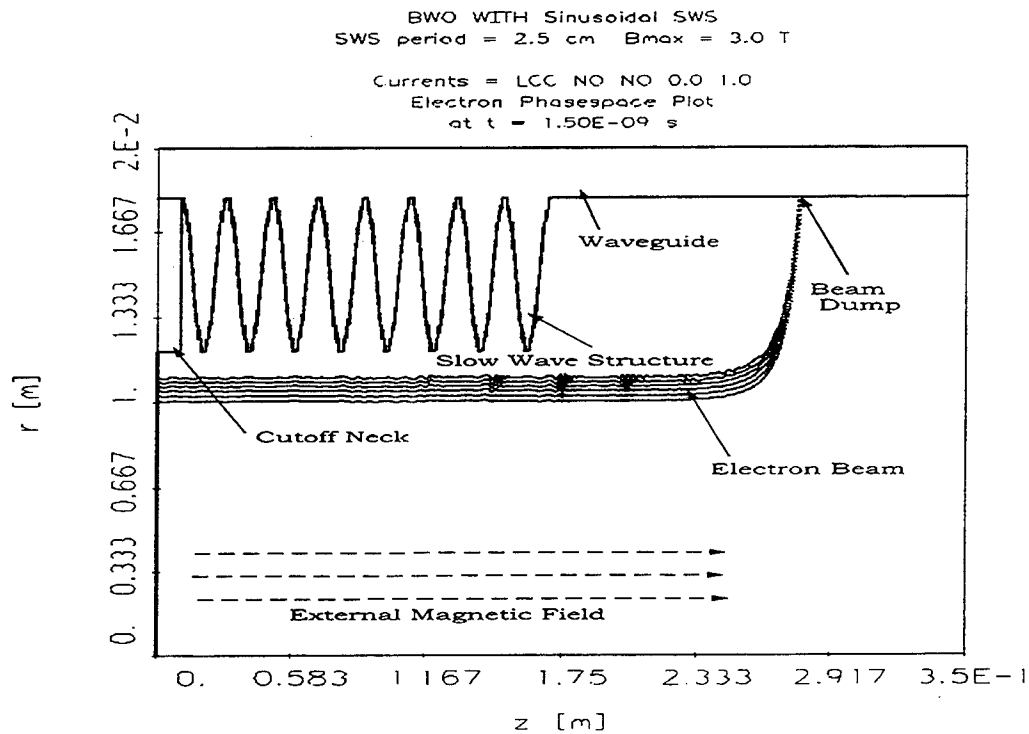
Figure 1. Geometry of BWO Simulation

In a typical BWO, an external axial magnetic field is applied to guide the electron beam down the waveguide and into the beam dump. This electron beam can be thought of as an infinite sequence of masses separated by springs drifting down the waveguide with a velocity v_b. Figure 2 illustrates this model of the electron beam.

22-4
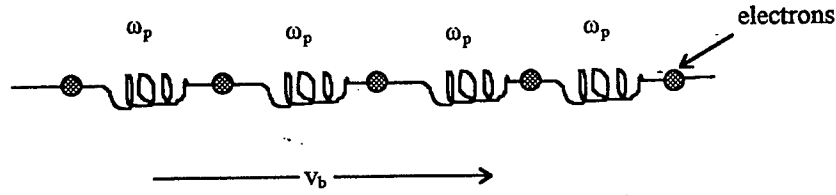
Figure 2. Mass-spring model of electron beam

In this model, a small density perturbation causes the masses, or electrons, to oscillate. These oscillations, in the frame of reference of the electrons in the beam, occur at the electron beam plasma frequency and are known as space charge waves. From this model, a dispersion relation for these space charge waves can be derived[4] and is given by,

$$\omega(k) = v_b k \pm \frac{\omega_p}{\gamma_b^{3/2}} \approx v_b k \quad (1)$$

where v_b is the drift velocity of the electron beam and ω_p is the electron beam plasma frequency,

$$\omega_p = \sqrt{\frac{n_0 e^2}{\varepsilon_0 m_e}} \quad (2)$$

and γ_b is the electron beam relativistic factor,

$$\gamma_b = 1 + \frac{e\phi}{m_e c^2} \quad (3)$$

In these expressions, e is the electronic charge, ϕ is the voltage across the diode, m_e is the electronic mass, c is the speed of light, ε_0 is the permittivity of free space, n_0 is the density of the electron beam, and k is the wave number of the wave.

To understand how a BWO produces microwaves, first consider the interaction of the space charge waves with a standard smooth walled waveguide. This interaction is best described by plotting both the dispersion relations of the waveguide and the electron beam space charge waves. A typical plot of this type is shown in Figure 3. From this graph, it is evident that there can be no intersection of the standard waveguide modes and the space charge waves curve since the waveguide modes always lie above

22-5

the light line (ω=ck) while the space charge waves, represented in Figure 3 by the beam line, lie below

the light line. No intersection of these curves means that any radiation produced by space charge waves

will not propagate inside the waveguide.
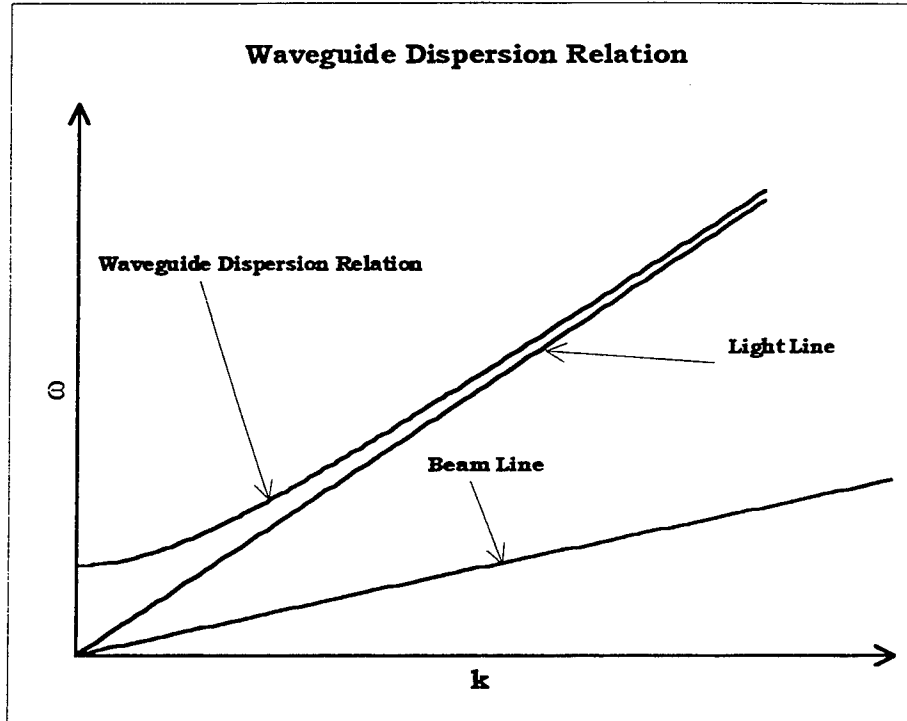
Figure 3. Waveguide dispersion relation

If a periodic ripple is introduced on the waveguide wall, the dispersion relation of the modified

waveguide becomes periodic, with a period which is related to the period of the ripple $h_0 = 2\pi / k_r$,

$$\omega(k) = \omega(k + nk_r) \quad (4)$$

A waveguide that is perturbed with this periodic ripple is know as a slow wave structure (SWS). Figure 4

illustrates the dispersion relation for this slow wave structure. Note that, from this figure, there is now

the possibility for an intersection between the space charge dispersion relation and the SWS dispersion

relation. This intersection means that radiation produced by the space charge waves could be extracted

by the modified waveguide. The intersection labeled B on Figure 4, in which the slope of the SWS

dispersion curve is positive at the intersection, produces a Traveling Wave Tube (TWT) interaction. The

intersection labeled A on Figure 4, in which the slope of the SWS dispersion curve is negative, produces a Backward Wave Oscillator (BWO) interaction.
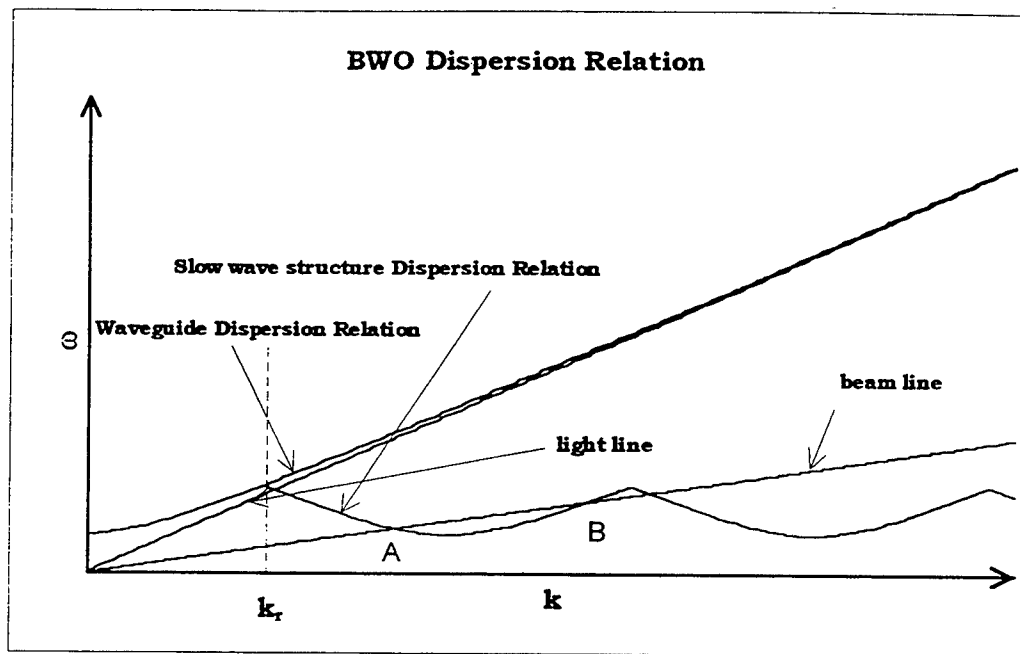
Figure 4. Dispersion Diagram illustrating BWO Operating Principles

The BWO interaction causes space charge oscillations to grow[5], and it is the resulting oscillations that produce the high power microwaves. Figure 5 is a series of phase space plots showing this growth. Figure 6 is an FFT plot of the E_z radiation field at the end of the waveguide showing the radiation produced by the BWO interaction and a plot of the output microwave power.

B. Grid Heating and MAGIC Plasma Simulation

To simulate plasma-filled BWOs, it is first necessary to simulate plasmas with a PIC code. In a PIC code, a plasma can be simulated by populating a portion of the grid with ion and electron macroparticles of equal charge. The electron and ion macroparticles in this simulation are distributed randomly throughout the simulated plasma region, and are given a gaussian thermal velocity distribution.
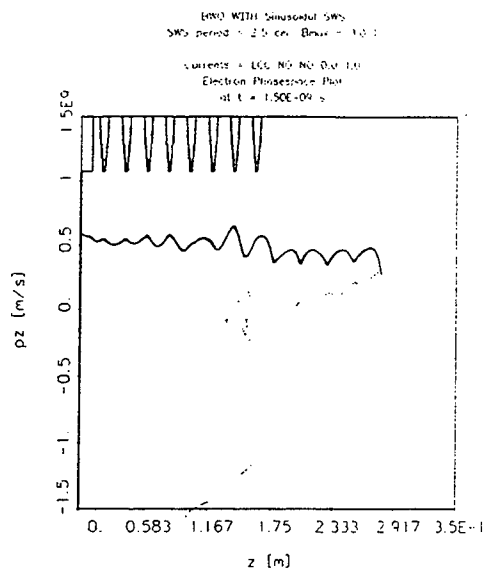
[a] at 1.50 ns
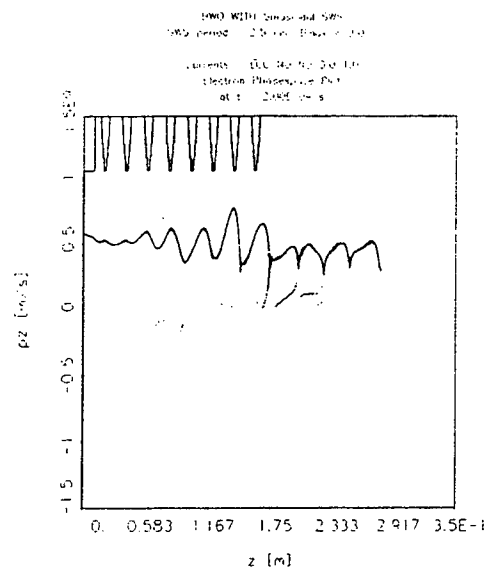
[b] at 2.0 ns
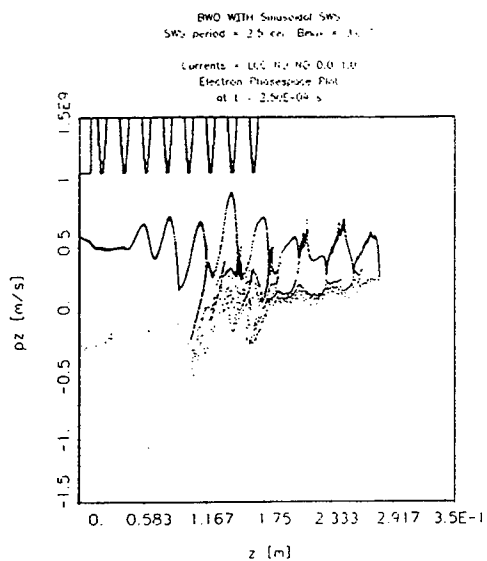
[c] at 2.5 ns
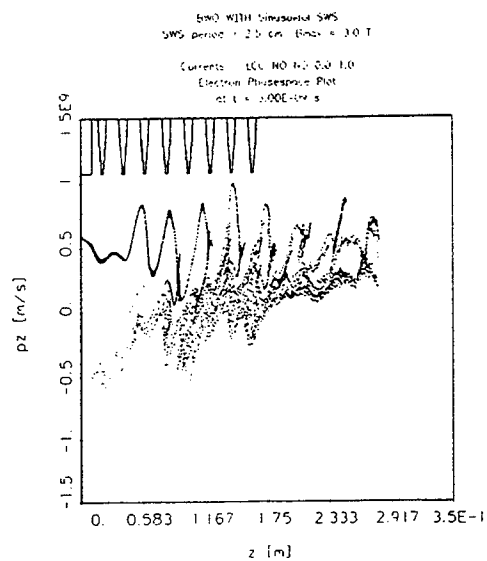
[d] 3.0 ns

Figure 5. Phase Space Plots Showing growth of BWO instability
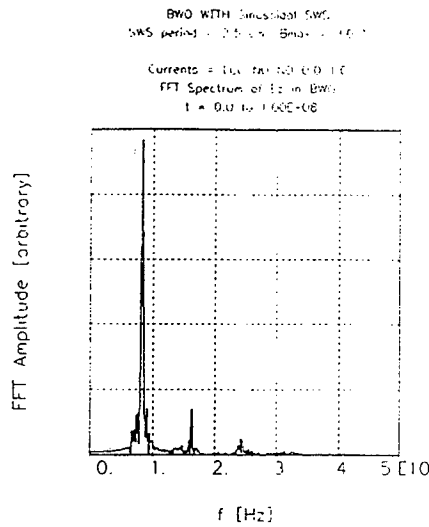
[a] Output Frequency of Standard BWO
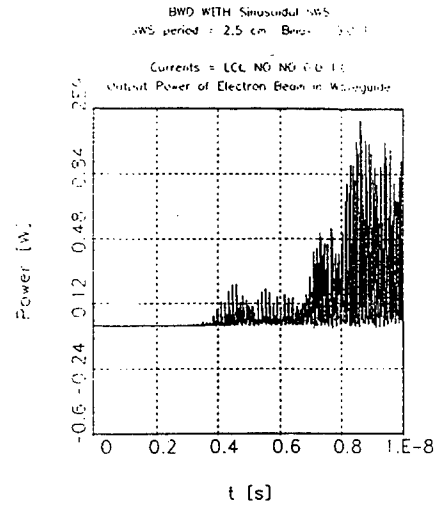
[b] Output Power of Standard BWO

Figure 6. Output Frequency and Power of BWO

In a PIC plasma simulation of the type described above, if the Debye length of the plasma, given by

$$\lambda_D = \sqrt{\frac{\varepsilon_0 kT_e}{n_0 e^2}} \quad (5)$$

with k as Boltzman's constant and T_e the plasma electron temperature, is smaller than the grid size in the simulation, then a non-physical effect known as grid heating will occur.   Grid heating causes the temperature of the plasma to increase until the Debye length of the simulated plasma matches the grid size of the simulation. An example of grid heating in a MAGIC simulation is shown is Figure 7. For this simulation, a waveguide is partially filled with a plasma, generated by the method discussed above. In Figure 7, the increase in the temperature is illustrated by the electrons occupying larger regions of phase space with increasing time.

In MAGIC, grid heating can be suppressed through the algorithm that controls the calculation of current density known as CURRENTS. In the CURRENTS algorithm, a routine can be used, which is known as SUPPERDEBYE and uses the ratio of the Debye length to the grid spacing $\lambda_D / \Delta x$, to

22-9

control grid heating. An example of Magic's ability of suppress grid heating is shown in Figure 8. Comparing this figure with Figure 7, the suppression of grid heating is easily seen.

C. Effects of Grid-Heating Suppression Algorithm on Standard BWO Simulation

Having demonstrated that MAGIC can suppress grid heating, the effects of the grid heating suppression algorithm CURRENTS/SUPPERDEBYE on a standard BWO simulation must be considered. These effects are shown in Figures 9 through 11.

Figure 9 is a comparison of phase space plots of a BWO simulations with the SUPPERDEBYE algorithm. This phase space plot looks very similar to the plot shown in Figure 5 [d] leaving the impression that there is no difference between the two cases. Very little difference is also seen in the frequency spectrums shown in Figure 10 and Figure 6 [a].

However, the output power of the two cases, shown in Figure 9 [c] and Figure 6 [b], does differ sharply. In particular, the output power of the SUPPERDEBYE BWO case is much less than the output power of the Standard BWO case. This difference could be attributed to the SUPPERDEBYE algorithm suppressing the oscillations of the space charge waves. In the SUPERDEBYE simulation, the ratio of the Debye length over the grid size was much smaller that one. It is possible that with a ratio closer to one that the output power in the SUPERDEBYE BWO case would more closely match the standard BWO case.
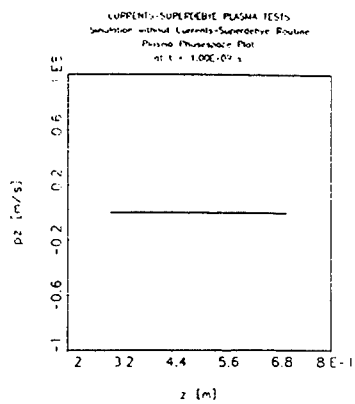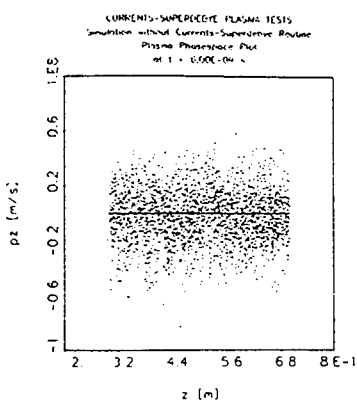
[a] at 1.0 ns
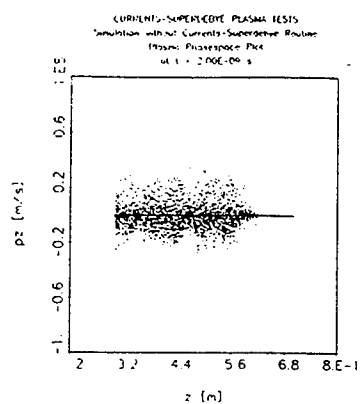
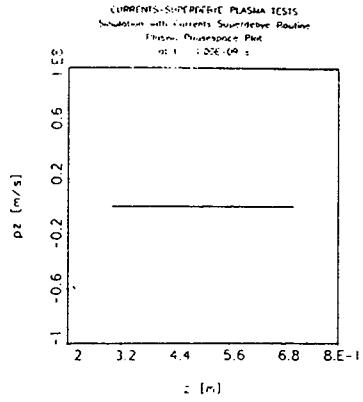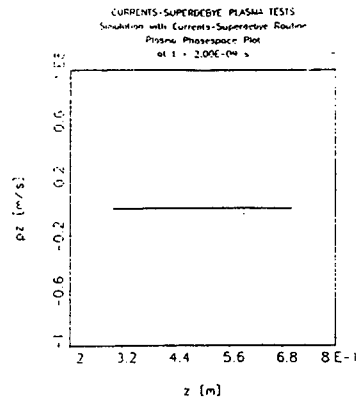[b] at 2.0ns
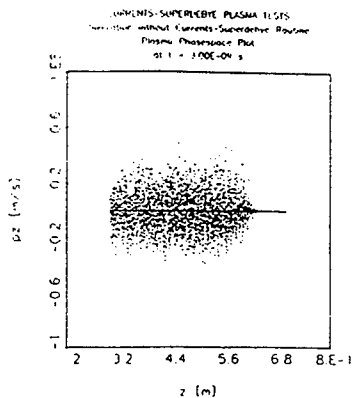
[c] at 3.0 ns
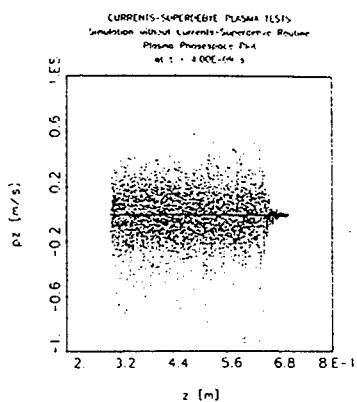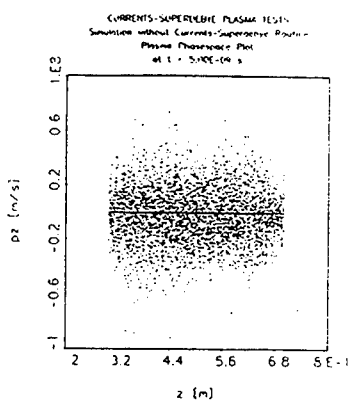
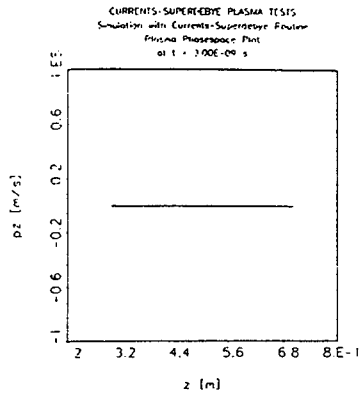[d] at 4.0 ns

[e] at 5.0 ns

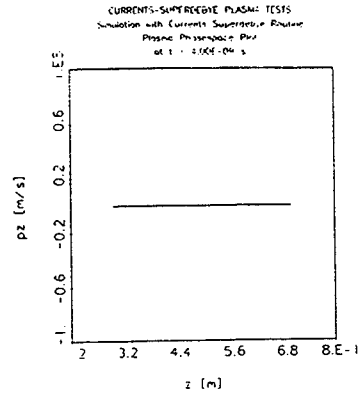[f] at 6.0 ns

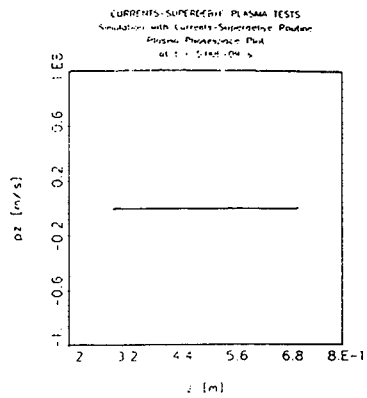Figure 8. Phase space plots illustrating grid heating.
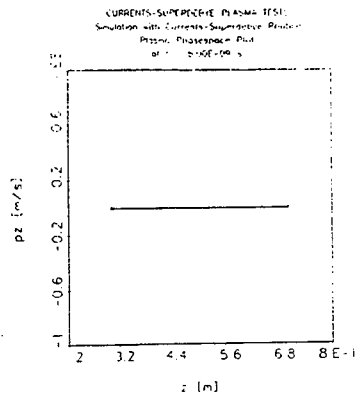
[a] at 1.0 ns

[b] at 2.0 ns
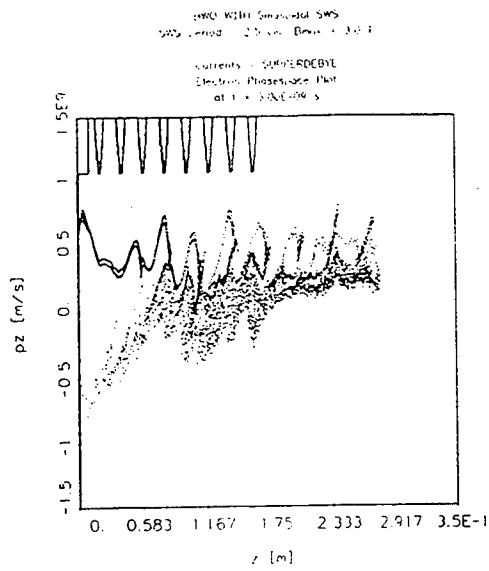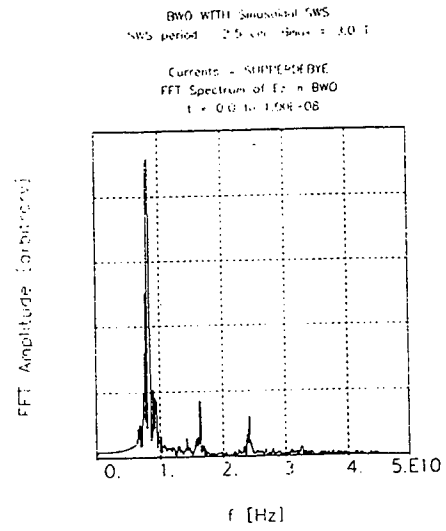
[c] at 3.0 ns

[d] at 4.0 ns
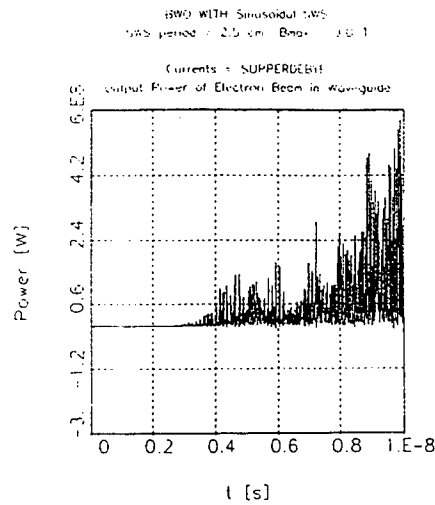
[e] at 5.0 ns

[f] at 6.0 ns

Figure 9. Phase space Plots illustrating Grid Heating Suppression

[a] Phase space plot of BWO with
Grid Heating Suppression

[b] FFT plot of BWO with
Grid Heating Suppression

[c] Output Power of BWO with Grid Heating Suppression

Figure 11. BWO plots with Grid Heating Suppression

Conclusions

In this report, the basic operation principles of high power microwave production in a BWO were reviewed. In this review, the PIC code MAGIC was used to simulate a BWO and illustrate its basic properties. In order to study MAGIC's ability to simulate plasma-filled BWOs, a simple simulation of a waveguide that is partially filled with plasma was done. The non-physical effect of grid-heating was observed in this simple plasma simulation. It was then shown that using the CURRENTS/SUPERDEBYE algorithm in MAGIC, grid heating can be suppressed in MAGIC. However, this grid heating suppression algorithm also reduced the output power in the simulation. It might be possible to use CURRENTS/SUPERDEBYE with $\lambda_D / \Delta x \approx 1$, but this would require either using simulated plasmas with a higher plasma temperature than that in the actual experiment, or reducing the grid step size Δx several orders of magnitude. Since a typical device length is about 1 meter, reducing Δx would dramatically increase the number of cells needed to simulate the problem. The amount of computer time needed to simulate the problem would also dramatically increase as well. Some combination of these two fixes might allow plasma-filled BWO simulations with the grid heating suppression routines. In any case, this report has shown that special care must be taken when using the CURRENTS/SUPPERDEBYE algorithm to suppress grid heating in plasma-filled BWO simulations. In the plasma-filled BWO simulations, it is expected that microwaves will be observed in the simulation. These microwaves will excite the electrons in the simulation and will eventually cause them to be lost through collisions with the waveguide. The same effect would occur with grid heating, only much more quickly. The need for grid heating suppression in plasma-filled BWO's is therefore unnecessary, as long as the effects of grid heating suppression is kept in mind during the simulation.

Acknowledgments

thank Jerry Sasser for making me feel at home in the Plasma Simulation group and for the many

enlightening conversations we had.

References

1.   Y. Carmel, W.R. Lou, T.M. Antonsen, Jr., J. Rodgers, B. Levush, W.W. Destler, and V.L. Granatstein, "Relativistic plasma microwave electronics: Studies of high-power plasma-filled backward-wave oscillators," Phys. Fluids B 4 (7) 2286-2292 (1990).

2.   L.S. Bogdankevich, M.V. Kuzelev, and A.A. Rukhadze, "Plasma mircowave electronics,"Sov. Phys. Usp. 24 (1) 1-16 (1981).

3.   Larald D. Moreland, Edl Schamiloglu, Raymond W. Lemke, S.D. Korovin, V.V. Rostov, A.M. Roitman, Kyle Hendricks, and T.A. Spencer, Efficiency Enhancement of High Power Vacuum BWO's Using Nonuniform Slow Wave Structures," IEEE Plasma Sci. 22 (5) 554-565 (1994).

4.   C.S. Liu and V.K. Tripathi, Interaction of Electromagnetic Waves with Electron Beams and Plasmas, (World Scientific, Singapore, 1994).

5.   John A. Swegle, James W. Poukey, and Gordon T. Leifeste, "Backward wave oscillators with rippled wall resonators: Analytic theory and numerical simulation," Phys. Fluids 28 (9) 2882-2894 (1985).